EXPERIMENTAL AND MODELLING ANALYSIS ON THE PERFORMANCE OF ANISOTROPIC CONDUCTIVE FILMS AS USED IN ELECTRONICS PACKAGING

by

Chunyan Yin

Centre for Numerical Modelling and Process Analysis, School of Computing and Mathematical Sciences, the University of Greenwich, London, U.K.

A thesis submitted in partial fulfilment of the requirements of the University of Greenwich for the Degree of Doctor of Philosophy

November 2006

Abstract

The aim of this research is to understand the failure modes and mechanisms of adhesive materials used to flip-chip bond a silicon die onto a polyimide substrate. The bonding material investigated in this research is called Anisotropic Conductive Film (ACF). This is a promising interconnection material and has gained extensive interest in the electronics packaging industry.

Both experimental and finite element analysis (FEA) methods were used in order to investigate the behaviour of the ACF materials when subjected to certain manufacturing and environmental testing conditions. The manufacturing condition investigated was a subsequent solder reflow process on an ACF flip-chip bonded device. The environmental testing condition investigated was the moisture test.

For the manufacturing condition, both experimental and modelling results demonstrate the impact of a subsequent reflow process on the behaviour of the ACF joint. Typical failures observed after this process were cracks at the pad/particle interface. This failure mode was more severe with a higher peak reflow temperature. This was also found using FEA where high tensile stresses were predicted in these regions. FEA modelling was also used to help identify the mechanisms leading to these failures. This is primarily due to the Coefficient of Thermal Expansion (CTE) miss-match in the materials and the elastic/plastic deformation behaviour of the conductive particle. Important design variables that can minimise these failures are the Young's Modulus and CTE of the adhesive and the height of the bump on the die.

For the environmental testing condition, an autoclave test at 121°C, 100%RH and pressure of 2atm was used. More than 85% of the ACF joints failed during the first 24 hours of testing. The failure mode observed was cracking along the interface between the adhesive and substrate and pad. A macro-micro modelling approach was used to help identify the mechanisms leading to these failures. It was found that most of the damage is caused by moisture diffusion and associated swelling. Important design variables that will help minimise this mode of failure are: Coefficient of Moisture Expansion (CME) and Young's Modulus of the adhesive and the height of the bump on the die.

Acknowledgments

I would like to sincerely thank both of my supervisors, Prof. Chris Bailey and Dr. Hua Lu for their supervision, guidance and encouragement during each stage of my study. Also I would like to thank all my colleagues at the University of Greenwich who have given me advices and shown the interests to my research.

I would like to express my deep gratitude to Prof. Yan-Cheong Chan within the Department of Electronic Engineering at City University of Hong Kong for initiating this joint Ph.D. program and all the support offered throughout my study. I would like to thank my colleagues at City University of Hong Kong for the support in the experimental work and in particular, Ms Sai Choo Tan, for her time and kind assistance for the work conducted at EPA Centre.

I would like to thank my parents for their encouragement through my Ph.D. study. My husband, Mr Guangbin Dou who is pursuing his Ph.D. at Loughborough University is deserved to be appreciated for his support and understanding, during the last ten years, we have been studying side by side all the time.

Finally, I would like to acknowledge the University of Greenwich and City University of Hong Kong for the financial support to undertake this research.

Table of Contents

List of Figures

List of Tables

Glossary

ACA	Anisotropic Conductive Adhesive
ACF	Anisotropic Conductive Film
ACP	Anisotropic Conductive Paste
AMLCD	Active Matrix Liquid Crystal Display
BGA	Ball Grid Array
CAD	Computer Aided Design
CFD	Computational Fluid Dynamic
COF	Chip on Flex
COG	Chip on Glass
CRT's	Cathode Ray Tubes
CTE	Coefficient of Thermal Expansion
CME	Coefficient of Moisture Expansion
DC	Direct Current
DOE	Design of Experiment
DSC	Differential Scanning Calorimeter
ECA	Electrically Conductive Adhesive
ELV	End of Life Vehicles
FCOF	Flip Chip on Flex
FEA	Finite Element Analysis
FEM	Finite Element Method
FPC	Flexible Printed Circuit
FPP	Four Point Probe
FTIR	Fourier Transform Infrared Spectrophotometer
FV	Finite Volume
HDD	Hard disk drive

HGA	Head Gimbal Assembly
IC	Integrated Chip
ICA	Isotropic Conductive Adhesive
I/O	Input/Output
ITO	Indium-Tin-Oxide
LCD	Liquid Crystal Display
LCP	Liquid Crystal Polymer
NCA	Non Conductive Adhesive
PCB	Printed Circuit Board
PCT	Pressure Cooker Test
PEN	Polyethylene Napthalate
PET	Polyethylene Terephthalate
RH	Relative Humidity
RS	Response Surface
RoHS	Restriction of Hazardous Substrates
SAC	Tin-Silver-Copper
SEM	Scanning Electronic Micrographs
SMT	Surface Mount Technology
TAB	Tape Automated Bonding
Tg	Glass Transition Temperature
2D	Two dimensional
3D	Three dimensional
UBM	Under Bump Metallization
UV	Ultraviolet
VFMW	Variable Frequency Microwave
WEEE	Waste from Electrical and Electronic Equipment

Chapter 1

Introduction

This Chapter describes the background to the research undertaken and the aims. Also discussed are the layout of this thesis and a summary of the achievements made from this research.

1.1 Background

Major trends for today's electronic products are to make them smaller, lighter and cheaper, while at the same time more friendly, functional, and reliable. These demands have induced the rapid development of high-density, multi-function electronic components with increasing functionality packaged into smaller and smaller spaces. For example, in 1992 the typical video camera consisted of over 1800 components, with a density of 12 components per cm^2, and occupied 2380mm^3. In 1998 the video camera consisted of only 848 components, with a density of 21 components per cm^2 and occupied only 1598mm^3. The size of the video camera was expected to be further reduced by 50 percent by year 2002 [1].

Electronics packaging is a key technology that must be addressed in making robust, miniaturized and integrated products. Packaging is defined as the bridge that connects the Integrated Circuit (IC) and other components into a system-level board to form the product [1][3]. Figure 1.1 shows a schematic representation of the packaging

hierarchy. The first interconnection occurs at the level where the input/output (I/O) pads on the IC are bonded to a substrate to form the first level of the packaging. This stage of packaging is referred to as an IC assembly. The second interconnection is achieved between the lead frame of the first-level package and the electrically conductive pads on the printed circuit board (PCB). This is referred to as a board assembly. The system-level board, with components assembled on either or both sides, typically completes the system.
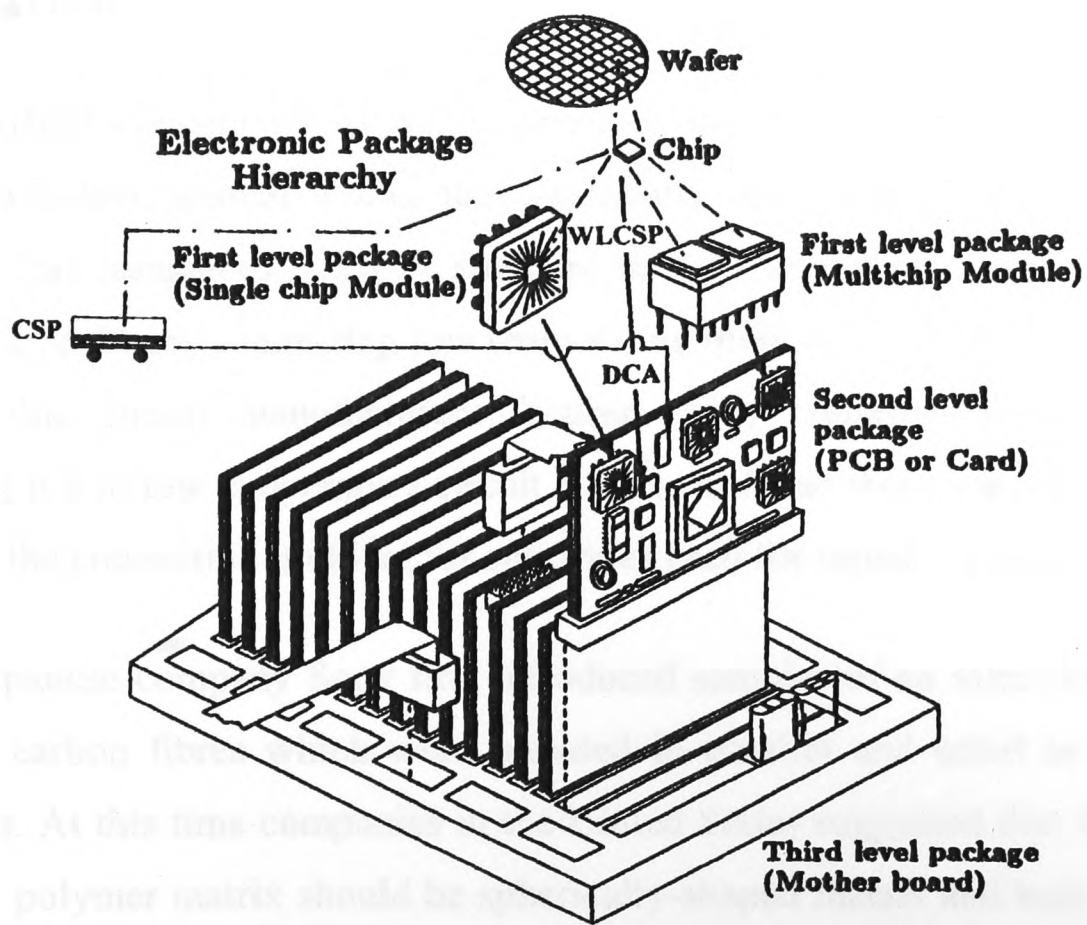
Figure 1.1: The first three levels in the electronics packaging [1]

Different packaging technologies and materials are required for different IC devices and applications. High density, high reliability, high yield and low cost as well as green packaging (lead-free) are currently the main issues in designing and developing electronic packaging technologies. One material that is a central theme to this research is anisotropic conductive adhesive (ACA). This material has the

capability to produce high density I/O using low temperature assembly which is very attractive for many applications which cannot withstand the high temperatures associated with metallic solder connections. Liquid Crystal Displays (LCDs) are one application where anisotropic conductive materials have made a major impact.

ACAs consist of electrically conductive particles within a polymer matrix. This material can be placed between an IC and a substrate to form the electrical interconnection. This connection is anisotropic as the current can only travel in the vertical direction.

The earliest concept of ACAs occurred in the 1950s and since then extensive research and development within the community has taken place [4]. In the early 1980s, several companies, such as Sheldahl in the United States and Sony in Japan, were facing problems connecting low temperature materials. At this time Sheldahl and other flexible circuit manufacturers focused many resources to the problem of connecting ICs to low temperature circuit boards. In Japan there was a concerted effort in solving the connection problem for substrates used for liquid crystal displays.

The Japanese company Sony first introduced samples of an interconnect film that contained carbon fibres which were oriented in parallel and acted as the electrical conductors. At this time companies in the United States suggested that the conductors within the polymer matrix should be spherically-shaped metals and both Sheldahl and Amp produced ACAs using silver particles in 1985. Since then, considerable research has been undertaken around the world to develop new ACA materials. Today, ACAs are available in just every form and type ranging from liquid pastes to dry films, using thermosets and thermoplastics.

Anisotropic Conductive Films (ACFs) are now popular interconnect materials especially in the flat-panel display, disk drive and smart card industries, where the traditional solder alloys are becoming very difficult to achieve both fine pitch and low temperature assembly requirements. For example, the requirements for better resolution and colour quality of LCD panels induce higher numbers of pixels and more

I/Os to be interconnected, thus the pitch size (i.e. the distance between the I/O pads) is becoming much finer. Using ACFs allows fine pitch connections of less than 100μm which is generally impossible to be connected using traditional solder alloys [5]. Lower processing temperature is another strength of ACFs compared to solder alloys since many components are sensitive to heat and cannot survive the solder reflow process where the peak temperatures can be as high as 250°C. For many electronic products and materials this temperature is far too high.

Adopting ACFs provides significant advantages of fine pitch connections and low temperature assembly. The material is also lead-free and hence satisfies many of the current environmental legislation restrictions stated in the European directives. The major concern with ACF materials is their reliability performance. Compared with the traditional metallic solder materials, especially the tin-lead solders, ACFs are very new with little documented reliability data.

1.2 Aims and Objectives of This Research

This research is motivated by the desire to improve the reliability performance of ACF materials and interconnections. The methodology used to undertake this research is based around both experimental work and finite element modelling.

The majority of published research for ACFs has focused on the bonding parameters (i.e. bonding temperature, pressure and time) and the behaviour of the material during accelerated life testing under thermal, vibration and moisture induced conditions. Although much work has been done, there are still some areas which are not fully understood and some questions still remain.

The electronic manufacturing industry is very interested in combining ACFs and solders onto the same board. This is for applications which require the fine pitch advantage of ACFs and the high reliability advantage of solders. The concern of this

combining process is the behaviour of the ACFs when subjected to the high reflow temperatures required for solders.

Humidity and moisture diffusion into the ACF material results in stresses and is probably the major cause of failures with these materials [7][8][9][10][11][12][13]. Currently the failure mechanisms are still not well understood. One of the limitations of previous modelling research is mostly using the two dimensional (2D) models due to the difficulties caused by the multi-length nature of the problem, and thus the global effect was ignored. In some cases, three dimensional (3D) models of ACF flip chips were built, but the structure of each ACF joint was simplified [48][49][61].

The overall aims of this research project is to use both computer modelling and experimental failure analysis to investigate:

a) The ability to use both ACFs and solders on the same board. Can the ACF material withstand the high solder reflow temperatures?

b) The failure mechanisms of ACF materials when subjected to high humidity environments.

These aims will be achieved through:

1) Investigate on Flip-chip assembled IC devices with ACF materials using different bonding conditions. Subject these devices to solder reflow temperatures and undertake a failure analysis study.

2) Building finite element models of the above assembly and predicting the locations of high stress throughout the package and ACF materials when subjected to a solder reflow temperature.

3) Using Flip-chip assembly of ICs onto flex substrates with ACFs and subjecting these to high humidity environments. Undertaking a failure analysis study.

4) Building finite element models using a macro-micro approach to predict the behaviour of the ACF materials when subjected to a humidity environment.

These aims and objectives will provide an insight into the stress magnitudes and locations for ACF joints when subjected to a solder reflow profile and to investigate important design parameters that can minimise these stresses. With regards to the performance of ACF joints when subjected to high humidity test environments the study will provide an insight into the failure mechanisms and how specific changes to the geometry/material properties can increase the reliability of these materials. The study will also show how novel modelling technology can be used with experiments to help characterize the performance of electronical packaging materials.

1.3 Layout of This Thesis

There are 7 chapters in this thesis. The research background is presented in Chapter 1, which outlines the challenges in the electronics industry at present and explains why the research on ACFs is important.

In Chapter 2, a literature review of the recent activities about ACA assemblies is presented. More than 50 papers are referred and classified into two main areas: experiments and computational modelling.

An introduction of flip chip technology is given in Chapter 3, the most common connection materials used in flip chips ranging from solder alloys to electronically conductive adhesives (ECAs) are described. The concepts of reliability and failure analysis of electronic products are discussed and the applications of ACFs in LCDs and disc drives are presented.

Chapter 4 details the whole process of the experimental work from sample preparation to reliability testing. The effects of bonding parameters, solder reflow temperature and moisture absorption on the electrical/reliability performance of ACF

joints are studied and the results are presented in joint resistance, curing degree, and Scanning Electronic Micrographs (SEM).

In Chapter 5, modelling analysis on the performance of ACF joints during solder reflow process is conducted. The parametric study considers the effect of the coefficient of thermal expansion (CTE), Young's modulus of adhesive and bump height on the interfacial stresses in an ACF joint. The failure mechanism of ACF joints during solder reflow is discussed based on both modelling and experimental results.

The moisture effects on the reliability performance of an ACF flip chip assembly are discussed in Chapter 6. The wetness fraction technique is introduced and the moisture diffusion in an ACF flip chip under autoclave test conditions is predicted. The moisture induced stress is analyzed and the effects of the coefficient of moisture expansion (CME) and Young's modulus of adhesive, and bump height, on the interfacial stresses are presented. The failure mechanism of the ACF joints in autoclave test is discussed based on both modelling and experimental results.

Finally, a summary of the achievements from this research and the possible further work are discussed in Chapter 7.

1.4 Original Techniques and Findings

Findings and developments from this research can be categorised as follows:

1. Conditions for the compatibility of ACF with traditional soldering technology have been demonstrated. Both reliability testing and computational modelling have been used to identify the impact of geometry and material properties on the performance of the ACFs after being subjected to the high reflow temperatures associated with soldering.

2. A moisture diffusion model was implemented into the finite element software: PHYSICA. This enabled the prediction of temperature, moisture and thermal/hygro stresses for the packaging components investigated.

3. A macro-micro modelling technique was developed to model phenomena taking place at the package (macro) and joint (micro) levels. 3D models of ACF flip chip assembly at both the macro and micro levels were developed.

4. In the solder reflow, the tensile stress along the interface between the conductive particle and metal pad tends to lift the bump from the pad causing the loss of the contact area and the increase in the contact resistance, this interfacial stress is much affected by the CTE value of the adhesive and the reflow peak temperature.

5. During the autoclave test, moisture diffuses mostly through the flexible substrate into the ACF layer; most ACF joints failed in the first 24 hours upon the moisture absorption. The moisture induced swelling effect contributes to the joint opening rather than the temperature effect.

This research work was involved in a collaboration research programme between the University of Greenwich and City University of Hong Kong. The computer modelling part of the work was undertaken at the University of Greenwich, and the experimental part of the work was undertaken at City University of Hong Kong. So far, this research work has resulted in 3 journal papers [126][127][128], 8 international conference papers [129][130][131][133][134][135][136][137] and 1 article for a trade magazine [138].

Chapter 2

Literature Review

This Chapter reviews the public domain literature on research for ACA materials. More than 50 publications are referred in order to provide a concise, structured overview in this research area. Most of the recent research is summarized and classified into two main areas, experiments and computer modelling. The research work undertaken by using experimental technique is presented first, and followed by computer modelling.

2.1 Experimental Studies

There is plenty of research can be found using experimental techniques in the academic literature. The topics can be classified into three main areas: ACA materials, curing method and bonding process, and environmental testing.

2.1.1 ACA Materials

ACA consists of an adhesive matrix and randomly distributed conductive particles. During the bonding process, some of the conductive particles are captured between the chip bumps and substrate pads, deformed to achieve the electrical path between the chip and substrate. The cured adhesive helps maintain the deformation of the conductive particles after the bonding process is finished. A typical ACA connection system is shown in Figure 2.1.
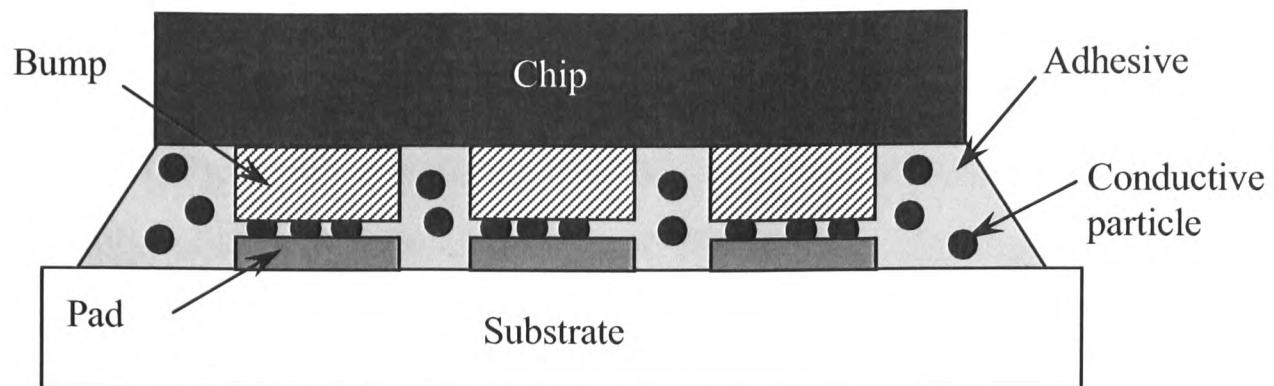
Figure 2.1: A typical ACA connection system

ACAs are available in two different forms, film and paste, which are called as ACF and anisotropic conductive paste (ACP) respectively. Also there are two types of adhesive matrix available: thermoplastics and thermosets. Thermoplastic adhesives are thermally reversible and therefore have the good rework ability since they melt if heated to high temperature. The cross-linked thermoset adhesives, however, are not thermally reversible and are more mechanically stable in service temperature. Generally, the thermosets form stronger bonds that are more durable than the thermoplastics.

Metal coated polymer particles are commonly used in fine pitch interconnection because the distribution of the diameter of the particles is fairly uniform, hence they can be dispersed uniformly into adhesive resin [91]. This kind of particle can be easily deformed and the high connection reliability can be expected based on the elastic deformation of the particles. Besides the metal coated polymer particles, metal particles are also available such as nickel for connecting the metal electrodes which can easily be oxidized.

ACAs can be used on several kinds of substrates, such as flex substrate, organic and ceramic substrates, Indium-Tin-Oxide (ITO) coated glass. The flex substrate is a flexible material that is widely used for the connection between the LCD to LCD drive ICs. Such assembly needs a dedicated machine to align the components and cure the

ACAs accurately. Much experiment research using flex substrates are found in the literature from the Department of Electronic Engineering, City University of Hong Kong [15][16][17][18][33][34][36][37]. Ceramic and organic substrates were studied by Ogunjimi *et al.* [19], it was concluded that the uniform conductivity and high yield were more readily obtained with ceramic substrates than the organics; however, improvements to the organic substrate pad geometries may increase substrate performance. A review of using chip on glass (COG) technologies in LCD applications has been undertaken [14]. The main advantages of using COG are the reduction in the cost and the size of the display module, since COG allows the chip drive to be bonded directly to the ITO traces on the glass. However, COG technology does cause difficulties, for example, the bonding pressure imposed on the backside of the IC must be controlled precisely, since an excessive pressure on bumps can cause glass breakage.

Due to the cost of the chip bumping process, bumpless dies are under investigation for the possibilities to be used in ACA assemblies. Without bumps, the bonding surface of a bumpless die is flat and normally made of Aluminium (Al) surrounded by a SiN insulation layer as shown in Figure 2.2.
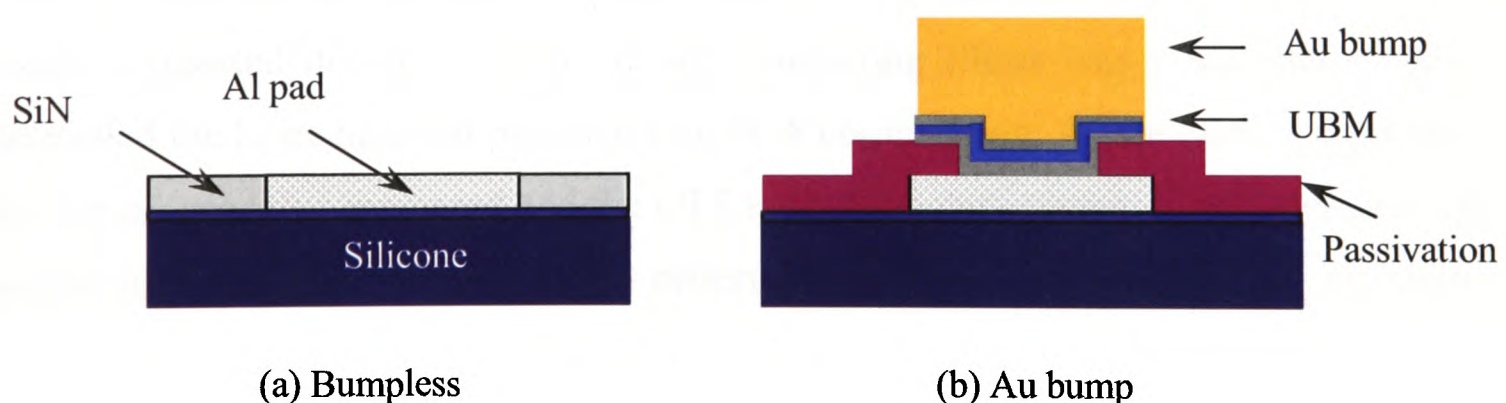
(a) Bumpless   (b) Au bump

Figure 2.2: Structure of bumpless and Au bump dies

The main concern of using bumpless dies is the oxidation of the Al after exposure to the high temperature and humidity environment which may cause an increase in the joint resistance [91]. The adhesion strength between the aluminium surface and the

11

cured adhesive was studied by Zhang *et al.* [18]. Good performance was observed after considering the influence of bonding pressure, bonding temperature and moisture absorption. Strength between the ACFs and the aluminium was not affected seriously by bonding pressure but it increased with bonding temperature. It was suggested that the oxidation reaction could provide a fresh rough surface that may enhance adhesion strength. Tan *et al.* [9] reported the reliability performance of ACF flip chip assemblies using bumpless dies during the pressure cook testing, the joint resistance increased during the test and some micro cracks were observed along the interface between the copper trace and the adhesive. The formation of the oxidation layer on the top surface of the aluminium metallization was concluded as one of the main reasons for stress-corrosion cracking.

The reliability performance of the ACF filled with nickel particles or metal coated polymer particles during the thermal cycling test was compared by Frisk *et al.* [21]. The ACF filled with metal coated polymer particles showed less delamination after reliability testing, the nickel particles were more rigid than polymer particles and had less potential to compensate the expansion of the adhesive matrix when the temperature increased. Paik *et al.* [22] studied the effect of the non-conducting silica fillers on the thermo-mechanical performance of the modified ACA materials. The results suggested that the content of non-conducting fillers was a key factor which controlled the basic material properties of ACA composition. As the content increased, the storage modulus increased and the CTE below the glass transition temperature (Tg) decreased. The changes in these material properties induced better reliability performance of ACA packaging when using higher content of non-conducting fillers. Yim *et al.* [23] proved the effect of the CTE of the ACA on the thermal strain distribution in an ACA assembly, the thermal strain decreased proportional to the CTE of ACA. In another paper [24], the same group studied how to improve the thermal conductivity by incorporating silicon carbide (SiC) fillers into the ACA formulation.

Besides the filler types, the structure of ACF was also studied. The structure of a double layer ACF is shown in Figure 2.3. Compared to the single layer ACF, double

layer ACF consists of a layer filled by conductive particles and an additional non-filled layer. It has been demonstrated that the number of conducting particles trapped between metal pads in a double layer ACF assembly was much higher than those in a single layer ACF. In this case, the risk of short circuits occurring in the double layer ACFs was expected to be lower than that in the single layer ACFs. Chiu *et al.* [95] studied the possibility of short-circuiting between adjacent joints in fine pitch ACF interconnections under the effects of electric field using both kinds of ACFs. The double layer ACFs consisting of nickel/gold (Ni/Au) coated particles showed the similar performance as the single layer ACFs which contains Ni/Au coated particles with insulation layer. For both kinds of ACFs, the possibility of short circuiting occurring is highly dependent on the curing degree of the adhesive. Curing degree above 80% was suggested to achieve stable conductive adhesive joints without short-circuiting under the effects of electric field.
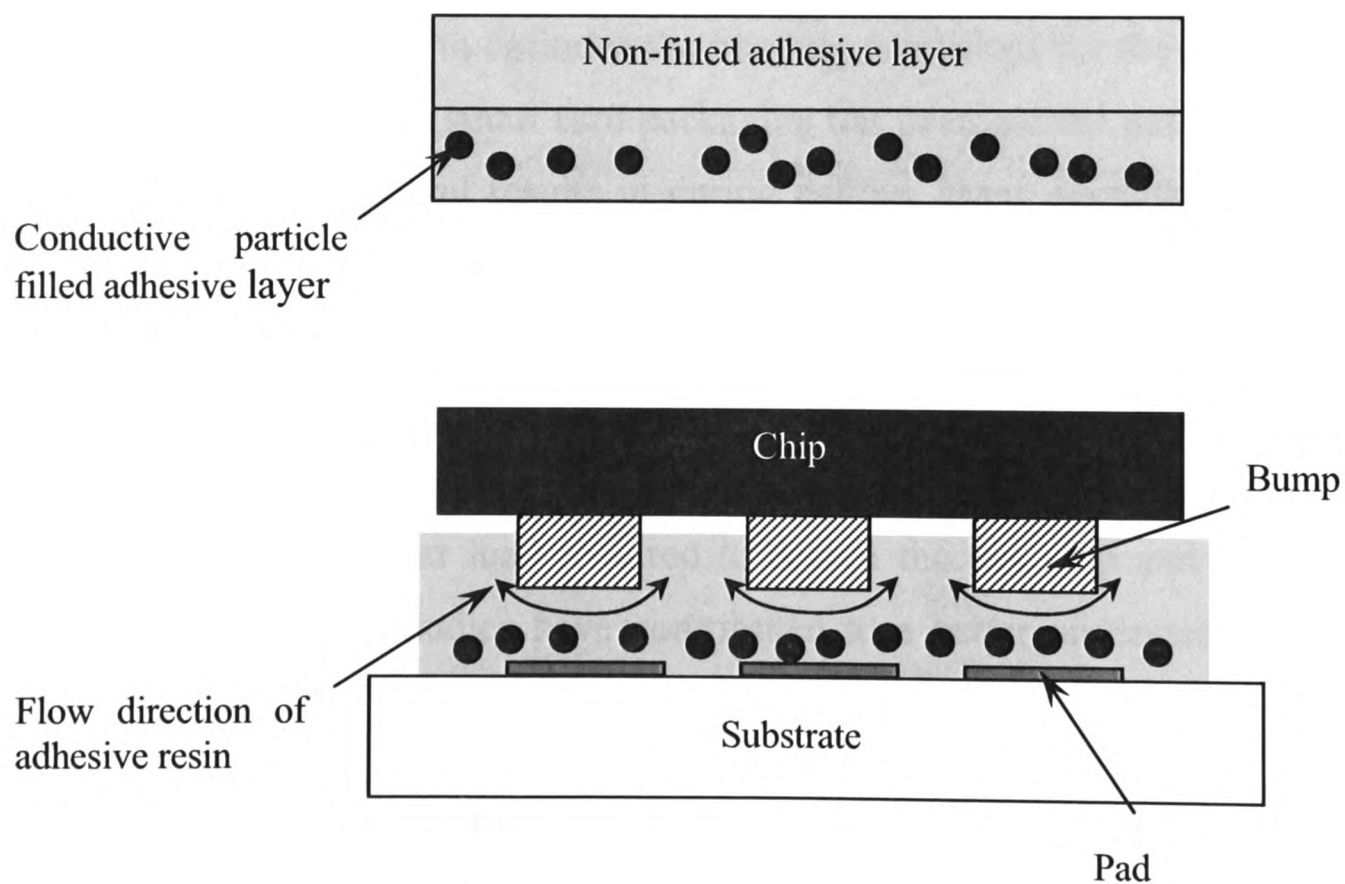
Figure 2.3: Structure of a double layer ACF and its assembly

2.1.2 Curing Methods and Bonding Parameters

The demand for lighter, faster, and smaller microelectronic devices has created a need for new materials and new material processing methods. One of the biggest contributions to the processing time for advanced, high performance ICs and for packages is the time required to cure polymer dielectrics. A number of papers have focused on finding alternatives to thermal processing techniques for curing polymer dielectrics [24]. There are three kinds of curing methods that can be used for ACA assemblies, thermal curing, ultraviolet (UV) curing and microwave curing. Currently, most of ACA assemblies are finished by thermal curing and there is plenty of research that has been focused on the reliability performance of thermal curing joints.

ACAs cured by UV radiation offers several advantages over the conventional thermal curing process, these include rapid cure, little to no emission of volatile organic compounds and without affecting other components in the assembly [25]. Recent developed UV type ACAs have been suggested for use in heat sensitive electronics packages. In order to optimize the bonding conditions for the fabrication of UV curable ACA, research on smart card packaging has been carried out [15][16][17]. By comparing the experimental results in curing degree, shear strength of the ACA joint and the reading distance of the smart card samples, a set of parameters which gave better performance of the chip on flex (COF) bonding were determined. The higher UV light intensity, the longer exposure time led to a higher curing degree of the ACAs. The longer the post-curing time and the higher pre-bonding light activation intensity, the greater the shear load required to detach the test chip and the flexible substrate. These reliability studies have contributed to a better understanding of the failure mechanism of the UV cured ACA joints in smart card applications.

Microwave heating can significantly speed up the curing process of polymer and polymer-based composites. It also offers other advantages over conventional thermal processing techniques, such as selective heating of materials through differential absorption, penetrating radiation, controllable electric field distribution, and self-limiting reactions [26][27]. Therefore, a number of researchers have recently

investigated the use of microwave radiation to cure adhesive joints [28][29][30], and single mode microwave cured adhesives for electronics packaging applications have been developed [31]. Recent theoretical work has studied the microwave transmission through the electrically conductive adhesive (ECA), heat generation and transfer inside the ECA and subsequently the microwave heating rate of the ECA. It showed that the penetration depth of the skin effect in the metal filler was significantly smaller than the one of a bulk metal material. The heat generation e.g. microwave power absorption was negligible in the metal filler due to its high electric conductivity [28]. Islam *et al.* [29] have studied the microwave preheating mechanism in order to decrease the bonding temperature of ACA assemblies and suggested if the microwave preheating was used for 2~3 seconds prior to the final bonding, the maximum curing temperature could be reduced by 10 to 170°C. Wang *et al.* [30] introduced a new technology called Variable Frequency Microwave (VFMW) and demonstrated it's capability in curing metal-filled ECAs.

With regards to the thermal curing joint, there are plenty of papers about the effects of the bonding parameters on the electrical and reliability performance of ACF joints [32][33][34][35][92]. It was proved that the performance of ACF interconnects was much affected by the curing level of the adhesive and the transformation degree of conductive particles which were mainly determined by the bonding parameters such as bonding pressure, bonding temperature and bonding time. The curing degree also affected the adhesion strength between the adhesive and the flex substrate. Hence the adhesion strength increased with the curing degree [36]. Tan *et al.* studied the thermal stability of ACF joints bonded at different bonding temperature ranging from 160°C to 225°C. ACF cured at a higher bonding temperature was thermally less stable, especially at 225°C as compared to at a lower bonding temperature. According to the Fourier Transform Infrared Spectrophotometer (FTIR) test results, high bonding temperature would promote a thermal oxidation reaction, this would later affect the reliability performance of the ACF [37].

2.1.3 Environmental Testing

Reliability of ACA assembles has presented a big challenge to the replacement of traditional soldering. The moisture effect on ACA packaging has been acknowledged as a key reliability issue and was studied experimentally [8][9][10][38]. Cao *et al.* [38] studied the interfacial adhesion of ACA assemblies under different environment conditions and found that the interfacial fracture toughness decreased by 25% after 48 hours exposure at 85°C/85%RH condition. The fracture usually occurred at the adhesive/polyimide substrate interface. It was also found that the moisture uptake was directly proportional to temperature and time as shown in Figure 2.4, where the higher the temperature, the higher the saturated moisture content was.
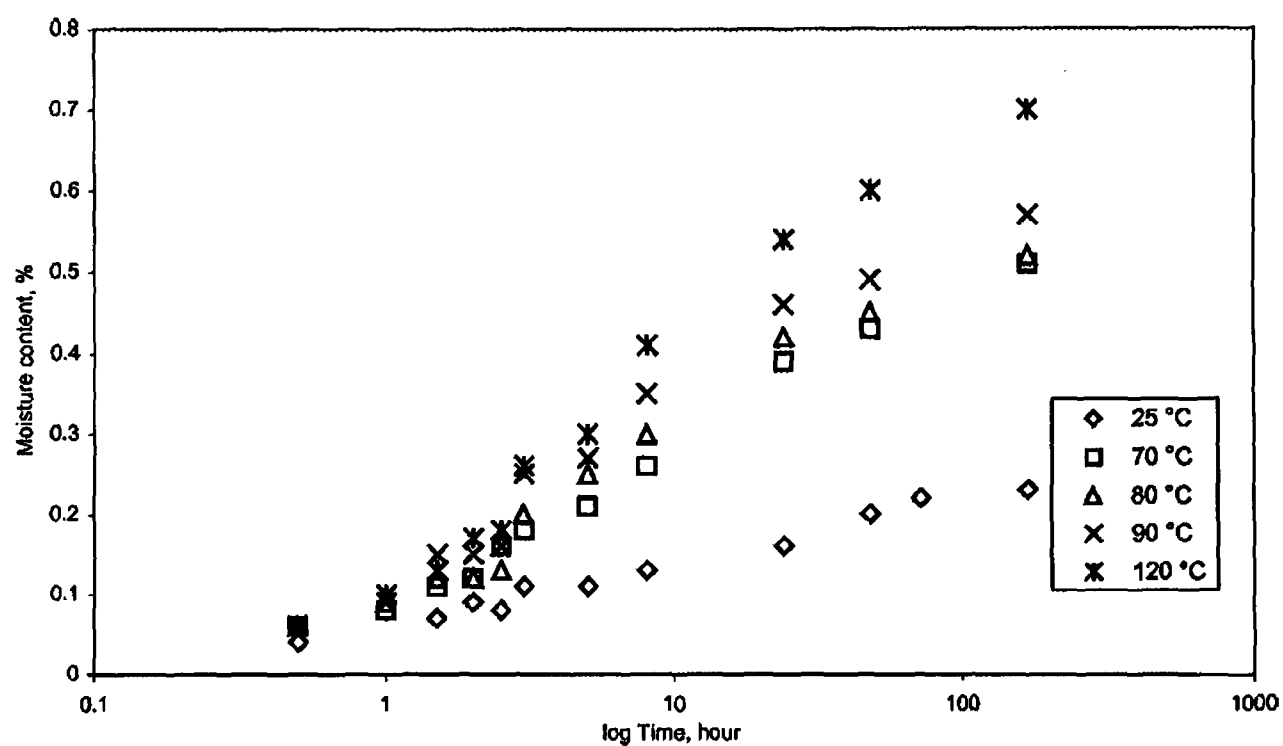
Figure 2.4: Water absorption at five temperature levels (100%RH, 1atm)
(courtesy of Cao *et al.* [38])

The effect of moisture and temperature on the interfacial toughness of a polymer/metal interface was studied by Ferguson *et al.* [8], the results proved that the interfacial toughness was severely affected by the presence of moisture rather than temperature and the dominant failure mechanism for the reliability of the interface was attributed to moisture being directly present at the underfill/copper interface. Moisture

was believed to be the most important factor in the degradation of an IC flip chip bonded on flexible substrates, especially cyclic exposure of adhesives to humidity and temperature was much more harmful to the quality of the flip chip on foil adhesive interconnects than continuous loading [44]. Lam *et al.* [40] developed a chemical kinetic model for describing the stress-assisted hydration of adhesion bonds; the model revealed that time to failure was dependent on the saturation water content, the stress gradient, and the water concentration gradient and was exponentially dependent on the peak stress. It was concluded that the bond degradation was governed by time-dependent stress-assisted hydration rather than governed by the water concentration alone.

Both the thermal cycling test (-40°C to 85°C) and humidity test (85°C/85%RH) were carried out by Frisk *et al.* [21] using ACF flip chip on Liquid crystal polymer (LCP) flexible substrate, delaminations were found within the ACF samples after 500 hours thermal cycling test, however, no delamination was found in the test samples after the humidity test. The thermal cycling reliability of ACF flip chips on organic substrates was studied by Kwon *et al.* [41]. The thermal induced deformation and warpages were investigated using in situ high sensitivity moiré interferometry and the effects of ACF materials on the thermal strain and susceptibility to delamination were studied. It suggested that the ACF properties had a significant role in overall reliability during thermal cycling testing, low CTE and high modulus can reduce the thermally induced shear strain in ACF layer and increased the overall thermal cycling lifetime. Ali *et al.* [42] also reported that the glass transition temperature of ACF had a significant effect on the reliability during the thermal cycling test. The test samples showed more increase in contact resistance when the thermal cycling profile exceeded the Tg of the ACF. Especially, the reliability of small pitch size flip chip on flex interconnections (pitch size < 80μm) was tested in 85°C/85%RH environment and -40 to 125°C thermal shock trials. It was suggested that reliable joints could be achieved by using suitable adhesive and optimum pad design [43].

The SMT-compatibility of adhesive flip chip on foil interconnections with 40μm pitch was studied by Vries et al. [45]. The samples were subjected to a certain well-defined humid environment (168 hours at 30°C/60%RH with an accelerated soak requirement of 40 hours at 60°C/60%RH) and then pass three times through a reflow oven. The gradual degradation in the subsequent humidity stress tests was observed and suggested due to the progressive decline of the initially present compressive force. The 40μm pitch assemblies have a failure distribution that is very much comparable to the 100μm type. The study has shown the feasibility in the moisure and reflow soldering test of such assemblies with a first level pitch down to 40μm.

The effect of solder reflow on the reliability performance of ACF assemblies was also studied by Chiang et al. [20] using bumpless dies. The ACF joint behaved differently under different reflow soldering profiles. The lower reflow temperature resulted in more reliable ACF joints by maintaining low contact resistance. By contrast, higher contact resistance was measured from the assemblies treated with higher reflow temperature. Under humidity aging (85°C/85%RH), bumpless chips proved to be unreliable due to a corrosion mechanism. Moreover, the ACFs showed degradation in chemical and physical properties, including modulus reduction, Tg depression, polymer hydrolysis, and surface swelling after exposing to humidity aging.

Other reliability tests results on ACFs include the impact test reported by Wu et al. [46], mechanical loading test reported by Tan et al. [47], the 3-points bending test reported by Rizvi et al. [48], and thermal aging test reported by Tan et al. [37] etc. All of this experimental research has generated much reliability data which is very useful for the electronics packaging industry.

2.2 Computer Modelling

Component package design and assembly process in electronics manufacturing require careful observation and pre-planning to achieve the ultimate goal of manufacturing low cost and reliable products. Use of simulation to help validate and

understand reliability is required to assure that technologies are deployed with reasonable risk. Computer modelling method to predict reliability are needed to speed development processes [50].

Computer modelling analysis, in particular the finite element analysis (FEA), is being used as a powerful tool to predict the behaviour and responses of ACA assemblies during bonding process and reliability testing. The ACA bonding process is quite complicated and there are a number of key steps including pre-assembly, component placements, heating, assembly pressure applications, resin flow and particle compression, resin cure, assembly pressure release, and cooling [51]. So far, computer modelling work has been mainly focused on three aspects including flow analysis, thermal mechanical analysis and hygro-mechanical analysis.

2.2.1 Flow Analysis of Bonding Process

The success of the ACA bonding technology is sensitive to the number and distribution of the conductive particles trapped between chip bumps and substrate pads. The final position reached by a particle is determined by the flow of the adhesive during the bonding process. Therefore, to understand the adhesive flow behaviour during the bonding process is important for improving the ACA technology.

During the ACA bonding process, the compression/flow of the adhesive resin is divided into two distinct types [51]. These are: Type I flow, where the bumps on the substrate of components penetrate into the adhesive and the adhesive flows into the gaps between the pads; and Type II flow, where all of the space between the pads has been filled and the adhesive must then flow out from under the component. A typical situation of the particle flow is given in Figure 2.5.

The ACA bonding process is ideally expected to be finished when the type I flow is fully completed and the type II flow just starts. If the type I flow is not finished, voids could remain under the components, and thus reduce the bonding strength and the reliability of ACA assemblies. In the potential type II flow process, when the free

19

space beneath the chip is filled, the adhesive will be squeezed over the whole chip area. Large pressure differences arise from the centre to the edge of the chip and this pressure gradient can lead to substantial distortion of the component and substrate [51]. Therefore, this part of the flow process is not desired and mainly eliminated by choosing the appropriate film thickness, bond pad size and height. However, limitations on the choice of these parameters always result in significant Type II flow. Thus, previous studies have modelled both of these two types of flow by using analytical or finite element models.
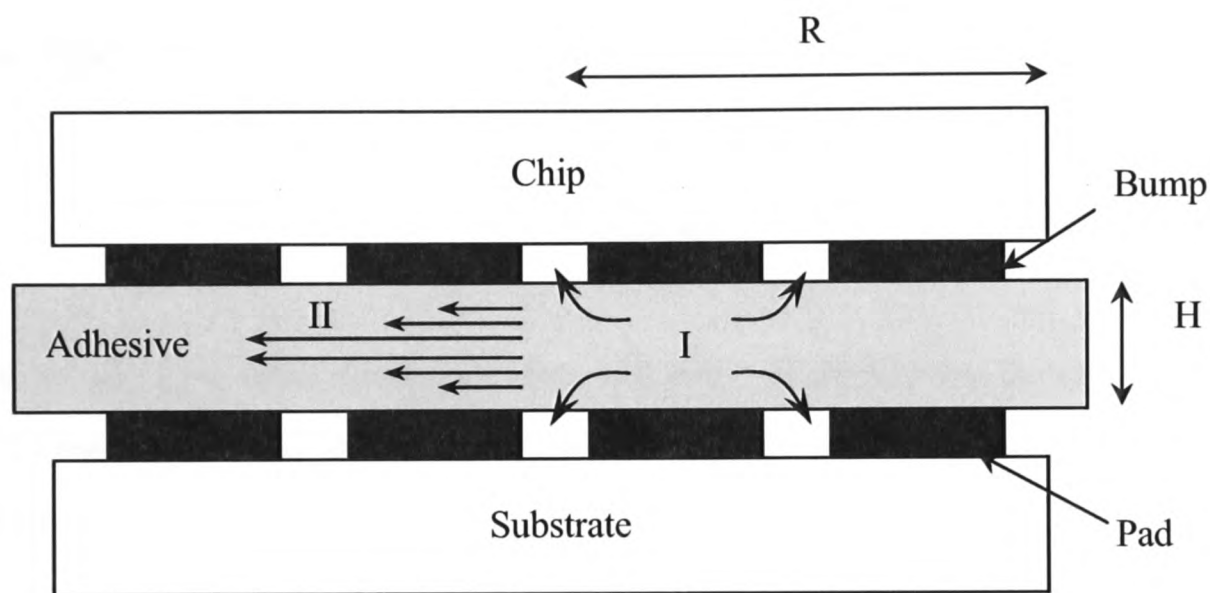
Figure 2.5: Schematic drawing of an ACA flow during the bonding [51]

Ogunjimi *et al.* [52] approximated the component as being circular, with a purely radial adhesive flow, and used the Scott equation to model the rate of compression of the adhesive *dh/dt* during the type II flow. The flow rate was dependent on the adhesive properties as well as the applied process assembly force, *F*, and the geometry, i.e.:

$$\frac{dh}{dt} = -\frac{n}{2n+1}\left(\frac{(n+3)Fh^{2n+1}}{2\pi\eta_0 R^{n+3}}\right)^{1/n} \qquad (2.1)$$

20

where R is an effective component radius and defined as $R = L/\sqrt{\pi}$, L is the component length/width. η_0 is the consistency of the adhesive and n is the power law index of viscosity and the viscosity, η, is given by:

$$\eta = \eta_0(\dot{\gamma})^{n-1}$$

(2.2)

Equation 2.1 assumes that $R \gg h$, however the comparison of the prediction from Equation 2.1 with computational fluid dynamics (CFD) models showed that this equation was applicable with only small errors down to $R/h \approx 3$ [53]. For $n=1$, i.e. for a Newtonian fluid, Equation 2.1 is simplified to:

$$\frac{dh}{dt} = -\frac{2Fh^3}{3\pi\eta_0 R^4}$$

(2.3)

Dudek *et al.* [54] also modelled the adhesive compression process analytically using a 2D representation rather than the rotationally symmetric approximation used by Ogunjimi:

$$\frac{dh}{dt} = -\frac{Fh^3}{\eta bL^3}$$

(2.4)

where L is the pad/component length and b is the pad width. The 2D approximation of Equation 2.4 is likely to be more appropriate for assemblies where the pads have high length to width ratio, such as LCD to flex connections. Equation 2.4 neglects the effects of shear thinning of the adhesive, which significantly affects the resin flow and can not be safely used for type II flow if the adhesive resin flow is non-Newtonian.

Dudek *et al.* [54] also analyzed the type I flow process using numerical analysis with a single bump. The conductive particles were treated as dimensionless points embedded in a viscous matrix during the bonding. It demonstrated that the temperature gradients in the thickness of the foil can cause the viscosity gradients over the gap

21

height which can slow down the process of particle emigration from the bumps remarkably.

Mannan *et al.* [53] modelled the initial stages of ACA joints assembly process and predicted the time required to squeeze out the adhesive from beneath the chip with the ignoring of the presence of the conducting particles in the adhesive. In the later report, Mannan *et al.* [55] studied the ACA squeezing process using a CFD software package: Fidap 7.52. This CFD modelling successfully took into account the detailed geometry of the assembly and showed the paths taken by infinitesimally small conducting particles.

Whalley *et al.* [56] successfully coupled the thermal conduction with flow process during the ACA bonding process using PHYSICA software with simplicity of the domain geometry. As the adhesive viscosity was highly temperature dependent and a temperature gradient through the adhesive film thickness was expected to create an asymmetrical flow distribution, this flow model was improved by allowing simulation of non-Newtonian behaviour with both shear rate and temperature dependent viscosity.

Based on the force versus displacement relationship measurement of a kind of particle, Whalley *et al.* took into account the stiffness of the particles and extended Equation 2.1 as below:

$$\frac{dh}{dt} = -\frac{n}{2n+1}\left(\frac{(n+3)(F - NK(D-h)^2)h^{2n+1}}{2\pi\eta_0 R^{n+3}}\right)^{1/n} \tag{2.5}$$

Where F is the total force carried by the particles, N is the total number of particles under compression and D is the particle diameter, K is a constant which, for the particles tested, was 0.20×10^{-9}, the predicted results showed that once the particles begin to compress they did slow down further flow out of the resin, but the flow did still continue and over compression of particles would still occur, although somewhat later than predicted by Equation 2.1.

2.2.2 Mechanical and Electrical Behaviour of Conductive Particles

The electrical performance of the ACA joint is dependent on the contact status between the conductive particles and pad metallization. During the bonding process, the conductive particles are deformed and locked in a compressive state which is maintained by the shrinkage force in the adhesive matrix. The stress created in the bonding process and reliability test process was studied in some reports by using modelling technique [54][58][59][60][61][62]. However, due to the phase change of the polymer foil from viscous to solid, the effect of the adhesive matrix on the stress generation of conductive particles during the bonding process was usually ignored.

Buratynski et al. [58] modelled the transient heat flow occurring during the curing process and the resulting residual stress. These models provided some extremely valuable insights, but assumed that the adhesive flow had completely finished and that all of the assembly force is therefore carried by the conductive particles before resin curing commences.

Wu et al. [59] simulated the stress generation during the bonding process using FEM, it was reported that both for rigid and deformable particles, significant stress was built up at the interface between the two contacts, as shown in Figure 2.6. This offered a useful insight into the stress distribution around the conductive particle during the bonding process, but only a very simplified finite element analysis of a particle embedded in a bonding system was used, and the effect of the adhesive matrix on the mechanical response was neglected in this research.

Pinardi et al. [60] and Wu et al. [61] made a complete analysis of the effect of bump height on the stress and strain distribution in the ACA joints during the compression, cooling process and thermal cycling test. The results showed that the residual stress was larger on rigid substrates than on the flexible substrate after bonding. The thermal stress increased with the thickness of the bump, also large strains were found with thicker bump. In these two papers, the particle was considered as infinitely small and ignored in the research.
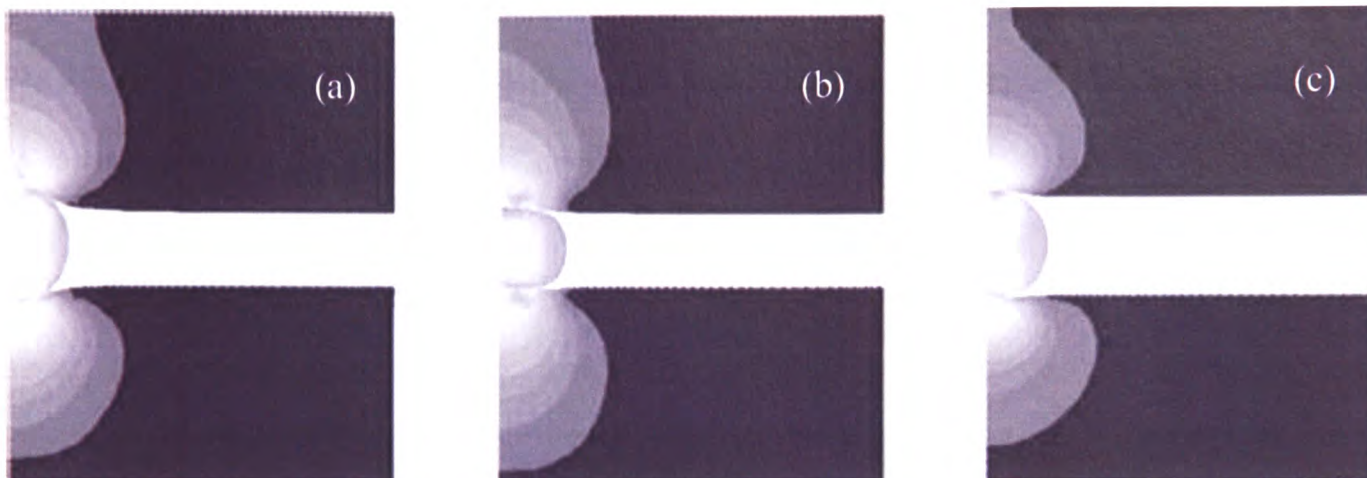
Figure 2.6: Deformation distribution of different particle systems, (a) rigid particle system, (b) deformable particle system and (c) fully deformable system (courtesy of Wu *et al.* [59])

The transient analysis of the temperature field during the bonding process was studied by Dudek *et al.* [54]. The result showed that the heat immediately spread over the whole chip, when an initial temperature jump was assumed as shown in Figure 2.7. The temperature at the bottom of the chip reached almost the upper chuck temperature within a few milliseconds. After 50ms, the temperature at the bottom of the adhesive layer was about 90% of its stationary value, while the solution became almost stationary after 0.5s.
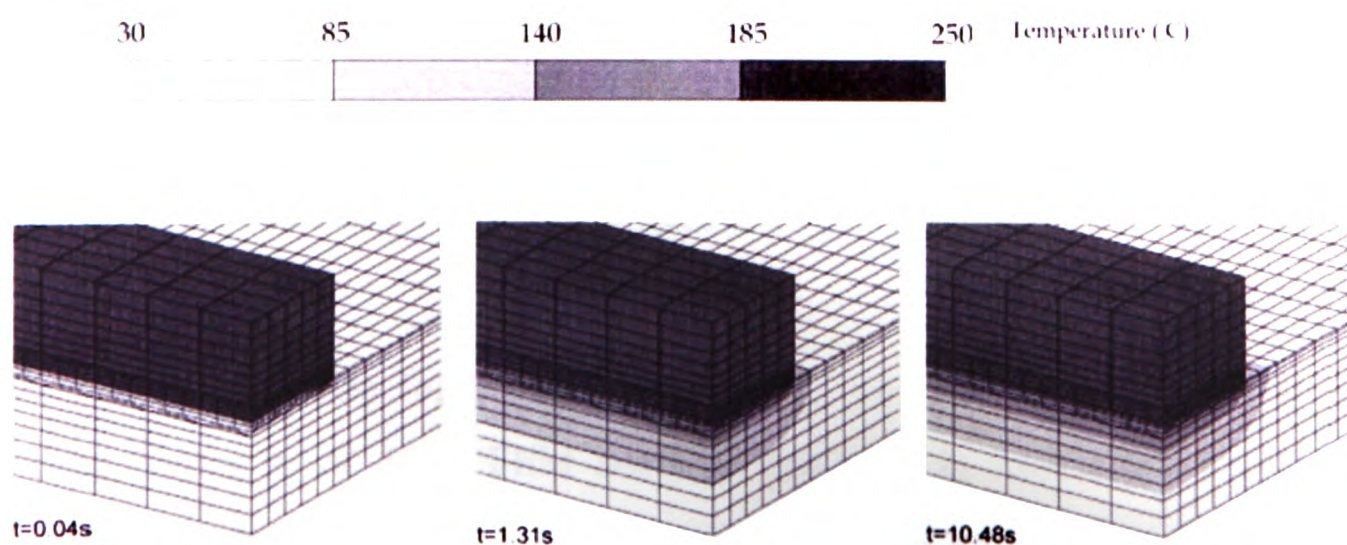
Figure 2.7: Temperature iso-surfaces during bonding at different times of the process (courtesy of Dudek *et al.* [54])

Dudek *et al.* [54] also studied the stress development and stress relaxation process in the ACA joints during the bonding process and the following cooling down process using a 2D model including two conductive particles. In this study, the mechanical influence of the polymer foil on the particle deformation was neglected during the particle deformation process in order to simplify the analysis. After the bonding process, the free stress polymer foil was added into the model to study the thermal induced stress during the cooling down process. The tensile stress distribution after the bonding and subsequent cooling down process is shown in Figure 2.8.
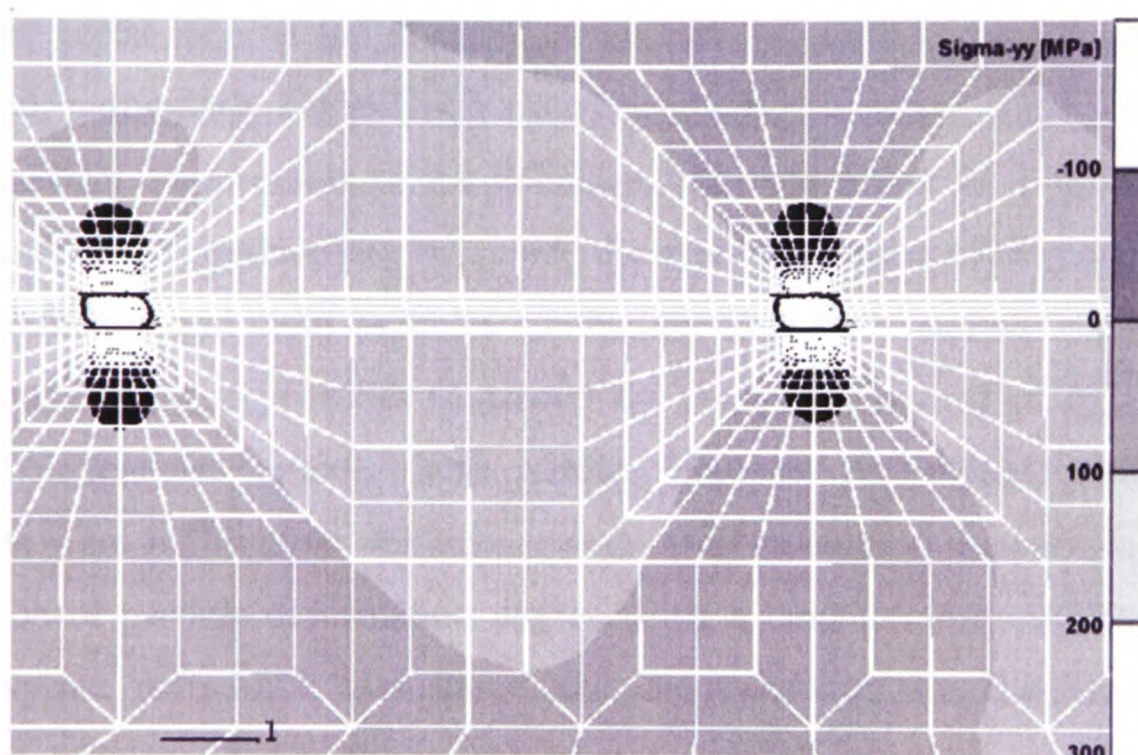
Figure 2.8: Stress σ_{yy} and particle deformation caused by bonding at 190 °C and subsequent cooling to room temperature (courtesy of Dudek *et al.* [54])

The effect of bonding force on the conducting particles with different sizes was studied by Yeung *et al.* [62]. FEM analysis was used to model the transient heat transfer problem and the mechanical influence of the conducting particle in the ACA assembly. The result showed that a larger bonding force and a smaller particle size would lead to a larger stress concentration, this would be a preferential site for crack

initiation and propagation. Moreover, the stress concentration was located at the edge area especially for the gold coating layer.

Some theoretical analysis was focused on the relationship between compression and the electrical conduction of ACAs. Williams *et al.* [63] analyzed the contact area and resulting contact resistance for a solid metal sphere on a yielding substrate and explored the effect of the conductor particles on the post assembly elastic properties of the adhesive. Williams *et al.* [64] then used this analysis to explore the effect of assembly pressure and contact particle size and density on conductivity. Yim *et al.* [65] presented analytical and FE based models of the contact resistance for both solid and polymer cored spheres and reported an increase in contact resistance due to over compression, particularly for polymer cored conductor particles. All of these studies assumed uniform compression of the adhesive, although Shi *et al.* [66] extended the analytical models of conductivity to include the size distribution of the particles, single particle conduction and multi particles conduction were both studied. Chin *et al.* [67] reviewed the existing approaches to predict the contact resistance of ACA assembly and the discrepancies among these models between the model prediction and experiments were highlighted. Määttänen *et al.* [68] calculated the particle resistance as a function of particle deformation degree using a conduction model for the metal coating polymer particle. It was found that the resistance was independent of the particle size, but depended on the resistivity of the particle, the thickness of metal layer and the degree of deformation as shown in Figure 2.9.

Dou *et al.* [69] further concluded that the greater the level of particle transformation, the thicker the metal coating layer and the greater the resin diameter, the lower the particle resistance was, according to the numerical analysis of the Ni/Au coated polymer particles. It showed that the ACF particle resistance was determined by the particle transformation and the particle geometries; however it was more sensitive to the transformation and the nickel layer thickness than the resin diameter and the gold layer thickness.
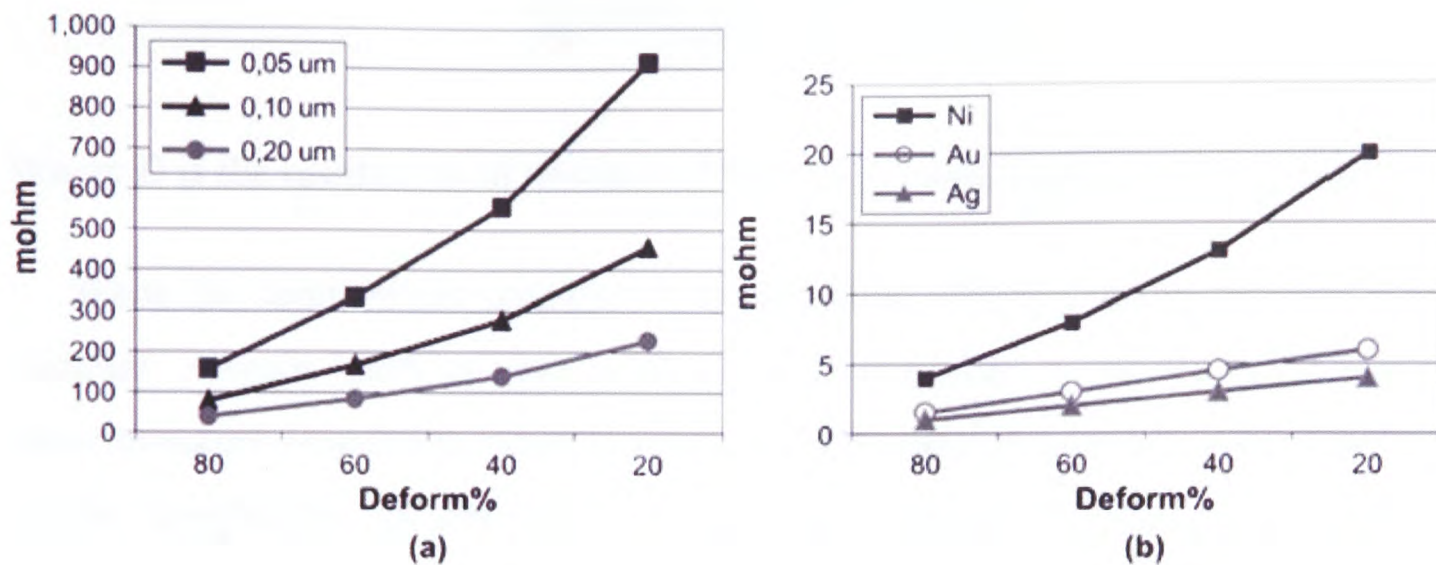
Figure 2.9: Predicted particle resistance for different degree of deformation, (a) for Au/Ni-polymer with various metal thicknesses, (b) for solid metal particles (courtesy of Määttänen *et al.* [68])

The most stable values of the transformation degree were reported as 40% for metal coated particles [70][71]. Research using mathematical models of ACF particle assumed that the transformation degree in a safety region (30%-60%) had successfully predicated the characteristics of ACF particle conduction [69][72].

2.2.3 Moisture Absorption and Induced stresses

Moisture induced failure is one of the most important issues with ACF materials. The adhesive can easily absorb moisture from the environment and moisture absorption can cause adhesive swelling, particle oxidation, and even metal corrosion etc. A significant amount of experimental work has been done based on the thermal-humidity test environment and autoclave test [7][8][9][10]. But few papers have been published using the computer modelling technique.

The moisture diffusion into an ACF package can be described by Fick's Law of diffusion [11][12]. That is, the process is governed by the following differential equation:

$$\frac{\partial C}{\partial t} = D\left(\frac{\partial^2 C}{\partial x^2} + \frac{\partial^2 C}{\partial y^2} + \frac{\partial^2 C}{\partial z^2}\right) \tag{2.6}$$

Where D is the coefficient of moisture diffusion, C is the moisture concentration.

When the temperature changes in an assembly which is made of more than one material, stresses build up due to the CTE mismatches in the materials. Similarly, when moisture absorption takes place in an ACF assembly, stresses also build up due to the mismatches in coefficient of moisture expansion (CME) or variations in moisture content. These are called hygroscopic stresses. Assuming that the mechanical, thermal, and moisture induced strains are independent of each other, then the mechanical strain is calculated as the total strain less the thermal strain and the hygro strain [12]. The calculation can be expressed as:

$$\varepsilon^{mechanical} = \varepsilon^{total} - \varepsilon^{thermal} - \varepsilon^{hygro} \tag{2.7}$$

According to the constitutive relations between the strain components and the corresponding stress components, for the thermal-hygro-elastic analysis, the stresses can be calculated as:

$$\sigma_{jk} = \lambda(\varepsilon_{11} + \varepsilon_{22} + \varepsilon_{33})\delta_{jk} + 2G\varepsilon_{jk} - \frac{E}{1-2\mu}(\alpha\Delta T)\delta_{jk} - \frac{E}{1-2\mu}(\beta C)\delta_{jk} \tag{2.8}$$

Where μ and E are the Poisson's ratio and the Young's modulus respectively, β is the CME, α is the CTE, ΔT is the temperature change (thermal load), and C is the moisture concentration. λ and G are known as the Lamé constant and shear modulus which are directly related to the Young's modulus and Poisson's ratio:

$$\lambda = \frac{E\mu}{(1+\mu)(1-2\mu)} \quad , \quad G = \frac{E}{2(1+\mu)}$$

Wei et al. [11] studied the moisture diffusion and moisture induced stress inside an ACF assembly under 121°C, 100%RH, 2atm condition. A 3D transit moisture

diffusion model was built up and the moisture gain versus the time was drawn. The moisture induced stress due to the moisture absorption was studied using a 2D model. Caers *et al.* [10] studied the moisture induced failures under 85°C/85%RH testing condition using experimental and modelling methods. The 2D model of the moisture ingress was illustrated and showed that the adhesive layer can be fully saturated with moisture after 1.5 hours of the test.

Moisture induced ACF swelling and interfacial delamination was reported as the major cause of ACF failures by Mercado *et al.* [12]. The test condition was the autoclave test at 121°C, 100%RH and 2atm. Both thermal induced compressive stress and the moisture induced tensile stress were studied using the 2D model as illustrated in Figure 2.10. With moisture absorption, due to the swelling effect of adhesive, the loading condition at the interface was found tensile dominant, which corresponded to lower interface toughness (or fracture resistance). This condition was concluded to be more prone to interface delamination. Kim *et al.* [13] processed the moisture diffusion analysis using 3D finite element method and calculated the vapour pressure in a flip chip package which was used to evaluate the delamination strength during the solder reflow.
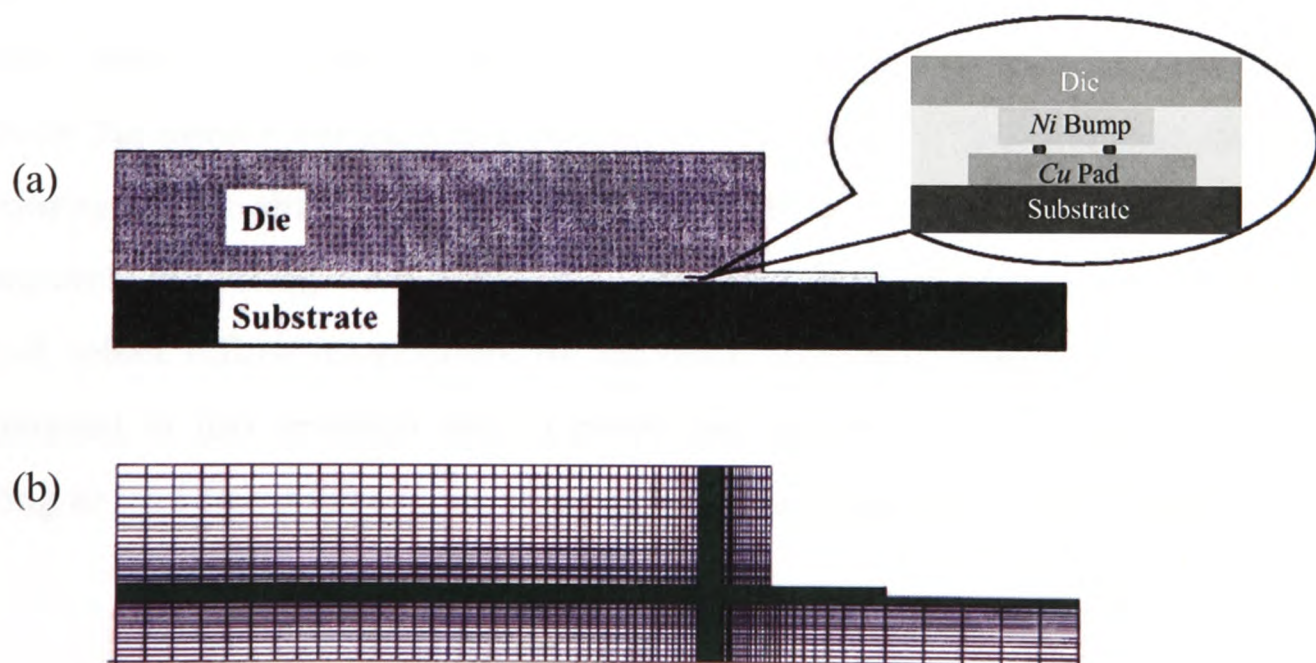
Figure 2.10: Finite element model (a) structure of the global and local area (b) mesh information (courtesy of Mercado *et al.* [12])

2.3 Summary

A literature review has been presented in this Chapter. The recent research achievements in this area are summarized into two areas, computer modelling and experiments, in order to give a clear summary of state of the art. There are plenty of papers published in this research area so far and most of them are related to the reliability performance of ACA assemblies.

Although much work has been done, there are still some areas which are not fully understood and some questions still remain. One of the limitations of previous modelling research is mostly using the 2D models due to the difficulties caused by the multi-scale nature of the ACF package. In some cases, 3D models were built, but the structure of ACF joint was simplified. In this PhD research, a 3D macro-micro modelling technique is developed which enables a more detailed 3D modelling analysis of an ACF package than previously. By using this technique, the failure mechanism of an ACF flip chip on flex substrate in an autoclave test environment is studied.

The issue of SMT-compatibility is attracting more and more attention in the electronic industry. Having the mixed board technologies containing both ACFs and solders on the same substrate has a number of advantages. The challenge and concern for industry is the ability for the ACF materials to survive the high solder reflow temperatures. By using both computer modelling and experimental techniques, the effect of solder reflow temperature on the reliability performance of ACF assemblies are analyzed in this research and in particular, the impact of moving from tin-lead soldering to lead free soldering on this combined technology is demonstrated.

Chapter 3

Flip Chip Technology

In this Chapter, the flip chip technology used for IC packaging is introduced and compared with other traditional technologies such as wire bonding and tape automated bonding (TAB). The materials used for the flip chip interconnection, ranging from metal alloys to conductive adhesives are introduced and compared with each other. Finally, The concepts of reliability and failure analysis of electronic products are discussed and the applications of ACFs in LCDs and disc drives are presented.

3.1 Introduction

Microelectronics devices are the basis of all modern electronic products. Since the invention of the transistor in 1947, electronic products began shifting from vacuum tubes to transistors in the 1950s, and to ICs in the 1960s. The first IC which incorporated two transistors and a resistor was developed by Jack Kilby in 1959. Driven by the functional and performance requirements of modern and future electronics, continuous developments in reducing the size of the transistors are allowing the progressive integration of many transistors in a single semiconductor chip. Figure 3.1 illustrates the famous Moore's Law which predicts that every 18 months chip makers will double the number of transistors that can be crammed into a unit area of a silicon wafer. To date, developments in the semiconductor industry have been accurately predicted by this Law [1][2].

31
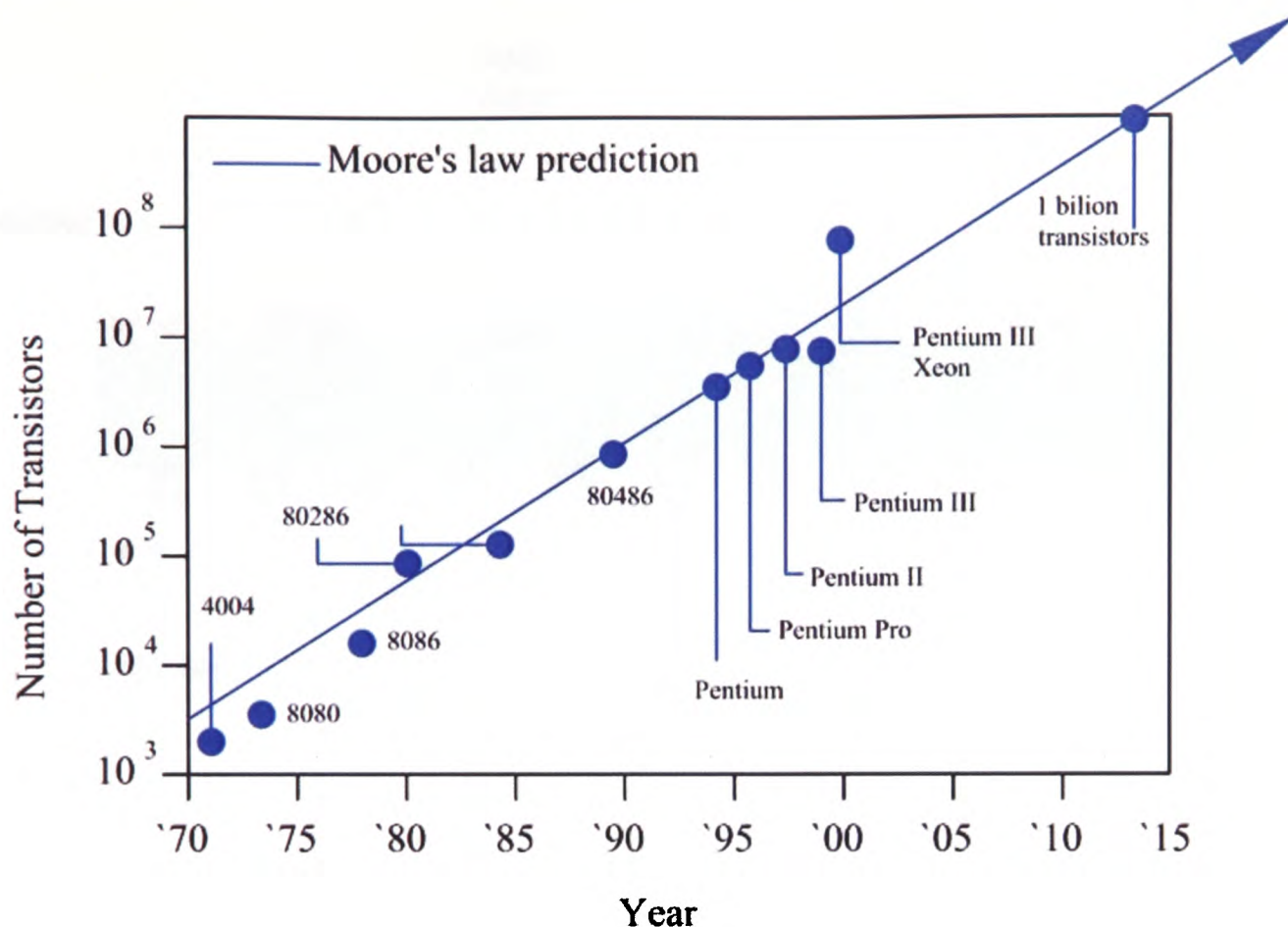
Figure 3.1: Moore's Law predicts the IC integration to double every 18 months

The IC die has to be packaged before it can be used in an electronics device. The purpose of an IC package is to protect, power and cool the microelectronic device and to provide electrical and mechanical connections between the IC and the circuit board. Typical parameters which are important for IC packaging include I/Os, power and size of the chip.

Generally, IC packaging includes three steps: firstly, the I/O connection pads on the IC are connected to corresponding terminal pads on the package once the IC is ready to be packaged. Secondly, the entire structure is sealed or moulded with a plastic or metal material with only the package terminals or pins being visible. Finally, the package is marked with the manufacturer's name, model name and other identification information. The side view of a typical IC package, flip chip Ball Grid Array (BGA), is shown in Figure 3.2 .
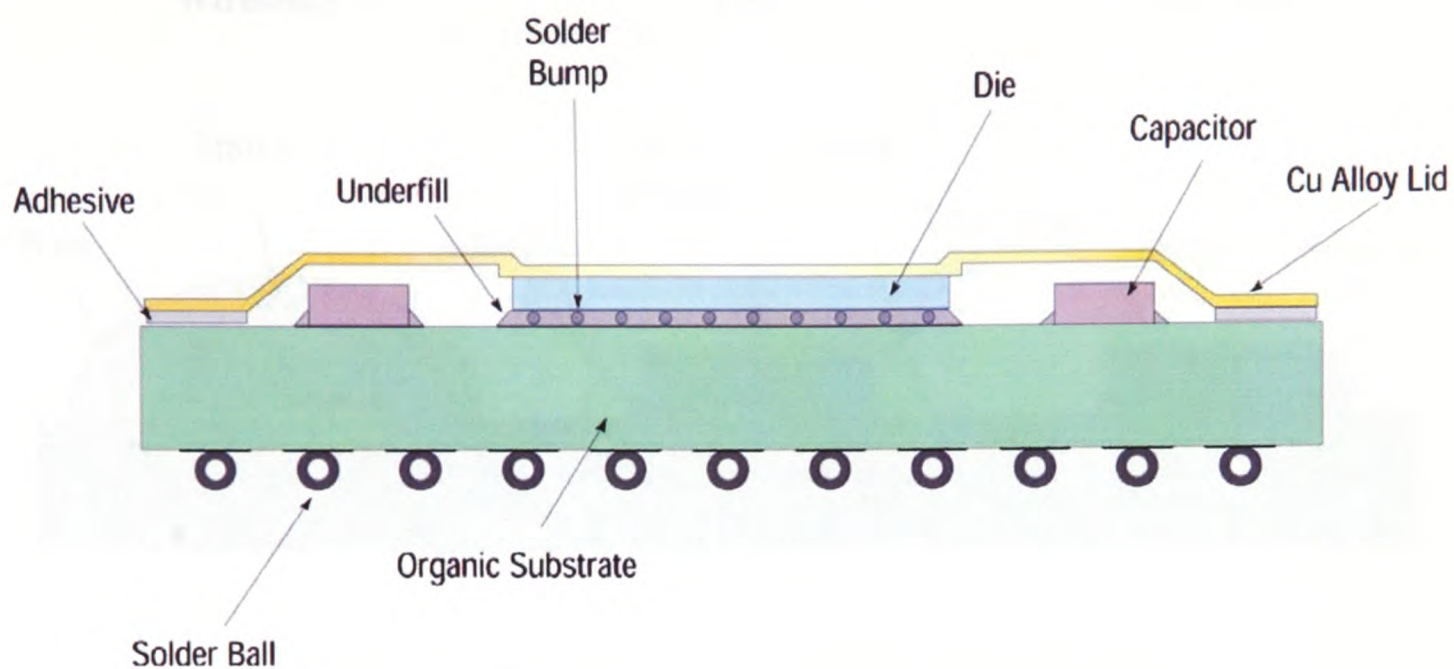
Figure 3.2: Example of an IC package

3.2 IC Assembly Technologies

IC assembly is the first processing step after wafer fabrication which enables IC to be packaged for system use. IC assembly is defined as the process of electrically connecting I/O bond pads on the IC to the corresponding bond pads on the package. This chip to package process can be accomplished using three primary interconnection technologies as illustrated in Figure 3.3. They are wirebonding, TAB and flip chip respectively.

3.2.1 Wirebonding

Wirebonding is a chip to package interconnection technique where a fine metal wire is attached between each of the I/O pads on the chip and its associated package pin, one at a time. This technology originated with AT&T's beam lead bonding in the 1950's [73]. Thermosonic and ultrasonic weldings are the most commonly used methods for wirebonding. The most common wire materials are gold for ball bonding and aluminium for wedge bonding.

33
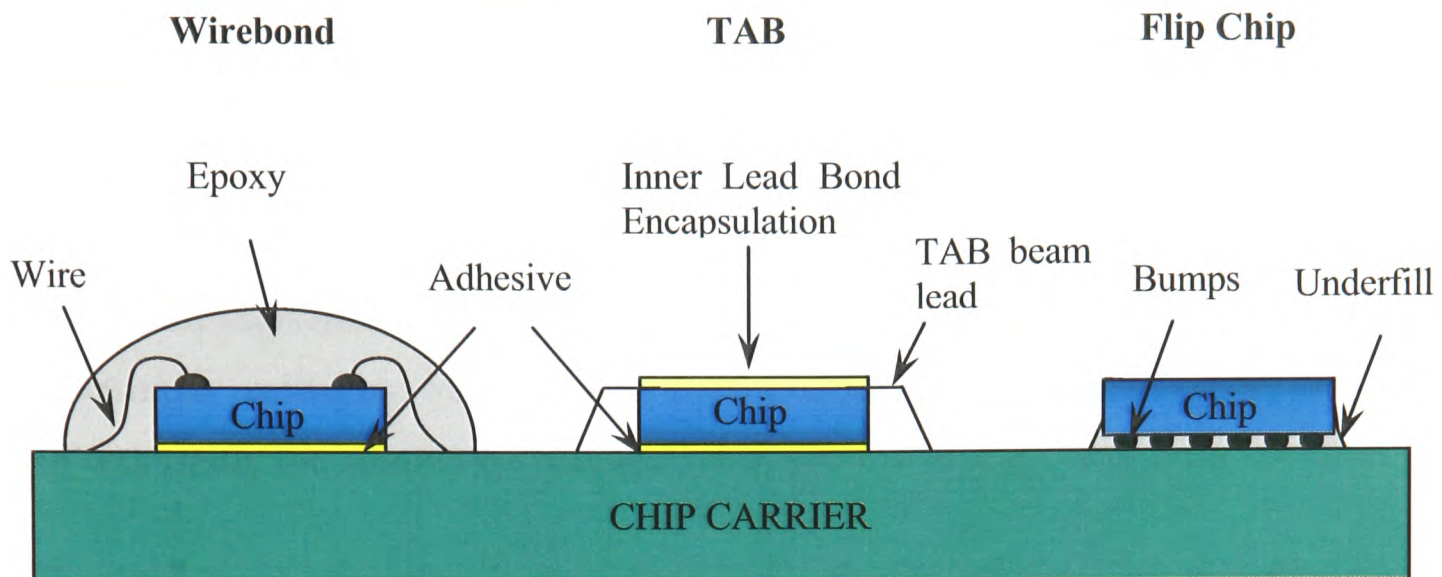
Figure 3.3: Chip on substrate interconnection technologies

The flexibility derived from this point to point process is one of the major advantages with wire bonding technology. Other advantages include the low defect rates, high reliability structure etc. The disadvantage is the low yield due to the point to point processing of each wire.

3.2.2 Tape Automated Bonding (TAB)

TAB is an IC assembly technique that mounts and interconnects ICs on metallized flexible polymer tapes. It is a fully automated bonding of one end of an etched copper beam lead to an IC, and the other end of the lead to a conventional package. TAB was invented by Frances Hugle in Silicon Valley and commercialized in 1966 by General Electric Research Laboratories (New York), who used it with small scale integration devices [73]. This technology was developed as a lower cost replacement of wirebonding technology by providing a highly automated reel-to-reel technology for packaging high-volume, and low I/O devices.

Compared to the wire bonding technology, the large wire loops in TABs are eliminated, therefore the heat conduction and electrical performance can be improved and the weight can be reduced. However, the disadvantages of using TAB technologies

are that additional wafer processing steps are required for bumping and the packages size tends to increase with larger I/O counts.

3.2.3 Flip Chip

One of the significant developments to improve cost, reliability and productivity in the electronics packaging industry have been the advancement of flip chip technology which was firstly introduced for ceramic substrates by IBM in 1962 [73].

Flip chip interconnection is the connection of an IC to a carrier or substrate with the active face of the chip facing toward the substrate. Electrical connection is achieved through conductive bumps built on the surface of the chips and substrate pads. During the mounting, the chip is flipped onto the substrate or carrier with the bumps being precisely positioned on their target locations. In flip chip technology, the whole area of the chip can be used for connecting rather than just the periphery, so that more connections can be achieved on the same size chip compared with wire bonding and TAB.

The flip chip process using solders consists of four steps: forming the solder bumps, placement of the chip onto the substrate, reflow process to attach the bumped die to substrate, and completing the assembly with an adhesive underfill as illustrated in Figure 3.4. In the flip chip assembly process, underfill materials are applied to help meet the reliability requirements. They protect the bumps from moisture or other environmental chemicals, and provide additional mechanical strength to the assembly. Furthermore, the most important purpose to use underfill, particularly with solder bumps connections on large die onto organic substrates is to compensate for the thermal expansion differences between the chip and the substrate [74]. Since most of the low-cost substrates are plastics which have a large CTE (20-30 ppm/°C) compared to Silicon (about 3 ppm/°C). Such a CTE mismatch can generate a large shear strain in the solder balls. The underfill serves as a compliant buffer reducing the shear strain of the solder balls by coupling the thermal mismatch into bending of the substrate, resulting in a significant improvement of the fatigue life of the solder balls [76].

Past printing

Die alignment & Attachment

Reflow

Underfilling
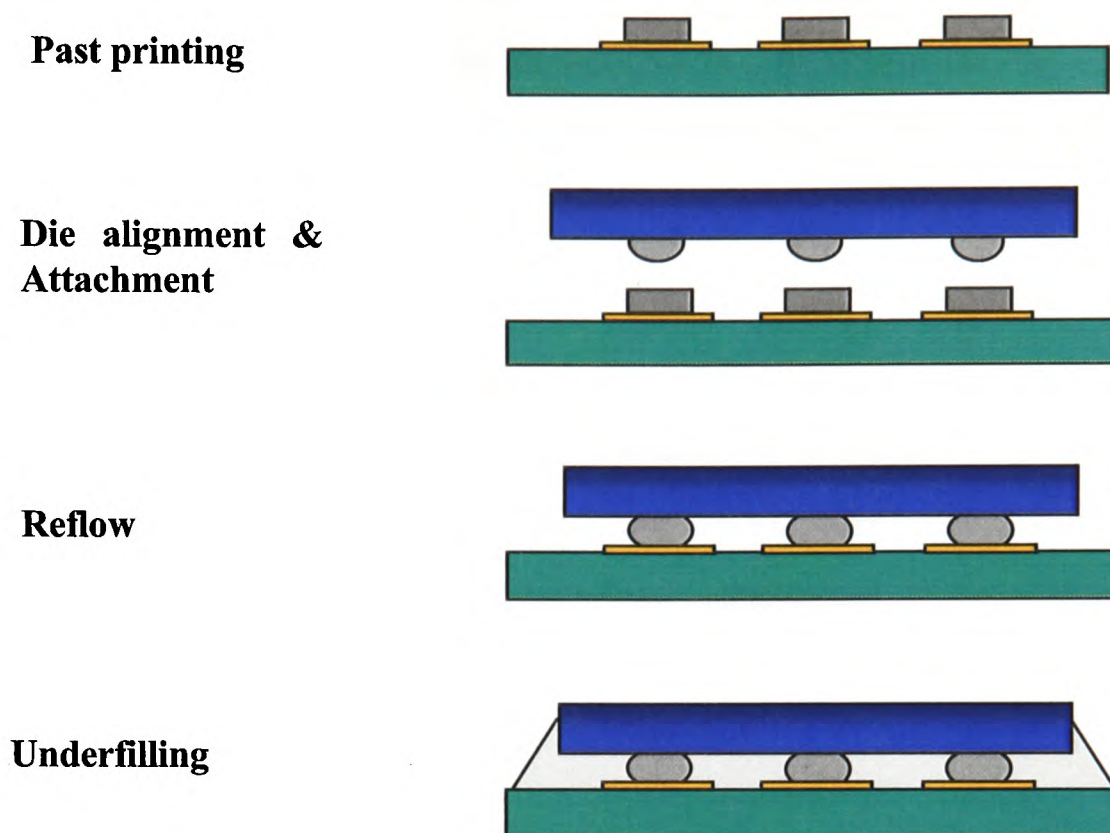
Figure 3.4: Flip chip process using solder alloy

Flip chip technology offers several advantages especially for high dense interconnects because the whole chip surface can be used for a large number of I/O pads in an area array configuration. Shortest interconnection lengths result in excellent electrical performance of interconnects as well [75]. Although wire bonding is still the dominant method used today, particularly for chips with a moderate number of I/Os, flip chip and TAB technologies are gaining popularity as a method for bonding chips with higher I/Os requirements. For very high I/Os, very high electrical performance, and very high reliability, flip chip becomes virtually the only viable IC assembly [1][3].

3.3 Materials Used for Interconnections

A typical flip chip assembly consists of three parts: an IC chip, a substrate and joints connecting the chip bumps with the substrate pads. IC chips are normally made

from a crystalline silicon wafer, the substrate materials can be flex, glass, ceramic, or organics such as FR4 etc. With the development of IC packaging technology, the materials to form the joints become versatile ranging from solder alloys to conductive adhesives.

3.3.1 Solder Alloys

There are two main kinds of metal alloys used in IC packaging including traditional tin-lead solder, and recently developed lead-free solder. The latter material is attracting more and more attention in the electronics packaging community due to the environmental concerns of using lead.

3.3.1.1 Tin-Lead Solder

Tin-lead solder (mostly Sn63/Pb37 or Sn60/Pb40) has been used as the interconnect material in the electronics packaging industry for more than 50 years. Up until now, it has been the main material used for the interconnection although a range of possible alternatives have been investigated. The function of the solder in the interconnection is to join two metal surfaces by alloying with their surfaces to achieve electrical conduction and mechanical support. Solder is always used with flux, the function of the flux is to remove the oxidized layer of the surfaces to be soldered and prohibit the metal from oxidation during the soldering process, and thereby improving the wetting ability of the solder alloy on the metal surfaces. There are many types of solder and flux, but both must be suited to the metals to be soldered together and to each other. One of the most popular tin-lead solders is Sn63/Pb37, which is called "eutectic," since it can pass directly from solid to liquid without a pasty stage and therefore can flow very easily. Most of the surface mount components are soldered with eutectic solders.

3.3.1.2 Lead-Free Solder

It is known that lead is a harmful metal to the environment. Lead and its compounds are ranked among the top 10 hazardous materials and it is also the number one environmental threat to children [77]. Environmental pressures are forcing

changes on the world market for electrical and electronic products which will result in a dramatic reduction in the use and possible long term elimination of lead based solders. In Europe the Restriction of Hazardous Substrates (RoHs) Directive [78] has banned the use of lead from most consumer products from 1st July 2006. Recycling and reuse legislation such as the Waste from Electrical and Electronic Equipment (WEEE) Directive [79] and the End of Life Vehicles (ELV) Directive [80] will make it more difficult and expensive to use exempt materials.

The impending ban on lead requires more research on lead-free solders, and increasing attention within the semiconductor and electronics industry is focusing on lead-free solder manufacturing. Nowadays, the reliability performance of lead-free solders has been a major concern to the industry since the lead in the solder can help reduce the surface energy of tin-lead solder, increase the wet-ability on the metal, improve the ductility of the solder paste and decrease the brittleness. Therefore, once the lead is taken out of the solder, several problems arises, such as poor wet-ability, higher melting temperature, lack of long-term reliability data and both tin-whisker and tin-pest risks due to the higher tin content [81][82].

Particularly, the changing from lead to lead-free will have a very significant impact on the manufacturers of flexible circuit boards and many manufacturers who assemble them. Flexible circuits are a rapidly expanding sector of the electronics market with an increasingly wide range of applications. The problem results from the fact that flexible circuit boards are relatively sensitive to temperature due to their base material (polymers) e.g. continuous service temperature: polyimide about 177°C, polyester about 74°C, this make them a particular concern during the change from tin-lead solder (e.g. melting point 183°C) to the high melting point lead-free solders (e.g. melting point of Sn/Ag/Cu 217°C) with the resultant increase in processing temperature of 20°C to 50°C.

Although it is now widely agreed that there is no drop-in replacement for the standard Sn/Pb solders which are currently used worldwide, a range of possible

alternatives have been investigated. Some consensus have developed for using one family of alloys based on tin, silver, and copper (SAC) alloys. These are mainly tin, typically 3%~3.5% silver and a small amount of copper with melting points around 210°C, which is about 30°C higher than that of traditional lead-containing counterparts. Other alloys under consideration are the tin-copper eutectic which has a lower material cost but higher melting point of 221°C. Also of interest for flexible circuits are lower melting point solders such as tin-silver-indium or tin-zinc, but the cost of indium and corrosive nature of zinc needs to be evaluated. A summary of the melting points of tin-lead solders and some lead-free solders are listed in Table 3.1. In general, the lead-free soldering is technologically possible, but many key issues have to be solved, both scientifically and industrially.

Table 3.1: Lead and Lead-free solder alloy under study [83]

Solder Alloys

Composition	Solidus (°C)	Liquidus (°C)
62Sn36Pb2Ag (Sn62)	179	Eutectic
63Sn37Pb (Sn63)	183	Eutectic

Some Proposed Lead-Free Alloys

86.9Sn10In3.1Ag	204	205
91.8Sn3.4Ag4.8Bi	211	213
96.2Sn2.5Ag0.8Cu0.5Sb	215	217
95.5Sn3.8Ag0.7Cu	217-218	Eutectic
95.5Sn3.9Ag0.6Cu	217-218	Eutectic

High Melting-Point Alloys

95Pb5Sn	308	312
90Pb10Sn	275	302

3.3.2 Electrically Conductive Adhesives (ECAs)

Different kinds of adhesives have been used in electronics packaging for decades such as the hybrid, die-attach and display assembly. Besides traditional sealing, a growing interest has been observed within the electronics industry in other kind of functions, such as the interconnection material. The main advantages of using adhesives as the connection materials compared with traditional tin-lead solders include:

- Fine-pitch capability especially when using ACAs for flip-chips;

- Low temperature processing capability. The bonding temperature is much lower than the reflow peak temperature of the soldering process;

- Flexible and simple processing, and low cost.

Basically, there are two different types of ECAs used in electronic packaging: conductive adhesives and non-conductive adhesive. The conductive adhesives include anisotropic conductive adhesives, and isotropic conductive adhesives (ICAs) that have different electrically conductive functions. Each of these adhesives will be discussed in the following sections and in particular the application of these materials in LCD assemblies will be introduced.

3.3.2.1 Isotropic Conductive Adhesives (ICAs)

Isotropic conductive adhesives are typically thermosetting polymers filled with conductive particles. The most common material system is epoxy filled with silver flake particles. They become conductive in all directions upon curing, yielding an electrically functional interconnection. ICAs are applied in the same way as conventional solder paste, but cured rather than reflowed. There is no self alignment effect during the curing since the adhesive does not have the high surface tension as solder alloy. Therefore, component placement requires more accuracy than with solders. The amount of ICA used should be less than the solder paste to prevent bridging effect. A typical structure of an ICA flip chip is shown in Figure 3.5a.

(a) ICA

(b) ACA

(c) NCA
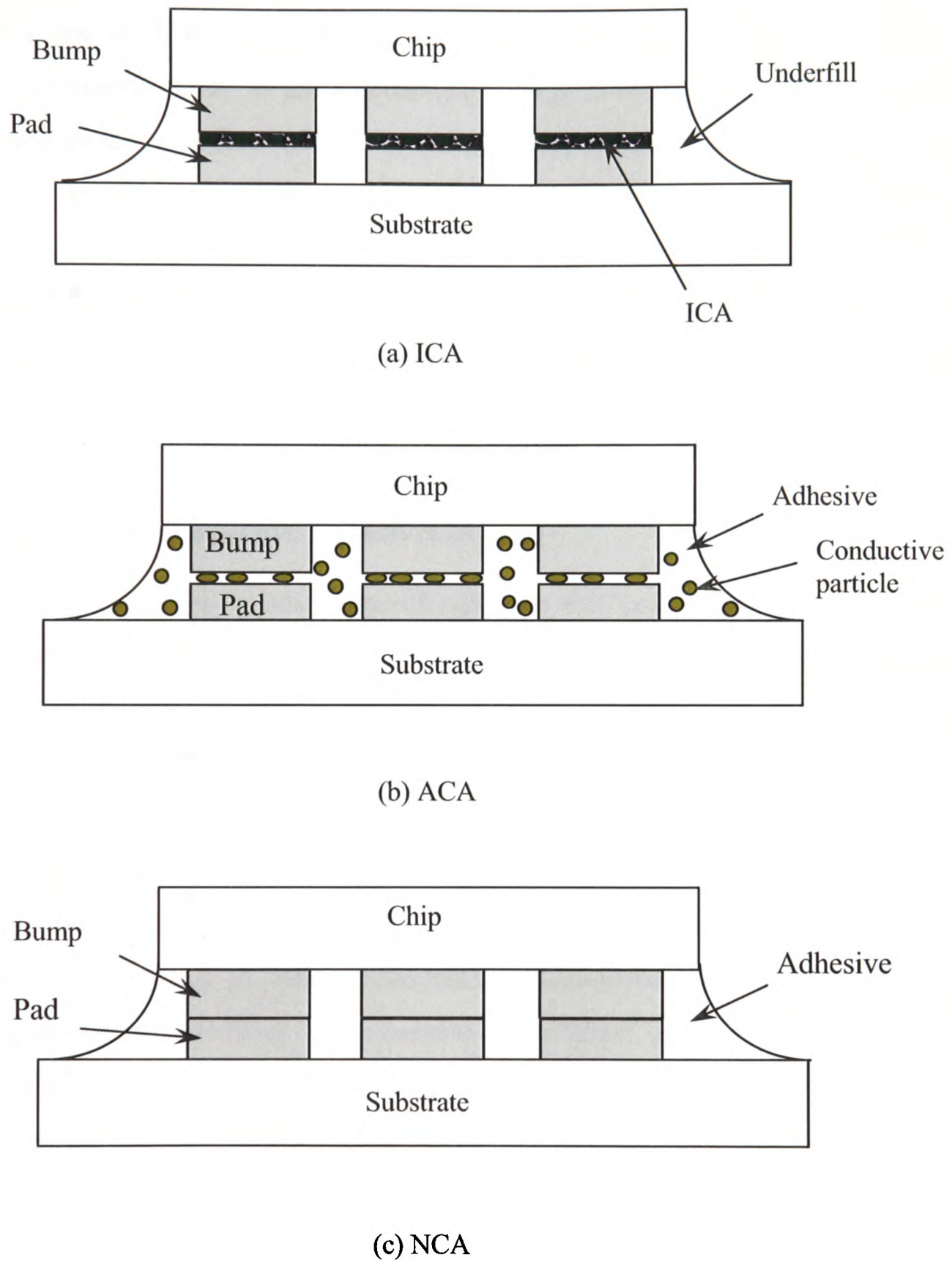
Figure 3.5: Typical interconnection systems using ICA, ACA and NCA

ICAs have been evaluated as potential replacements for lead-containing solders. These adhesives are being used to some extent in LCD applications due to the low processing temperature. However, there is not much work reported that tries to establish a fine pitch ICA flip chip technology, and up until now the use of ICA for flip chip is limited mainly to the assemblies of large contact area components such as chip capacitors and resistors [83]. ICAs are normally screen or stencil printed onto the circuit pads in order to obtain isolation between the adjacent pads. For fine pitch applications, this process is limited for two reasons. Firstly, printing paste at fine pitches is difficult without applying so much adhesive that shorts adjacent traces during assembly. Secondly, the small amount of adhesive deposited on the contact pads, coupled with the very high conductive filler content, lowers the adhesive bond strength.

3.3.2.2 Anisotropic Conductive Adhesives (ACAs)

In the last few years, another type of adhesive that is conductive in one direction only has attracted more and more attention. These are referred to as anisotropic conductive adhesives which can be obtained either in films or pastes. Conventional ACA is an adhesive consisting of conductive particles dispersed in an adhesive matrix. These particles can be pure metals such as gold, silver, or nickel, or metal-coated particles with plastic or glass cores. The volume fraction of particles is well below the percolation threshold with the particles typically ranging from 3-15μm in diameter. ACAs provide electrical as well as mechanical interconnections between conductive pads on parts to be assembled. The conductivity of these materials is restricted to the vertical direction (perpendicular to the plane of the board) with electrical isolation provided in the plane direction. Due to the anisotropic conduction, ACA can be deposited over the entire contact region, and thus significantly facilitates the material application. The low conductive filler content can also improve the adhesive bond strength to help achieve the robust interconnects. The most significant advantages of using ACAs are the capability of fine pitch connections and low processing temperature; interconnections with pitches of 100μm or less have been demonstrated with these materials [84][85]. A typical ACA connection is shown in Figure 3.5 b.

The use of ACAs in LCD products has stimulated significant interest since the last decade. The low processing temperature of ACA is one of the primary reasons for its widespread use for LCD drive attachment. In addition, it is supporting a fine pitch attachment process due to the lack of solder bridging or smearing of conductive adhesive. Using an ACA simplifies the mounting process, as there is no need for precise placement of the adhesive, and it is lead-free. However, the danger for damaging the ITO contact pads is particular concern when using chips with hard electroless nickel/gold (Ni/Au) bumps during the thermo-compression [84].

3.3.2.3 Non Conductive Adhesives (NCAs)

The function of non-conductive adhesives is to provide a mechanical connection between the bumps on the chip and corresponding pads on the substrate. This mechanical connection provides the needed conductive paths. Instead of introducing new conductive particles into the system, the NCA bonding method relies upon direct electrical contact between the two conductor surfaces as illustrated in Figure 3.5c. With mechanical pressure, a "metal to metal" contact is created and the contact points are responsible for the transport of electrical current. The epoxy filled cavities supply the adhesive forces which are needed to keep the materials together. Once the connections are made, the shrinkage force in the cured adhesive is responsible for the compressive force which is needed to maintain the electrical contacts.

Conductive joining with NCAs provides a number of advantages compared with ICA or ACA technologies. NCA joints avoid short-circuiting and they are not limited by particle size or distributions. Further advantages are cost effectiveness of the adhesives and ease of processing. However, the reliability and failure mechanisms of NCA joints are still not well understood; when two nominally flat surfaces are forced into contact, they meet only in a limited number of small areas, and the co-planarity of the metallization will affect the connection quality significantly. There are a few papers [88][89][90] that have studied the reliability performance of NCA under different testing conditions.

3.4 Reliability Testing

ACAs are becoming promising interconnection materials in electronics packaging and even thought of as one of the best alternatives to the traditional tin-lead solders in the future. However, the main challenge with ACA materials is reliability. As a result, more and more research activities are involved in this area , dedicated to improving the reliability performance of ACA components under variable testing conditions such as thermal cycling, and temperature/humidity test.

3.4.1 Reliability and Failure

The term reliability is defined as the ability that an item can perform its intended function for a specified interval under stated conditions [92]. In classical reliability, a single product, unit or component is generally considered to have two states, operational and failed. A failure occurs when an item does not perform a required function. The idealized bathtub curve is shown in Figure 3.6, which represents three phases of product hazard rates.
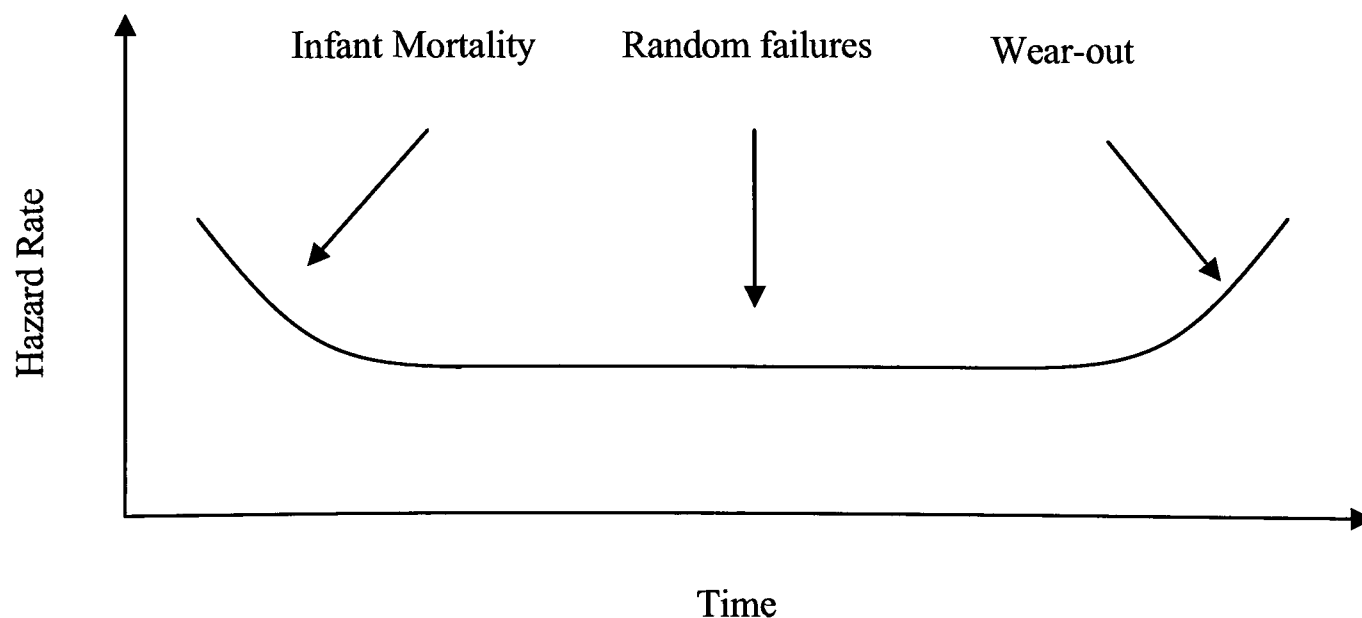
Figure 3.6: Idealize bathtub curve

The first phase, often called "infant mortality" represents the early life of the product when manufacturing imperfections or other initial failure mechanisms may appear. The hazard rate decreases during this time as the product becomes less likely to experience failure from one of these mechanisms. The second phase, sometimes called "useful life" represents the majority of the product operating time. During this period, the hazard rate of the product appears to be constant (constant failure rate). The third phase, often called "wear-out" occurs near the end of the expected product life and often involves failure mechanisms caused by cumulative damage. Electronic components are subject to wear-out due to electro-migration, material degradation and other mechanisms. Weibull, lognormal or other statistical distributions can be used to describe hazard rates during both infant mortality and wear-out.

3.4.2 Reliability Test and Standard

Reliability prediction can be carried out based on test data, stress and damage models or reliability handbook. Reliability tests can be divided into non-accelerated test and accelerated test which are introduced in the following sections.

3.4.2.1 Non-Accelerated Test

The traditional approach to reliability evaluation involves tests carried out within the products 'expected environment' or using actual operational conditions. In these tests, there is no attempt to relate the test temperature, humidity, voltage or other environmental stimulus to an additional test level that will increase the hazard rate, thereby reducing the test time. When analyzing test data, it is important to determine a distribution that provides a good fit to the data and is representative of the failure mechanism type. A good fit is important so that the distribution parameters can be used to extrapolate behaviour, or predict the reliability beyond the period over which the data is generated. There are two kinds of non-accelerated tests which are used to predict the data for reliability analysis, manufacturing tests and actual tests.

3.4.2.2 Accelerated Test

The purpose of accelerated testing is to verify the life-cycle reliability of the product within a short period. Thus, the goal in accelerated testing is to accelerate the damage accumulation rate for relevant wear-out failure mechanisms. There are two common forms of accelerated life testing, which are (1) eliminating "dead time" by compressing the duty cycle and (2) reducing the time-to-failure by increasing the stress levels beyond what is expected in the life-cycle. The latter can be run by enhancing a variety of loads such as thermal loads (e.g. temperature, temperature cycling, and rates of temperature change), chemical loads (e.g. humidity, corrosive chemicals like acids and salt) electrical loads (e.g. steady-state or transient voltage, current, power) and mechanical loads (mechanical deformation, vibration and shock/impact).

In the electronic industry, when life cycle reliability testing is the primary purpose, test types such as Highly Accelerated Stress Testing (HAST), Highly Accelerated Stress Screening (HASS), Highly Accelerated Life Testing (HALT) are specified. The test procedures are normally carried out according to the standards of Electronic Industries Association (EIA) [93], Joint Electronic Device Engineering Council (JEDEC) [94] and various Military Standards test handbook.

HAST also stands for "Highly Accelerated Temperature/Humidity Stress Test". It was developed as a shorter alternative to Temperature Humidity Bias (THB) testing in which 85°C/85%RH condition is always used. If THB testing takes 1000 hours to complete, HAST results are available within 96~100 hours. Because of this, the popularity of HAST has continuously increased in recent years. HAST test which is also known as the autoclave or pressure cooker test (PCT) uses a high temperature over 100°C, high relative humidity (RH) about 85%, under high atmospheric pressure conditions (up to 4atm).

3.4.3 Failure Models

In many cases, the stress and damage models are combined to form a single model which is referred to as a failure model. Examples of conditions that are known to induce failures include, but are not limited to, a temperature cycle, a sustained temperature exposure, a repetitive dynamic mechanical load, a sustained electrical bias, a sustained humidity exposure, and an exposure to ionic contamination. Examples of damage include exceeding a material strength, reduction in material strength, removal of material, change in material properties, and growth of a conductive path or separation of joined conductors [92].

Failure models may be classified as overstress and wear-out. Models for overstress calculate whether failure occurs based on a single exposure to a defined stress condition. For an overstress model, the simplest formulation is comparison of an induced stress versus the strength of the material. Die fracture, pop-corning, seal fracture, and electrical overstress are examples of overstress failures. Models for wear-out failures calculate an exposure time required to induce failure based on a defined stress condition. Fatigue, crack growth, creep rupture, metallization corrosion and electro-migration are examples of wear-out mechanisms. In the case of wear-out failures, damage is accumulated over a period until the item is no longer able to withstand the applied load. Therefore, an approximate method combining multiple conditions must be determined for assessing the time to failure.

3.5 Applications of ACF Flip Chips

Typically, flip chip on flex (FCOF) using ACF is being used in the flat display, smart card and disk drive etc. As examples, the applications of ACF flip chips in LCDs and disk drives are introduced in the following sections.

3.5.1 Liquid Crystal Display

The importance of display devices as the most common user-machine interface has increased during the current progress of our information oriented society. LCDs are the most common type of flat panel displays and have been widely used since the early 1970's. Compared to the traditional cathode ray tubes (CRT's) they combine a compact and flat shape with low power consumption. In addition, LCDs are low in weight and are compatible with large scale integrated chips. In the field of flat panel displays, packaging technology has a significant influence on display performance. The electrical interconnect between a LCD and a LCD drive circuit is an area that needs improvement to achieve finer pitch, easier assembly and greater connection reliability. For LCD drive packaging, the ideal assembly process would possess the following characteristics: high density, low processing cost, fine pitch capability and low product profile etc.

A typical LCD assembly using ACF is shown in Figure 3.7, in which the ACF connects the drive chip with the polyimide film and also connects the polyimide film with ITO glass. The main advantages of using ACF compared with the traditional solder material are the low assembly temperature and high potential in fine pitch interconnections.
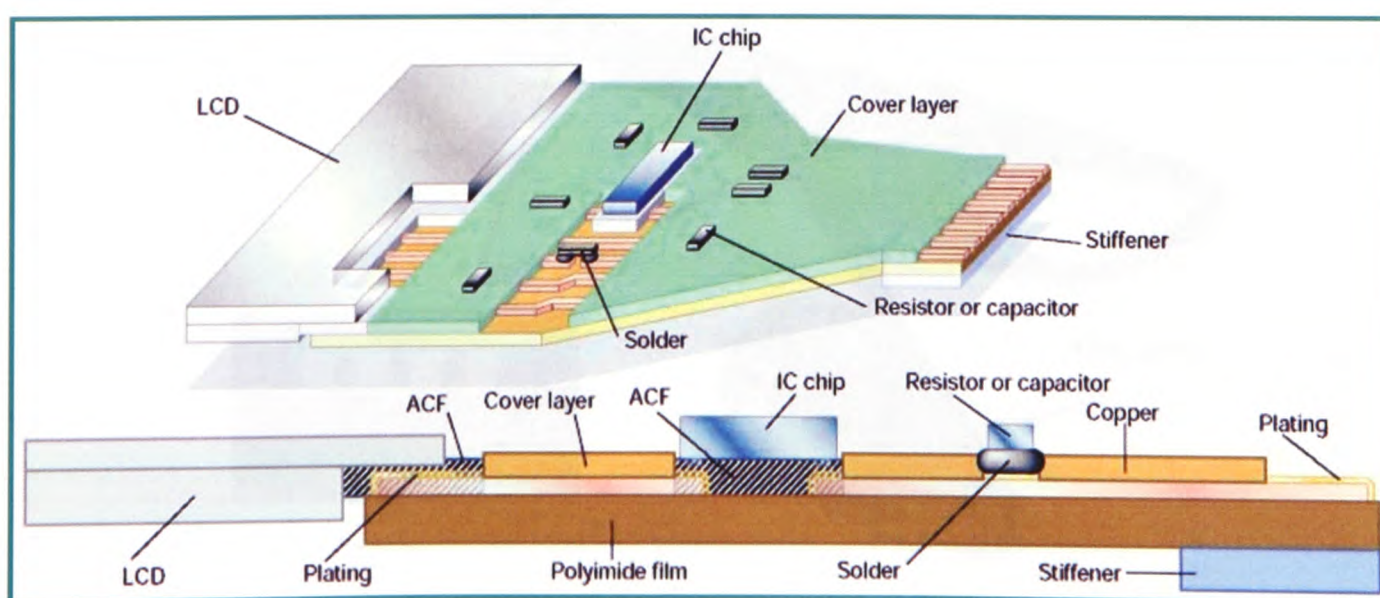
Figure 3.7: A typical LCD assembly [96]

3.5.2 Disk Drive

Current market conditions demand that hard disk drive (HDD) manufacturers adopt advanced technology in every area of drive design to improve drive capacity and performance and simultaneously reduce unit cost. Head stack suppliers in HDD industry are currently working on high density interconnect technologies to provide faster and higher capacity and cheaper head stack components for disk drives.

The ultrasonic TAB bonding and hot bar soldering process are currently widely used in HDD manufacturing. However, both methods are limited by the drawbacks of high cost and low productivity. Therefore, a low cost method to manufacture HDD head using ACF bonding is being developed. Figure 3.8 shows the basic structure of a typical HDD head for hard disk drive. The head gimbal assembly (HGA) is a transducer where the read/write exchange process takes place. The electrical connections with the pre-amplifier ICs, passive components, connector etc. are connected via the flexible printed circuit (FPC) assembly. The feasibility of applying ACF bonding method to the flex-to-flex interconnection between the HGA and FPC bond pads was studied [97].
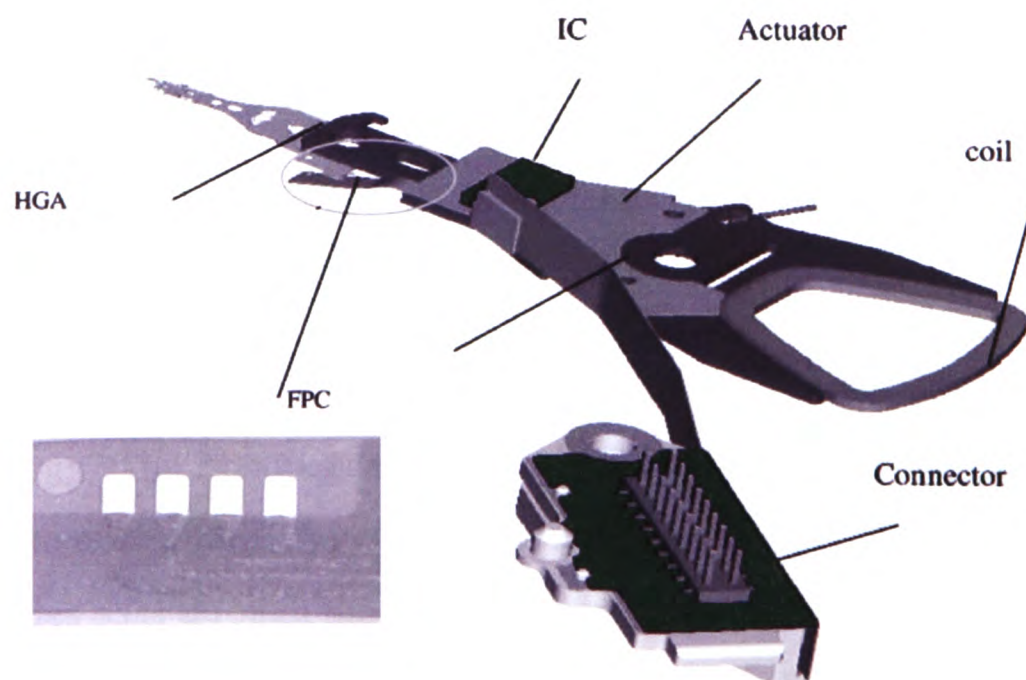
Figure 3.8: The disk drive using ACF technology [97]

3.5.3 Limitations for Further Applications

Currently, the devices assembled using ACAs are widely used in applications where the fine pitch connection or low processing temperature are required which can not be fulfilled by the traditional soldering. However, the application of ACAs is still limited in some specific areas. The limitations for the further applications are summarized below.

(1) Lack of reliability data: ACA is a new material compared to the traditional tin-lead solders, the reliability data is not well known and the failure mechanisms not well understood, especially in high humidity environments.

(2) Today, tin-lead solders are still the main connection materials used in the electronic industry; the facilities used for tin-lead soldering can also be used for lead free soldering. However, these facilities can not be used to assemble ACA components since the procedures of the two technologies, ACAs and soldering, are completely different.

(3) During the bonding process, the adhesive does not have the self-alignment capability as solders. Therefore, there is higher requirement for alignment accuracy when working with ACAs than working with solders. Also, ACA joints are formed under mechanical forces, the connections between the particles and metal pads are not as strong as the solder joints which are formed under physical, chemical reactions.

(4) The compatibility of the ACA assembly process with traditional soldering technology. The bonding temperature of ACAs is much lower than the peak reflow temperature. Therefore, there is a reliability issue when the ACA assemblies pass through the solder reflow process.

Any research that generates the reliability data or helps understand the above issues is deeply welcomed by the electronics packaging industry. It is also the main motivation for this research.

Currently, ACA is gaining wide acceptance among Asian end-users and semiconductor packaging houses. Its relatively slower acceptance in the United States and Europe may reflect Asia's 30 years of favourable experience with ACA in displays [98]. However, the packaging and cost advantages of ACA cannot be long ignored. Particularly in the hypercompetitive semiconductor arena, where cost, functionality, and reliability are being driven to new levels, ACA represents a bright future for middle and high-end manufacturing. As I/O counts become higher, more and more IC designers and users may find that fine-pitch, small-package, high-reliability ACA is their best choice.

3.6 Summary

In this Chapter, flip chip technology which is now popular within the electronics packaging is introduced and compared with traditional wire bonding and TAB technologies. The connection materials used in flip chips ranging from the solder alloys to conductive adhesives are presented.

To date, tin-lead solders are still the main connection materials used in flip chips due to the available long term reliability data and facilities. However, the harmful effect of the lead on the environment is becoming a serious concern for the industry and customer. The lead-free solders and electrically conductive adhesives are being investigated as the possible alternatives to traditional tin-lead solders. The study on the lead-free solders is extensive since the facility for the tin-lead solders can also be used for lead-free solders and the soldering technology is so mature. However, the wide application of lead-free soldering is still limited due to some difficulties which are caused by taking the lead out of the solder alloy that includes the poor wetting performance and high reflow temperature.

Conductive adhesives are being popularly used in the electronic industry especially in fine pitch and low temperature applications where the tin-lead solders are limited to fulfil the requirements. Among them, ACAs are the most popular ones used in flip

chips currently since they have potential for fine pitch connections due to the anisotropy in electrical conduction. However, the reliability performance and the compatibility with soldering technologies are the major concerns with ACA assemblies which will be addressed in the following Chapters 4, 5 and 6.

Chapter 4

Reliability of ACFs for Flip Chip on Flex Applications: An Experimental Study

This Chapter details the experimental work undertaken to complement the modelling efforts. Data was gathered on both the assembly process and reliability testing for ACF materials. The effect of bonding parameters on the electrical performance of ACF assemblies was studied. ACF components were also subjected to a solder reflow profile, this is important to characterise the behaviour of these ACF bonds to subsequent surface mount assembly for other solder joint components on the same board.

For reliability testing, the assembled ACF components were subjected to humidity and temperature environments. An autoclave test at 121°C, 100%RH and 2atm condition was used. Two sets of samples, with and without reflow treatment, were tested in order to examine the effect of solder reflow on the reliability performance of ACF assemblies.

4.1 Introduction

Soldering as a mature joining method has been used for many years in electronics packaging. It is the lowest temperature metallurgical joining method used with metals and plastic materials [6]. For many years, the reliability of solder joints has been

studied and a huge amount of data exists especially for the tin-lead eutectic solders. However, green legislation is demanding the removal of lead from solders and this means that the industry has to investigate reliable replacements. At present other metallic solders are being investigated with the favourite being the tin-silver-copper (SAC) Alloy, but also being investigated are conductive adhesives with or without metal solder on the same board.

A prototype product which was manufactured using both metal soldering and ACF technologies is shown in Figure 4.1, where the chip drive was connected onto the flex substrate using ACF material first. This was then followed by a metal soldering process where other surface mount components were connected to the same substrate.

Soldered components

ACF boned flip chip   **Flex substrate**
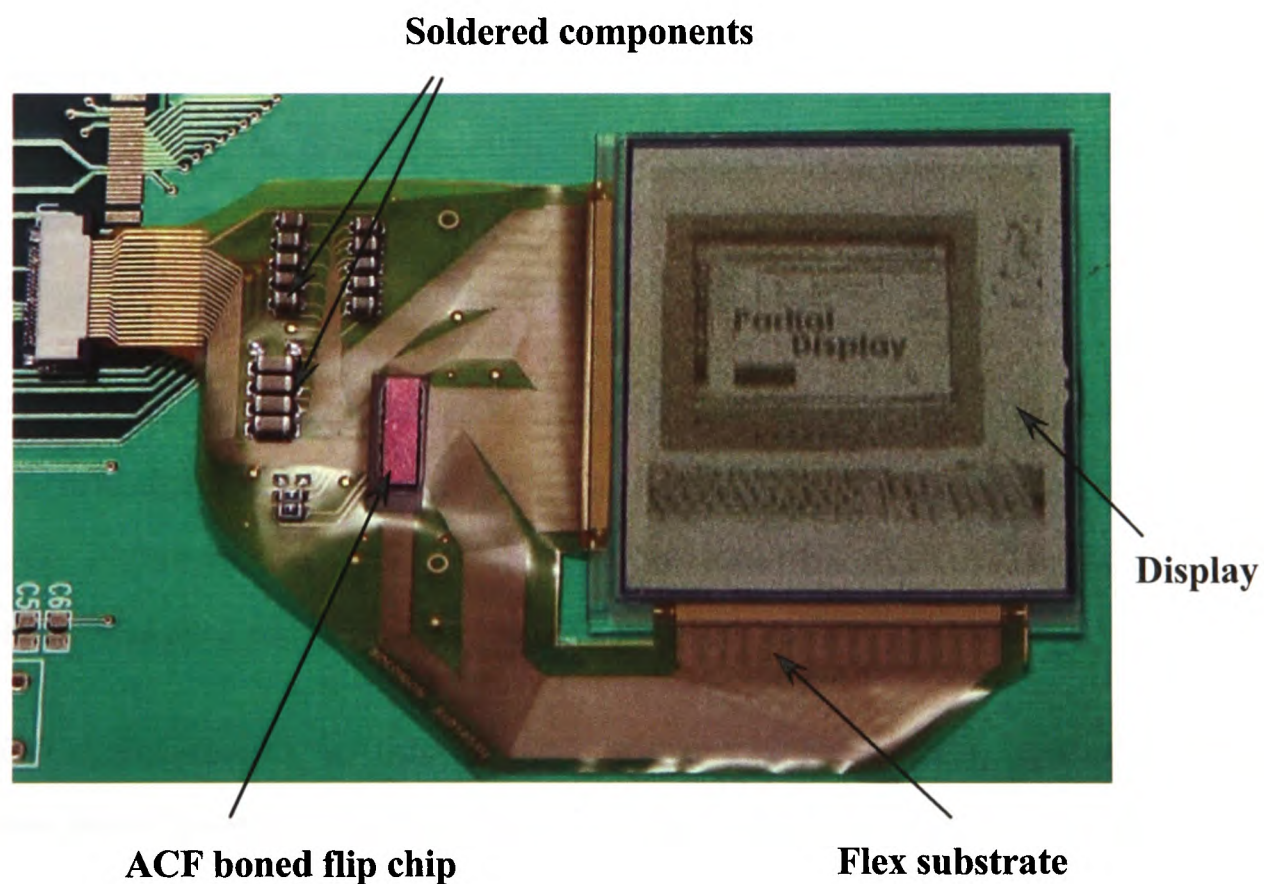
Figure 4.1: A typical display using ACF and solder together

Having mixed board technologies containing both ACFs and solders on the same substrate has a number of advantages. The challenge and concern for industry is the

ability of the ACF materials to survive the high solder reflow temperatures which are much higher than the temperature required to bond and cure the ACF material [20][45].

Although the ability of ACF to withstand multiple solder reflows is considered as the major milestone in its acceptance within the semiconductor packaging industry [98], there has been very little research undertaken in this area. The work presented here was one of the first studies in this area.

Compared with the traditional solder assembly process, the ACF assembly process is simplified since there is no need to use flux, stencil printing and a reflow oven. However, the selection of the bonding parameters is crucial and the following issues must be addressed in any ACF bonding process:

(1) Sufficient conductive particles must be trapped between the pads on the substrate and the die. This is to guarantee enough electrical contact with both conductor surfaces. Care must be taken to ensure that not too many particles are present as this can lead to short circuiting between adjacent pads.

(2) For the ACFs made with metal coated polymer particles, the amount that the particle deforms is important. The bonding process determines the contact area between the conducting particle and the die/substrate pads. This is important as a smaller area leads to greater contact resistance.

(3) The curing degree of the adhesive and the residual stress state after assembly can significantly influence the reliability of the ACF interconnections under hash testing conditions.

Therefore, the combination of the bonding parameters needs to be designed to achieve the best performance of the adhesive joints where the optimum deformation of the conductive particles and the proper curing degree of the adhesive matrix are achieved.

4.2 Experimental Design

Figure 4.2 illustrates the process undertaken in the experimental work which consists of the following four steps:

(1) The chips were first bonded to the substrate using ACFs and after this the joint resistance was measured.

(2) Some of the bonded samples were passed through a solder reflow oven and the joint resistance was again measured.

(3) Two sets of samples, with and without reflow treatment, were put into a pressure cooker for reliability analysis.

(4) Finally failure analysis was conducted to find out the root cause of the failures and the measured increases in joint resistance.

Using the above methodology allowed us to investigate the effects of (a) bonding parameters, (b) solder reflow temperature and (c) moisture absorption on the reliability performance of ACF materials and assemblies.

```
┌─────────────────────────┐
│  Material preparation   │
└─────────────────────────┘
            │
            ▼
┌─────────────────────────┐
│    Flip chip bonding    │
└─────────────────────────┘
            │
            ▼
┌───────────────────────────────┐
│ Joint resistance measurement  │◄──────────┐
└───────────────────────────────┘           │
            │                                │
            ▼                                │
          ╱─────────────╲          Yes       │
        ╱                 ╲──────────────────┘
        ╲  Solder reflow? ╱
          ╲─────────────╱
            │
            │ No
            ▼
┌─────────────────────────┐
│   Pressure cooker test  │
└─────────────────────────┘
            │
            ▼
┌─────────────────────────┐
│     Failure analysis    │
└─────────────────────────┘
```
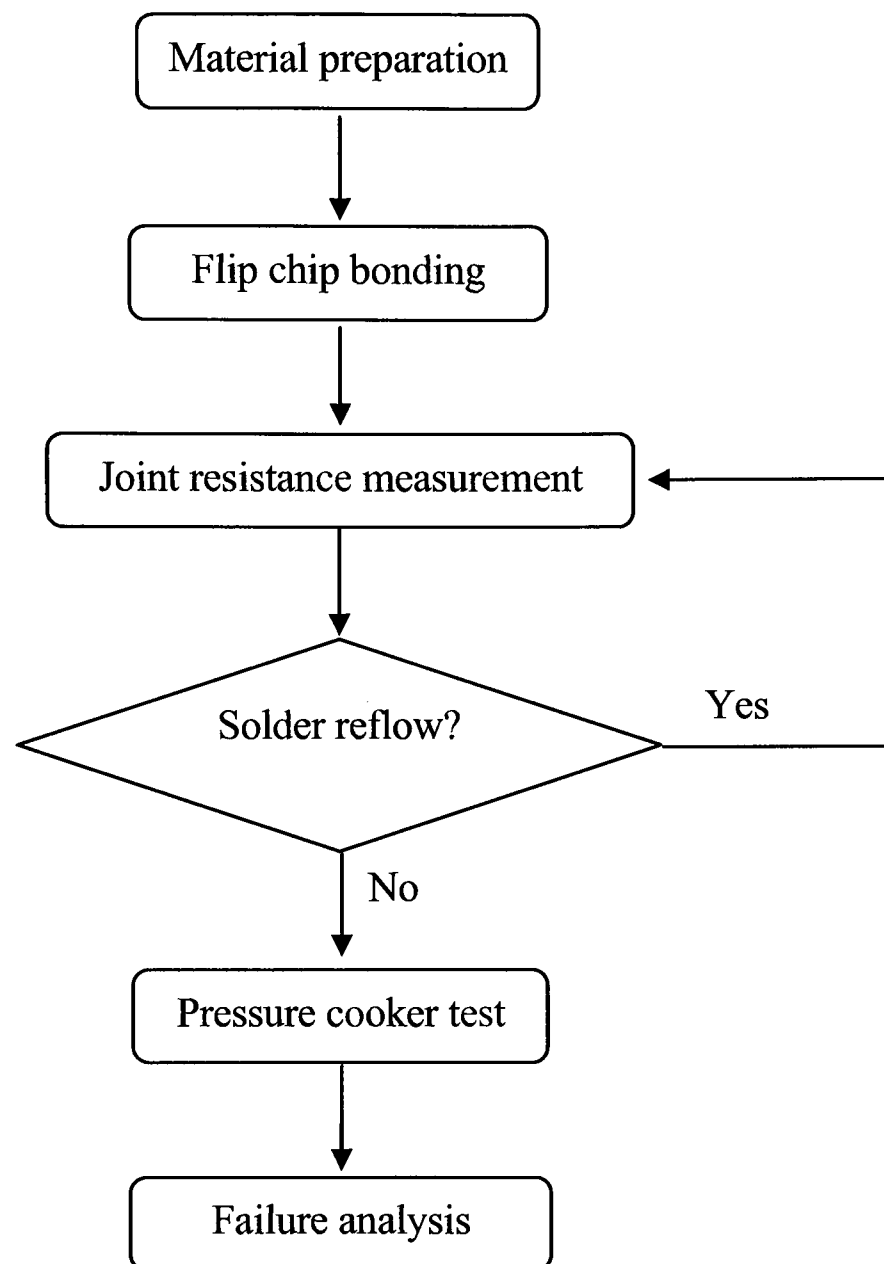
Figure 4.2: The flow chart of the experimental procedure

4.2.1 Materials

Three materials were used in these experiments. These are the silicon die, polyimide substrate, and a commercial ACF. The specifications of each material are available and detailed in the following sections.

4.2.1.1 Silicon Die

The chips used in the experiment analysis are bare dies with Ni/Au bumps. These are non functional chips that were specially designed for reliability test purpose.

The size of the silicon die is 11mm in length, 3mm in width and 1mm in thickness. There are a total of 368 square shaped bumps around the periphery, 300 of them make up the 60 sets of 5 daisy-chained bump groups which run parallel to the length of the chip for electrical connection. The remaining 68 bumps are placed along the width of the die and only contribute to mechanical support. The pattern of the die is shown in Figure 4.3, where the bump area is 50μm × 50μm.
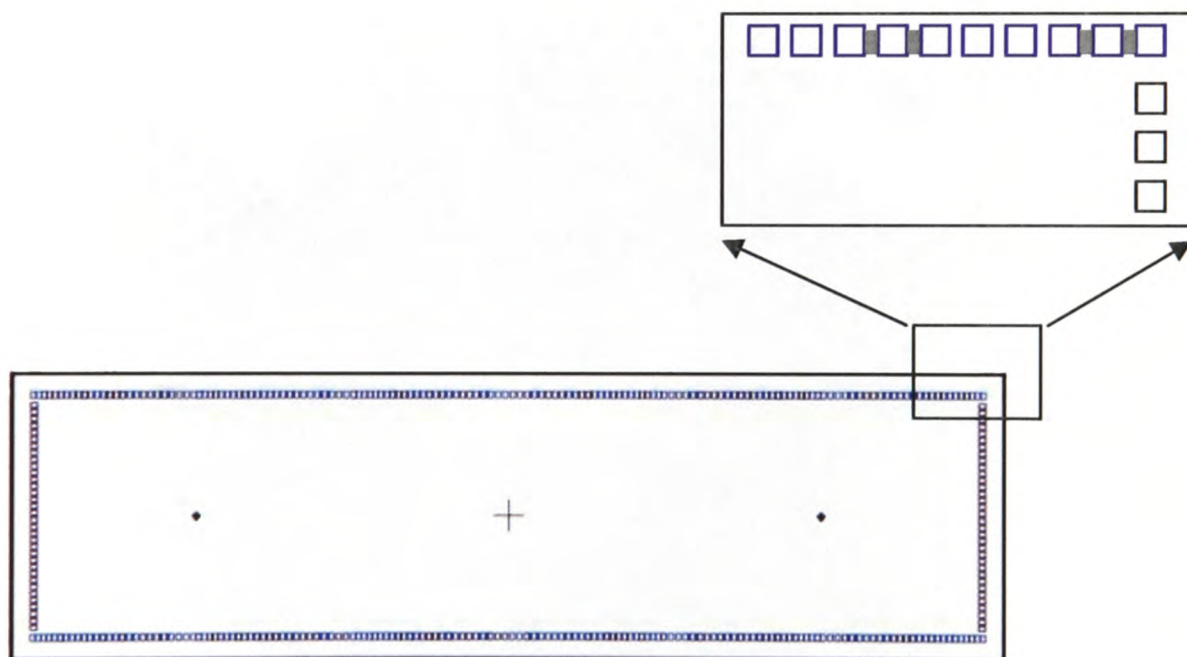
Figure 4.3: Pattern of the silicon die

4.2.1.2 Flexible Substrates

Flexible substrates can be made from polyimide, Liquid crystal polymer (LCP), Polyethylene Napthalate (PEN), and Polyethylene Terephthalate (PET) etc. Among them, polyimide is the most popular material being used in the electronics packaging industry due to its temperature profile.

Compared with the FR4 printed circuit board, glass or ceramic substrates, flexible substrates offer advantages such as reduction in size and weight and shape flexibility. Flexible substrates are widely used in LCDs, disc drives and smart cards etc.

The flexible substrate used in this research was made from polyimide and specially designed with daisy-chained circuitry which matched the die's bump pattern. The substrate has a thickness of 25μm and an area of 50mm × 50mm. The metal pad on the flexible substrate is made up of three layers consisting of copper (about 12μm in thickness), electro-plated nickel (4.0μm in thickness) and gold (0.5μm thick). The layout of substrate pattern is shown in Figure 4.4.
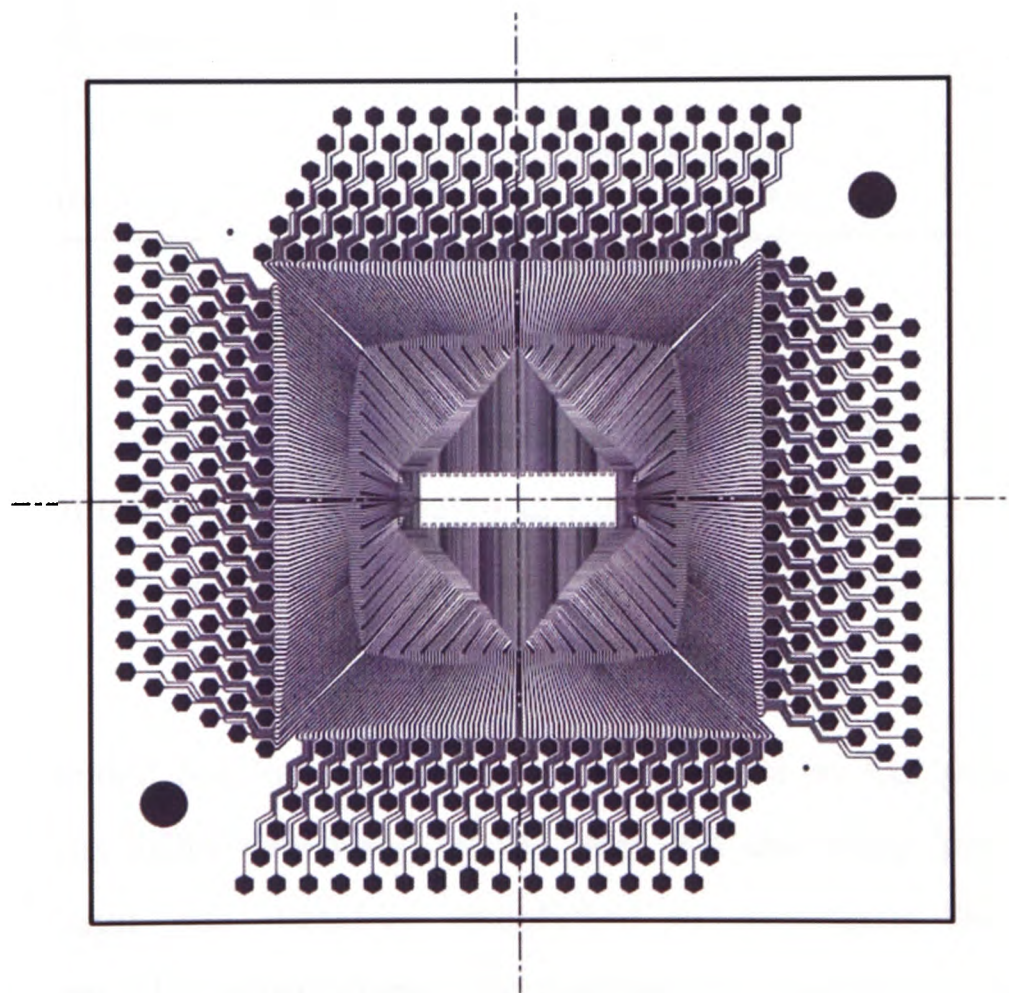
Figure 4.4: Pattern of the polyimide substrate

4.2.1.3 Anisotropic Conductive Film (ACF)

The ACF used in this experiment is a thermosetting epoxy adhesive with a random distribution of conductive particles. It is commercially available and believed to have

the capability for fine pitch interconnections. The detailed specifications provided by the manufacturer are summarised in Table 4.1.

Table 4.1: Specification of the ACF used in this experiment

Description	
Thickness (μm)	35
Structure	Single layer with particles
Conductive particle	Ni/Au coated resin ball
Insulating layer	Yes
Particle diameter (μm)	3.5
Tg (°C)	131
Density of conductive particles	3.5 million/mm^3

The conductive particles are polymer balls with Ni/Au coating. The structure of the ACF material and the particles are shown in Figure 4.5. ACFs are normally stored at low temperature, and subjected to ambient temperature several hours prior to the bonding process.

The recommended bonding conditions were provided by the supplier. However, bonding conditions differ depending on the chip size and bump pattern. A detailed experimental design was therefore established to investigate the best bonding conditions for new ACF applications. The parameters investigated were (a) bonding pressure, (b) bonding temperature and (c) bonding time. These are listed in Table 4.2.
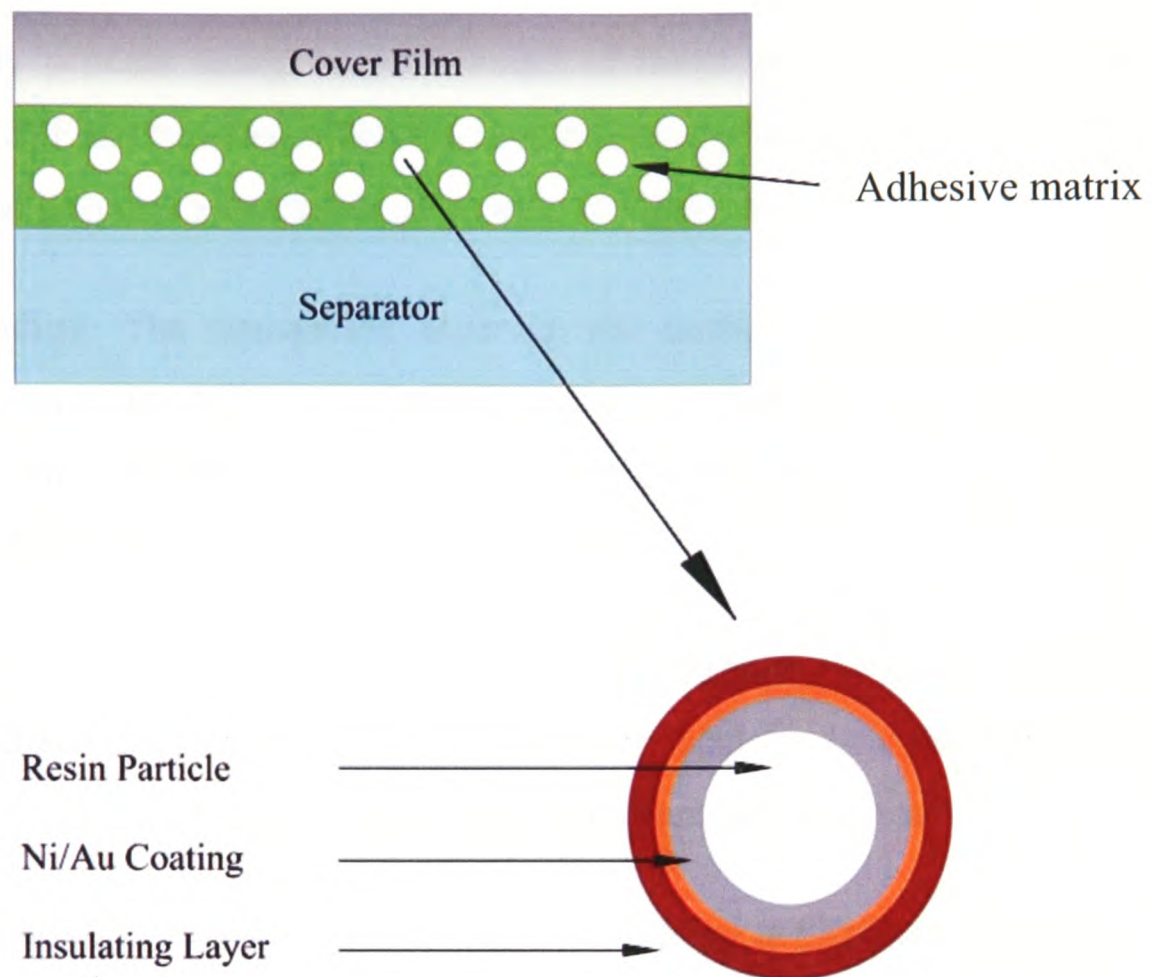
Figure 4.5: A typical ACF made by Ni/Au coated polymer particles

Table 4.2: The bonding parameters used in experiments

Pre-bonding	
Temperature (°C)	90
Pressure (MPa)	0.18
Time (s)	3
Final bonding	
Temperature (°C)	140, 160, 180, 200, 220
Bonding pressure (MPa)	43.1, 86.2, 129.3, 172.4
Time (s)	5, 8, 10

4.2.2 Flip Chip Bonding Process

The assembly process using ACFs consists of three steps: (1) Pre bonding, (2) Alignment and (3) Final bonding. The flip chip bonding process using the ACFs made with metal coated polymer particles is illustrated in Figure 4.6.

(1) Pre bonding: The transparent layer on the surface of the supplied ACF is removed and the ACF is laminated onto the surface of the substrate. Then a pressure of 0.18MPa is applied over the bonding area for a few seconds at 90°C. The separator layer is then removed.

(2) Alignment: The chip is then aligned to the substrate by using the marks on the chip and substrate. Since the ACF is mainly used for fine pitch applications, there is always significant requirement for alignment accuracy.

(3) Final bonding: Heat and pressure are now applied at the back side of the chip which cures the ACF. Before cure takes place the ACF material is soft and can flow between the bond pads allowing the conductive particles to move and distribute evenly throughout the ACF joints. When the curing process is completed, the ACF becomes hard. The deformed particles are then trapped between the pads and this creates the anisotropic electrical contact between the chip and the substrate.
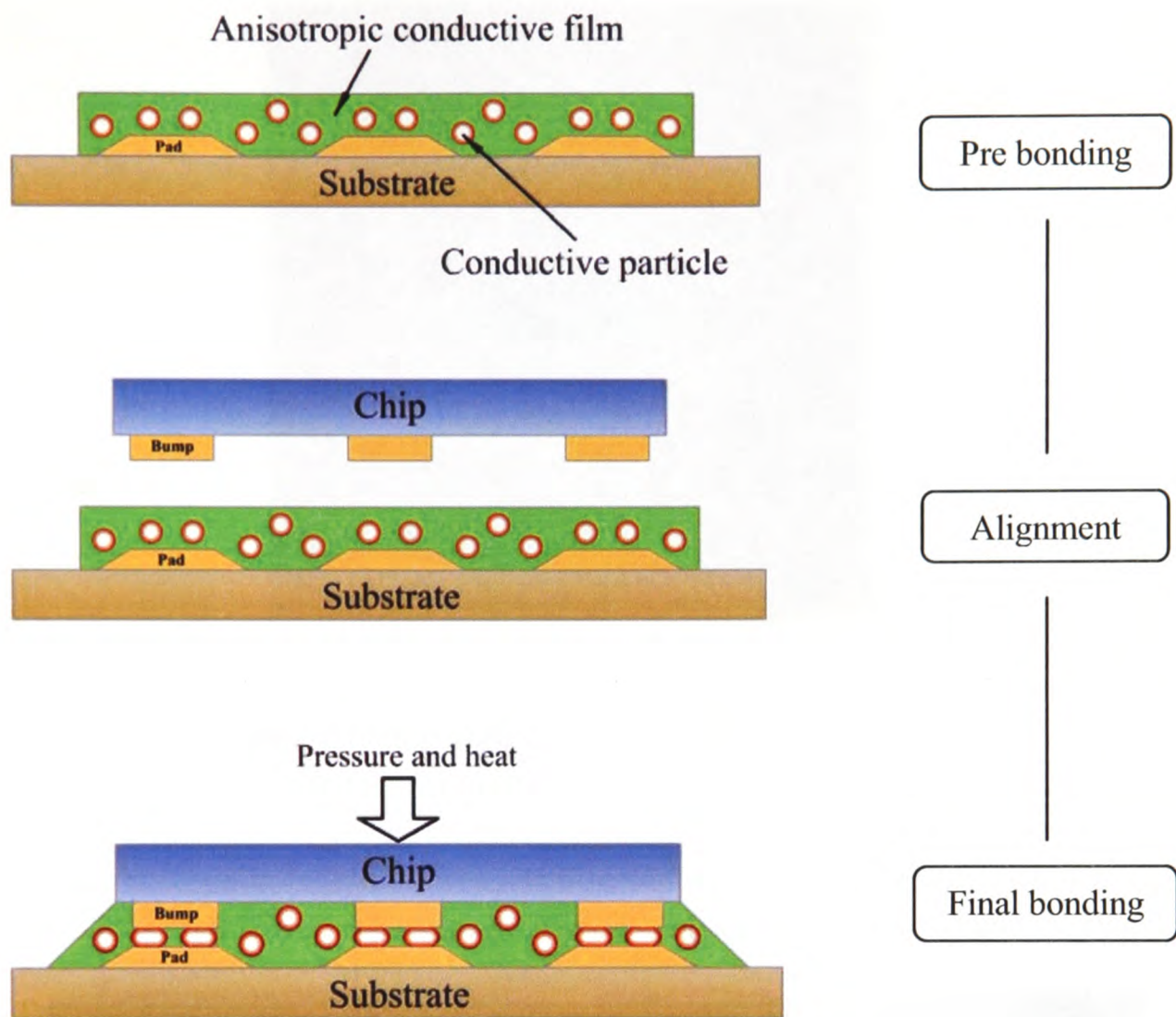
Figure 4.6: Flip chip bonding process using the ACF

The top view of the final sample is shown in Figure 4.7. The final bonding process was finished with the Semi Automatic Flip Chip Bonder (Toray SA2000) as shown in Figure 4.8, this machine is specially designed for fine pitch ACF flip chip bonding and the alignment accuracy of this machine is less than 2μm.
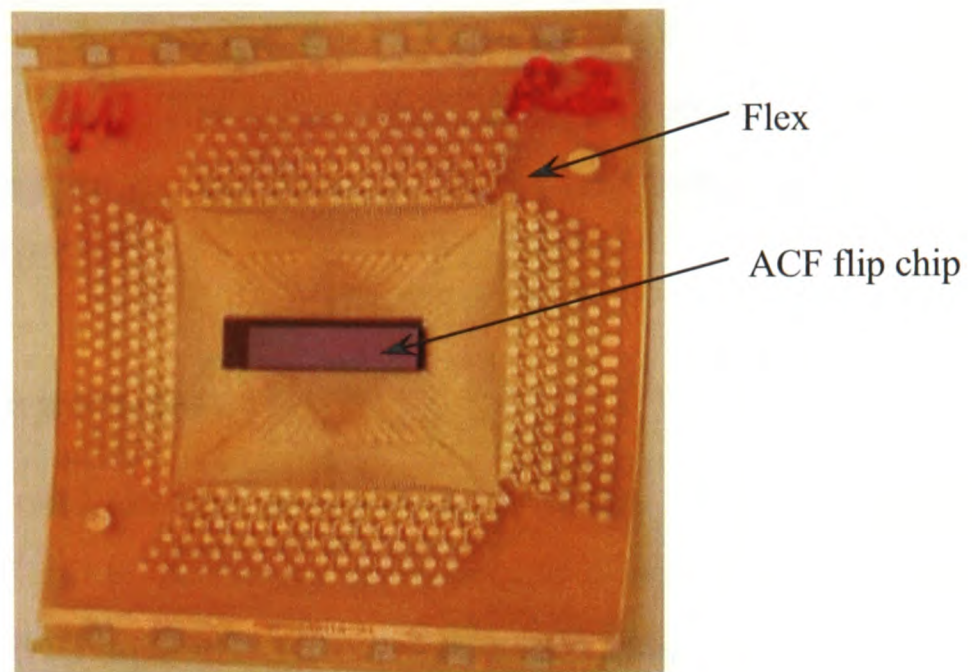
Figure 4.7: Top view of the ACF flip chip sample
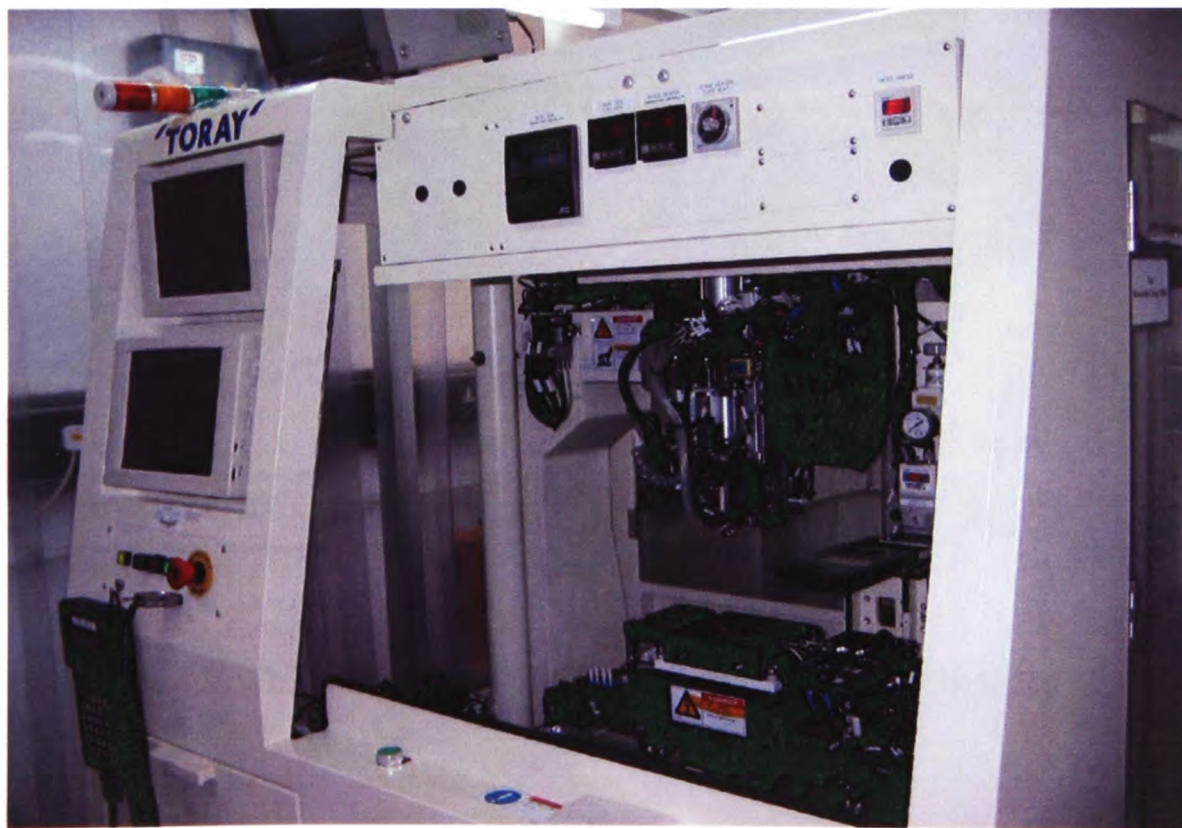
Figure 4.8: Toray semi-auto flip chip bonder (Toray SA2000)

In order to study the effect of solder reflow on the electrical performance of the ACF assemblies, some of the samples were fixed onto FR4 board and then passed through a solder reflow oven. The reflow profiles were defined in advance using thermo-couples according to the specification for tin-lead solder paste. The reflow peak temperature was 210°C.

4.2.3 Joint Resistance Measurement

Joint resistance is used as the indicator to evaluate the electrical/reliability performance of the ACF joints. A popular method used to measure joint resistance is the four-point probe (FPP) method. The specially designed circuit for these FPP measurements in this experiment is illustrated in Figure 4.9. In this test, 1mA constant direct current (DC) was applied to the circuit and the voltage was read from a HEWLETT PACKARD multimeter. The joint resistance was obtained by using Ohm's Law, $R = V/I$.
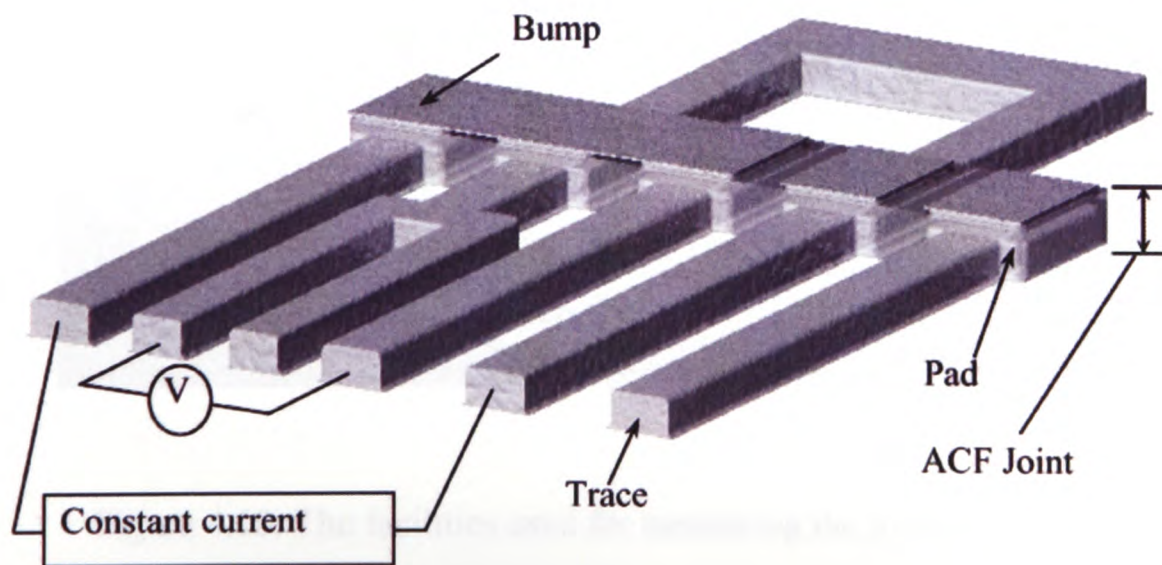
Figure 4.9: The four point probe method to test the joint resistance

The joint resistance measured was the total of the resistance of the bonding electrodes, the contact resistance between the conductive particles and bonding electrodes, and the resistance of the conductive particles. Therefore, for the same

bonding electrodes and the same kind of ACF, the variation of the joint resistances can reflect the changes in contact resistances which are highly dependent on the quality and size of the contact area at the interface between the conductive particles and metal pads.

For the ACF flip chip using the daisy chained circuit shown in Figure 4.7, sixty measurement points can be achieved from each ACF assembly. The facilities used for the joint resistances including a mulitmeter, amperemeter and a power supply, as shown in Figure 4.10.
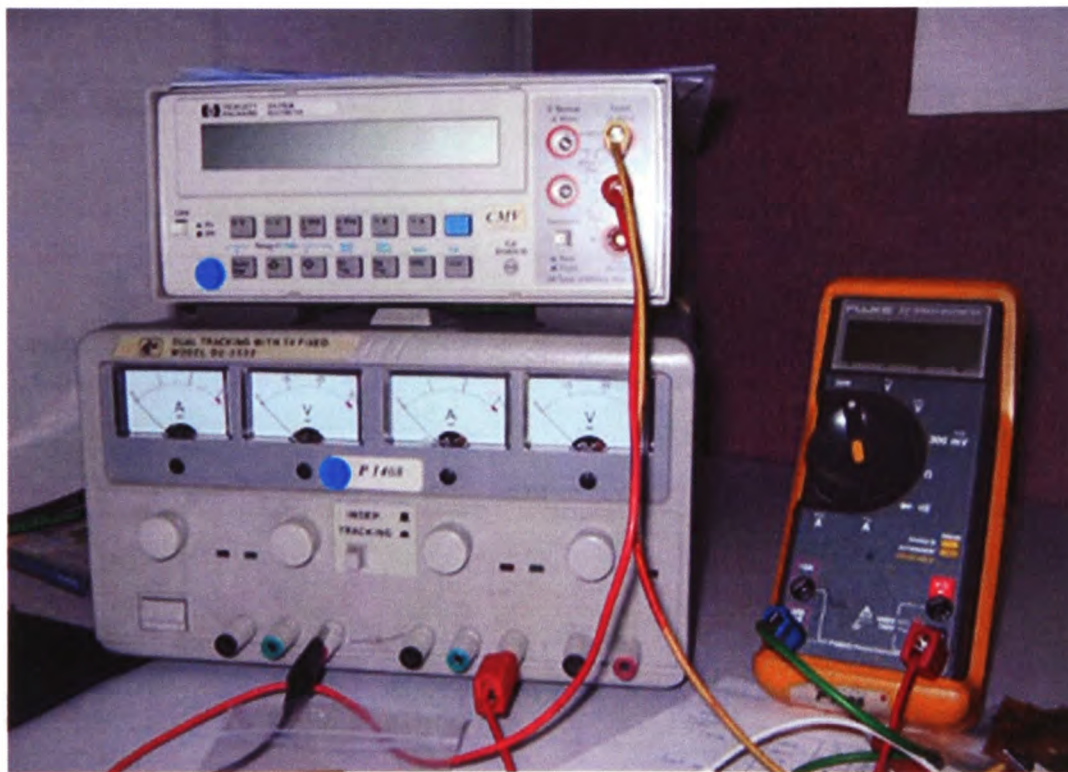
Figure 4.10: The facilities used for measuring the joint resistances

4.3 Results and Discussion

The effect of the bonding parameters on the joint resistance is presented for both sets of samples, with and without reflow treatment and then followed by Differential Scanning Calorimeter (DSC) test results and the autoclave test results.

4.3.1 Bonding Conditions

Different bonding parameters were used. Twelve sets of ACF assemblies were bonded in order to compare the joint resistance. The baseline bonding parameters were Bonding Temperature (200°C), Bonding Pressure (86.2MPa) and Bonding Time (10s). The subsequent solder reflow profile used for the tin-lead solder had a peak temperature of 210°C.

4.3.1.1 Bonding Pressure

Figure 4.11 details the average results from twelve assemblies analysed for joint resistance and bonding pressure. The vertical bars showing the standard deviation of the results for each bonding pressure value. In these experiments, the bonding temperature and bonding time were kept constant at 200°C and 10s respectively.
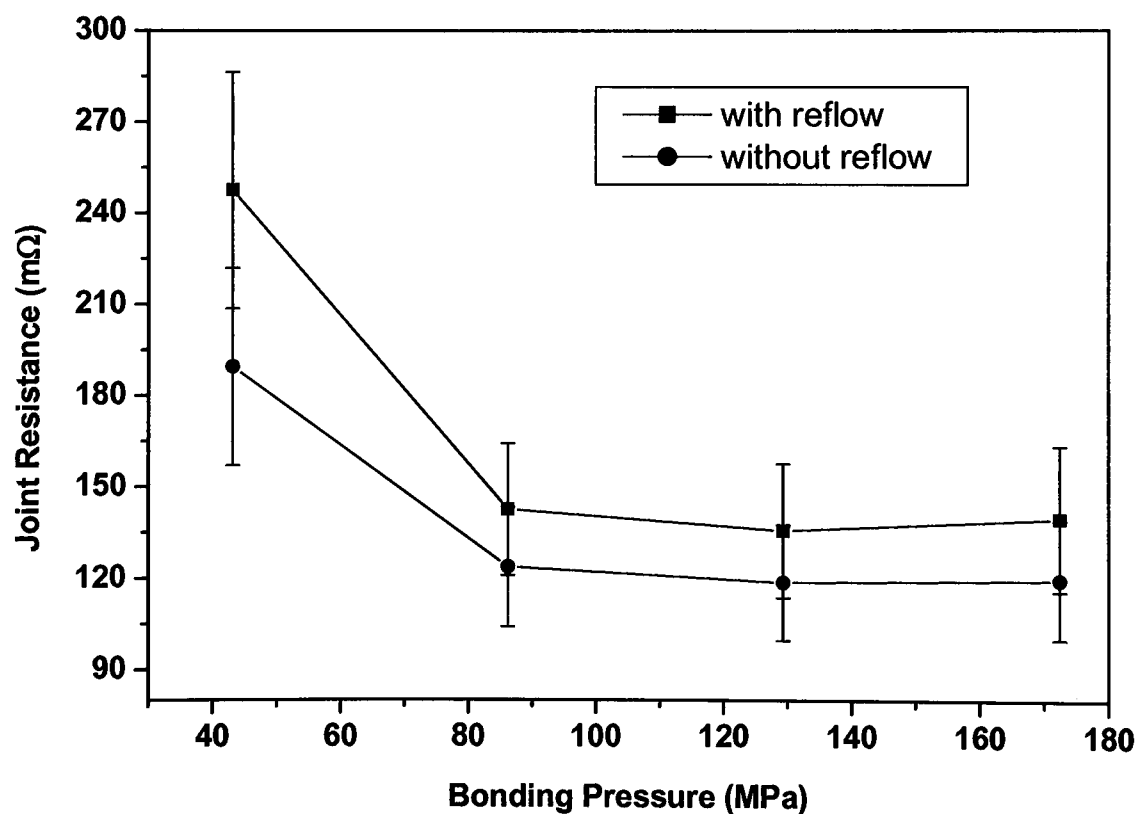
Figure 4.11: Variation of joint resistance with bonding pressure

For the samples without the reflow treatment, the mean values of the joint resistances decreased as the bonding pressure increased from 43.1 to 86.5MPa. After

this the joint resistance remained constant around 120mΩ. A possible explanation for this is that the small bonding pressure could not deform the particle and the contact area was too small to achieve a lower contact resistance. Compared to these as-bonded samples, the joint resistance of the samples that have passed through a reflow process were higher. However, the tendency of the profile of the joint resistance versus bonding pressure was similar in each experiment, with or without reflow process.

After the reflow process, the mean values of the joint resistances of Chip on Flex (COF) assemblies increased by 20 to 60mΩ compared with the corresponding non-reflowed ones. The joint resistance was particularly higher for the samples bonded at lower or higher pressures.

Deformation of the conducting particles is held by the shrinkage forces in the adhesive matrix. Therefore, during the reflow process the expansion of the adhesive may cause a reduction of the holding force and thus reduced the contact area between the conductive particles and metal pads as the assembly heats up. Contact resistance increased the most when the using the lowest bonding pressure, 43.1Mpa. When using a high bonding pressure the contact resistance change after the reflow process was not as severe. This is probably due to the fact that these over deformed particles were firmly held by the cured adhesive. However the worse reliability performance may be expected in this case as there is a high probability that some of the particles could be crushed during the bonding process.

The big error bars, shown in Figure 4.11, when the ACF is bonded at 43.1Mpa, also indicate that the electrical performance of these samples was not as stable as when the sample was bonded at higher pressures. It is also noticed that the stability of the electrical contact in the reflowed samples was reduced compared to the corresponding non-reflowed ones.

In order to prove the effect of the bonding pressure, optical photos were taken on samples using transparent glass substrates as the bonding medium. Figure 4.12a shows the ACF joints bonded at lower bonding pressure. The particles captured between the

metallizations were deformed gently and the contact areas were too small to obtain low contact resistances.
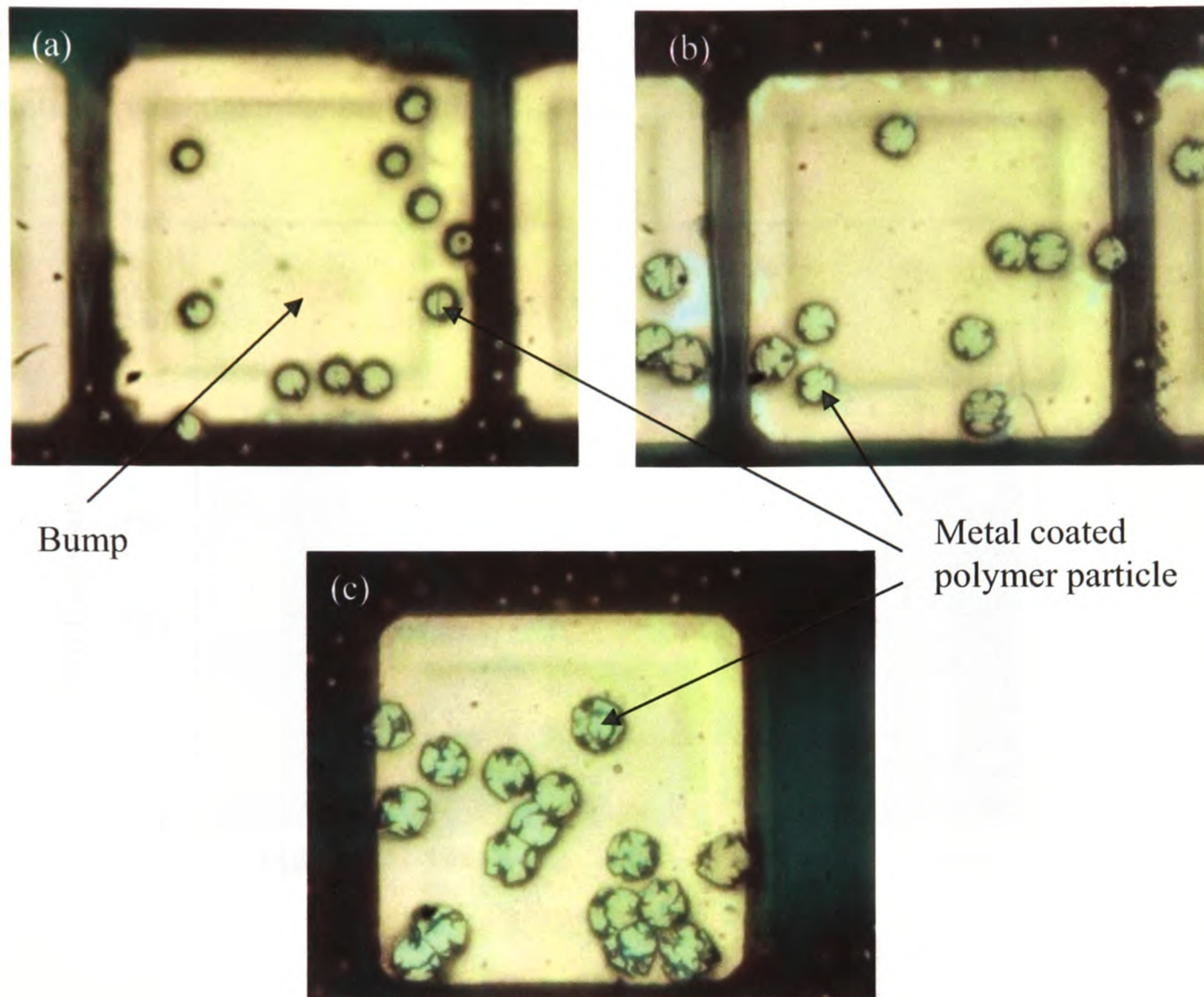
Figure 4.12: ACF joints, bonded at (a) lower (b) appropriate and (c) higher pressure

Figure 4.12c shows the ACF joints bonded at higher bonding pressure. Clearly, this bonding pressure was too high as most of the captured particles were crushed. Some of these particles may still conduct electricity, but they will likely have very poor reliability. The ACF joints bonded at the appropriate bonding pressure are presented in Figure 4.12b.

4.3.1.2 Bonding Temperature

The relationship between the joint resistance and bonding temperature is shown in Figure 4.13, where the bonding pressure and bonding time were kept constant at 86.2MPa and 10s respectively. The results are for the mean value of the joint resistances, with the error bars indicating one standard deviation variation.
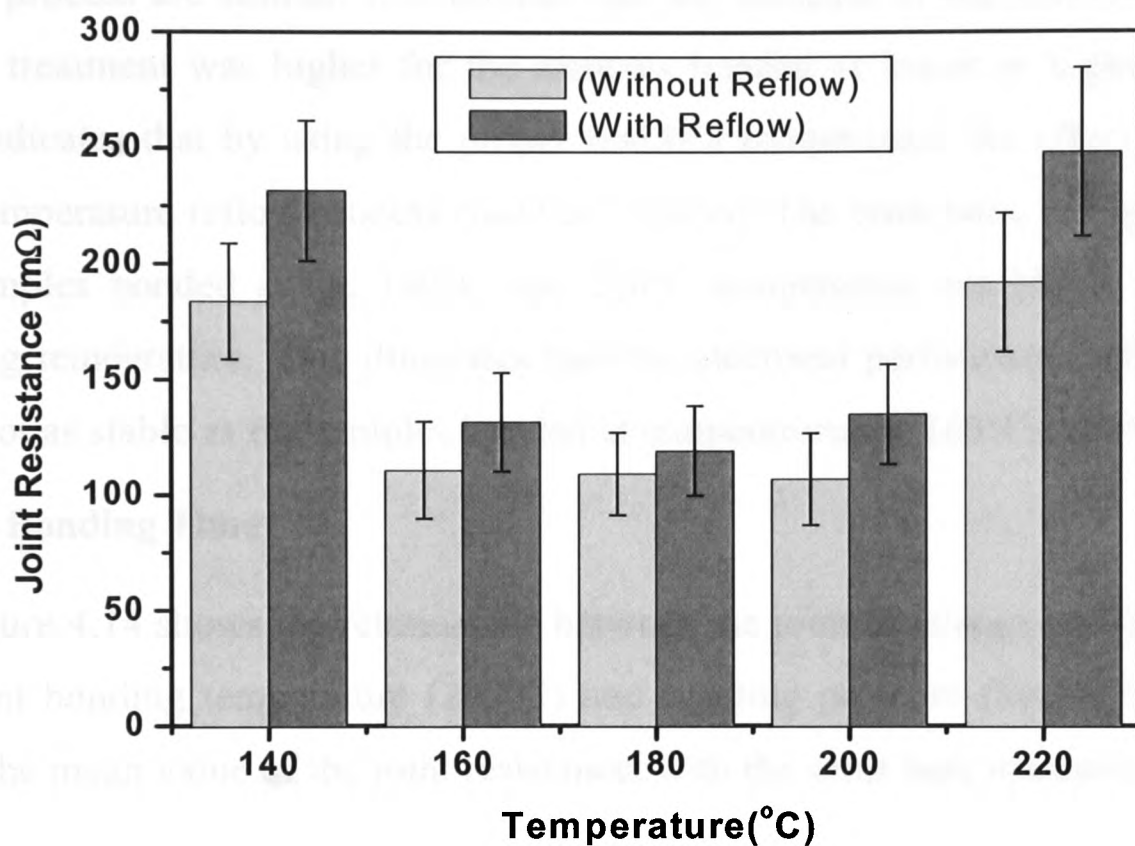
Figure 4.13: Variation of joint resistances versus bonding temperature

These results indicate that when the bonding temperature was at its lowest (140°C) or highest (220°C), the mean joint resistances of the ACF joints were found to be higher. The possible reason for this is: when the bonding temperature is lower, the ACF may not be cured sufficiently, the elastic deformation of the conductive particles maintained by the shrinkage force in the adhesive could recover to some extent; the contact resistances are therefore higher due to the unstable contact between the particles and the metal pads. However, if the bonding temperature is too high, the ACF will be cured quickly; the curing process will complete before the particles deform as much as they can providing maximum contact area and spread evenly between the

bumps and the pads, hence, the contact areas between the particles and the bump/pad are not big enough for stable conduction resulting in higher contact resistances.

After the reflow treatment, the joint resistances increased by $10m\Omega$ to $60m\Omega$ compared to the corresponding as-bonded samples. The trends between the joint resistances versus the bonding temperature of the COF samples with and without reflow process are similar. It is noticed that the increase of the resistances due to the reflow treatment was higher for the samples bonded at lower or higher temperature. This indicates that by using the proper bonding temperature the effect of subsequent high temperature reflow process could be reduced. The error bars, in Figure 4.13, from the samples bonded at the 140°C and 220°C temperature are bigger than the other bonding temperature. This illustrates that the electrical performance of these samples were not as stable as the samples bonded at temperatures of 160°C, 180°C and 200°C.

4.3.1.3 Bonding Time

Figure 4.14 shows the relationship between the joint resistance and bonding time at constant bonding temperature (200°C) and bonding pressure (86.2MPa). The results show the mean value of the joint resistance, with the error bars indicating one standard deviation variation.

When the bonding time was less than 10s, the mean joint resistance of COF samples decreased as the bonding time was reduced. For the COF samples with reflow treatment, the similar curve was obtained except an averaged increase of $20m\Omega$ to $30m\Omega$ in joint resistance. It is suggested that sufficient bonding time is required to achieve the good electrical performance of ACF joints since the adhesive may not be cured properly in a short time bonding. The electrical contact in the reflowed ACF joints are not as stable as the corresponding non-reflowed ones which is reflected by the length of the error bars.
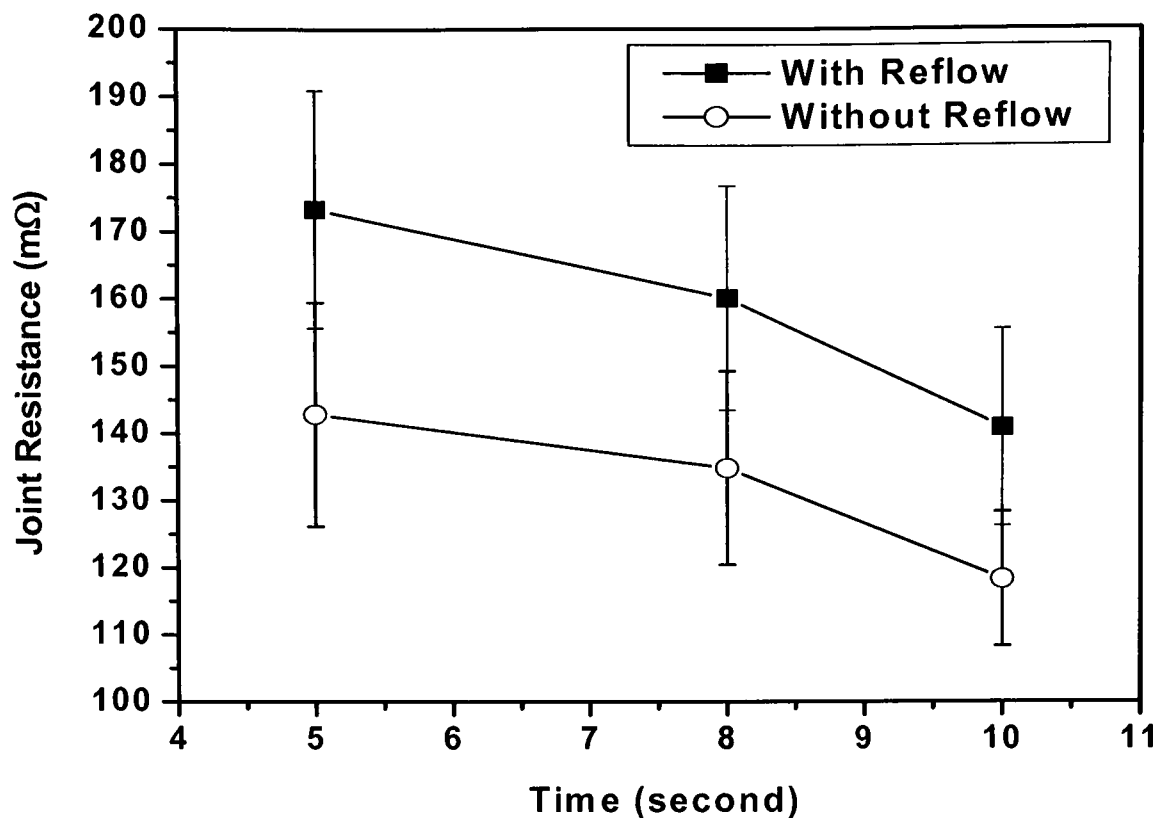
Figure 4.14: Variation of joint resistance with bonding time

4.3.2 DSC Test Results

For the epoxy based ACFs, when the temperature increases, the ACF melts and transforms into a low viscosity liquid. It then cross-links to form the three dimensional crystallized structure which contributes to its stable physical properties [48]. The density of the cross-linkage can be indicated by the degree of adhesive cure that has taken place. This degree of cure plays an important role in determining the reliability performance of the final ACA joints. A minimum cure degree is required to provide a certain level of mechanical and electrical performance. When the material is not fully cured it will be too soft to restrain the conductive particles in place and hence these particles may easily loose contact with the metal pads.

The degree of cure in a conductive adhesive can be examined by using a Fourier Transform Infrared Spectrophotometer (FTIR) or Differential Scanning Calorimeter (DSC) [37][92][95]. In these publications it was shown that the degree of cure in the ACA joints was very dependent on bonding temperature.

In this research, the degree of cure in the ACF was examined using a Modulated DSC instrument (by TA Instruments, Model 2910). Both the heat capacity of endothermic and the exothermic transitions were measured for a particular test sample. This provides quantitative information regarding the enthalpic changes during the cure process.

Three kinds of samples were prepared for the DSC test, including:

(1) Raw ACF: In this case the ACF material was not cured or sent through a subsequent reflow process

(2) Cured ACF: In this case the ACF material was cured at the bonding temperature of 200°C for 10 seconds.

(3) Cured and Reflowed ACF: In this case the ACF was cured at the bonding temperature of 200°C for 10 seconds and then subjected to a tin-lead solder reflow process.

For the cured samples detailed in (2) and (3) above, these were prepared as follows: firstly, the ACF material was placed onto a glass substrate and then the cover film was peeled off. After the pre-bonding process (where the assembly ws subjected to 100°C temperature), the separator layer was peeled off. Then an aluminium foil was put on the surface of the ACF to avoid adhesion of ACF with the flip-chip bonding head. This glass/ACF/Aluminium-film assembly is then subjected to the usual cure temperature process with the parameters of bonding temperature, pressure and time as detailed above. Sample (3) above, was then subjected to a lead-based solder reflow process which had a peak temperature of 210°C. Before the DSC test, the aluminium foil was taken off the ACF carefully, and then the ACF was peeled off the glass substrate to provide the samples for the DSC tests.

The three samples were then analysed using the DSC test in an inert nitrogen environment. The temperature changes in this DSC test were from ambient to 220°C with a heating rate set at 10 °C/min.

As shown in Figure 4.15, for the non-reversing heat flow, an exothermic enthalpy of 187.3 J/g of heat was released during the curing process for the raw ACF. For the second sample where the ACF was cured at bonding temperature, as most of the curing reaction had occurred during the final bonding process, only an exothermic enthalpy of 23.30 J/g of heat was released. Suggesting that most of the reaction had already taken place.
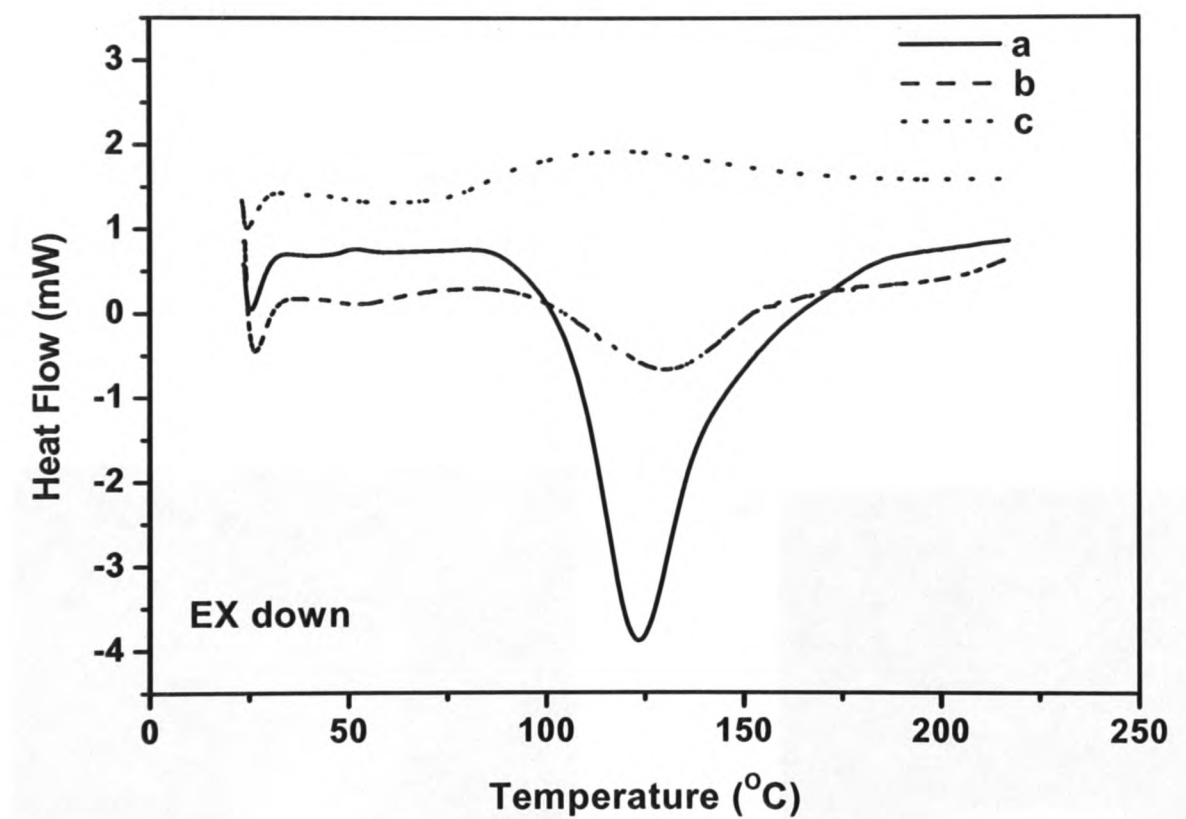
Figure 4.15: Curing profile of (a) Raw ACF (b) Cured ACF and (c) Cured ACF with reflow treatment

For the cured ACF that was also subjected to the reflow treatment, the curing reaction was completed fully as it passed through a long high temperature process. Interestingly, the peak direction of the DSC curve indicates that some endothermic

reaction had taken place. This could be due to over curing of the ACF when subjected to the reflow process or due to some other chemical reactions.

4.3.3 Reliability Tests

In this research, the autoclave test was used to evaluate the reliability performance of ACF assemblies in a humid environment. According to the JEDEC standard [94], test conditions were set to 121°C, 100%RH at 2atm for 24, 48, 96 and 168 hours duration. Relative Humidity is defined as the ratio of the water vapour density to the saturation vapour density, usually expressed in percent:

$$Relative \ \ Humidity = \frac{Actual \ \ vapour \ \ density}{Saturation \ \ vapour \ \ density} \times 100\%$$

Moisture diffusion in the test samples is highly dependent on the temperature and RH of the surrounding environment. The facility for the autoclave test is shown in Figure 4.16.
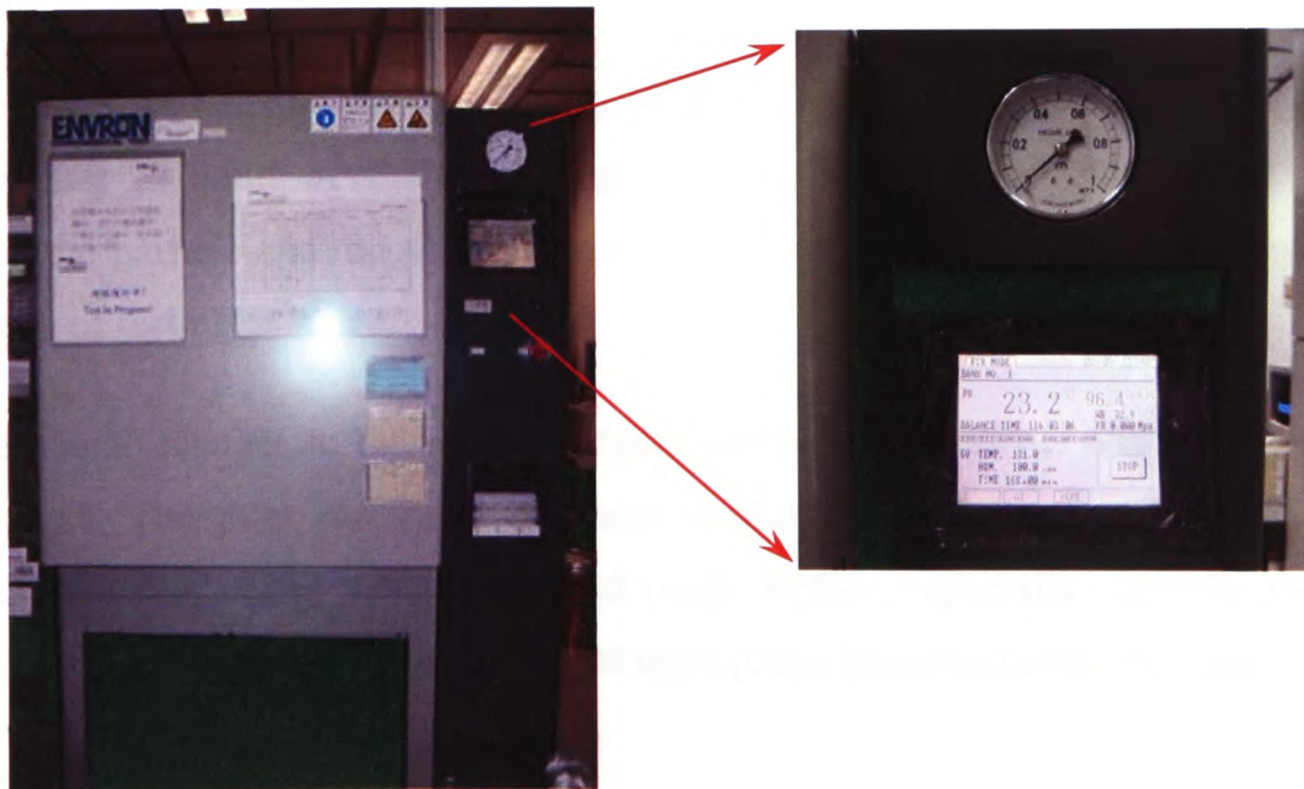
Figure 4.16: The facility used for autoclave test

After each test, some of the samples were cross sectioned and then examined using a Scanning Electron Microscope (SEM) in order to analyse the root cause of any measured increase in contact resistance that would be due to delamination type failures.

The flip chip on flex samples used in this reliability test were bonded at 200°C, 86.2MPa for 10 seconds. Both assemblies, with and without a subsequent reflow profile, were tested. For the assemblies without a reflow treatment, results were obtained at 24, 48, 96 and 168 hours of the reliability test. For the assemblies with a reflow treatment, the results were only obtained at 24 hours after the start of the test.

4.3.3.1 Joint Resistances and Failure Rate

The joint resistances of the ACF joints were measured at 0, 24, 48, 96 and 168 hours during the test. Any joint that exhibited greater than 100% increase in joint resistance (over the time zero value) was considered to have failed. As illustrated in Figure 4.17 more than 85% of ACF joints were assessed to be failed in the first 24 hours of the test. This was for the assemblies that had not been subjected to a subsequent reflow profile.

However, visualising the joints using SEM showed that there were no open joints present after 24 hours of testing. An open joint is seen through clear delamination between the particle and the pad. 25% of the ACF joints were found to be open after 168 hours of testing.

The actual changes to the joint resistance during the autoclave test are plotted in Figure 4.18. The joint resistance increased slightly in the first 24 hours, where it doubled its value. After this it increased much further, especially over the next 72 hours. This is probably due to a number of open joints forming during this period.
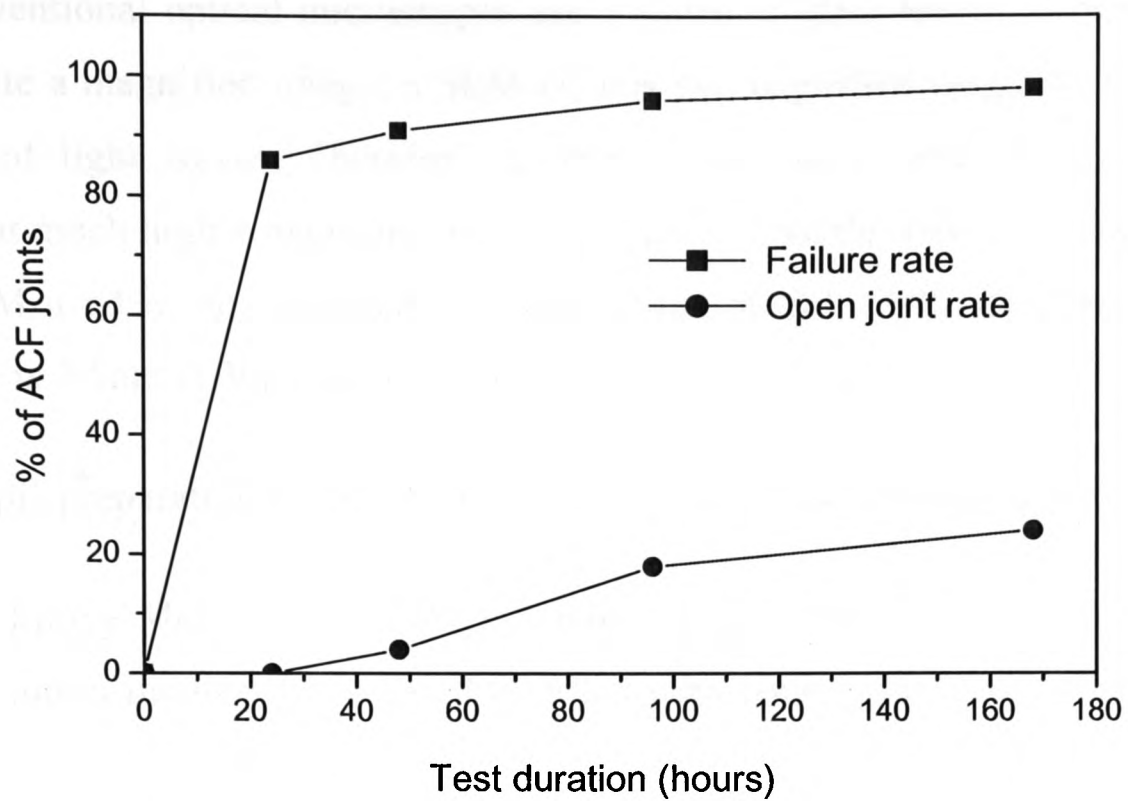
Figure 4.17: ACF joint failure rate and open joint rate
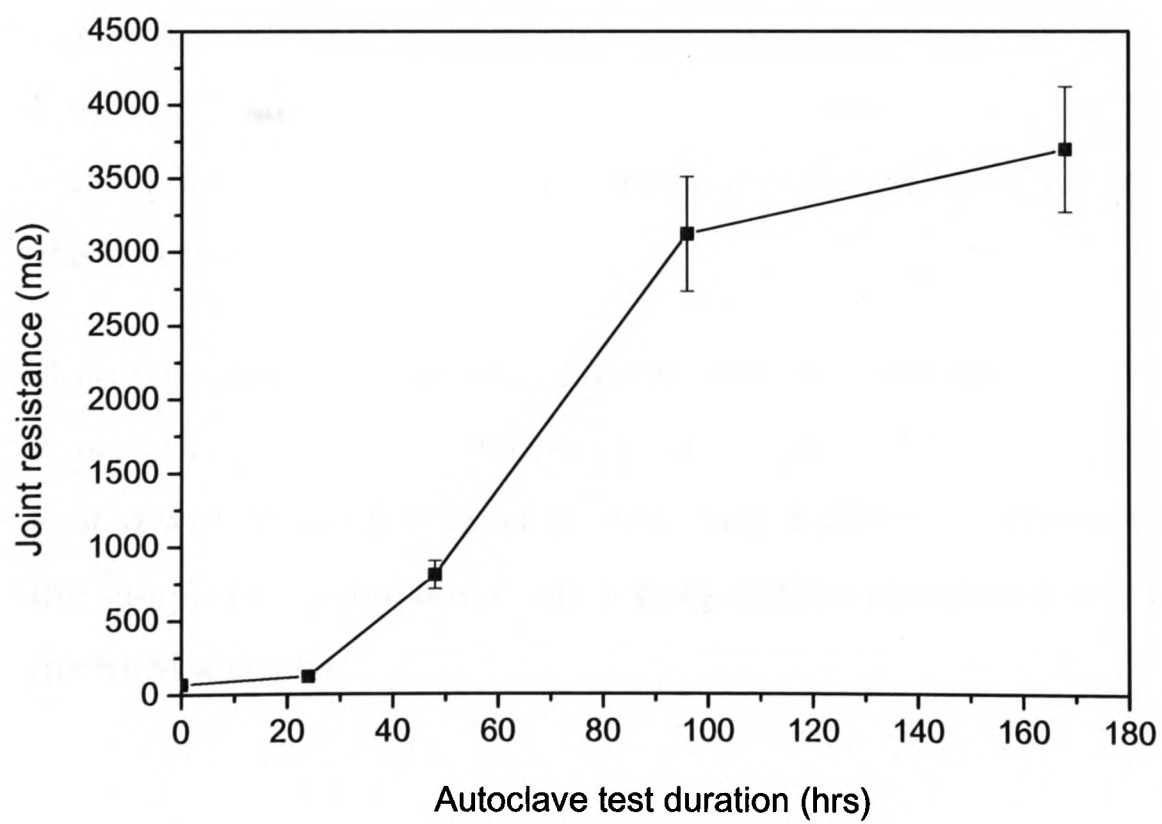
Figure 4.18: Joint resistance of ACF joints during autoclave test

4.3.3.2 Scanning Electron Microscope (SEM) Photos

Conventional optical microscopes use a series of glass lenses to bend light waves and create a magnified image, a SEM creates the magnified image by using electrons instead of light waves. Therefore, a SEM shows very detailed three dimensional images at much higher magnification than what is possible with an optical microscope. The SEM used in this research was the Philips Model XL40. The resolution of this machine is 2.5nm at 30kV and 5nm at 1kV.

Sample preparation for SEM analysis consisted of the following three steps:

(1) Epoxy Moulding: The ACF samples were firstly cut into small size and put into a mould which was then filled with epoxy adhesive and then the mould was left for several hours until the adhesive solidified.

(2) Grinding and Polishing: The moulded sample was then ground to remove material to expose the face of the sample that we wish to visualise. Care needs to be taken in this process to ensure that not too much material is removed and loose the features of interest. Once the interested surface was captured, the surface was then polished using micro powders to remove any rough surface characteristics.

(3) Gold Coating: Since SEM illuminates the surface with electrons, the sample must be able to conduct electricity. To achieve this, the sample surface was coated with a very thin layer of gold using a sputter coating machine. Finally, the samples were mounted onto a plug using a conductive tape and ready for the SEM analysis.

Figure 4.19 shows the SEM photos of an ACF joint after bonding (without reflow) and the ACF joint which had subsequently undergone 48 hours of autoclave test. Figure 4.19a, illustrates the state of the conductive particle before being subjected to an autoclave test. Clearly the particle was captured between the bump and the pad and had deformed showing good contact with the pad. However, after 48 hours pressure
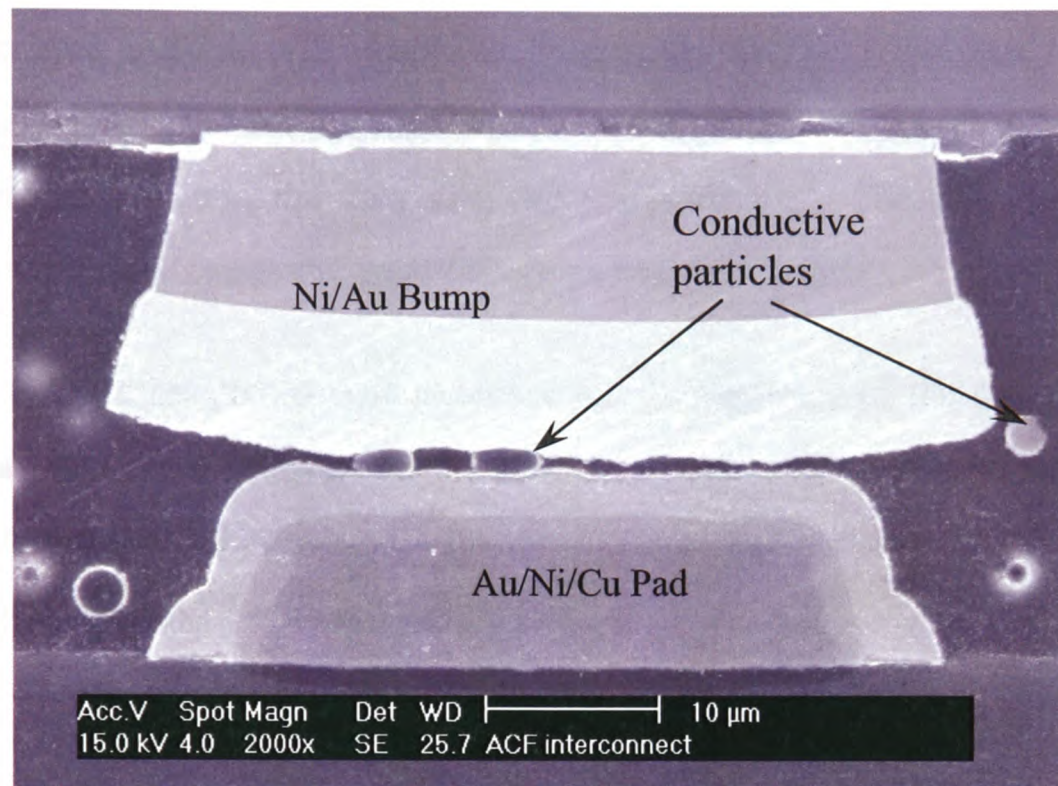
(a) ACF joint as bonded
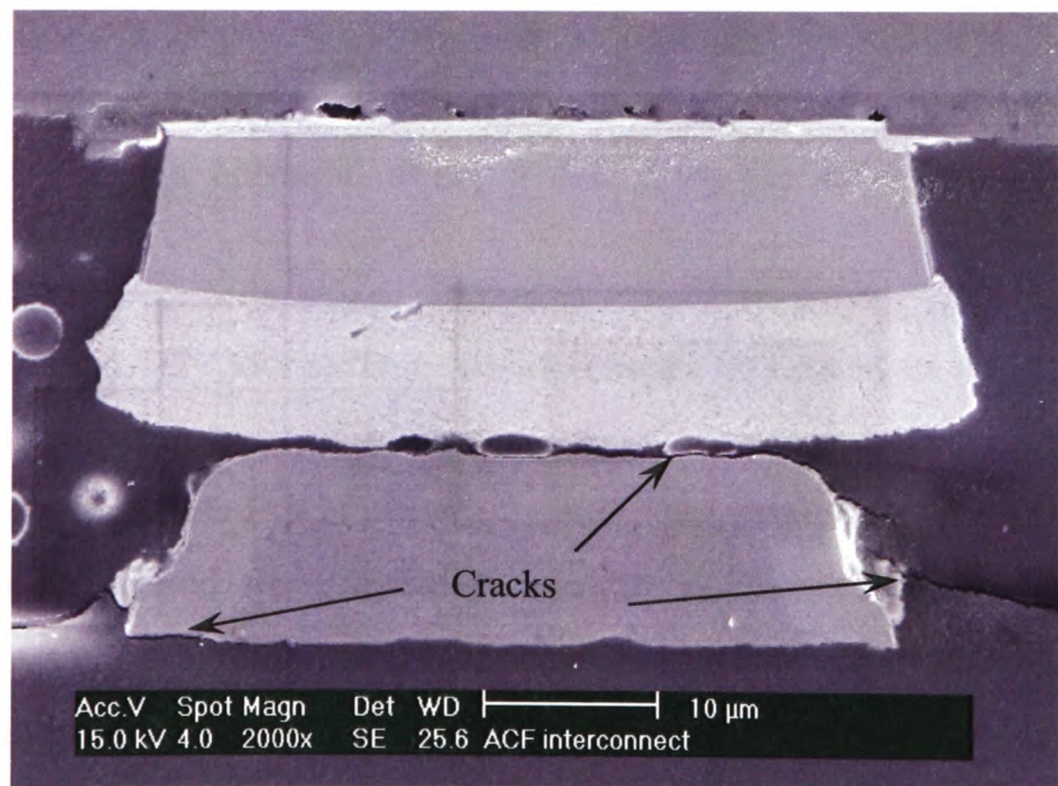
(b) ACF joint after 48 hours Autoclave test

Figure 4.19: SEM photos showing the ACF interconnections

79

cooker test, a delamination gap between the conductive particles and the metallization was clearly visible as shown in Figure 4.19b. The formation of this gap signalled a loss of the contact area and this will lead to an increase in contact resistance. Moreover, the cracks can be also seen along the interface between the adhesive and the flex substrate, and the interface between the flex and the substrate pad. The propagation of these cracks may eventually cause the total failure of the ACF joints.

In general, there are two possible causes for the increase of the contact resistances in ACF joints that have undergone the autoclave tests: debonding at ACA joints and corrosion of the metallization. Both can reduce the contact areas between the conductive particles and the metallization [9].

For the samples used in this study, the metal pads were plated with a gold layer so that the effect of electrochemical corrosion was negligible. If corrosion is negligible then the dominant mechanisms resulting in an increase in contact resistance is the loss of contact area between the particle and the pad. Moisture through hygro-swelling will enhance this process. Moreover, it not only diffuses into the adhesive layer, but it can also penetrate into the interfaces between the adhesive and the substrate/chip resulting in a reduction of the adhesion strength and even the formation of micro-cracks [9][110].

Epoxy has relatively low surface tension energy compared to Au, SiO_2 and many other materials, therefore good adhesion is usually expected when it applied to the surface of these materials [5]. However, the adhesion strength at the interface between the epoxy adhesive and the polyimide substrate is not as strong as others in this assembly due to the similar surface tension energy values of these two materials. Therefore, the interface between the adhesive and the flex is more vulnerable to water molecule attacks, and once the degradation at the adhesive/flex interface has started, water can move along the interface. When combined with the stress due to the swelling effect of the adhesive, this may cause further degradation of the interfaces.

Furthermore, high degrees of interfacial degradation in the adhesive joints can result in the presence of high water activity.

Computer modelling analysis will help provide a better understanding of the failure mechanism of ACF joint in this humid environment, these modelling results will be presented in Chapter 6.

4.3.3.3 Effect of Solder Reflow

Four samples subjected to the tin-lead solder reflow were tested for 24 hours at the autoclave test conditions stated above. The joint resistance of each ACF joint was then measured and the SEM photos were taken to show the failure information, the results were also compared with samples without reflow treatment.

The joint resistance results are shown in Table 4.3. These compare both the "as bonded" samples, i.e. not subjected to a reflow process with bonded samples that have been subjected to a reflow process. It is interesting to note that samples that were subjected to a reflow treatment show a large increase in the contact resistance and therefore will have poor reliability performance.

Table 4.3: The results to show the reflow effect

	Joint resistance (mΩ)		Open joints	
	Autoclave test (hour)		Autoclave test (hour)	
	0	24	0	24
As bonded	69.29±20.1	128.62±32.1	0	0
With reflow treatment	90.54±30.2	700.95±67.6	0	6%

For the samples without the reflow treatment, there were no open joints visualised after the 24 hours autoclave test. Only micro-cracks were detected along the interface between the adhesive and the flex as shown in Figure 4. 20a. For the samples with

solder reflow treatment, delamination along the interface between the adhesive and the flex/pad was clearly observed as shown Figure 4. 20b.
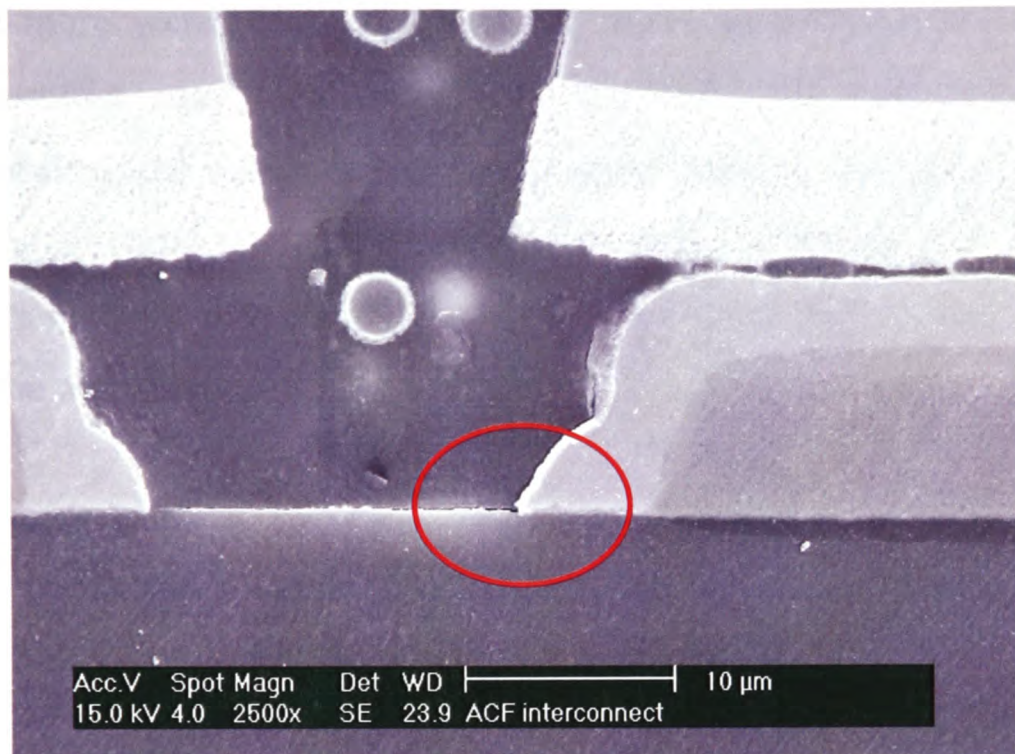
(a) Without solder reflow
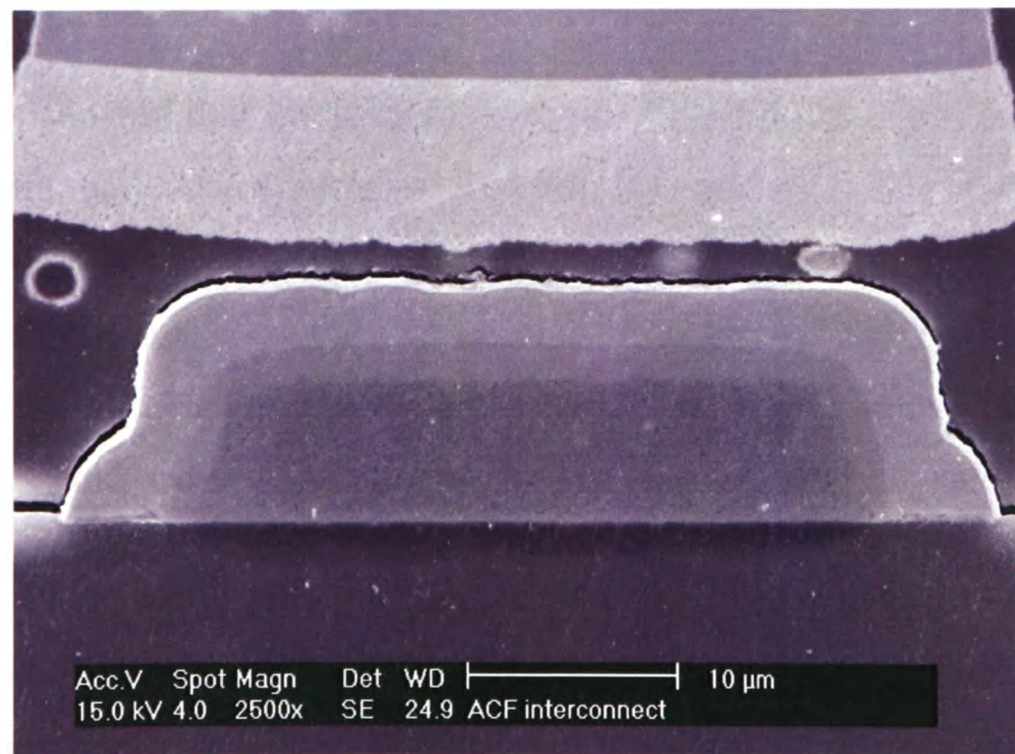
(b) With solder reflow

Figure 4. 20: SEM photos of the ACF interconnections after 24 hours autoclave test

According to other studies [99][100] on the water absorption and diffusion in epoxy-resin systems, moisture uptake increases with the cross-linking density (curing degree). This is because the cross linked region has a bigger free volume that can accommodate more water. This suggests that after the solder reflow process, more moisture absorption may take place with the fully (or even over)-cured ACF. Furthermore, during the solder reflow the thermal stresses inside the package due to the CTE mismatch could reduce the contact area between the conductive particles and the metallization. This may explain why the reflowed ACF joints showed worse reliability in the autoclave test.

4.4 Conclusions

This Chapter has described the flip chip bonding process using Ni/Au-coated polymer-filled ACFs and studied the effects of (1) bonding parameters, (2) solder reflow and (3) moisture absorption on the electrical/reliability performance of ACF flip chip assemblies.

The results showed that the joint resistances of ACF joints were highly dependent on the bonding parameters such as Bonding Temperature, Bonding Pressure and Bonding Time. These strongly affected the magnitude of deformation of the conductive particles and also the degree of cure in the adhesive. The quality of the final joint, as monitored through the joint resistance, was strongly influenced by all three variables and care was required to ensure that the correct combination of parameters was used.

The subsequent solder reflow treatment always causes an increase in the joint resistance. The magnitude of this increase was governed by the parameters used in the bonding process and the state of deformation of the particles and the degree of cure in the surrounding polymer matrix.

During the autoclave test, the joint resistance of the ACF joints increased. More than 85% of the ACF joints were assessed to have failed within the first 24 hours based on the failure criteria being a 100% increase in the joint resistance. However, open joints were not observed until after 48 hours of testing. The formation of delamination cracks between the conductive particles and the metallization was observed at this time. It is believed that this de-bonding process is due to absorption of moisture at the interfaces of the materials. This was the major cause of ACF failure.

Samples that had been subjected to a reflow process failed earlier in the autoclave test. This could be due to the greater degree of absorption in the reflow samples where the degree of cross linking in the polymer material was greater. The work outlined in this Chapter has contributed to one journal paper [126], and a number of international conference papers [129][133][136].

Chapter 5

Modelling of the Effect of Solder Reflow on ACF Performance

Experimental studies in Chapter 4 revealed that the solder reflow process had a substantial effect on the electrical and reliability performance of ACF flip chip assemblies. The change from tin-lead solder to lead-free solder results in an extra 20-50°C increase in the reflow peak temperature. This could damage the flip-chip assembly and the ACF materials. In this Chapter, the performance of ACF assemblies is further studied using computer modelling techniques. A parametric analysis investigates the impact of adhesive material properties (CTE and Young's modulus) and geometrical height of the bump (or pad on the silicon die). This analysis shows that the CTE of the adhesive matrix is proved the most important design variable in minimising the damage in the assembly when subjected to higher reflow temperatures. These modelling results are compared with the experimental findings in Chapter 4.

5.1 Computational Modelling

The software package PHYSICA was employed to investigate the primary cause of the failures observed in the experiments. This work focused on modelling the thermally induced stress in the ACF joints as they passed through the solder reflow process.

5.1.1 Geometry and Mesh Model

A conductive adhesive particle has a diameter of 3.5μm with a surface coating of thickness 200nm. These details need to be captured within a finite element model of these particles to accurately predict their deformation. The dimension of the silicon die are: length of 11mm, width of 3mm and height of 1mm. Between the die and the flexible substrate there are over 300 pads with possible 10-15 conductive particles on each pad.

The finite element method represents the domain to be modelled as a mesh over which the governing stress and thermal equations can be solved. Obviously, to model in detail the whole flip-chip assembly and each conductive particle would be infeasible due to the excessive mesh and computing resources required. In order to simplify the model and reduce the computing time, a single joint located at the centre of an ACF flip chip assembly was built. This is illustrated in Figure 5.1.
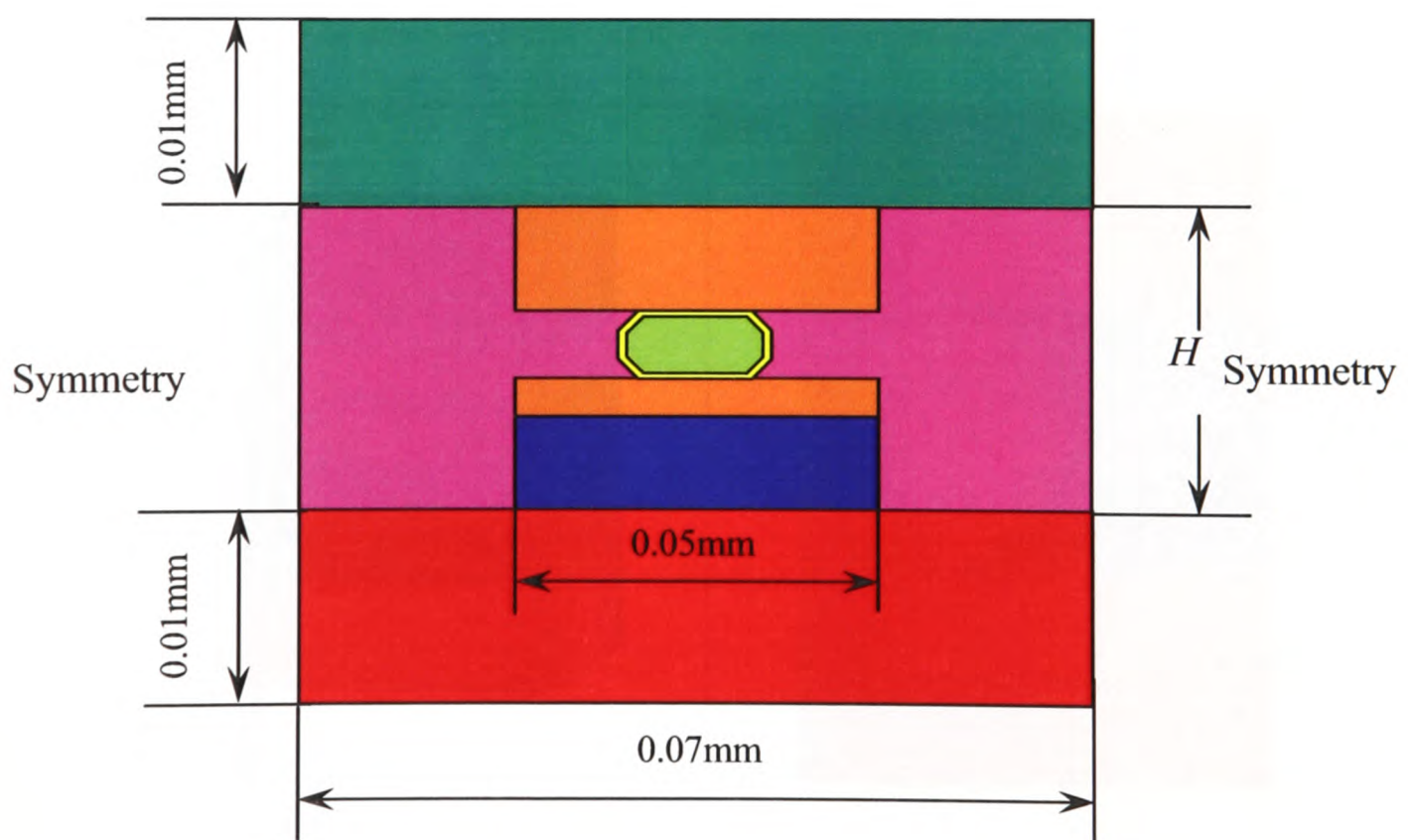
Figure 5.1: Section view of the structure of the ACF joint

The size of the bump and the pad are kept the same as in the tested sample. The thickness of the adhesive matrix is defined as H which will be used to explain the bump height effect in a later section. In this model, a single conducting particle is assumed to be located in the middle part of the area between the bump and the pad. The particle is also assumed to be in its deformed shape as it would be after the bonding process. The contact between the particle and the pads is perfect.

Due to the symmetry of an ACF joint, only one quarter of the geometry was modelled. The 3D mesh of this quarter model is presented in Figure 5.2, where an enlarged section around the particle area is illustrated so that the particle and the coating layers are visible. The settings for the boundary conditions are illustrated in Figure 5.3. The displacements at Point A are fixed to zero in all directions; displacements of the points on Plane A and B are fixed to be zero in the X and Z directions respectively.
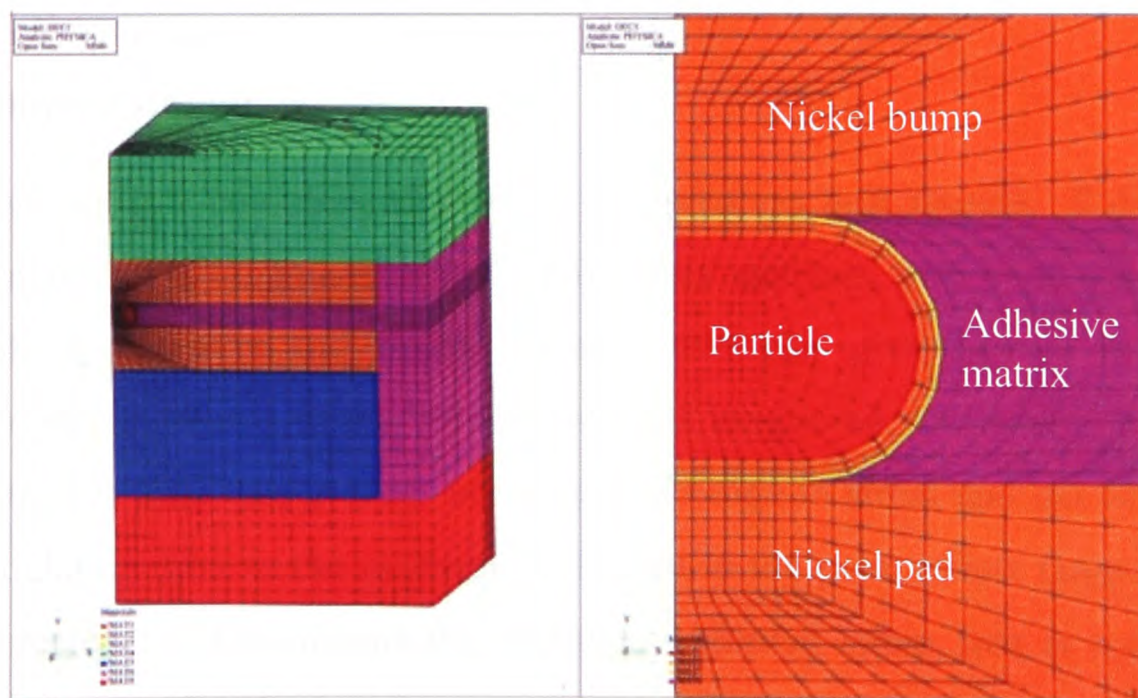
Figure 5.2: FE model of an ACF joint
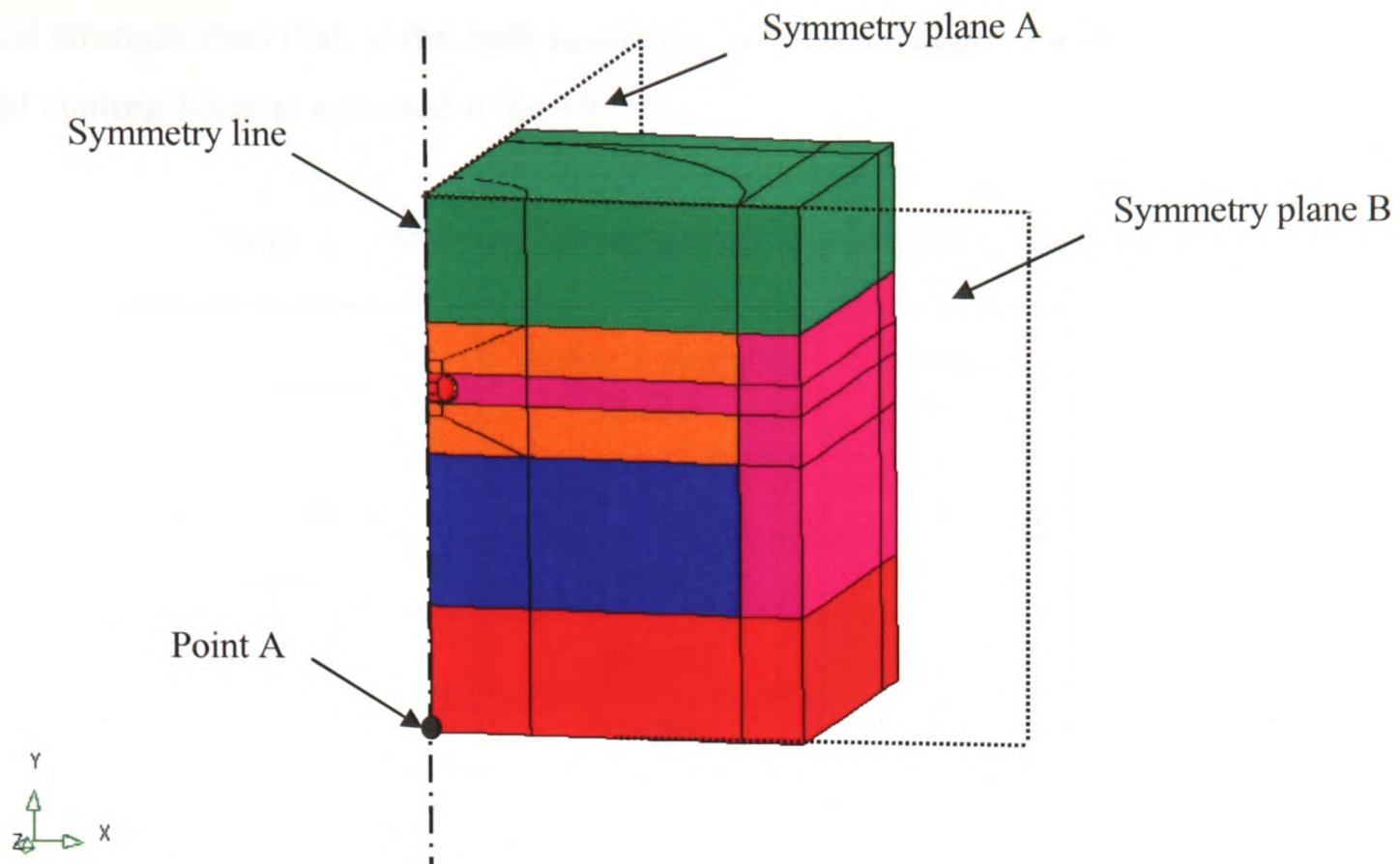
Figure 5.3: Boundary conditions used in the modelling

5.1.2 Modelling Assumptions

ACF bonding is a complicated process that involves heat transfer, fluid flow and solid deformation [101]. In order to simplify this analysis, and focus on the stress changes taking place in the reflow process that can give rise to failures, the compressive stress created in the bonding process is ignored. Of course there will be locked in stresses after this process but it is the change in stress and the likelihood of interfacial delamination as the assembly is heated to the peak reflow temperature that we are interested in. This means the model is assumed stress free at the reference temperature (25°C) after the bonding process.

The material properties are listed in Table 5.1. The die, the substrate, the polymer foil and the core of the conducting particles are treated as elastic, all the metals are assumed to behave in an elasto-plastic manner. The coating characteristics of the

particle are accounted for by assuming a lower Young's modulus but a higher initial yield strength than that of the bulk material [54]. For example, the yield strength of the gold coating layer is assumed to be 190Mpa.

Table 5.1: Material characteristics used for this simulation

Material	Young's modulus (MPa)	Poisson's ratio	CTE (ppm/K)
Chip	131700	0.3	2.7
Substrate	4000	0.3	20
Nickel	205519	0.3	13.14
Copper	132400	0.34	16.7
Gold	77000	0.3	14.2
Polymer in particle	1600	0.4	70
Adhesive matrix	1600	0.4	133

5.1.3 Modelling Results

The deformation and normal stress distribution at the peak reflow temperature of 210°C is presented in Figure 5.4. The deformation is magnified by 15 times in order to provide clear information. It shows that the adhesive matrix, which has a high CTE value, expands much more than the tiny conductive particle. Higher stress is also identified around the particle where the stress in the coating layer is the highest. Along the interface between the conductive particle and metal pad, the highest stress is identified along the outer edge of the contact interface. This area could be the weakest point and a location for interfacial delamination.

The plastic strain distribution is shown in Figure 5.5, where the coating layers undergo plastic deformation and strain which are highest along the coating/adhesive matrix interface. These plastic strains are much less at the particle pad interface.
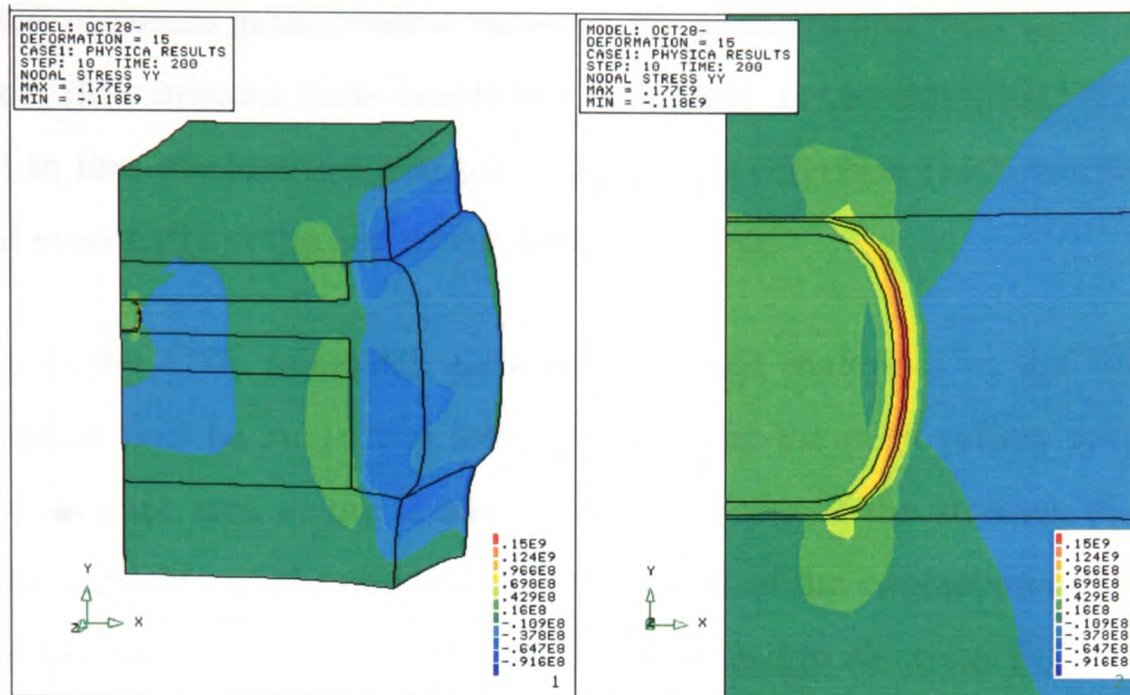
Figure 5.4: Stress σ_{yy} distribution in the ACF joint
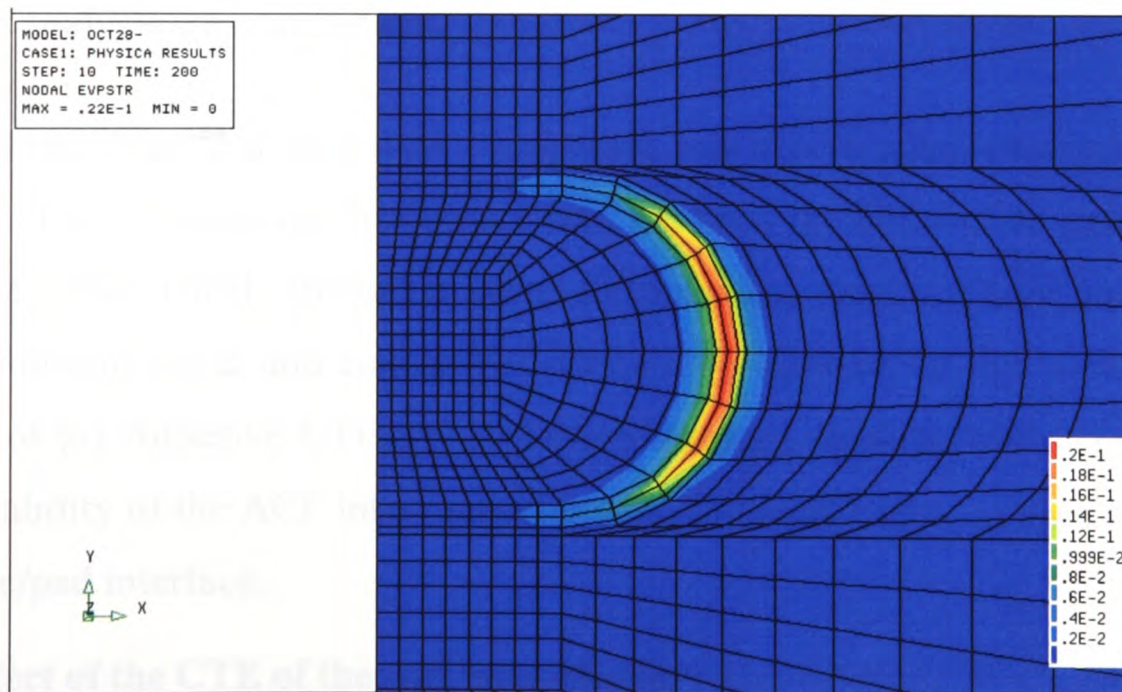
Figure 5.5: Plastic strain distribution in the ACF joint

During the bonding/cure process, the bonds produced between the conductive particle and its surroundings are strong. There will also exist a state of compression

after the cure process which results from a temperature drop of 190°C to 25°C. These stresses will maintain good contact between the particles and their surroundings. Now during the reflow process these bonds can be broken due to materials swelling and this will result in loss of electrical contact in the Z-axis direction [110] which can become permanent eventually at the end of the reflow process.

Owing to the CTE mismatch between different materials in the ACF joint, the contact regions will be subject to tensile stresses at the peak reflow temperature and the loss of contact area in the connections may occur if the stresses at the interface between the particle and the pad are high. This loss of the contact area will result in an increase in the contact resistance. In time this will lead to electrical failures.

5.1.4 Parametric Study

In order to understand how material properties and geometric changes affect the stress levels in the ACF flip chip assemblies during a solder reflow, a detailed parametric analysis was carried out.

In the experimental work, contact resistance was used to characterise failure of the ACF joint. This depends on the contact area between the conductive particle and the pad surface. When tensile stresses occur at this interface there is a high probability that delamination will occur and contact resistance will increase. In this modelling work, the effect of (a) Adhesive CTE, (b) Adhesive Young's modulus and (c) bump height on the reliability of the ACF interconnections is discussed based on the stress levels at the particle/pad interface.

5.1.4.1 Effect of the CTE of the Adhesive Matrix

The CTE of the adhesive matrix is 133ppm/°C which is much higher than the CTE of the conductive particle and other metal materials. During a temperature cycle, this large CTE mismatch between different materials can induce high stresses inside the ACF flip chip assembly. This may reduce the reliability performance of the ACF joints. Previous research work [23] revealed that ACA materials with low CTE could

significantly enhance thermal cycling reliability of ACA interconnections. To prove this, models with different CTE values were analyzed. The values of the normal stress σ_{yy} at the interface between the particle and the pad were recorded at the peak reflow temperature of 210°C. These results are shown in Figure 5.6. The abscissa represents the distance from the centre of the interface to the out edge of the contact area. It is found that the CTE of the adhesive matrix has a strong impact on the stress at the interface. The interfacial stress increases with an increase in the CTE of the adhesive matrix. Therefore the reliability of the ACF assembly will be enhanced when using an adhesive with a lower CTE.
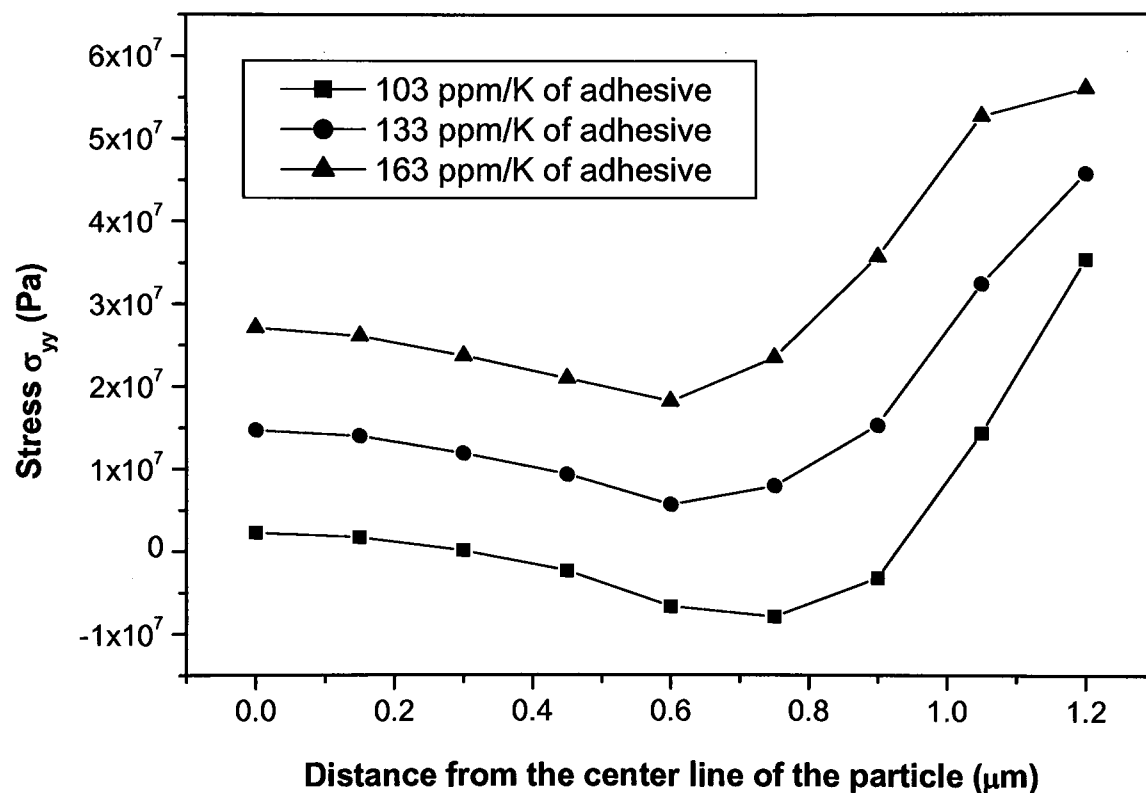
Figure 5.6: The relationship between the interfacial stresses and the CTE of the adhesive matrix

5.1.4.2 Effect of the Young's Modulus of the Adhesive Matrix

The effect of the Young's modulus of the adhesive matrix was also studied. The values of the normal stress σ_{yy} at the interface between the particle and the pad at peak reflow temperature are shown in Figure 5.7. Clearly we can see that the interfacial

stress σ_{yy} decreases firstly and then increases, reaching its highest value at the point where the particle, adhesive and metal pad meet. This is a potential location of initiation of delamination. In general the stress magnitude at this location is lowered with an increase in the Young's modulus. Therefore reliability of the ACF assembly can be enhanced when using an adhesive with a higher Young's modulus.
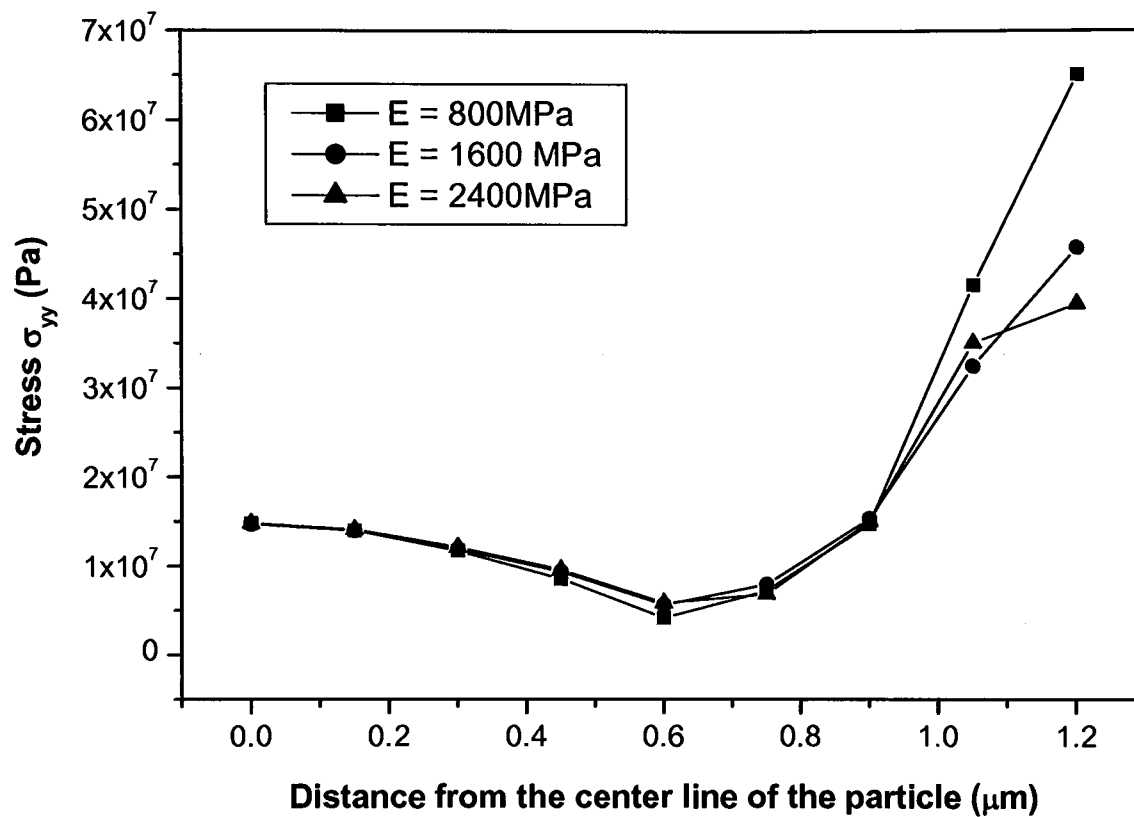
Figure 5.7: The relationship between the interfacial stress and Young's modulus of adhesive matrix

5.1.4.3 Effect of the Bump Height

Three different bump heights were analyzed to investigate their effect on the stress predictions. The distance between the chip and the substrate is dependent on the bump height, pad height and the deformed particles. Therefore, with a bigger bump height more adhesive will be in place between the chip and the substrate.

The stress values at the interface between the particle and the pad with different bump heights is shown in Figure 5.8. It can be seen that the tensile stress at the interface between the conductive particle and the pad metallization increases when the

bump height increases. This conclusion contradicts what has been observed in solder based flip chips but corroborates well with experimental results for ACF joints [60][61].
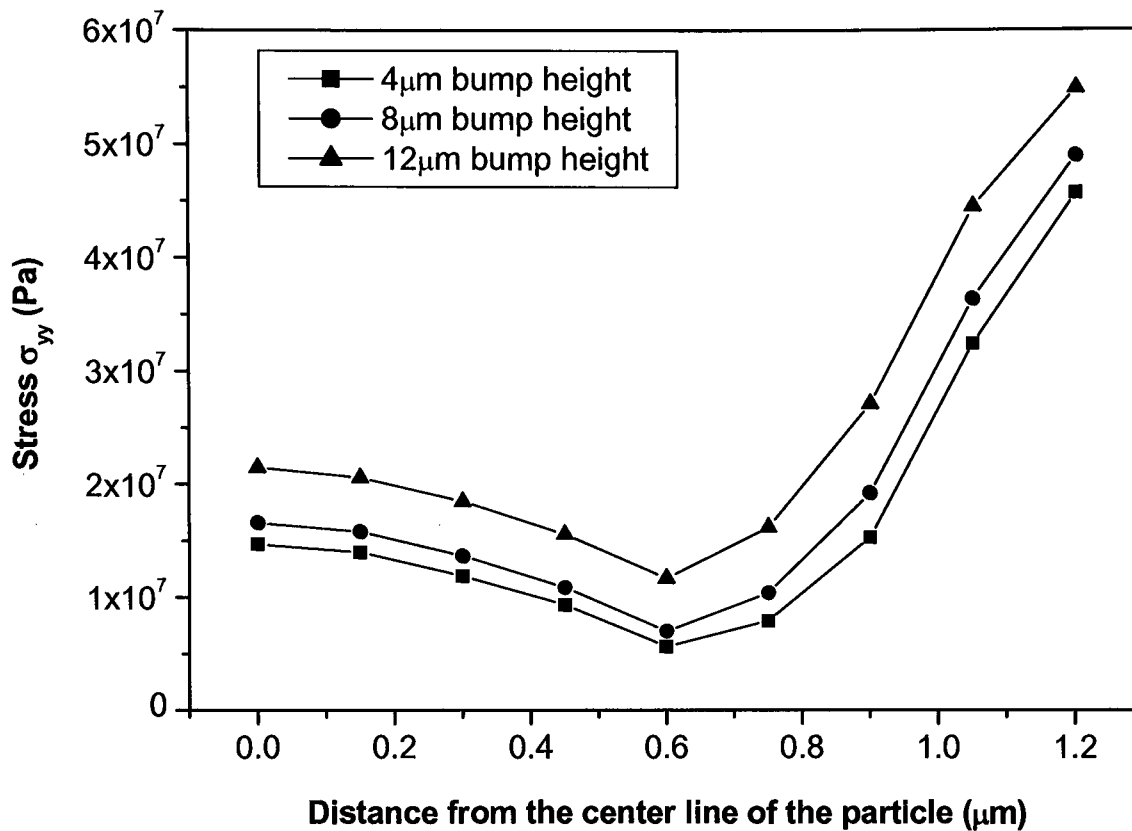
Figure 5.8: The relationship between the interfacial stresses and the bump height

In order to prove the modelling results, two sets of ACF assemblies were bonded with (a) a chip with Ni/Au bumps and (b) a chip with Au bumps. Both of these were subjected to the solder reflow profile. Owing to the different processing technology, the chips used have different bump heights, about 17μm for Au bump and 4μm for Ni/Au bump. The height of Cu/Ni/Au pad on the substrate is about 17μm. The joint resistance for both kinds of ACF assemblies was measured before and after a tin-lead solder reflow. The results are listed in Table 5.2.

For the assembly with Au bumps, the joint resistance was about 25mΩ, this value increased by more than 100% after solder reflow. For the assembly bonded with Ni/Au bumps, the joint resistance only increased by 18% after the solder reflow process.

Table 5.2: The results to show the reflow effect

	Joint Resistance (mΩ) Mean Value (Standard deviation)	
	With Au bump	With Ni/Au bump
As bonded	26 (10)	124 (24)
After reflow treatment	53 (15)	147 (31)
Percentage of increase	110%	18%

The SEM micrograph of a cross-section of the ACF interconnection bonded using Au bump is shown in Figure 5.9. Normally, ACF joints bonded using Au bumps show
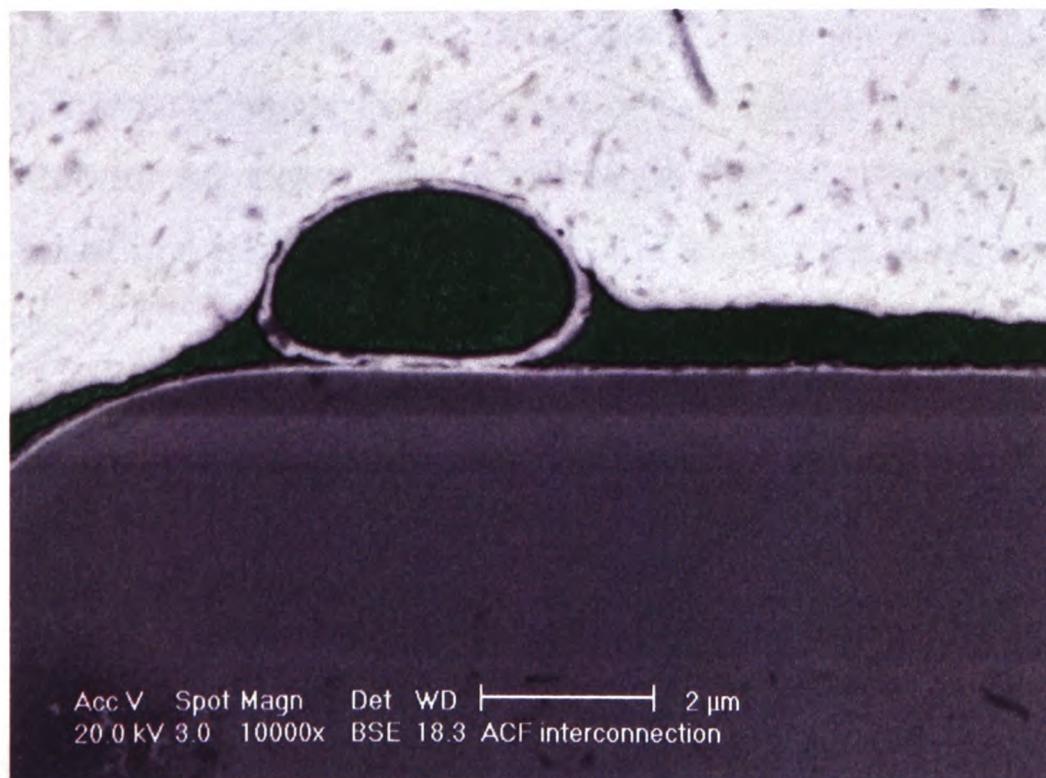
Figure 5.9: ACF interconnection with Au bump

a lower contact resistance than the ones bonded using Ni/Au bumps because gold is soft and a larger contact area can be achieved between the gold bump and the

95

conductive particles. Also gold does not suffer from oxidation as easily as nickel. Currently, world wide efforts are focused on the development of Ni/Au bumping technologies due to the cost concerns of gold and the complexity of gold bumping technology.

As shown in Figure 5.1, if the distance between the chip and the substrate is defined as H, and the coefficient of thermal expansion of ACF matrix in the Z direction is α, then during the temperature rise of the reflow process, the expansion of the adhesive matrix in the Z direction, ΔH can be approximated by:

$$\Delta H = H \times \alpha \times (T_2 - T_1)$$
(5.1)

where T_1 is room temperature and T_2 is the peak temperature of the reflow process. In this case, the expansion of the adhesive matrix in the Z direction for ACF assemblies with Au bump is nearly twice that of ACF assemblies with Ni/Au bump for the same reflow profile. Therefore, higher thermal stress in the Z direction was accumulated for ACF assemblies with Au bump. This higher stress will try to lift the chip from the substrate and result in a high probability of loss of contact areas between the particle and pad surfaces.

Clearly from the experiments we can see that the design with the higher bump height also has greater change in contact resistance. This matches the results obtained from the modelling results above.

5.2 Sensitivity Analysis

This section discusses the results from a sensitivity analysis. This technique allows us to fully characterise the sensitivity of the reliability of the ACF assembly to small changes in particular design variables.

The design variables under investigation are (a) Adhesive CTE, (b) Adhesive Young's modulus and (c) the bump height. In this study, finite element calculations

were undertaken for different combinations of these design variables and using statistical techniques a response surface (RS) was established that related reliability to these design variables. This response surface is a polynomial and reliability is characterised based on the magnitude of tensile stress at the point where the adhesive, particle and metal pad meet which is taken as the design response of interest.

Normally design variables of interest have different units of measurement rendering a direct comparison of the parameter variation difficult. The sensitivity analysis in such cases requires dealing with the above issue in a certain way. The best way is to consider a RS model developed as a polynomial approximation in a normalized design space. In the normalized design space the lower limits of the design variables correspond to -1, and the upper limits to +1.

5.2.1 Scaled and Un-scaled Design Points

When dealing with experimental designs, it is often convenient to scale the design variables with respect to their upper and lower limits (i.e. the maximum and the minimum values). One of the common ways to do this is as follows [102]:

$$x_i = \frac{z_i - (\max[z_i] + \min[z_i])/2}{(\max[z_i] - \min[z_i])/2} \quad i = 1,..., N$$

where z_i is natural (i.e. un-scaled) design variable, x_i is scaled design variable, and N is the total number of points (i.e. simulation results) in the experimental design. When the maximum and the minimum are taken over all the values of the particular design variable (over all the points in the experimental design), each design variable scaled in such a way assumes that values are between -1 and 1.

In this study, the chosen polynomial order for the RS approximation is a full quadratic with mixed linear terms. The number of design variables is three. The construction of such a polynomial approximation requires the estimation of 10

unknown coefficients. To build the RS model and to find the values of these coefficients, at least 10 or more experiment points are required.

Design of experiments (DOE) was performed to identify these sets of design points at which the finite element analysis was undertaken to provide the stress predictions for the ACF flip chip assemblies at different combinations of design variable values. The DOE method exploited here is the "Latin Hypercube" with 15 experiments. The 15 set of design variables predicted from the DOE analysis are listed in Table 5.3.

Table 5.3: Scaled values of the design variables

	Variable 1	Variable 2	Variable 3
1	1.0	1.0	1.0
2	1.0	1.0	-1.0
3	1.0	-1.0	1.0
4	1.0	-1.0	-1.0
5	-1.0	1.0	1.0
6	-1.0	1.0	-1.0
7	-1.0	-1.0	1.0
8	-1.0	-1.0	-1.0
9	1.0	0.0	0.0
10	-1.0	0.0	0.0
11	0.0	1.0	0.0
12	0.0	-1.0	0.0
13	0.0	0.0	1.0
14	0.0	0.0	-1.0
15	0.0	0.0	0.0

The un-scaled values of these design variables were calculated and listed in Table 5.4. In total 15 sets of simulations were conducted using these design variables. The stress values at each DOE design location were predicted and used to establish the response surface and to undertake the required sensitivity analysis.

Table 5.4: Un-scaled values of the design variables and response of interest

	Design variables			Stress (MPa)
	Young's modulus (MPa)	CTE of adhesive (ppm/°C)	Bump height (μm)	
1	2400	163	12	270
2	2400	163	4	243
3	2400	103	12	128
4	2400	103	4	109
5	800	163	12	419
6	800	163	4	375
7	800	103	12	198
8	800	103	4	162
9	2400	133	8	183
10	800	133	8	281
11	1600	163	8	307
12	1600	103	8	138
13	1600	133	12	242
14	1600	133	4	213
15	1600	133	8	222
Lower bound	800	103	4	
Higher bound	2400	163	12	

5.2.2 Sensitivity Test Results

Figure 5.10 illustrates the sensitivity of the interfacial stress to the terms in the RS approximation generated in the normalized design space. This sensitivity analysis shows that the CTE of the adhesive matrix is the most influential linear term in this RS model, followed by the Young's modulus of the adhesive and the bump height. Generally, the stress is influenced mainly by the linear terms in this model. However, there are also important contributions from the design variable interactions and the pure quadratic terms. The most influential cross term is the interaction between Young's modulus and the CTE of the adhesive matrix (E*a), a positive scaled unit increment in both design variables results in a decrease of 19.75MPa. With respect to the quadratic terms in this polynomial approximation, the Young's modulus term E**2 has the highest contribution.
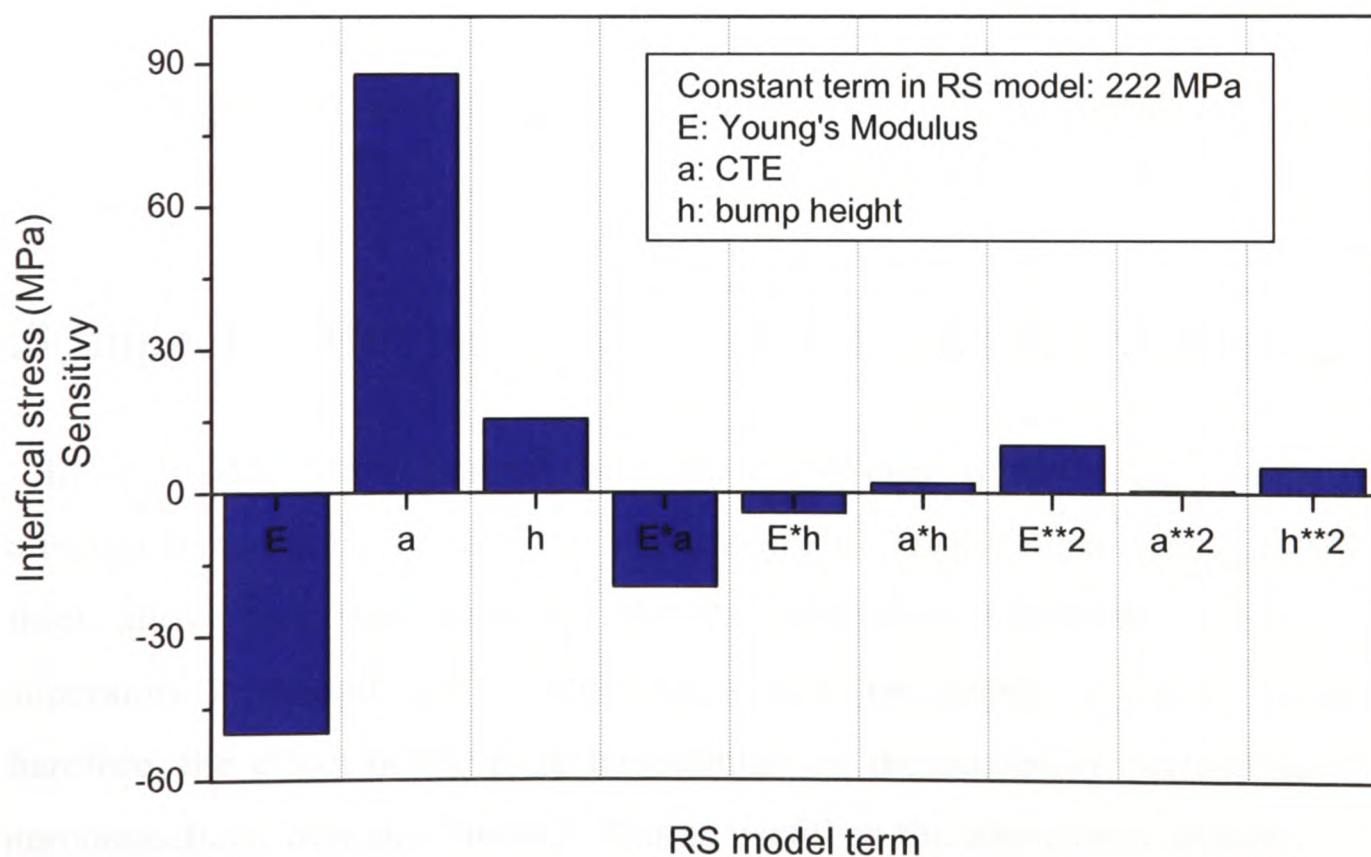
Figure 5.10: Sensitivity of interfacial stress of design variables and their interactions

Figure 5.11 illustrates the quality of this response surface approximation that relates the tensile stress at the corner of the pad/particle/adhesive to the design variables stated above. Clearly we can see how closely the response surface polynomial compares with the actual finite element calculations.
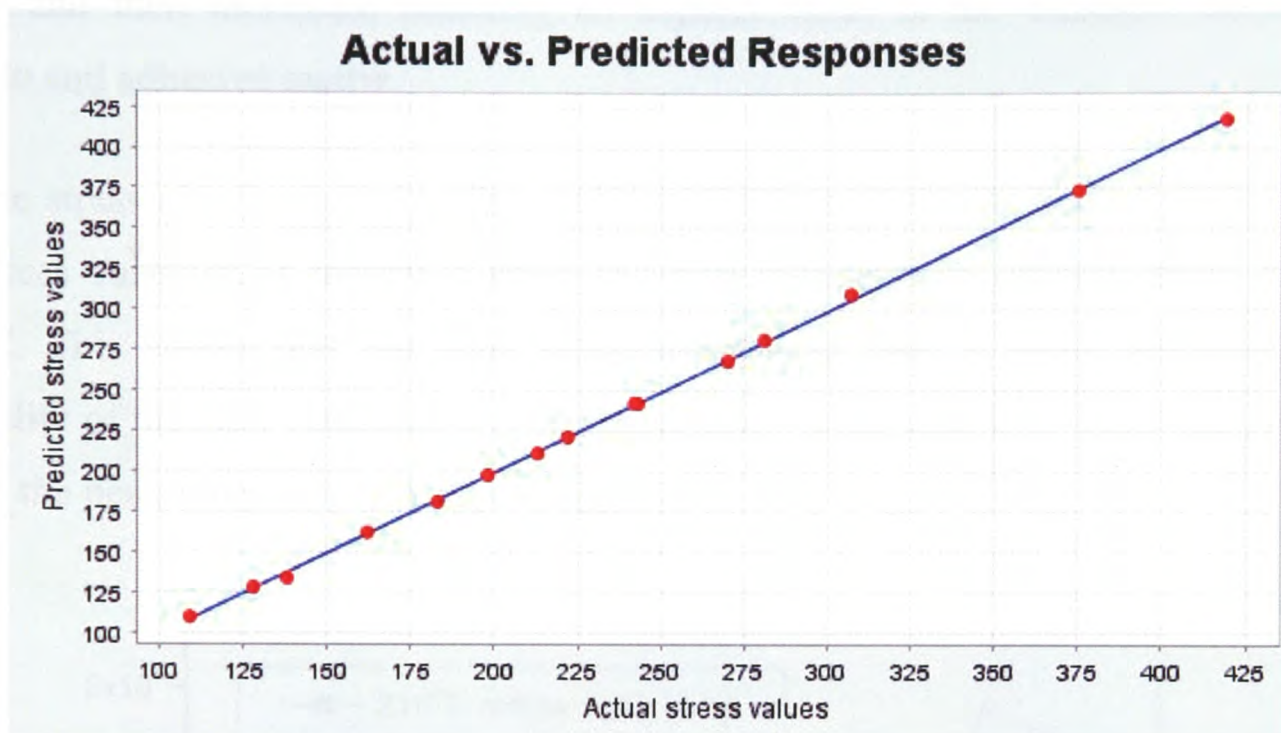
Figure 5.11: Response Surface predictions .vs. Finite Element predictions

5.3 Impact of Moving From Lead to Lead Free Soldering

In the solder reflow process the peak temperature is much higher than the glass transition temperature of the ACF material. This peak temperature depends on the solder alloy used. For example, for the traditional Sn60Pb40 solder, the peak temperature is around 215°C, while for a lead free solder, it can be much higher. Therefore, the effect of the peak temperature on the reliability performance of ACF interconnections was also studied. This is useful as the electronics industry is moving away from lead solder to lead-free solder.

Three peak temperatures: 210°C, 230°C and 260°C were analysed. These peak temperatures cover the range of reflow temperatures for both eutectic tin-lead and

lead-free solder materials. The values of the normal stress σ_{yy} at the interface between the particle and the pad at the three peak temperatures are shown in Figure 5.12. The abscissa represents the distance from the centre of the interface to the out edge of the contact area between the particle and metal pad. It shows that the stress σ_{yy} decreases firstly and then increases, reaching its highest value at the interface between the particle and adhesive matrix.

The stress also increases as the peak temperature increases. In fact, about 50% of the stress variation is observed when the peak temperature changes from 210°C to 260°C. This shows that the peak temperature may have a great influence on the reliability of the ACF interconnections, especially for the lead free soldering process in which the peak temperature is much higher.
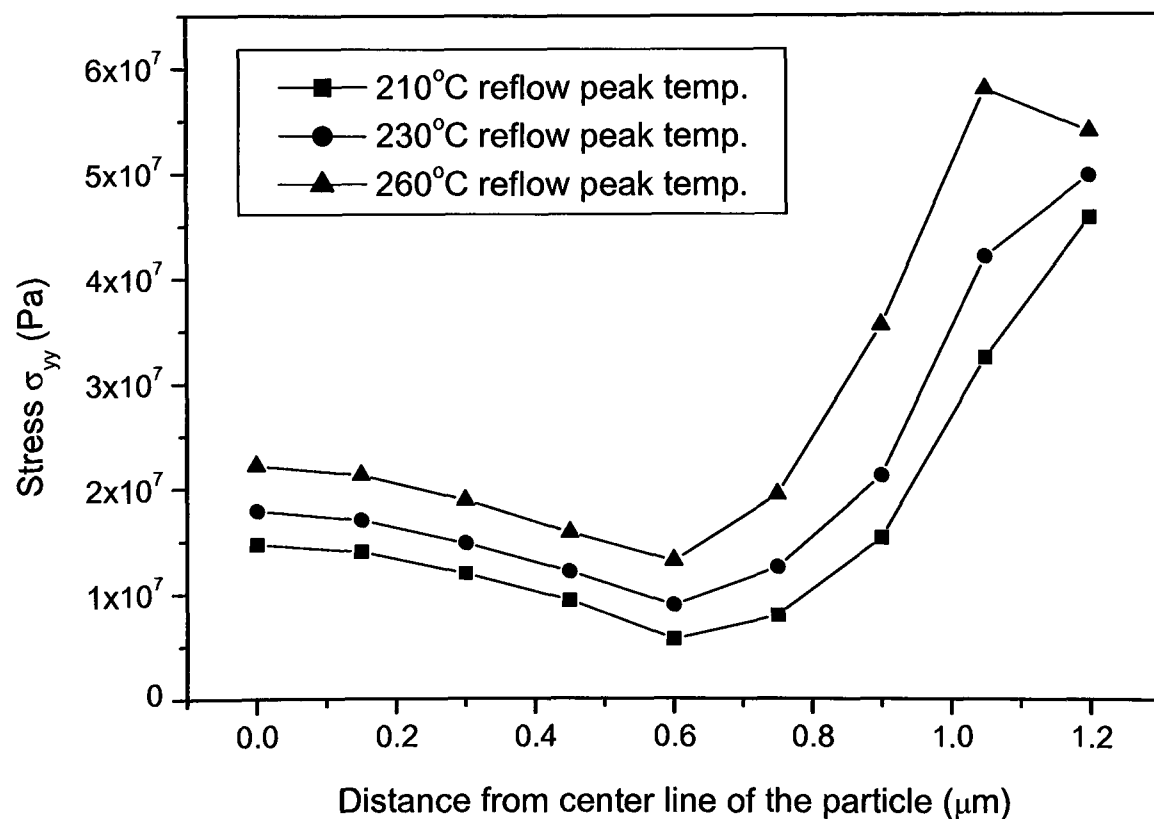
Figure 5.12: Relationship between the interfacial stress and the peak reflow temperature

The effect of the peak temperature on the reliability performance of ACF joint was also studied experimentally. The joint resistance was used as the indicator and

measured using the four-point probe method which is shown in Figure 4.9, Chapter 4. Also the SEM photos of the interfacial area between the conductive particle and the pad metallization were taken to illustrate the failure information.

The reflow profile conditions and the related joint resistance test results are summarized in Table 5.5. Three sets of ACA assemblies with Ni/Au bumps were used in this experiment. When the peak temperature was 210°C, no open joints were found and the joint resistance increased by 23mΩ after the reflow process. When the peak temperature was 230°C, 5% of joints were open, and the joint resistance variation increased to 29mΩ. When the peak temperature was 260°C, nearly 40% joints were found open, and the joint resistance increased by 60mΩ. In conclusion, the peak reflow temperature has a substantial effect on the electrical performance of the ACF samples.

Table 5.5: Joint resistance with different peak temperature of reflow profile

No	Peak temperature (°C)	Time up melting point (s)	No. of test joints	Electrical Resistance (mΩ) Mean Value (Standard deviation)		No. of open joints
				Before reflow	After reflow	
1	210	60	53	124 (24)	147 (31)	0
2	230	60	36	126 (28)	155 (41)	2
3	260	60	48	123 (26)	183 (55)	16

It is clear that the conductive particles deformed very well and had a good contact with conductive metallization surfaces before the reflow process, as shown in Figure 5.13a. Although it should be noted that no delamination was found after the reflow process with peak temperatures of 210°C and 230°C, the contact area between the particles and conductive metallization surfaces decreased to some degree and this can be attributed as the main reason for the increase of contact resistance after reflow.
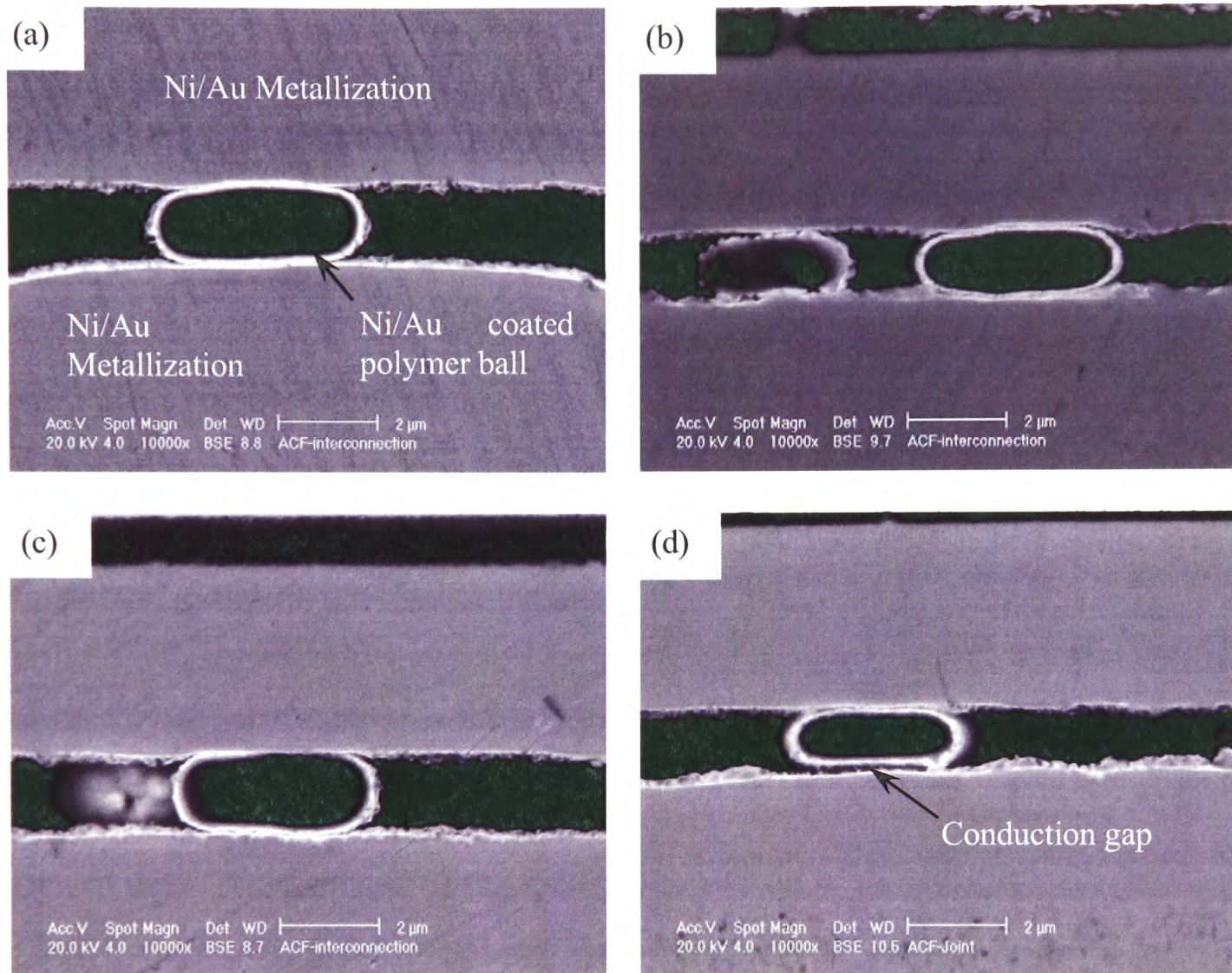
Figure 5.13: SEM photos showing the ACF interconnection through conductive particles (a) as-bonded at 200°C, 86.2MPa, 10s, and after reflow with the peak temperature at (b) 210°C (c) 230°C and (d) 260°C

The formation of a gap between the particle and pad was obvious after the reflow process with peak temperature of 260°C. This is illustrated by the arrow in the Figure 5.13d. According to the CTE values listed in Table 5.1, the CTE mismatch between the adhesive matrix and conductive particles is clear. When the COF samples are heated to over 200°C during the reflow process, the expansion of adhesive matrix in the Z-axis is much more than that of the particles. Inevitably, a gap (conduction gap) will emerge between the particle and the bump or pad if the reflow peak temperature is high enough. It will cause the contact resistance to increase and, occasionally, lead to electrical failure.

Based on both modelling and experimental results, the solder reflow process shows substantial effect on the electrical performance of COF samples, especially when using a lead-free solder reflow process which has a high peak temperature. The material property of the adhesive matrix and the geometry design of the flip chip can offer solutions to decrease this effect and enhance the reliability performance of ACF flip chip assembly during the reflow process.

5.4 Conclusions

In this Chapter, the effect of the solder reflow process on the reliability of ACF interconnection was studied using computer modelling. Design variables such as (a) Adhesive CTE, (b) Adhesive Young's modulus and (c) bump height were investigated to see their effect on the stresses formed within the joints. These predictions and trends were validated with experimentation.

Due to the CTE mismatch of the materials in the ACF flip chip, the stresses at the interface between the particle and its surrounding materials were significant. These were at their highest magnitude at the interface between the particle and the adhesive matrix. Through a detailed parametric analysis, it was found that the interfacial stresses increased when the CTE increased, the bump height increased and finally when the Young's modulus decreased. Sensitivity analysis showed that the most important design variable was the CTE of the adhesive.

The interfacial stresses also increased with an increase in the peak reflow temperature. For the same ACF materials, the expansion of the adhesive matrix in the Z-axis direction was related to the original distance between the chip and the pad which was proved in the experiments by using different bump chips.

The work in this Chapter has contributed to one journal paper [127] and a number of international conference papers [132][133][133].

Chapter 6

Hygro-Mechanical Analysis of an ACF Assembly in Autoclave Test

This Chapter presents modelling results for the autoclave test of flip-chip bonded components onto flexible substrates using ACF materials. These models exploit a multi-scale modelling approach known as three-dimensional macro-micro or global-local modelling technique. In this technique the relevant physics, temperature, moisture and stress, are modelled both at the ACF particle level and at the package level.

This Chapter starts with a discussion of the macro-micro modelling methodology adopted in this study. This is firstly illustrated for a study of a solder joint to demonstrate the efficiency and accuracy of the macro-micro modelling technique implemented in an in-house code PHYSICA. The moisture diffusion and moisture induced stresses within an ACF flip chip assembly when subjected to the autoclave test are predicted using these techniques.

The modelling results from this study are then compared with the experimental results presented in Chapter 4. Possible failure mechanisms for the ACF assemblies are then discussed. Parametric studies detail the sensitivity of package reliability to design variables such as the package geometry and properties of the materials used.

6.1 Introduction

Moisture is one of the most important factors that can affect the reliability of ACF components. Previous studies have revealed that the reliability of ACF components is strongly affected by moisture, which is predominantly considered as the most important factor of ACF component failures [8][9][10][11][12][13].

Previous modelling work [10][11][12] has been mostly limited to the analysis of simplified 2D models. Three dimensional models have focused on the micro-domain and ignored the global effects at package level, or they have modelled the whole package and used gross assumptions at the micro interconnect level [48][49][61][62]. The recognised difficulty here is that due to the vast range of length-scales in an ACF flip chip assembly, and the large number of conductive particles, an 'exact' model which includes all the particles and interconnections is simply not achievable with today's computer technology.

In this study, a 3D macro-micro modelling method is used to overcome the difficulty caused by the multi-length-scale nature of this problem and to enable a more detailed 3D representation and analysis of an ACF flip chip assembly. Two models: the macro and micro models, with different mesh sizes were built. The macro model was used to predict the overall behaviour of the whole package under moisture conditions. The displacement obtained from this global model was then used to set the boundary condition of the micro model so that the detailed stress analysis in the region around the conductive particle and between the pads can be undertaken.

6.2 Computer Modelling Technique

The experimental work presented in Chapter 4 proved that moisture absorption had a large effect on the reliability performance of ACF interconnections. In order to better understand the role that moisture plays on the reliability performance of ACF

assemblies, a 3D modelling analysis of an ACF flip chip when subjected to an autoclave test was conducted.

6.2.1 Challenges in Modelling the ACF Assembly

The ACF flip chip assembly consists of the silicon chip, polyimide substrate and ACF bonding material. The diameter of the conductive particles in the ACF material is around 3.5µm and the thickness of the particle metallization is about 50nm. The die is 11mm in its length, this means that the ratio of the two is approximately 1:200,000!! In addition, there are thousands of conducting particles in a typical ACF material used to bond a flip chip component to a substrate. This means that an 'exact' model which includes all the particles and interconnections would require millions if not billions of mesh elements to be used in a finite element model. This is simply not achievable with today's computer technology. Therefore, a 3D macro-micro modelling technique is required in order to provide the ability to accurately model the behaviour of the conductive particles during the autoclave test. This is the first time that such a technique has been used in this context.

6.2.2 Macro-Micro Modelling Technique

The macro-micro modelling analysis, also referred as global-local, or sub-modelling analysis, is defined as "a procedure to determine the detailed local stress states for specific regions using information obtained from an independent global stress analysis" [103].

The global modelling allows us to study the overall effect of the entire structure. The global mesh, although relatively coarse, should be fine enough to ensure that the critical regions can be identified. These regions are then subjected to a local modelling analysis to obtain the detailed local behaviour and stress distribution. Therefore, the local model adopts a much finer mesh that can accurately represent finer geometric features at this length scale. It should be noted that the local model is independent of the global model and its nodes need not coincide with those in the global model.

The boundary conditions applied to the local model can be obtained from the global solution with interpolation. Due to the difference in mesh refinement in the local region, there is a violation in equilibrium at the global/local boundary which can be eliminated with global/local iteration. However, in engineering practice, the initial global solution is often assumed to be accurate enough and no iteration is performed [104], therefore the present study assumes such engineering procedure.

Sub-modelling is based on St. Venant's principle, which states that if a system of forces acting on a small region of a body is replaced by a different but statically equivalent system of forces acting on the same region, then such a replacement does not cause significant changes in the predicted stresses and displacements at points in the body remote from the region concerned [105][106]. It also implies that if the boundaries of the sub-model are far enough away from the stress concentration, reasonably accurate results can be calculated in the sub-model. This is the case with the sub-models used in the following analysis where the stress concentrations are located around the conductive particles.

The procedure for a macro-micro modelling analysis consists of the following four steps:

(1) Create the Global and Local Models: the global mesh refers to the mesh that models the entire structure. The local mesh refers to the mesh that models the local area of interest and is a more detailed mesh, designed to capture the local stress/strain variations.

(2) Solve the Global Model: the global model is solved and the displacement results will be used to set up the boundary conditions for the micro model.

(3) Interpolation between the Models: Interpolation of displacements from the global solution along the boundary of the local area in the global mesh is made in this step. The interpolation of data from the global mesh is necessary

because there are fewer global nodes in the global model that interface with the finer mesh for the local model at their common boundary.

(4) Solve the Local Model: the interpolated displacements are now applied to the boundaries of the local model, and the problem is consequently solved.

This modelling technique is thought to be the best approach when large-scale structures are analyzed and where the local-scale factors are crucial for the structural design of the assembly [107].

6.2.3 Interpolation of the Displacement Fields

In the finite element literature, the functions used to represent the behaviour of a field variable within an element are called interpolation functions or shape functions. Although it is conceivable that many types of functions could serve as interpolation functions, only polynomials have received widespread use since they are relatively easy to manipulate mathematically [108].

The basic ideas to use the interpolation function in the macro-micro modelling process can be illustrated by a simple example in two-dimensional space which is illustrated in Figure 6.1. Suppose that there is one element in the global mesh and its coordinates remain the same in the local mesh, but there are finer elements in the corresponding area. The question is how to solve the displacement of the nodes in the local mesh based on the known displacement of nodes in the global mesh.

In the global mesh, the displacement is solved and stored at each node in the element. In two dimensions, the simplest complete polynomial has four nodal quantities of the element. Let's assume that the polynomial for a displacement variable, d, is defined as:

$$d(x,y) = g_1 + g_2 x + g_3 y + g_4 xy \qquad (7.1)$$

where x and y are Cartesian coordinates in the 2D space.

(a) In global mesh   (b) In local mesh
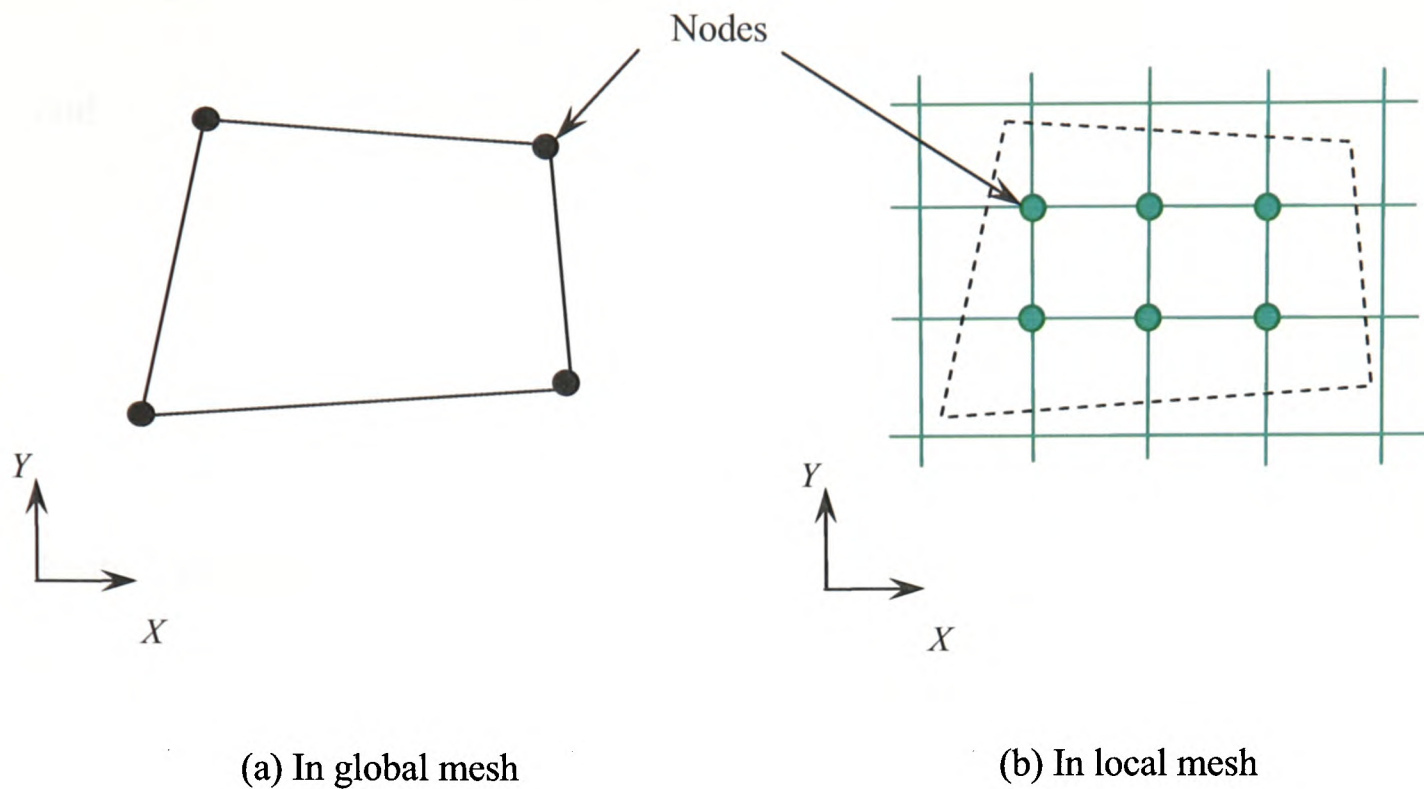
Figure 6.1: Interpolation from the global to local mesh

Assuming that the displacement values at the four nodes of the global element are d_1, d_2, d_3 and d_4, the coefficients of g_1, g_2, g_3 and g_4 may now be found by evaluating this equation at each of the four nodes of the global element, and then inverting the resulting set of simultaneous equations. Thus we can get:

$$d_1 = g_1 + g_2 x_1 + g_3 y_1 + g_4 x_1 y_1$$
$$d_2 = g_1 + g_2 x_2 + g_3 y_2 + g_4 x_2 y_2$$
$$d_3 = g_1 + g_2 x_3 + g_3 y_3 + g_4 x_3 y_3$$
$$d_4 = g_1 + g_2 x_4 + g_3 y_4 + g_4 x_4 y_4$$

where x_i and y_i are the coordinates of the i_{th} node.

Or, in matrix notation:

$$\mathbf{d} = \mathbf{Gg}$$

(7.2)

111

where $\mathbf{d} = \begin{bmatrix} d_1 & d_2 & d_3 & d_4 \end{bmatrix}^T$, $\mathbf{g} = \begin{bmatrix} g_1 & g_2 & g_2 & g_2 \end{bmatrix}^T$,

and

$$\mathbf{G} = \begin{bmatrix} 1 & x_1 & y_1 & x_1 y_1 \\ 1 & x_2 & y_2 & x_2 y_2 \\ 1 & x_3 & y_2 & x_3 y_3 \\ 1 & x_4 & y_2 & x_4 y_4 \end{bmatrix}$$

From Equation (7.2), we have:

$$\mathbf{g} = \mathbf{G}^{-1}\mathbf{d} \tag{7.3}$$

Expressing the terms of the interpolation polynomial Equation (7.1) as a product of a row vector and a column vector, we can write:

$$d(x, y) = \mathbf{P}(x,y)\mathbf{g} \tag{7.4}$$

where $\mathbf{P} = \begin{bmatrix} 1 & x & y & xy \end{bmatrix}$, by submitting Equation (7.3) into Equation (7.4), we have:

$$d(x, y) = \mathbf{P}(x, y)\mathbf{G}^{-1}\mathbf{d} = \mathbf{N}(x, y)\mathbf{d} \tag{7.5}$$

where $\mathbf{N} = \mathbf{P}\mathbf{G}^{-1}$, which is called the interpolation function or shape function. This function is also used in the descritization process of finite element method, which is described in the appendices.

Finally, the displacement at the nodes in the local mesh illustrated in Figure 6.1b can be easily achieved by using Equation (7.5). In general, Equation (7.5) can also be written as:

$$d(x, y) = \sum_{i=1}^{m} N_i(x, y)d_i$$

where m is the total number of the nodes in one global element.

In the macro-micro modelling procedure, the displacements at the nodes of the global mesh are calculated first, then the displacement information from the local area in the global mesh is imported into the micro model so that the displacements of all the nodes on the boundary surface in the micro model can be calculated using the above interpolation technique. These displacements are then used as the fixed displacement boundary conditions of the local model for the detailed stress analysis.

6.3 Demonstration of the Macro-Micro Modelling Technique

In order to verify the macro-micro modelling technique implemented in PHYSICA, a thermal mechanical analysis of a solder joint was carried out. Three models were built: the macro model (coarse mesh), micro model (fine mesh) and a global model with refined mesh. The results predicted from these models were compared in order to demonstrate the accuracy and efficiency of the macro-micro modelling technique.

6.3.1 Geometry and FE Models

The structure of a greatly simplified solder joint is shown in Figure 6.2. It consists of a chip, a PCB board and a solder joint.

In order to reduce the computing time, a slice model was adopted which means that one of the plane surfaces of the materials was fixed in the Z direction and another plane surface was free to move in the Z direction. The symmetry line was fixed in Y direction and the point A on the symmetry line was fixed in the X direction. For verification purposes, three models were built as follows:

(1) The macro model with a coarse mesh. As shown in Figure 6.3a, this model has all the components of the solder joint and the mesh is coarse. It contains 372 elements and 2646 degrees of freedom.

(2) The micro model with a fine mesh. This model contains only the copper pad and solder joint as shown in Figure 6.3b. The model contains 1024 elements and 6534 degrees of freedom, typically the mesh density is 24 by 32 in the solder area.

(3) The global model with a fine mesh. This model consists of all the components of the solder joint and was built with a fine mesh as shown in Figure 6.3c, it consists of 2664 elements and 17094 degrees of freedom. The mesh density in solder area is 24 by 32 which is same as in the micro model.
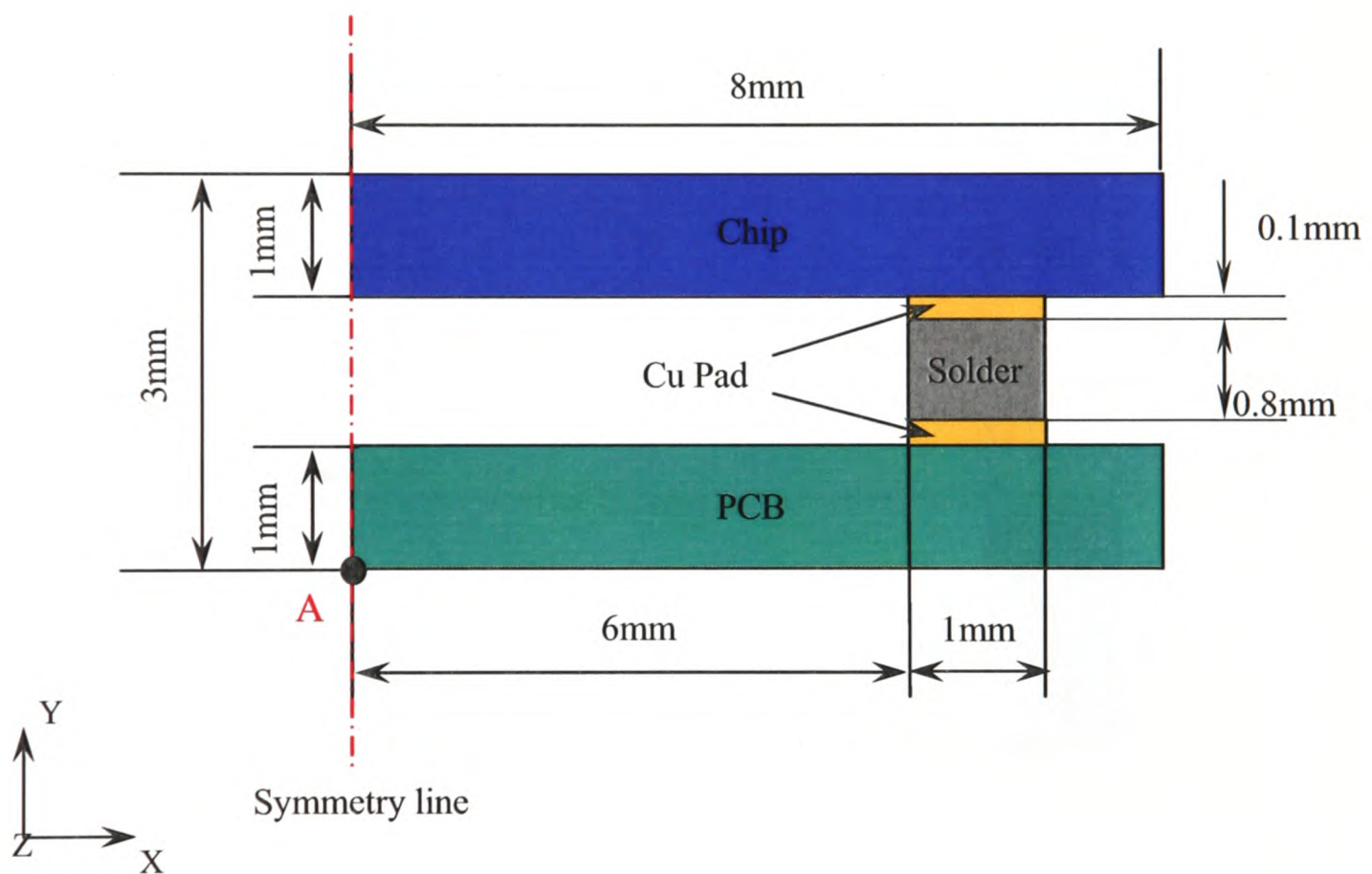
Figure 6.2: Structure and geometry of a simplified flip chip solder joint

(a) Macro
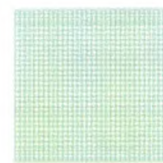
(b) Micro
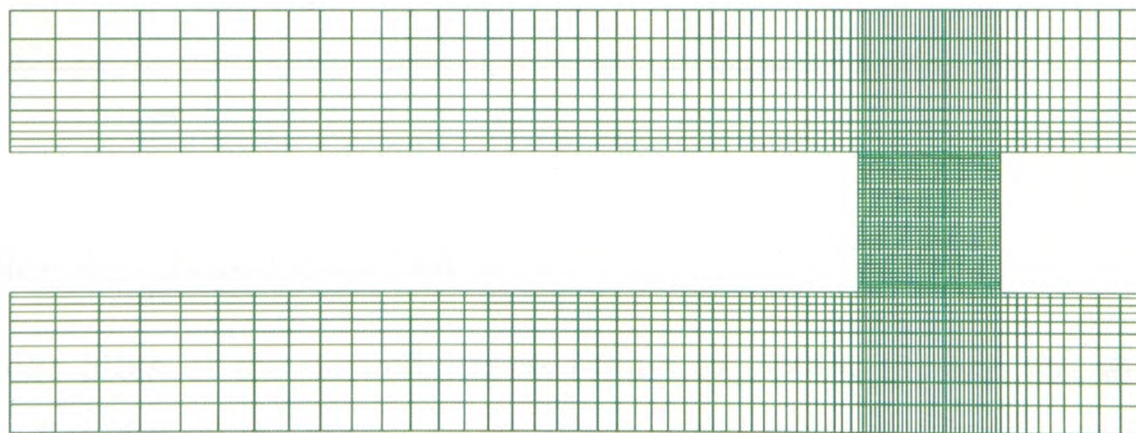
(c) Global

Figure 6.3: Mesh details of the macro, micro and global model

In the macro-micro modelling analysis, the macro model was only used to provide the displacement boundary condition for the micro model; the micro model was the one to obtain the final solution. To demonstrate the accuracy of the macro-micro method, a "true" solution was required. Since an analytical solution can not be

achieved for this problem, the FE solution of a well refined mesh (a globally refined mesh) was used as the "basis" solution.

6.3.2 Material Properties

The material properties used in this simulation are listed in Table 6.1. The chip, the substrate and the copper were considered as linear-elastic materials, solder was considered as elastic-plastic material, the yield strength of solder was 30.3 MPa [109].

Table 6.1: Material characteristics used for this simulation

Material	Young's modulus (MPa)	Possion's ratio	CTE (ppm/K)
Chip	131700	0.3	2.7
PCB	4000	0.3	20
Copper	205519	0.3	13.14
Solder	132400	0.34	16.7

6.3.3 Modelling Results and Error Analysis

The contour plots of the normal strains (strain xx, strain yy) and the shear strain (strain xy) predicted from the macro-micro solution and the basis solution are shown in Figure 6.4 a, b, and c respectively. The first column of the results was obtained from the macro-micro models and the second column was obtained from the globally refined mesh model. It is shown that the results predicted from the macro-micro solution are very close to the "basis" solution, the strain distribution is very similar and there is only a slight difference in the value.

(a) Strain *xx*
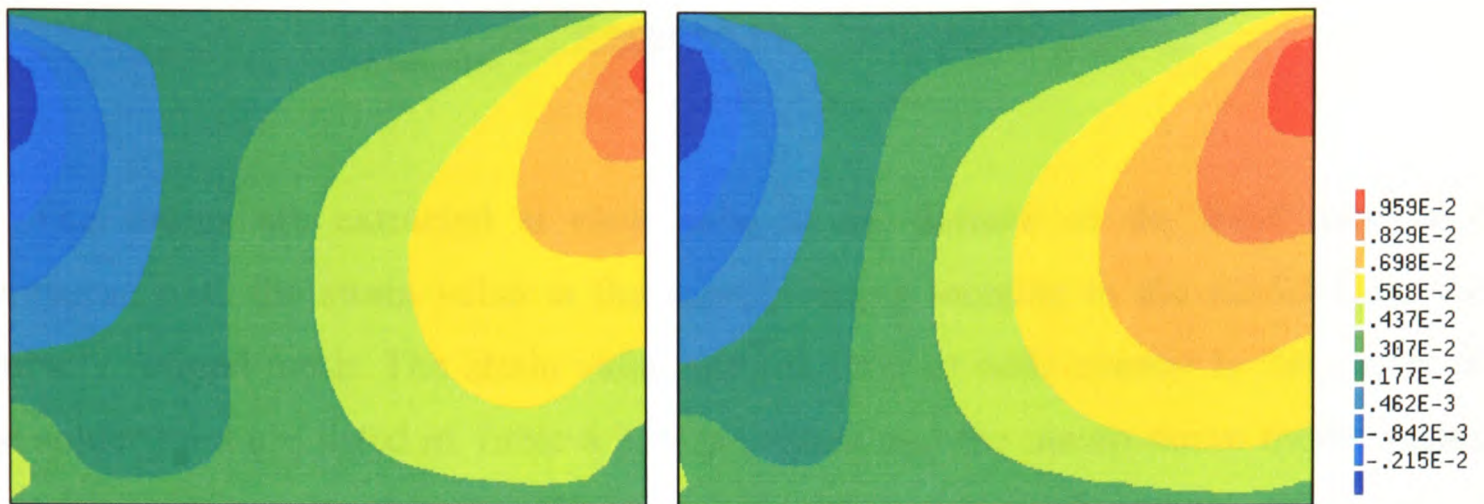
(b) Strain *yy*
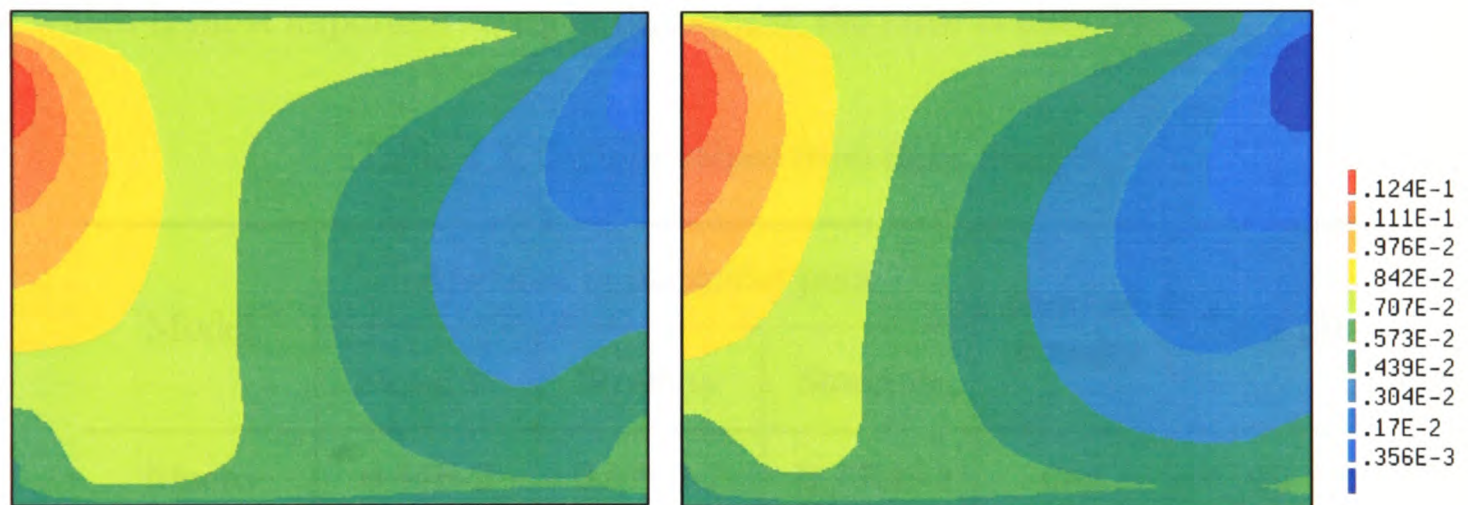
(c) Strain *xy*
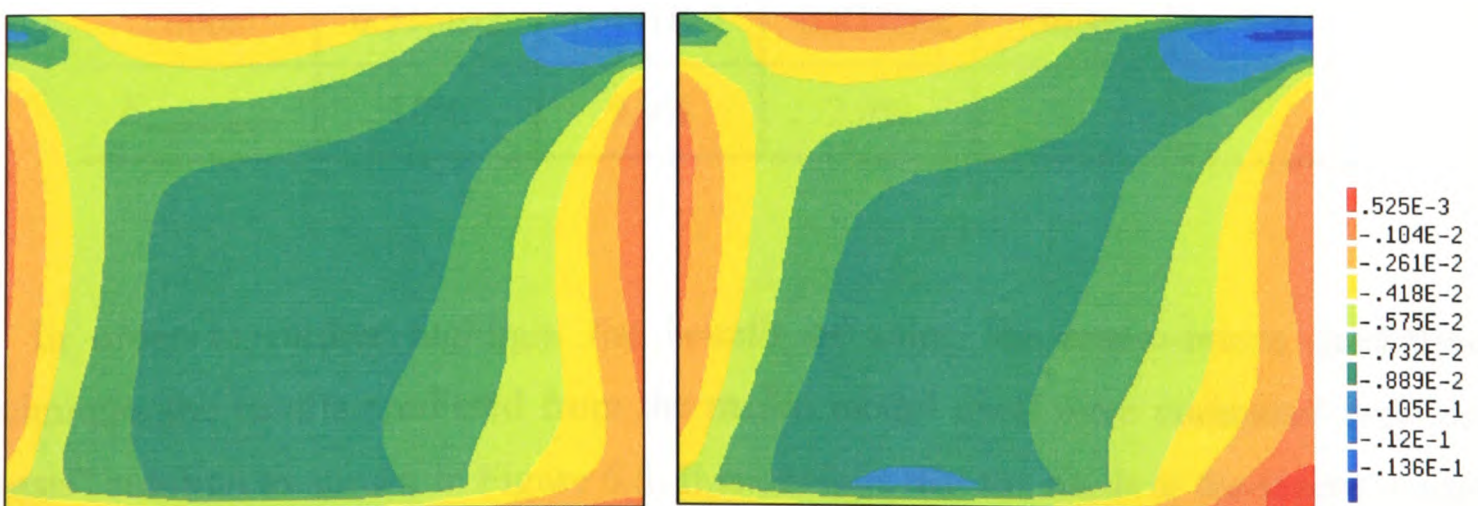
Figure 6.4: Strain distribution predicted by using the macro-micro model (the left row) and the global model (the right row)

The relative error of the macro-micro solution at each node can be defined as

$$E_{macro-micro} = \frac{\varepsilon_{globall-refined\ solu} - \varepsilon_{macro-micro\ solu}}{\varepsilon_{globall-refined\ solu}} \times 100\%$$

The strains are extracted at each node in the domain of the local mesh and compared with the strain value at the corresponding location in the model from the globally refined mesh. The strain value and the error at node nearest to the centre of the solder joint are listed in Table 6.2. It is evident that the macro-micro model yields more accurate results than the global model with coarse mesh and the macro-micro model uses much less computer time than the global model with a fine mesh. For strain xy, which is most important strain in this model, the error is only 2%.

Table 6.2: Certain values from three models

Model	At centre of the solder joint			Number of nodes	Time (s)
	Strain xx	Strain yy	Strain xy		
Macro	0.44E-2	0.579E-2	-0.738E-2	882	10
Micro	0.480E-2	0.535E-2	-0.843E-2	2178	56
Global	0.536E-2	0.491E-2	-0.827E-2	5698	238
$E_{macro-micro}$	10%	9.0%	2.0%		

In order to further highlight the benefit of using the macro-micro modelling technique, the results predicted from the macro model itself were compared with the "basis" solution as shown in Figure 6.5. It is obvious that the mesh in the macro model was too coarse to capture the deformation details in the solder, so that the results were very different from the "basis" solution, both in distribution and in value.

(a) Strain *xx*

.959E-2
.829E-2
.698E-2
.568E-2
.437E-2
.307E-2
.177E-2
.462E-3
-.842E-3
-.215E-2

(b) Strain *yy*

.124E-1
.111E-1
.976E-2
.842E-2
.707E-2
.573E-2
.439E-2
.304E-2
.17E-2
.356E-3

(c) Strain *xy*

.525E-3
-.104E-2
-.261E-2
-.418E-2
-.575E-2
-.732E-2
-.889E-2
-.105E-1
-.12E-1
-.136E-1
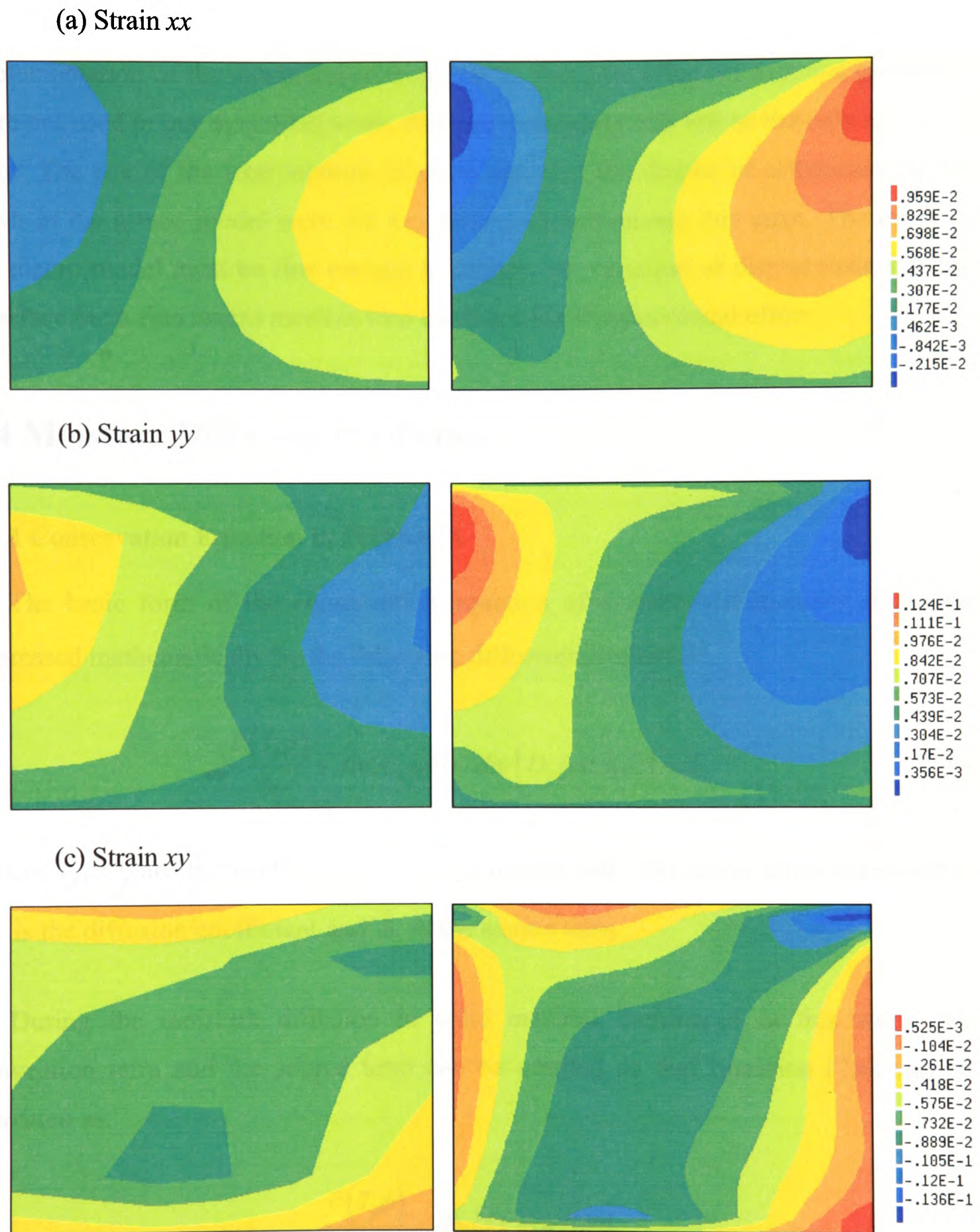
Figure 6.5: Strain distribution in solder predicted by using the macro model (left row) and the global model with a fine mesh (the right row)

119

When we use the macro-micro modelling technique, two sources of error can be identified. One is from the use of effective material properties and the other is from the implementation of the numerical scheme [107]. Since the effective material properties were not used in our modelling work, the numerical error was left as the only source of error. The use of the interpolation function and also the degree of refinement of the mesh in the macro model were the key factors in minimising this error. The mesh in the macro model must be fine enough to capture the variation of displacements at the interface but a fine macro mesh in turn increases the computational effort.

6.4 Moisture Diffusion Prediction

6.4.1 Conservation Equation in PHYSICA

The basic form of the conservation equation of a conserved quantity ϕ can be expressed mathematically by the following differential equation:

$$\frac{\partial(T_\phi\phi)}{\partial t} + div(C_\phi\underline{u}\phi) = div\left\{D_\phi grad(\phi)\right\} + S_\phi \tag{7.6}$$

Where T_ϕ, C_ϕ are the coefficients of the transient and convection term respectively, D_ϕ is the diffusion coefficient and S_ϕ is the source term.

During the moisture diffusion in solid material considered in this work, the convection term and the source term can be omitted so that Equation (7.6) can be rewritten as:

$$\frac{\partial(T_\phi\phi)}{\partial t} = div\left\{D_\phi grad(\phi)\right\}$$

If the diffusion coefficient D_ϕ is a constant in a material, the above equation can be written as:

$$\frac{\partial\left(T_\phi\phi\right)}{\partial t} = D_\phi\left(\frac{\partial\phi}{\partial x^2} + \frac{\partial\phi}{\partial y^2} + \frac{\partial\phi}{\partial z^2}\right) \tag{7.7}$$

By setting $T_\phi = 1$, substituting the moisture concentration C for the scalar variable ϕ, and replacing the general diffusion coefficient D_ϕ with the moisture diffusion coefficient D, Equation (7.7) can be used for the moisture diffusion analysis.

However, Equation (7.7) which is available in PHYSICA can not be used directly if there is more than one material in the solution domain. This is because that unlike the temperature distribution which is continuous in nature. The moisture concentration C is discontinuous at material interfaces because the saturated concentration values are not the same for different materials. This problem is illustrated in Figure 6.6. Due to the discontinuity at the interface between different materials, Equation (7.7) can not be used for moisture prediction for multi-material solution domain unless the discontinuity is removed.

(a) Unsaturated   (b) Saturated
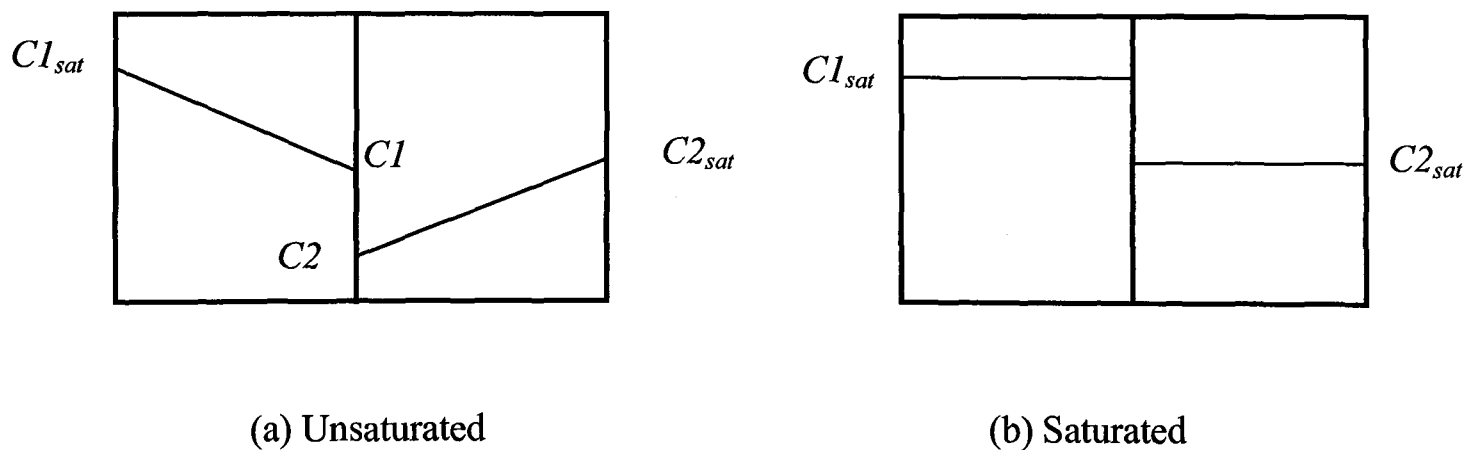
Figure 6.6: Moisture concentrations across bi-material interface

6.4.2 Wetness Fraction Approach

A wetness faction approach is introduced to solve the above problem [114]. A new field variable named wetness fraction, W, is defined as

$$W = \frac{C}{C_{sat}}, \quad 1 \geq W \geq 0$$

where C_{sat} is the maximum moisture concentration that can be absorbed by the material under certain temperature, the lower limit ($W = 0$) means the material is fully dry, and the upper limit ($W = 1$) means the material is fully saturated with moisture. The wetness fraction W was proved to be continuous across bi-material interface [114]. The wetness fraction profile corresponding to Figure 6.6 can be depicted as Figure 6.7.

(a) Unsaturated   (b) Saturated
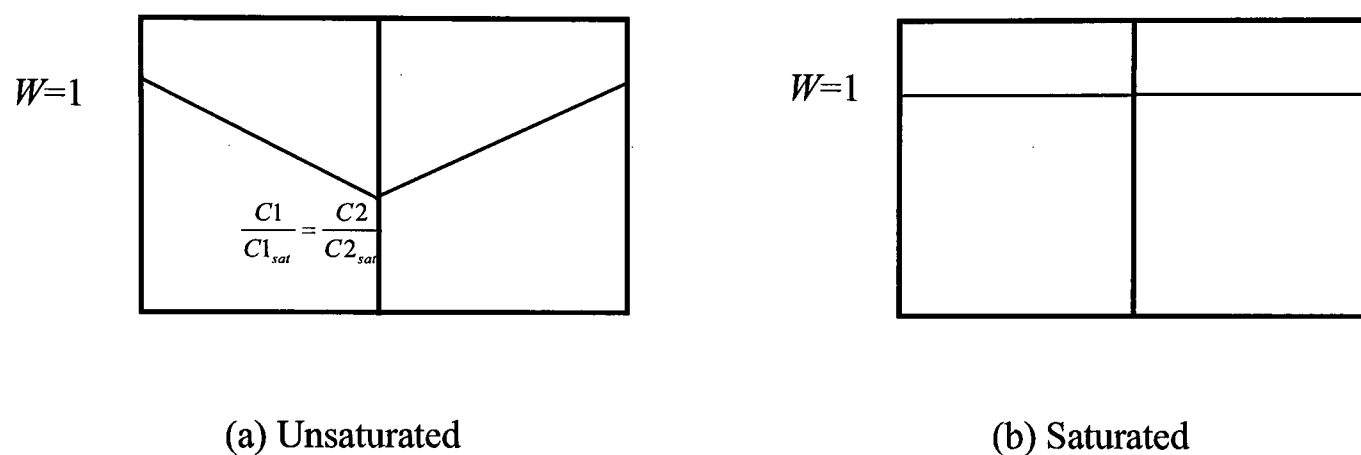
Figure 6.7: Wetness fraction across bi-material interface

Therefore, if we define wetness faction W as the concerned scalar variable ϕ, Equation (7.7) can be written as:

$$\frac{\partial (C_{sat}W)}{\partial t} = D\left(\frac{\partial^2 (C_{sat}W)}{\partial x^2} + \frac{\partial^2 (C_{sat}W)}{\partial y^2} + \frac{\partial^2 (C_{sat}W)}{\partial z^2} \right) \tag{7.8}$$

In a domain with only one material, C_{sat} is independent of the location and the above Equation (7.8) can be simplified as:

$$\frac{\partial W}{\partial t} = D\left(\frac{\partial^2 W}{\partial x^2} + \frac{\partial^2 W}{\partial y^2} + \frac{\partial^2 W}{\partial z^2} \right)$$

When Equation (7.8) is used to predict the wetness fraction distribution in a multi-material system, the transient coefficient T_ϕ is then defined as C_{sat} and D_ϕ is defined as the product of C_{sat} and D. Once the wetness fraction W is solved, the moisture concentration C can be easily obtained by:

$$C = C_{sat} \times W$$

This wetness fraction method was firstly introduced by Wong et al. in 1998 [114] for predicting the moisture absorption in an IC package. Due to the improvement in simplicity and computational efficiency, this method is becoming widely used for predicting the moisture concentration in IC packages [115][116][117][118][119]. Most importantly, the wetness fraction method enables the use of commercial thermal analysis software to model the transient moisture diffusion phenomenon in a multi-materials package. The relationship between them is shown in Table 6.3.

Table 6.3: The relationship of the thermal and moisture simulation [115]

Properties	Moisture	Thermal
Field variable	Wetness(C/C_{sat})	Temperature (T)
Density	1	ρ
Conductivity	$D*C_{sat}$	k
Specific Gravity	C_{sat}	c_p

Because of the analogy between thermal conduction and moisture diffusion, the simulation of moisture diffusion process in a multi-material package can also be done using the HEAT Module in PHYSICA package. The implemented moisture prediction technique could therefore be tested by solving moisture diffusion as a typical thermal problem. In this research, the moisture diffusion analysis was predicted using the SCALAR module in PHYSICA and the moisture induced stress was predicted using EVP module, so that the thermal conduction and moisture diffusion analysis can be coupled when the thermal effect has to be taken into account.

6.4.3 Test Case: One Dimensional Moisture Diffusion

In order to validate the moisture prediction technique in PHYSICA, a one dimensional diffusion problem is analyzed numerically and the results are compared with the analytical solution. This one-dimensional problem is an approximation of a diffusion process that happens in a thin plate where diffusion flux is mainly perpendicular to the plate. If it is assumed that the solution domain has a size of $2l$, the concentration values at the two ends of the domain are kept at a constant concentration C_l at all time and at t = 0 the concentration throughout the domain is C_0. The concentration of diffusion substance within the solution domain can be expressed by the following equation [111]:

$$\frac{C-C_0}{C_1-C_0} = 1 - \frac{1}{\pi} \sum_{n=0}^{\infty} \frac{(-1)^n}{2n+1} e^{-D(2n+1)^2 \pi^2 t / 4l^2} \cos \frac{(2n+1)\pi x}{2l} \qquad (7.9)$$

where D is the diffusion coefficient, t is the diffusion time. The right hand side of Equation (7.9) can be evaluated by using MathCAD software and n was set as 1000.

In the numerical analysis, the FEA model employed is illustrated in Figure 6.8. The model consists of 50 brick elements. The material properties used in the simulation are listed in Table 6.4.
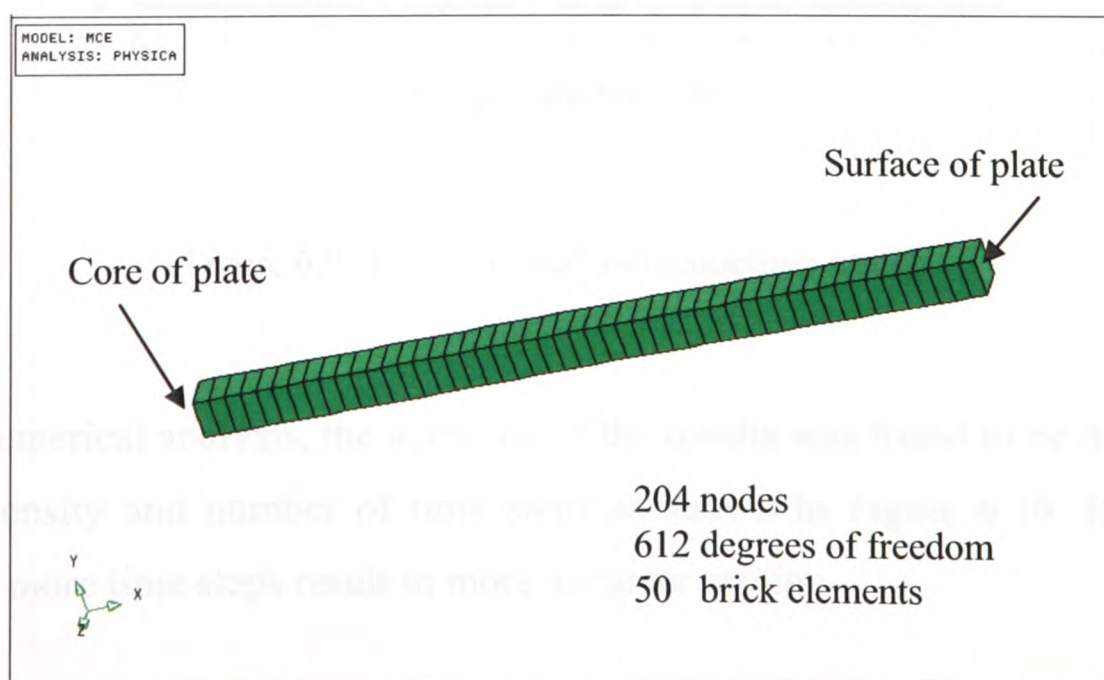
Figure 6.8: The mesh of the 1D model diffusion model

Table 6.4: Material properties used for the 1D diffusion simulation

D (mm^2/s)	t (s)	l (mm)	C_0 (g/mm^3)	C_1 (g/mm^3)
1.00	20	10	0	1

Both analytical and numerical results of $(C - C_0)/(C_1 - C_0)$ along the x direction are plotted in Figure 6.9. It shows that the numerical results have a good match with the analytical results and the overall difference is less than 2%.
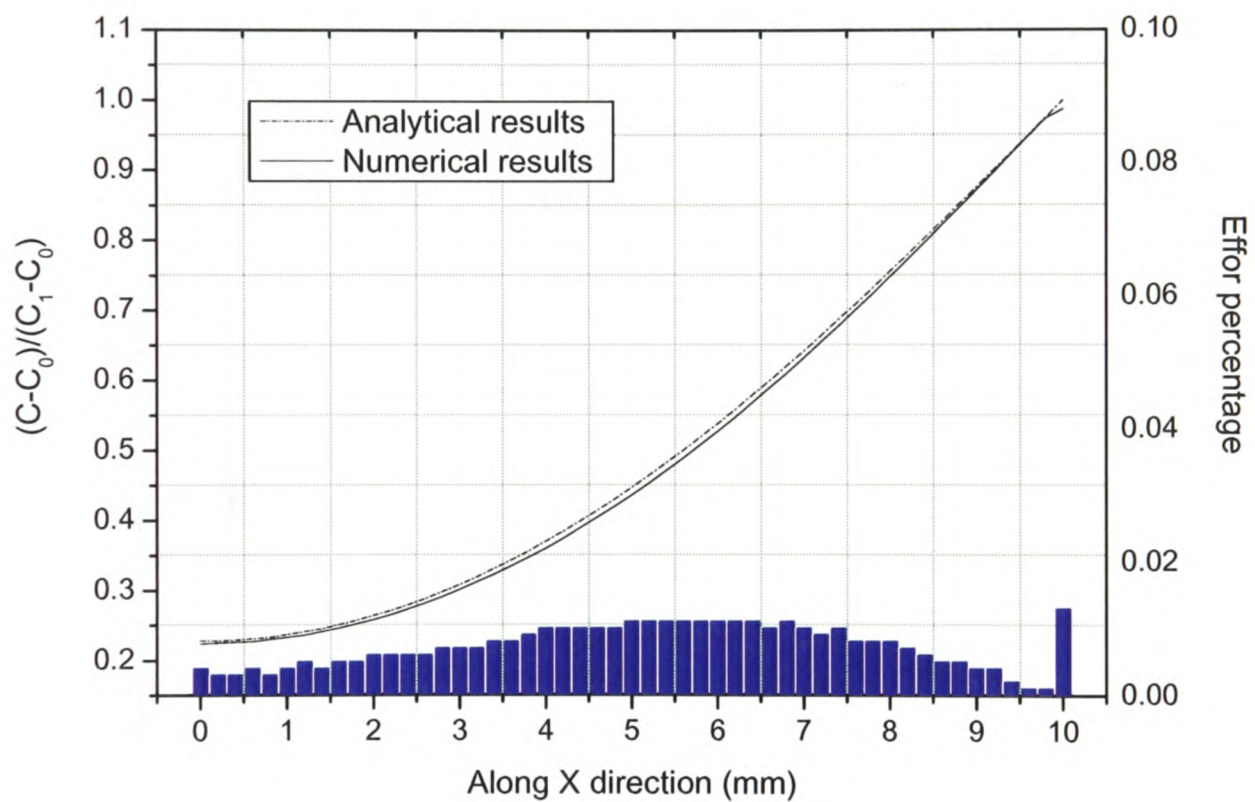
Figure 6.9: The analytical and modelling results

In the numerical analysis, the accuracy of the results was found to be dependent on the mesh density and number of time steps as shown in Figure 6.10. Higher mesh density and more time steps result in more accurate results.
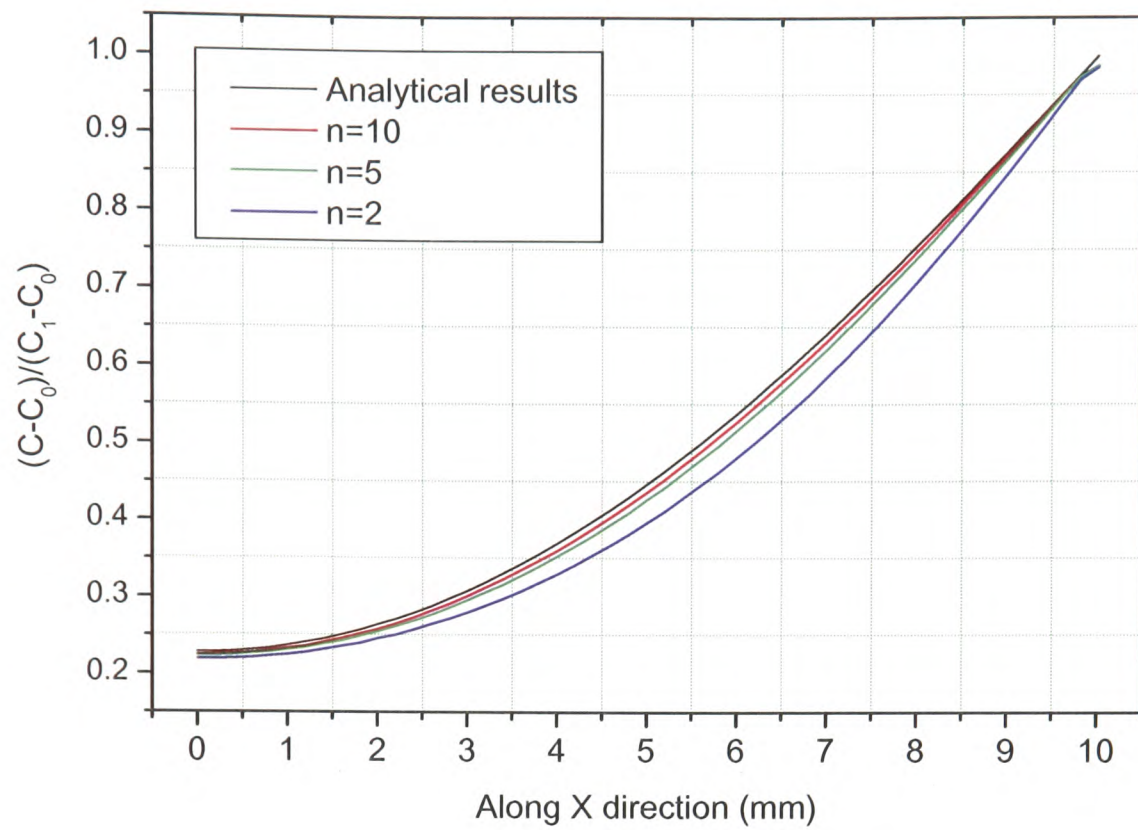
(a) Time step
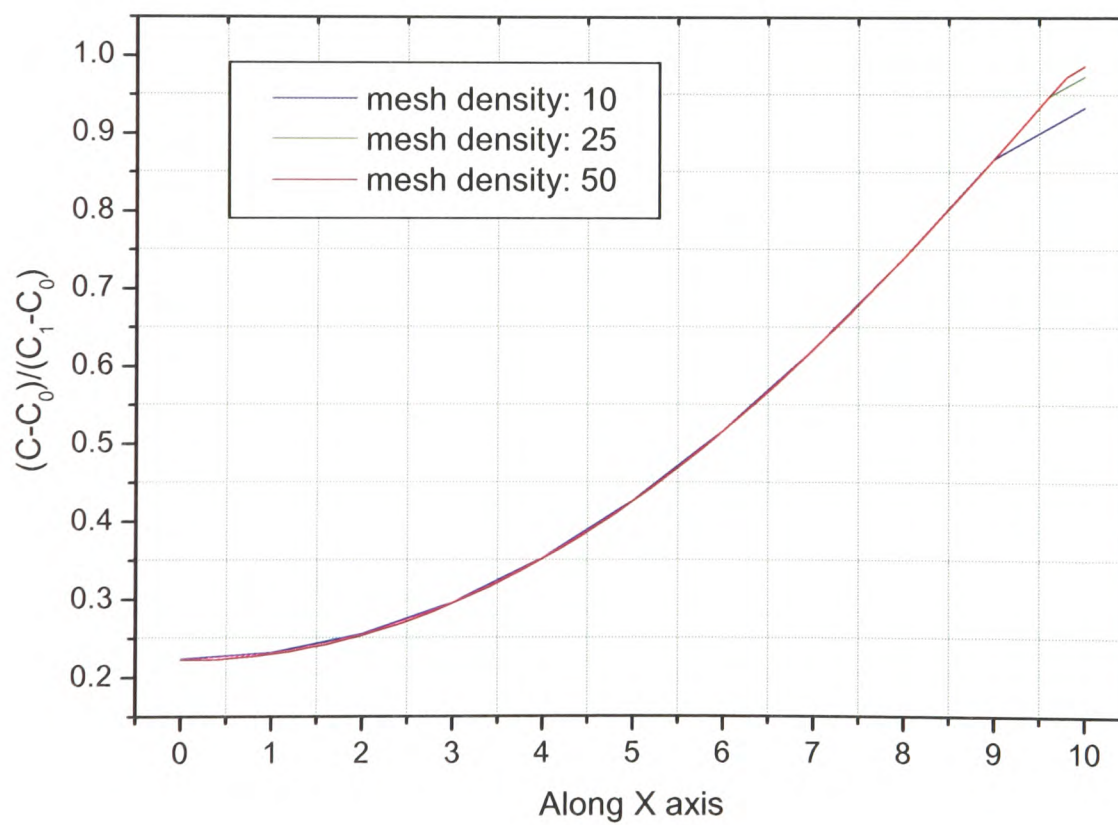
(b) Mesh density

Figure 6.10: Effects of the mesh density and time step on the numerical results

6.5 Modelling Analysis of an ACF flip chip Assembly

In this section, the hygro-thermal mechanical analysis of an ACF flip chip assembly using a 3D macro-micro modelling technique is explained and the results of moisture concentration and moisture induced stresses are presented.

6.5.1 Geometry and Mesh Model

In order to compare the computer modelling results with the results from the experiments, a typical flip chip on flex (FCOF) assembly with an 11mm × 3mm × 1mm chip and a total of 368 Ni/Au peripheral pads was used throughout this analysis. The dimensions of the bumps were 50μm × 50μm × 20μm. The substrate was made of polyimide, 25μm in thickness and the metal pads on the substrate were made of nickel-gold plated copper. The thicknesses are 12μm, 4μm and 0.5μm for the copper pad, nickel layer and gold coatings respectively. The gold layer was neglected in the model since it is very fine in thickness. The layout of the chip is shown in Figure 6.11.
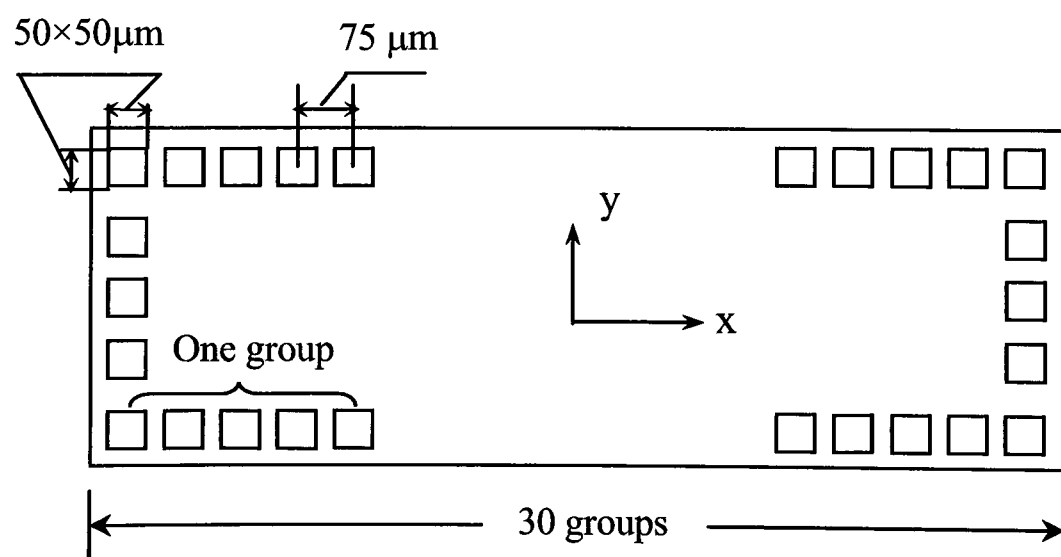
Figure 6.11: The layout of the silicon chip

The macro model of this ACF flip chip assembly is shown in Figure 6.12. In order to reduce the size of the FEA model and save the computing time, the modelled

substrate's size was the same as the chip. Further more, only one quarter of the ACF flip chip assembly was simulated due to the symmetry of the package. This model consists of a total of 32198 hexahedral elements.
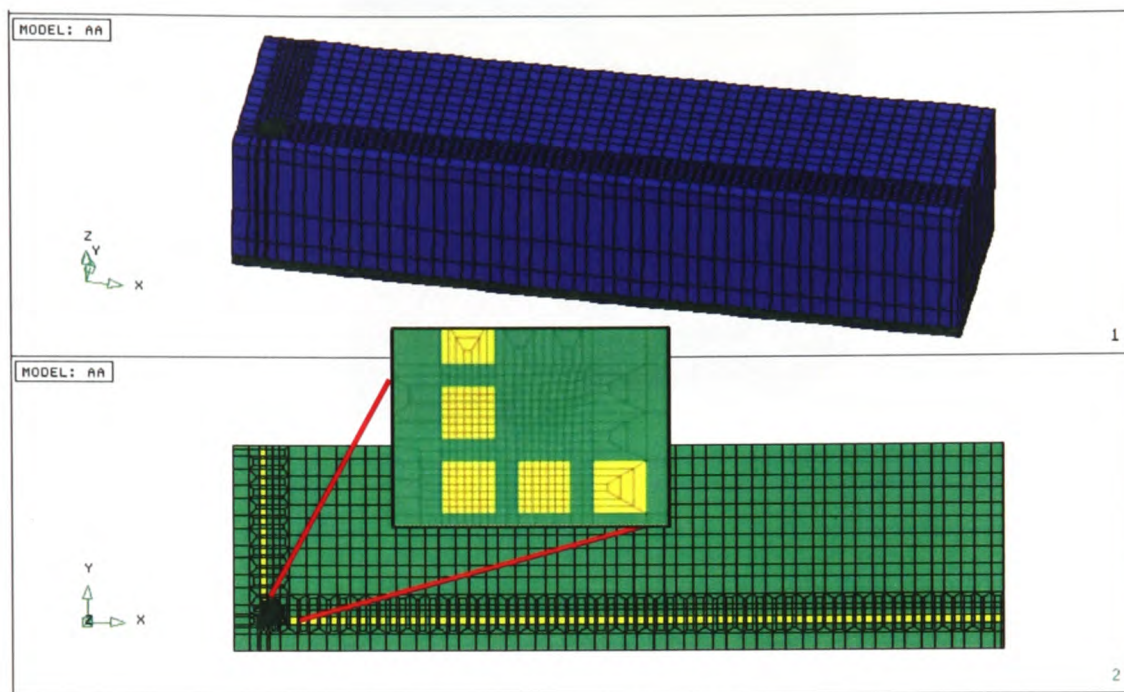
Figure 6.12: The mesh of the macro model

The micro finite element model is shown in Figure 6.13. This model represents the ACF joint located at the corner of the ACF flip chip where the stress level is usually the highest. A representative conductive particle was included and a finer mesh was employed around the particle in order to capture the details of the particle. The conductive particle was assumed to be Ni/Au coated polymer particle with a diameter of 3.5μm. A total of 23376 elements were used in this micro model. It can be seen clearly that much finer mesh was used in the micro model than the corresponding area in the macro model in order to capture more detailed stress information around the conductive particle.
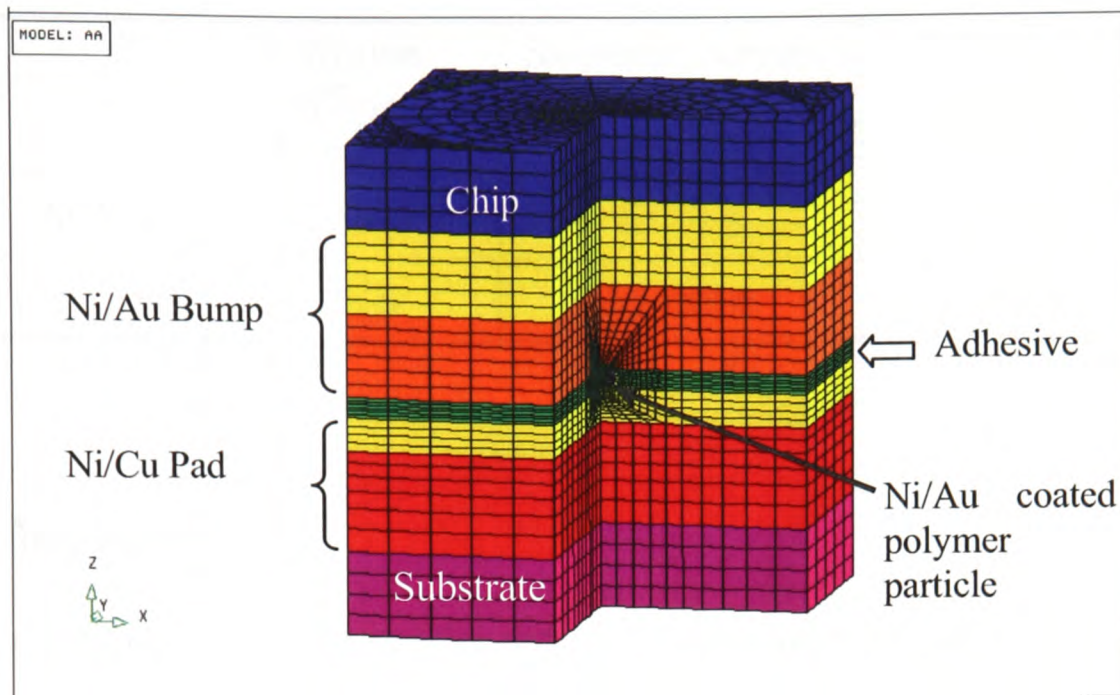
Figure 6.13: The mesh information of micro model

6.5.2 Material Properties and Modelling Assumptions

ACF flip chip bonding is a complicated process which involves heat transfer, fluid flow and solid deformation. In order to simplify the FEA analysis, the residual stress created in the bonding process was assumed to be negligible. This means that the model was stress free at the reference temperature. As a further assumption, all materials in the model were assumed to be homogenous, isotropic, and the temperature dependence of material properties was neglected. All the materials were assumed to be elastic. The basic material properties used are as listed in Table 5.1. The moisture properties used are listed in Table 6.5 which are based on the work described in Ref. [7][13][112].

The diffusion coefficient of moisture in polyimide, D, was reported to be of the order of 10^{-7}mm^2/s at room temperature (25°C) [112]. At autoclave test conditions, the moisture diffusion rate of adhesives can be ten times higher than what it is at the room temperature [13], therefore the diffusion coefficient of moisture in the polyimide substrate was assumed of the order of 10^{-6}mm^2/s at autoclave test conditions.

129

Table 6.5: Moisture properties of the ACF and polyimide substrate

	Diffusion coefficient (mm^2/s)	Saturated moisture Concentration (g/mm^3)	CME (mm^3/g)
ACF	12.3E-6	32.3E-6	1.7E2
Polyimide	1.0E-6	16.15E-6	1.0E2

6.5.3 Modelling Results

Three groups of modelling results are presented: moisture diffusion, moisture or temperature induced stresses, and parametric analysis. The moisture diffusion was predicted using the macro model and the detailed stress analysis was carried out using the micro model. In the parametric analysis, the effects of the CME, the Young's modulus of the adhesive matrix, and the bump height of the chip on the moisture induced interfacial stresses were studied.

6.5.3.1 Moisture Diffusion

The moisture diffusion analysis was coupled with the stress analysis so that the displacement field and the moisture concentration were solved simultaneously. Figure 6.14 shows the wetness fraction at the centre of the package versus the time, it is noted that the time it took for the adhesive to be fully saturated is very much dependent on the moisture properties of the polyimide substrate. The package is not saturated in the first 50 hours of the autoclave test if we assume that the substrate does not absorb any moisture. However, the polyimide substrate does absorb moisture and the ACF package can be fully saturated within the first 12 hours of the autoclave test and the duration can be even shorter when higher moisture diffusion rate of the polyimide is used. This result implies that the moisture property of the polyimide substrate is a crucial factor in the reliability performance of the flip chip on flex in a humid environment.
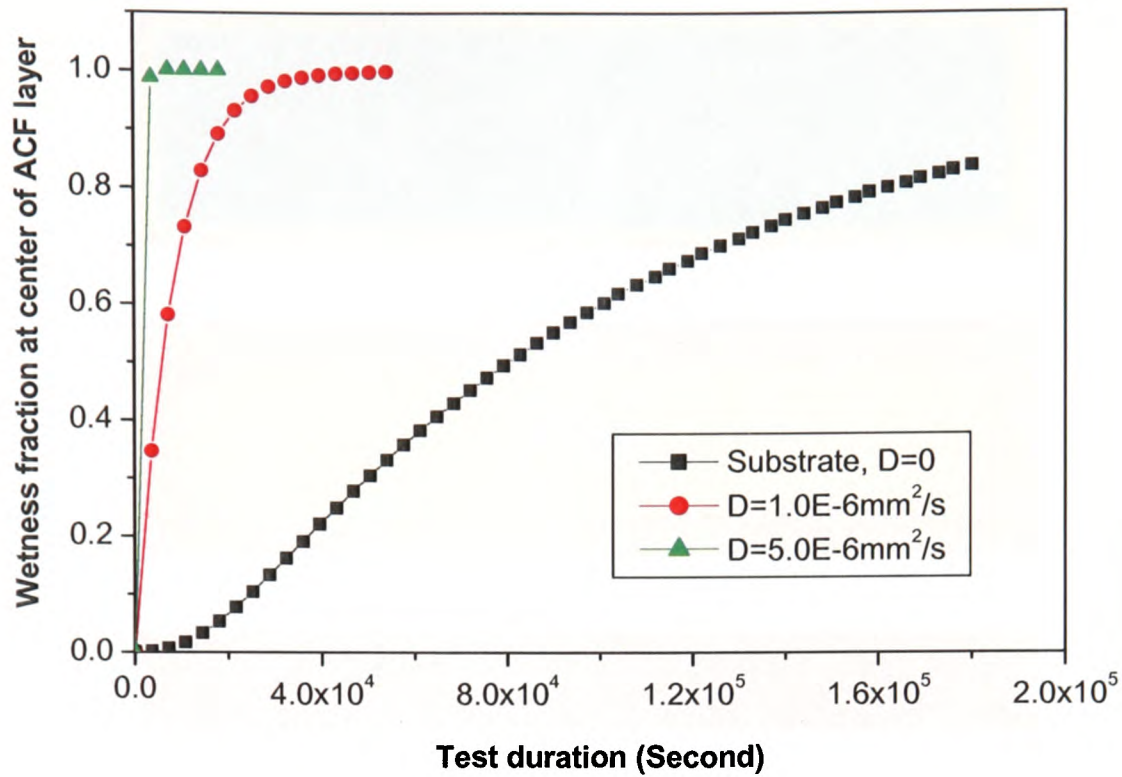
Figure 6.14: Wetness fractions at the centre of the ACF layer

The wetness faction distribution in the ACF layer in the first 12 hours' test is shown in Figure 6.15. It is noticed that there is no obvious wetness fraction gradient in the ACF layer, since the polyimide substrate is 25μm in thickness and the width of the ACF is 3mm, moisture can quickly diffuse into the adhesive from the polyimide substrate, rather than the perimeter sides of the ACF layer.

131
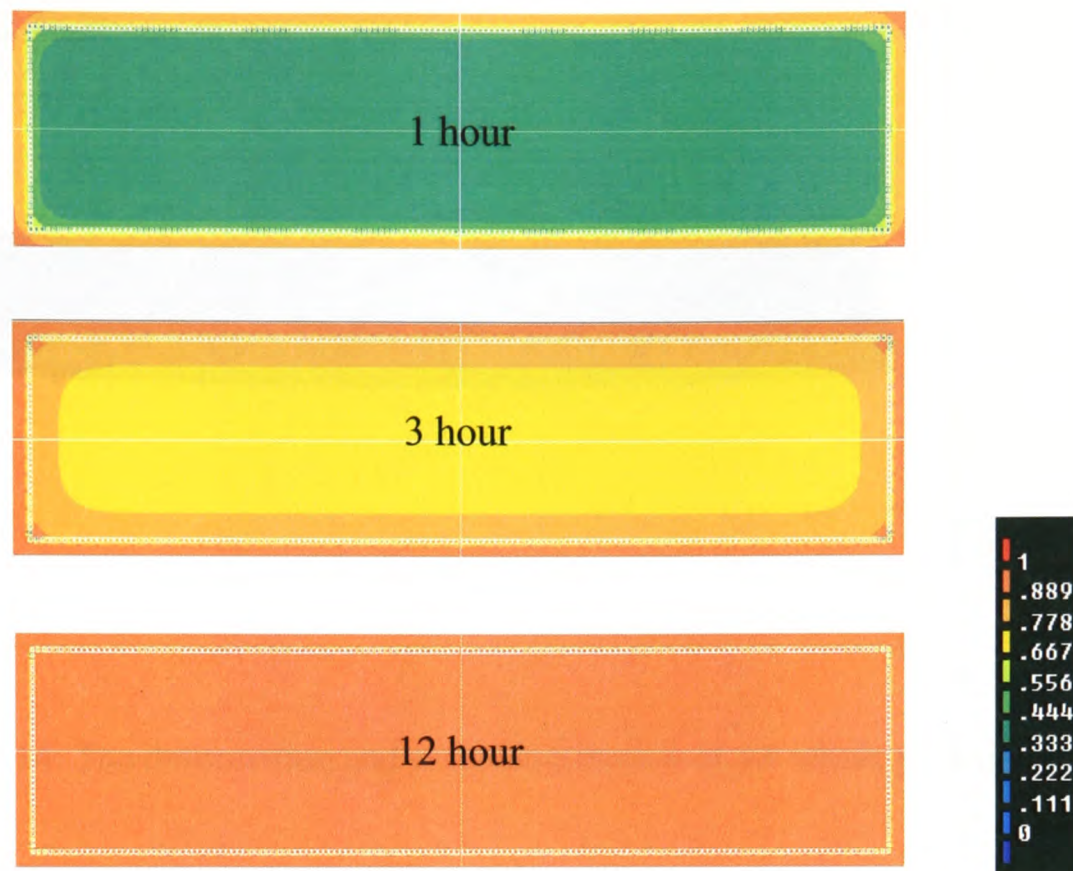
Figure 6.15: The wetness fraction distribution in ACF layer

The effective stress distribution and the warpage of the package due to the moisture absorption are shown in Figure 6.16. The deformation is magnified by 400 times in order to give clear information. The package bends upwards since the flex substrate absorbs water and expands, while the chip absorbs virtually no water at all and therefore does not expand.

The displacement, temperature and moisture concentration resulting from the macro model are then used as the boundary conditions of the local model. In this work, the boundary mesh of the micro model is finer than in the corresponding parts of the macro model so that the nodes of the two models do not coincide at the boundaries. As mentioned in Section 6.2.3, interpolation techniques can be used to transfer the displacement values from the macro model to the micro model's boundary nodes.

```
ASSEMBLY: GLBAL
DEFORMATION = 400
CASE1: PHYSICA RESULTS
STEP: 1  TIME: .144E6
NODAL ESTRES
MAX = 75  MIN = .159
```

68.2
61.4
54.6
47.8
41
34.2
27.4
20.6
13.8
6.97
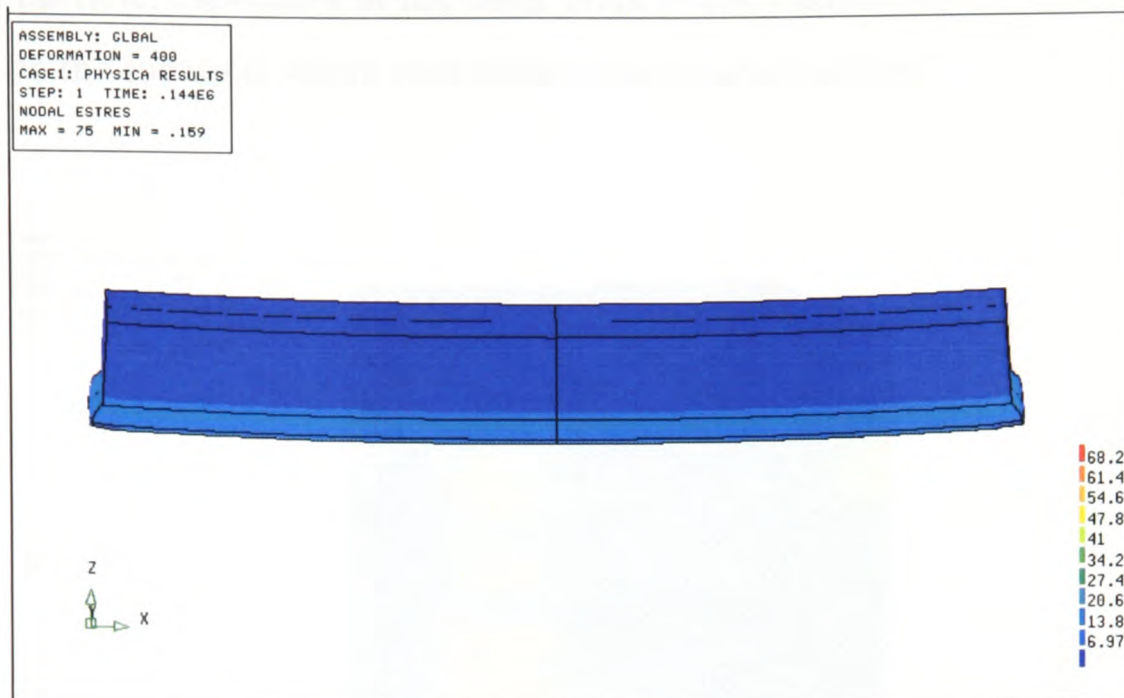
Figure 6.16: The deformation and stress distribution of the whole package

6.5.3.2 Moisture Induced Stress

The conductive particles play an important role in the ACF interconnections. They work as the electrical conductors providing current paths in the fine pitch electronics packaging as well as physical parts connecting chip bumps and substrate pads through the mechanical deformation interfaces [69]. Therefore, it is very important to understand the local stress distribution in an ACF joint, especially the area around the conductive particle.

The Von-Mises stress distribution in this ACF joint due to the moisture absorption is shown in Figure 6.17. Stress concentration is found at the interfaces between the adhesive and the bump/pad. The stress level is highest around the spot where the pad, the flex substrate and adhesive meet. In the experiments, this was usually the location where the micro cracks were found. The normal stress distribution around the conductive particle in the ACF joint is shown in Figure 6.18 . The highest normal stresses are identified in the coating layer of the conductive particles. Along the interface between the adhesive and metal pad, higher stress are identified around the

conductive particle, especially at the outer edge of the particle/pad contact region. This area could be the location where interfacial delamination occurs.
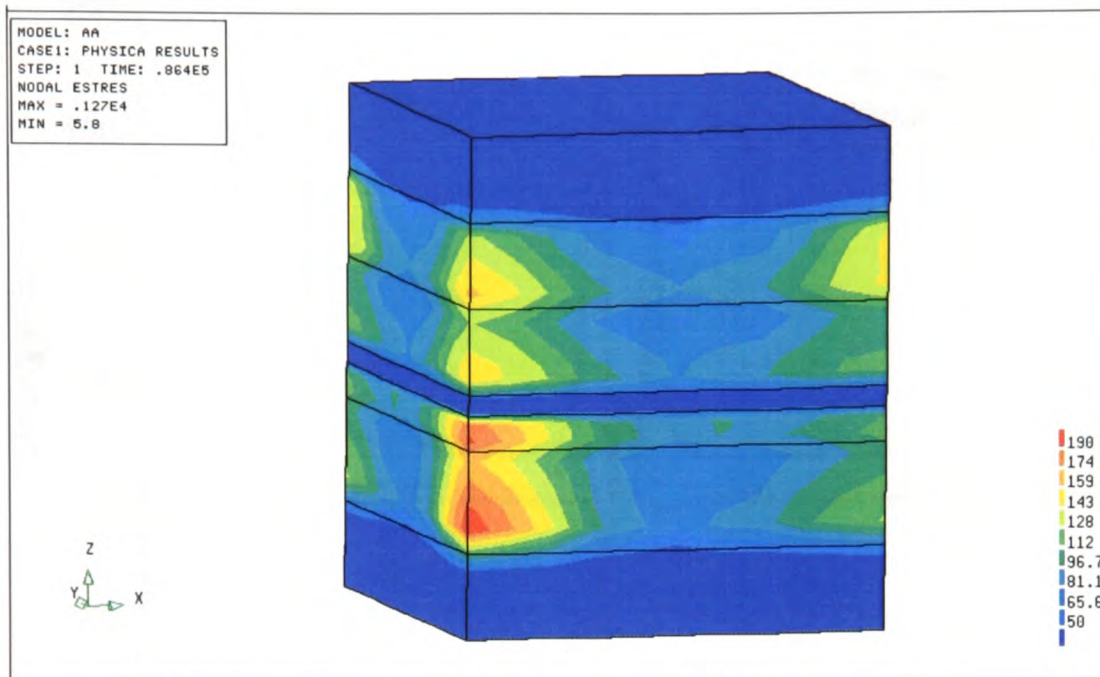
Figure 6.17: Pattern of the Von-Mises stress distribution
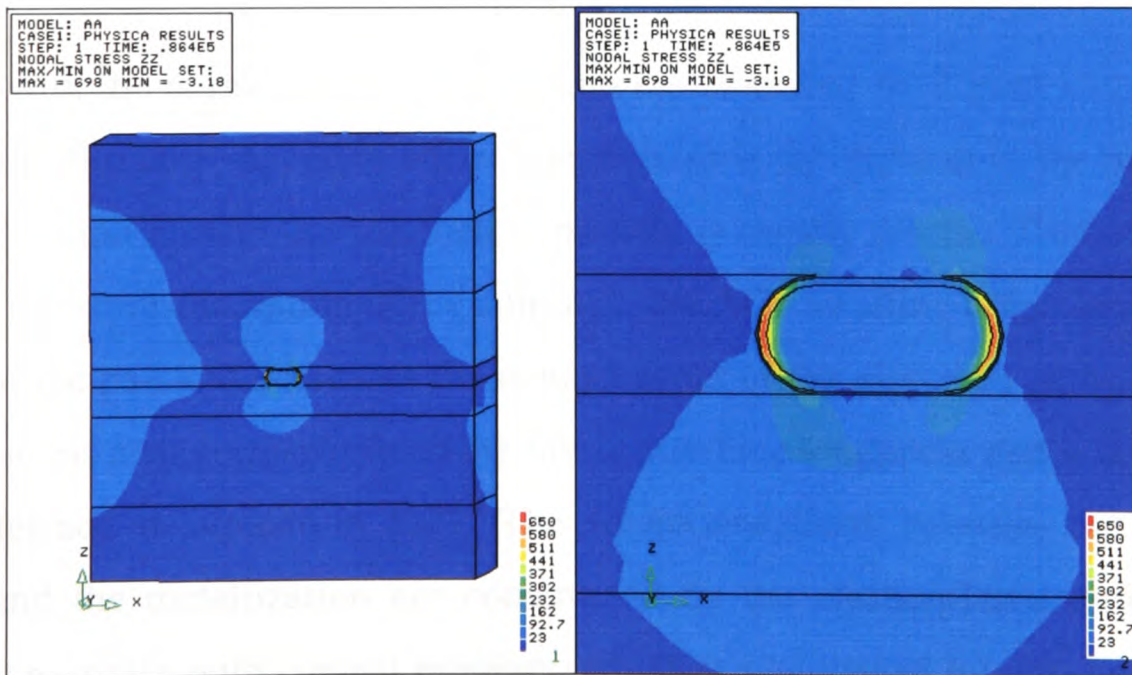
Figure 6.18: Pattern of the tensile stress distribution

Both normal stresses and shear stresses along the interface between the conductive particle and metal pad are shown in Figure 6.19. The shear stress is not significant
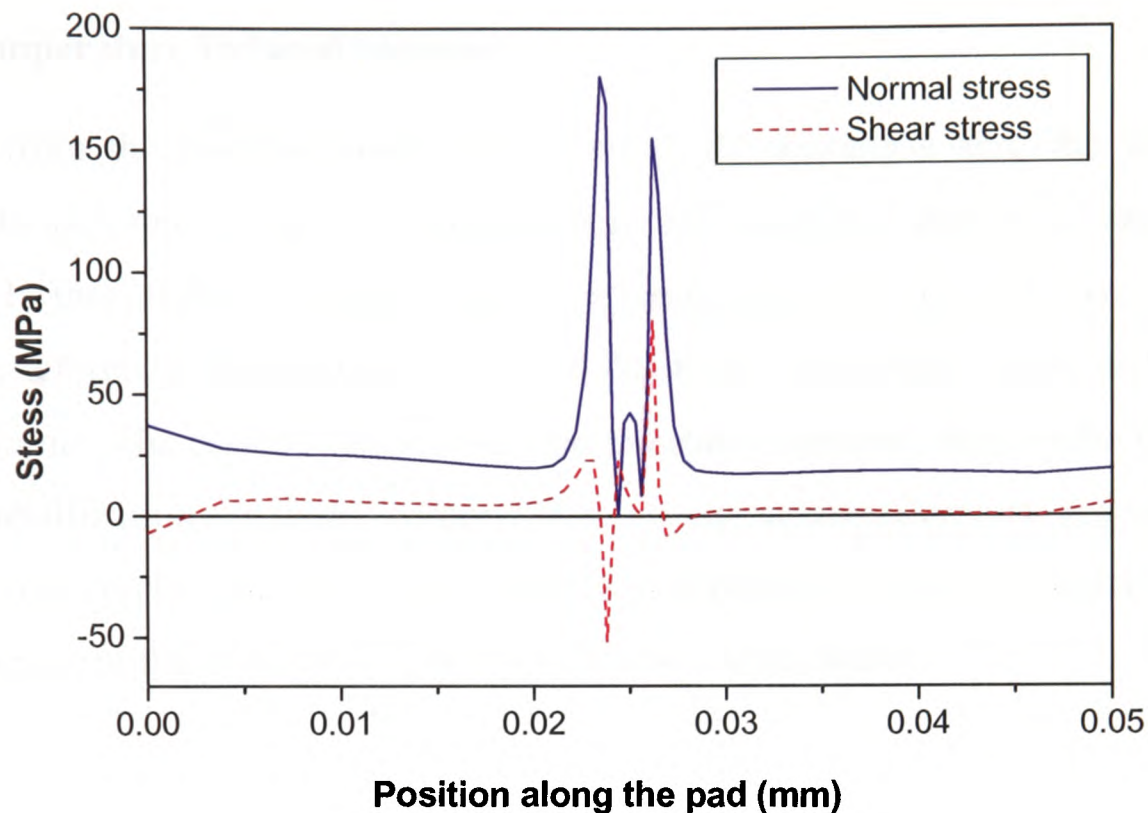
Figure 6.19: The interfacial stresses due to moisture absorption

compared with the normal stress even though the modelled ACF joint is located at the corner of the flip chip assembly where shear stress is the greatest in the package. The loading condition around the conductive particle is mostly tensile. This indicates that due to the moisture absorption of the adhesive, the ACF swelling effect tends to lift the bump from the pad and decreases the contact areas of the electrical paths. The tensile dominant stress also corresponds to the lower interface toughness and it is more prone to the interface delamination [12]. The interconnections between the conductive particles and the metallization are constructed by the elastic/plastic deformation of conductive particles with contact pressure, which is maintained by the shrinkage force in the cured adhesive. Once the adhesive expands in the vertical direction due to the moisture absorption, the shrinkage force in the adhesive could be released and deformed particles may recover their original shape due to the loss of the contact

135

pressure. As the consequence the contact area decreases and the contact resistance increases. In the worst case, joint opening occurs when the contact area is completely lost.

6.5.3.3 Temperature Induced Stresses

Apart from the moisture-induced stresses in the autoclave test, the temperature-induced stresses due to the CTE mismatch in the assembly were also simulated and analyzed. In this analysis the glass transition temperature Tg of 131°C was used as the stress-free reference temperature. Figure 6.20 shows the normal stress distribution in the ACF joint. The result suggests that the interfaces between the conductive particle and the metallization are under compression, i.e. the stress values are negative, so that the interface cracks are not open and the compressive forces maintain the good contacts between the conductive particles and the metallization.
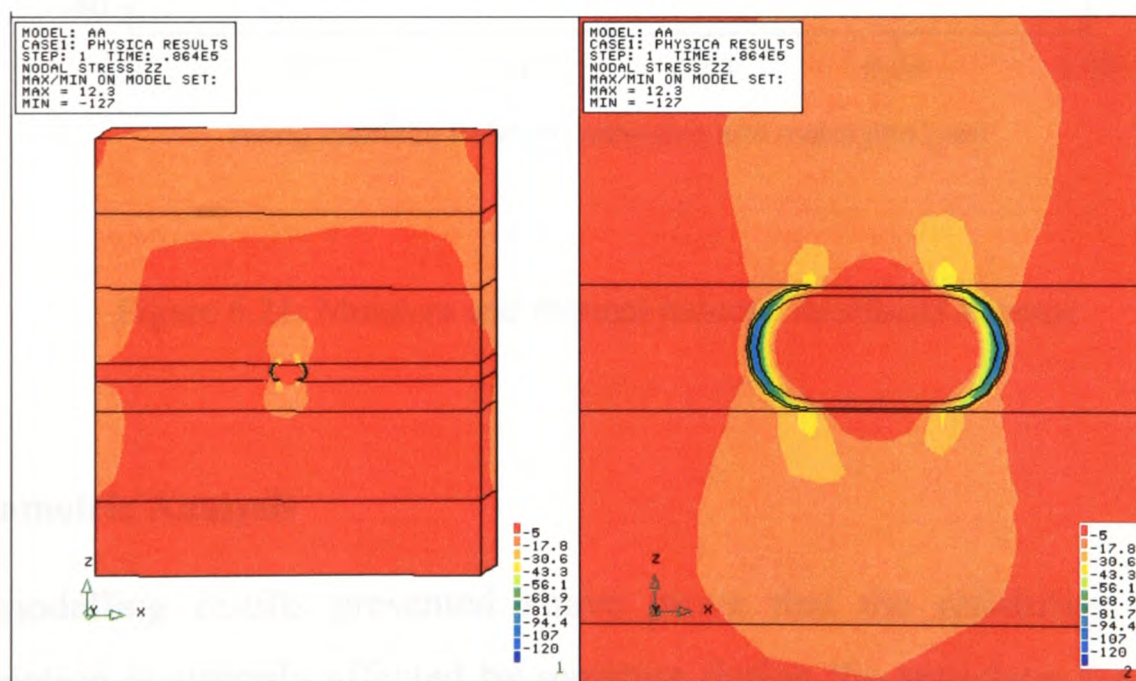
Figure 6.20: The pattern of the normal stress distribution due to temperature change

Along the interface between the conductive adhesive and the metal pad, the normal stresses due to the moisture absorption or temperature changes are both shown in Figure 6.21. The magnitudes of the moisture induced tensile stresses are much higher

than the thermal induced compressive stresses and therefore the coupled normal stresses along the interface are tensile dominant. Therefore, in autoclave test, the moisture induced tensile stresses play a more important role in the joint opening rather than the thermal stresses.
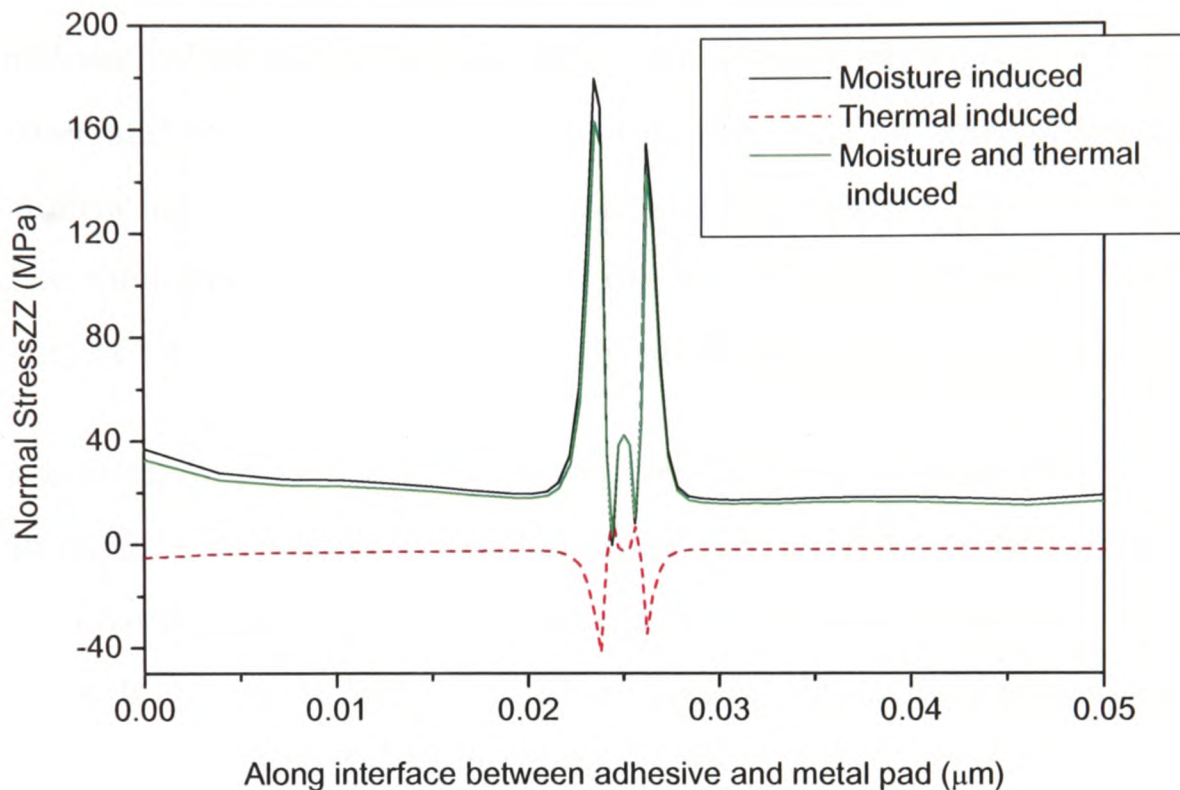
Figure 6.21: Moisture and thermal induced interfacial stresses

6.5.4 Parametric Analysis

The modelling results presented above prove that the reliability of the ACF interconnection is strongly affected by moisture during the autoclave test. In order to improve the reliability of ACF flip chip assemblies in such circumstances, a detailed parametric analysis was carried out, and the effect of the CME, Young's modulus of the adhesive matrix and the bump height on the moisture induced stresses along the interface between the conductive particle and pad metallization was analyzed.

137

6.5.4.1. Effect of the CME of the Adhesive Matrix

According to Equation (2.8), the value of hygroscopic stress is proportional to the product of CME and moisture concentration. The CME of the adhesive, β, was chosen as an example to show how the moisture property affects the reliability of the ACF flip chip assembly. The values of the normal stress σ_{yy} at the interface between the particle and the pad with different adhesive CME values were recorded at a fixed moisture concentration and the results are shown in Figure 6.22. It shows that the CME of adhesive matrix has a large effect on the stress at the interface. The interfacial stress is tripled when the adhesive CME changes from 85mm^3/g to 340mm^3/g. Therefore, high adhesive matrix CME value results in an increased possibility of joint opening.

Also according to Equation (2.8), hygroscopic stress is proportional to the moisture concentration C. In the autoclave test, moisture saturation occurred quickly so that the maximum moisture concentrations in the assembly are dictated by the materials' saturated moisture concentration, C_{sat}. Therefore, to reduce the damaging hygroscopic stress, both β and C_{sat} should be minimized.
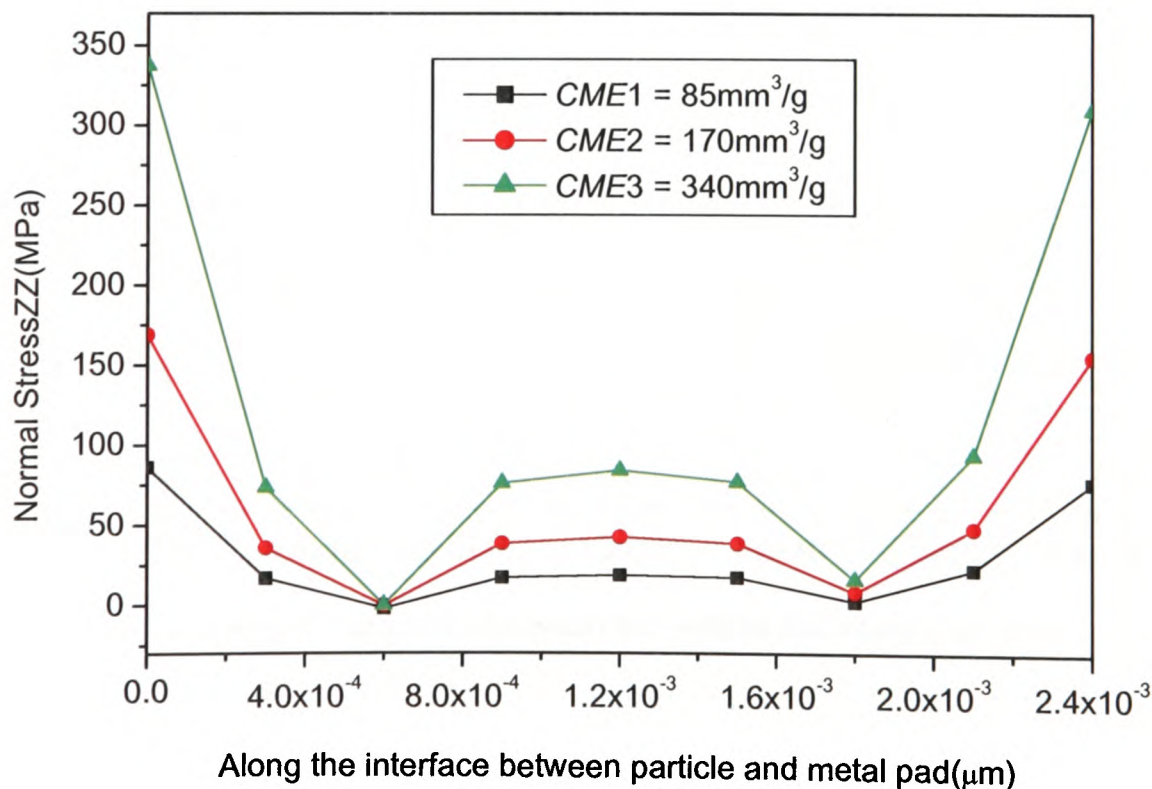
Figure 6.22: The interfacial stresses with different CME values of the adhesive matrix

6.5.4.2. Effect of the Young's Modulus of the Adhesive Matrix

Previous research work [11] revealed that ACF materials with high Young's modulus could significantly reduce the joint opening of ACA interconnections in a humid environment. To prove this and to estimate the extent at which the Young's modulus has on the reliability of ACF joints, the values of stress σ_{yy} along the particle/pad interface were predicted as shown in Figure 6.23. It is found that in general the interfacial stress increases as the Young's modulus of the adhesive increases. Since the point where the adhesive, metal pad and particle meet is regarded as the weakest along the contact, the reliability of ACF flip chip assemblies could be improved if the ACF with higher Young's modulus is used. However, the effect of the Young's modulus on the interfacial stresses is clearly not as significant as the CME values of the adhesive matrix. About 30% of the stress variation is observed when the Young's modulus changes from 800MPa to 2400MPa.
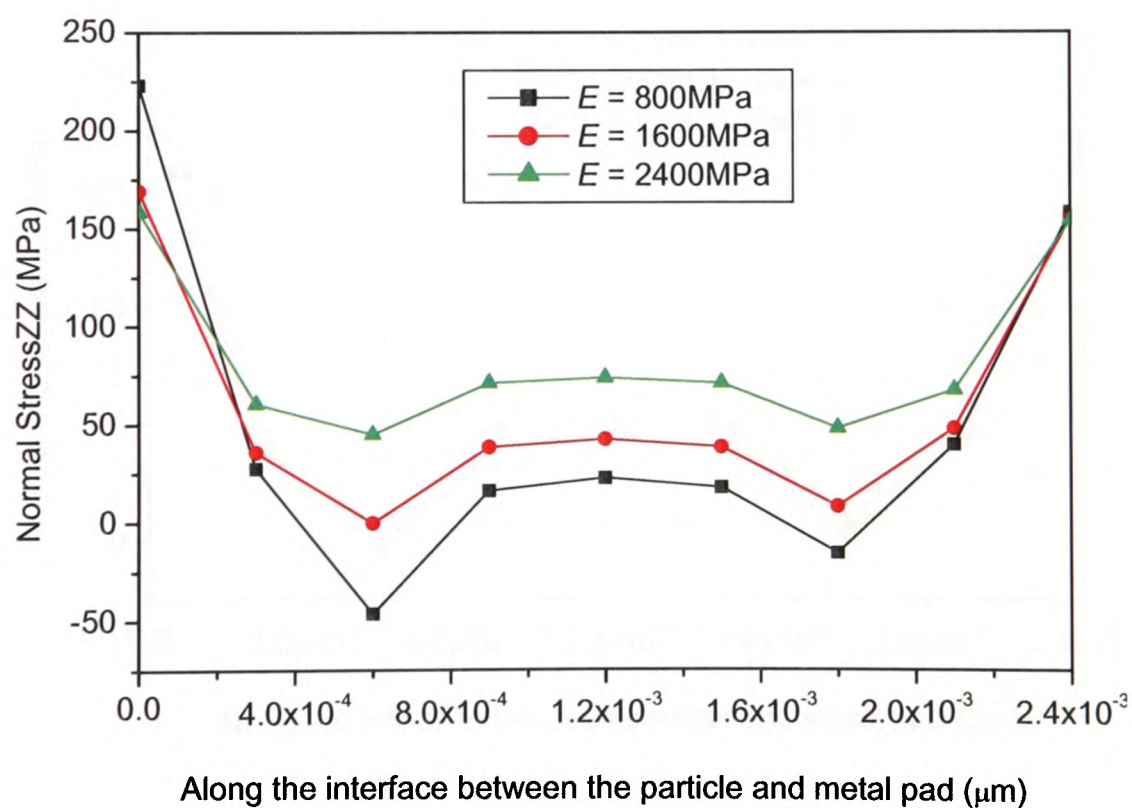
Figure 6.23: The interfacial stresses with different Young's modulus value of the adhesive matrix

139

6.5.4.3. Effect of the Bump Height

The bump height was chosen to be an example to show how geometric design parameters affected the reliability of ACF flip chip assemblies in a humid environment. Models with three different bump heights were used for this analysis. The pad height was kept at a fixed value of 17μm in all the models. The values of the stress σ_{yy} at the interface between the particle and the pad with different bump height are shown in Figure 6.24. It shows that the interfacial stress increases modestly as the bump height increases. About 20% of the stress variation is observed when the bump height changes from 6μm to 20μm. This suggests that the influence of this parameter is not as significant as the other two parameters discussed earlier. However, if thinner bumps are not difficult to achieve, then reducing the bump height is still a useful means of enhancing the reliability of the ACF flip chip assemblies in a humid environment.
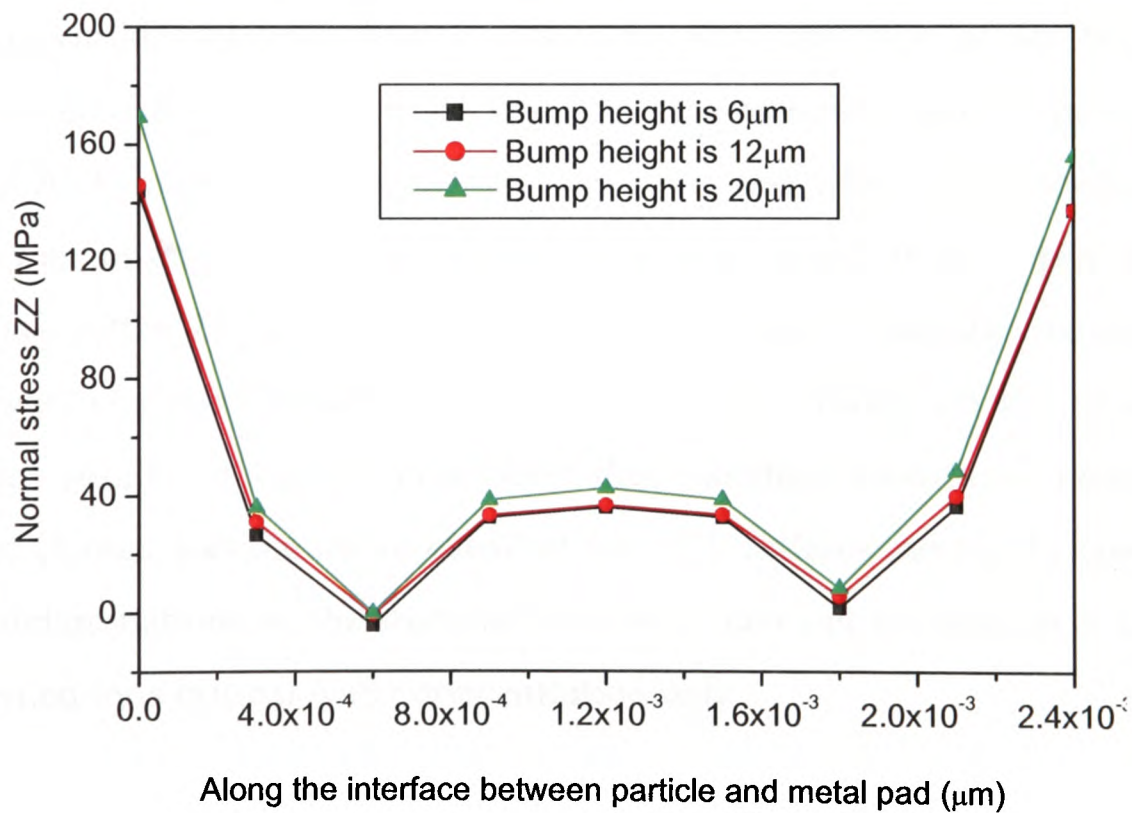
Figure 6.24: The interfacial stresses with different bump height

140

6.6 Failure Mechanisms

In the past many researchers have suggested a variety of driving forces responsible for the ACF joint failures in humid environment. These include polymer expansion due to moisture absorption, the loss of the adhesion strength [8][12], the degradation of the polymer [8], and stress corrosion and oxidation of the metal particles [9]. However, no definitive conclusion was made and no direct evidence was found to pinpoint the major cause of the electrical failures in the ACF assemblies for flip chip on flex applications.

According to the modelling results reported in this research, for an ACF flip chip on a polyimide substrate, the time to moisture saturation is strongly dependent on the moisture properties of the polyimide substrate. Most of the moisture that diffuses into the ACF layer is via the polyimide substrate rather than the perimeter of the ACF layer since the polyimide substrate is very thin. The full saturation of an ACF flip chip assembly can be expected in the first 12 hours of the autoclave test. In the experiments, 85% of the ACF joints failed in the first 24 hours test when 100% increase in joint resistance was observed in these joints. However, most of the open joints were observed only after 24 hours' test and therefore a more dramatic increase in joint resistance was observed between 24 to 96 hours' test. Based on the modelling and experimental results, it can be concluded that moisture absorption rather than the temperature change was the major cause of the ACF failures during the autoclave test. However, delaminations at the material interfaces can not be seen as a catastrophic event governed by a critical water concentration only.

Lam *et al.* [40] developed a chemical kinetic model of interfacial degradation of adhesive joints and concluded that the time to failure of an adhesive joint in a humid environment was dependent on the saturation water content, stress gradient, water concentration gradient, and exponentially dependent on the peak stress in the adhesive joint. Moreover, the loss of adhesive strength was thought to correlate directly to the interfacial moisture concentration [8][28]. According to the surface energetics, the

water layer can form at the interface between the polymer and the metal which decreases the adhesive strength of the interface. Small portion of moisture can also diffuse through the interfaces between the adhesive and the other materials if there was de-adhesion at these interfaces [110][119]. The remaining difficulty is that the rate at which moisture is delivered to the interface and the degradation of the mechanical properties of the adhesive due to moisture uptake are not well understood. Further experimental and modelling work is required to solve this problem.

In summary, the adhesive matrix and polyimide both absorb moisture easily. In the autoclave test, moisture absorption in these materials induces tensile stress that contributes to the joint opening. The moisture absorption and induced stress plays an important role in the ACF failures in the autoclave test.

6.7 Conclusions

The technique of computer modelling of moisture diffusion in multi-material assembly has been incorporated into the PHYSICA multi-physics modelling framework. A macro-micro modelling technique was applied in the hygro-mechanical analysis of an ACF flip chip assembly so that a more detailed analysis could be carried out.

It was found that the reliability performance of ACFs in assemblies of flip chip on flex substrate was strongly affected by moisture. During the autoclave test, moisture diffused mostly through the substrate into the ACF layer and the time to be fully saturated with water in the adhesive was strongly dependent on the moisture properties of polyimide substrate. Due to the CME mismatch in the system, higher stress was identified along the interface between the adhesive and the bump/pad. The predominantly tensile stress found at the interface between the conductive particle and the metallization reduced the contact area, while the thermal stress had the opposite effect. The parametric analysis suggested that the tensile stress at the particle/pad interface increased with the CME of the adhesive matrix and decreased with the

Young's modulus of the adhesive matrix. The interfacial stress showed slight increase with bump height. It is believed that higher stresses would cause more loss of contact area and therefore a larger increase in the contact resistance.

The work in this Chapter has contributed to one journal paper [128], a number of international conference papers [133][135][137] and one paper for a trade magazine [138].

Chapter 7

Conclusions and Further Work

This Chapter presents a summary of the major conclusions resulting from this research project and ideas for future work.

7.1 Conclusions

Driven by the desire to protect the environment, the electronics packaging industry is eager to replace the traditional Sn/Pb solder materials. Currently, there are several alternative materials being investigated which include lead-free solder alloys, conductive adhesives and non-conductive adhesives. Anisotropic Conductive Film (ACF) is a conductive adhesive which is gaining popularity for use in products such as flat panel Liquid Crystal Displays (LCD), Smart Cards and Disk Drives. This material is attractive as it is low cost and enables fine pitch connections, low processing temperature and satisfies environmental legislations such as RoHS.

However, the reliability performance of ACF, particularly in harsh conditions is a concern and it is widely acknowledged that further research is required in this area. This has been the focus of this PhD study. In particular, the PhD has investigated the effect of (i) solder reflow temperatures and (ii) moisture absorption on the reliability of this material. The methodology used in the study was based on both experimental techniques and finite element analysis.

Chapter 4 (Experiments) and Chapter 5 (Modelling) discuss the effect of Sn/Pb solder reflow on the stress magnitudes and failure modes in an ACF joint. The experimental results demonstrated that a subsequent solder reflow process has a substantial effect on the stress magnitudes around the ACF particles. It is clearly shown that the adhesive expands during the reflow process and this breaks the contact between the conducting particle and the pads on the chip and substrate. This also creates high stress levels at the interface between the conductive particle and the metal pads. The magnitude of this interfacial stress increases with the reflow peak temperature. This means that the reflow effect on the reliability performance is greater when moving from a Sn/Pb soldering process to a lead free soldering process.

Key design variables identified during this study are (i) adhesive CTE (ii) adhesive Young's modulus and (iii) bump height. The interfacial stress decreases when the CTE decreases and when the Young's modulus increases. It also decreases when the bump height is lower. Another finding is that ACF components when subjected to a subsequent solder reflow profile fail quicker than those that are not subjected to a reflow profile. The reliability test used in this case was autoclave test as discussed in Chapter 4.

The moisture effect on the reliability performance of ACF joints was discussed in Chapter 4 (Experiments) and Chapter 6 (Finite Element Modelling). The experimental results showed that moisture had a major effect on the reliability performance of the ACF joint. Here the measured joint resistance increased and some cracks were also observed around at the pad/adhesive/substrate interfaces using SEM.

A 3D macro-micro finite element modelling technique was adopted in order to couple the moisture effects at package and joint levels in much greater details than what has been undertaken before. The results show that the ACF assembly is fully saturated with moisture after 12 hours of autoclave test. The majority of moisture diffused into the ACF layer comes from the substrate side rather than the perimeter of the ACF. This is because the polyimide substrate is very thin and hence moisture can

145

diffuse quickly through the base of the substrate. This rate of absorption is dependent on the moisture properties of the polyimide substrate which are key parameters. As expected an increase in the moisture diffusion of the polyimide accelerates the rate at which moisture propagates into the ACF significantly.

Moisture induced stress is predicted using the micro model. Here results from the macro (package) model are used for setting up the boundary condition for the micro-model. Results from the macro model show that higher stress is found at the interface between the adhesive/substrate/pad. This is the location where cracks are always observed to occur. The stress between the conductive particle and the metallization is tensile and this indicates that moisture is swelling the adhesive which tries to move the pads away from the conductive particle – hence increasing the contact resistance. The parametric analysis shows that this interfacial stress will increase when the saturation concentration (C_{sat}) increases and/or when the bump height increases. It will decrease when the Young's modulus of the adhesive increases.

In the autoclave test there are two external forces that can result in stress and failure. These are Temperature and Moisture. This study has clearly shown that Moisture is much more severe than temperature in this test. Although the debonding of ACF joints can be caused by many factors, the stresses due to adhesive swelling are significant. This was also reported by Lam et al. [40].

7.2 Further Work

Some possible further work is discussed from two aspects: experiment and computational modelling. The overall challenges with ACFs are summarized at the end of this Chapter.

146

7.2.1 Experiments

Further experimental work is required to fully understand the failure mechanisms of ACF joints when subjected to variable service conditions. This would be analysed using combination tests that combine thermal cycling, with moisture and vibration. Like all of the joint types this is a very challenging area.

This study only tested the performance of reflowed ACF joints using the autoclave test. Further work should investigate the performance of these joints when subjected to other reliability tests based on thermal cycling or vibration to fully characterise the impact of subsequent reflow profiles on joint performance and reliability.

7.2.2 Computational Modelling

Good qualitative comparisons have been made between the finite element results and the experiments in this research. A number of assumptions have been adopted in this study. Future work should aim to address the following:

(1) Characterise the effect of the Bonding Stress on the results presented here. In this research, the stress created during the bonding process was neglected for simplicity. This should be investigated in future work.

(2) Use Visco-elastic material data for the ACF matrix. In this modelling analysis the ACF is assumed to be elastic. This was due to difficulty in obtaining suitable materials data. In future as non-linear materials data becomes available this should be built into the model.

(3) Extend the Macro-Micro modelling approach to other conductive adhesive systems. The modelling technique developed for the moisture diffusion and moisture induced stress analysis can be easily applied to study other adhesive connections such as Non-Conductive Adhesive and Isotropic Conductive Adhesive joints.

7.2.3 Future Challenges with ACAs

Based on the literature review, more research is required in the future in order to achieve wider usage of ACAs. The overall challenges with this material are concluded as follows:

- High frequency behaviour. High frequency modelling is necessary to understand the high frequency characteristics of flip chip interconnections using ACFs [121]. This is especially the case at the frequency range beyond 20GHz. The maximum current carrying capability at high frequency after exposure to various environmental tests needs to be understood.

- The co-planarity effect of the substrate on the ACA joint reliability. Generally, there are two kinds of bonding tolerance in ACA packaging. This can be (i) in-plane misalignment between the chip and the substrate, which may be translational or rotational, and (ii) co-planarity variations between the joint planes. Experimental research on the in plane misalignment of components in ACA assemblies had been carried out in previous research [123]. However, to our knowledge, there has been no previously reported detailed research into the effects of co-planarity variations. Bad co-planarity ACA packaging can be caused by the rotated chip alignment, distorted components and different height pads [124].

- Life time prediction models of ACA joints. Various aspects of the processing, manufacturing, thermal, mechanical and electrical performance and reliability testing data of the ACA material have been examined. However, there are today no methods available that can be used to predict ACA joint life. This is because many of the failure mechanisms that are not well understood [125].

Appendices

These appendices detail both the theory of mass diffusion and solid mechanics. The manner in which a material behaves is discussed and the governing mathematical equations for elasticity, plasticity and rate dependent material behaviour are outlined. The discretisation of these mathematical equations, over a computational mesh using the finite element method, is then discussed. Finally, the PHYSICA multi-physics software framework is presented and demonstrated through the analysis of a Liquid Crystal Display (LCD).

A. Differential Equation of Diffusion

Diffusion is the process by which mass is transported from one part of a system to another as a result of random molecular motions. The mathematical theory of diffusion in isotropic substances is based on the hypothesis that the rate of transfer of diffusing substance through a unit area of a section is proportional to the concentration gradient measured normal to the section, i.e.:

$$F = -D \frac{\partial C}{\partial x} \tag{A.1}$$

Where F is the rate of transfer per unit area of the section, C is the concentration of diffusing substance, x is the space co-ordinate measured normal to the section, and D is called the diffusion coefficient and can be reasonably taken as constant in most cases [111]. The fundamental differential equation of diffusion in an isotropic medium which is known as the Fick's second law of diffusion can be derived from Equation (A.1) as follows.
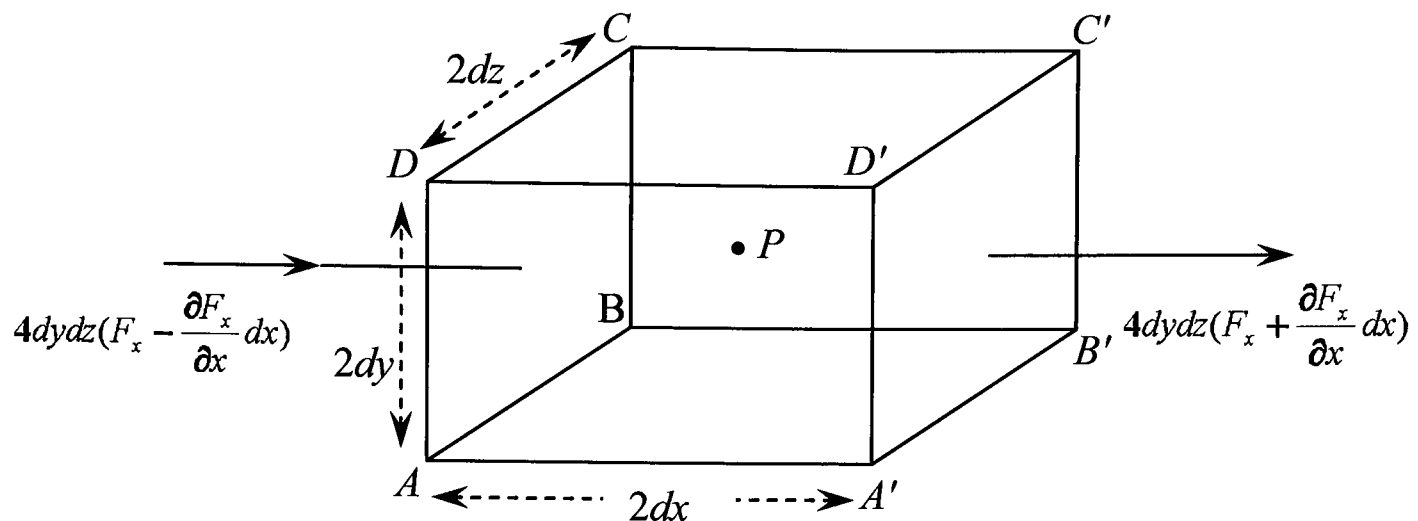
Figure A.1: Element of volume

Consider an element of volume in the form of a rectangular parallelepiped whose sides are parallel to the axes of coordinates as shown in Figure A.1, the contribution to the rate of increase of diffusing substance in the element from the face *ABCD* to *A'B'C'D'* is equal to

$$-8dxdydz\frac{\partial F_x}{\partial x}$$

Similarly from the other faces we obtain:

$$-8dxdydz\frac{\partial F_y}{\partial y} \text{ and } -8dxdydz\frac{\partial F_z}{\partial z}$$

Since the rate at which the amount of diffusing substance in the element increases is also given by $8dxdydz\frac{\partial C}{\partial t}$, hence we can get:

$$\frac{\partial C}{\partial t}+\frac{\partial F}{\partial x}+\frac{\partial F}{\partial y}+\frac{\partial F}{\partial z}=0$$

If the diffusion coefficient is a constant in a material, the above equation can be written as follows which is known as Fick's second law of diffusion:

$$\frac{\partial C}{\partial t} = D\left(\frac{\partial^2 C}{\partial x^2} + \frac{\partial^2 C}{\partial y^2} + \frac{\partial^2 C}{\partial z^2}\right)$$

(A.2)

The moisture uptake in one material can be predicted by using the above equation [11][12][114]. When used for moisture prediction, C (g/mm^3) is the moisture concentration which describes how much moisture is absorbed in the material; D (mm^2/s) is the coefficient of moisture diffusion which describes how fast the mass diffuses.

The general transport equation for a scalar variable ϕ can be expressed as:

$$\frac{\partial\left(T_\phi\phi\right)}{\partial t} + div\left(C_\phi \underline{u}\phi\right) = div\left\{D_\phi grad\left(\phi\right)\right\} + S_\phi$$

(A.3)

where T_ϕ, C_ϕ are the coefficients of the transient and convection term respectively, D_ϕ is the diffusion coefficient and S_ϕ stands for the source term. ϕ could stand for any physical quantity that obeys the transportation law.

Each of the terms in the general conservation equation represents a different phenomenon or aspect of quantity transportation. The first term on the left side of Equation is the transient term and the second is the convection term. On the right side of the equation, there are the diffusion term and the source term respectively. Depending on the nature of analyzing process, all or just some of these terms will exist in the equation to govern the corresponding physical phenomenon.

When ϕ stands for the temperature in the heat transfer equation, the equation governing the heat transfer phenomenon can be written as:

$$\frac{\partial\left(\rho c_p T\right)}{\partial t} + div\left(\rho c_p \underline{u} T\right) = div\left(kgrad\left(T\right)\right) + S_\phi \qquad (A.4)$$

where ρ is the density, c_p is the specific heat, k is the thermal conductivity and the conserved variable is temperature T. If without the convection and source terms, Equation (A.4) can be written as:

$$\frac{\partial\left(\rho c_p T\right)}{\partial t} = div\left(kgrad\left(T\right)\right)$$

or

$$\frac{\partial\left(\rho c_p T\right)}{\partial t} = k\left(\frac{\partial^2 T}{\partial x^2} + \frac{\partial^2 T}{\partial y^2} + \frac{\partial^2 T}{\partial z^2}\right) \qquad (A.5)$$

Considering the analogy of the Equation (A.5) with Equation (A.2), the heat governing Equation (A.5) can be used for the moisture prediction in one material based on the transformation of the transient and diffusion coefficients as listed in Table A.1.

Table A.1: The relationship of the thermal and moisture simulation

Properties	Moisture	Thermal
Field variable	Concentration (C)	Temperature (T)
Density	1	ρ
Conductivity	D	k
Specific Heat	1	c_p

B. Material Behaviours

The material behaviours in solid mechanics can be classified into three categories, material linearity, rate independent material non-linearity and rate dependent material

non-linearity. Some of the most important cases are described for each category in the following sections.

B.1 Elasticity

An elastic material returns to its original shape when external forces that deformed it have been removed. The material can be classified as both linear and non-linear. With a linear elastic material, the strains and displacements produced are all directly proportional to the applied forces. The general form of the constitutive equation that describes a linear elastic material is:

Stress = E × Strain,

Where E is a constant and called Young's modulus or the modulus of elasticity of the material. Most metallic materials, when subjected to sufficiently small strains, exhibit linear elasticity [105][139].

Non linear elasticity is defined when the stress is not linearly related to the strain, in this case the deformation is still recoverable and the material returns to its original shape and no energy is lost from the system.

B.2 Plasticity

When a material deforms plastically its does not return to its original shape when the external forces are removed. The material remains permanently deformed and energy, generally in terms of heat is lost in the system. The stress at which plastic deformation begins is called the yield point. At stresses below this yield point the material will deform elastically. When the stress is above this threshold, a combination of elastic and plastic deformation occurs. Most engineering materials in solid mechanics exhibit elasto-plastic behaviour. Figure B.1a illustrates the stress-strain behaviour for an elastic, perfectly plastic material and Figure B.1b for an elastic, linear work-hardening material. Work hardening, *i.e.* strain hardening, is an increase in mechanical strength due to plastic deformation.
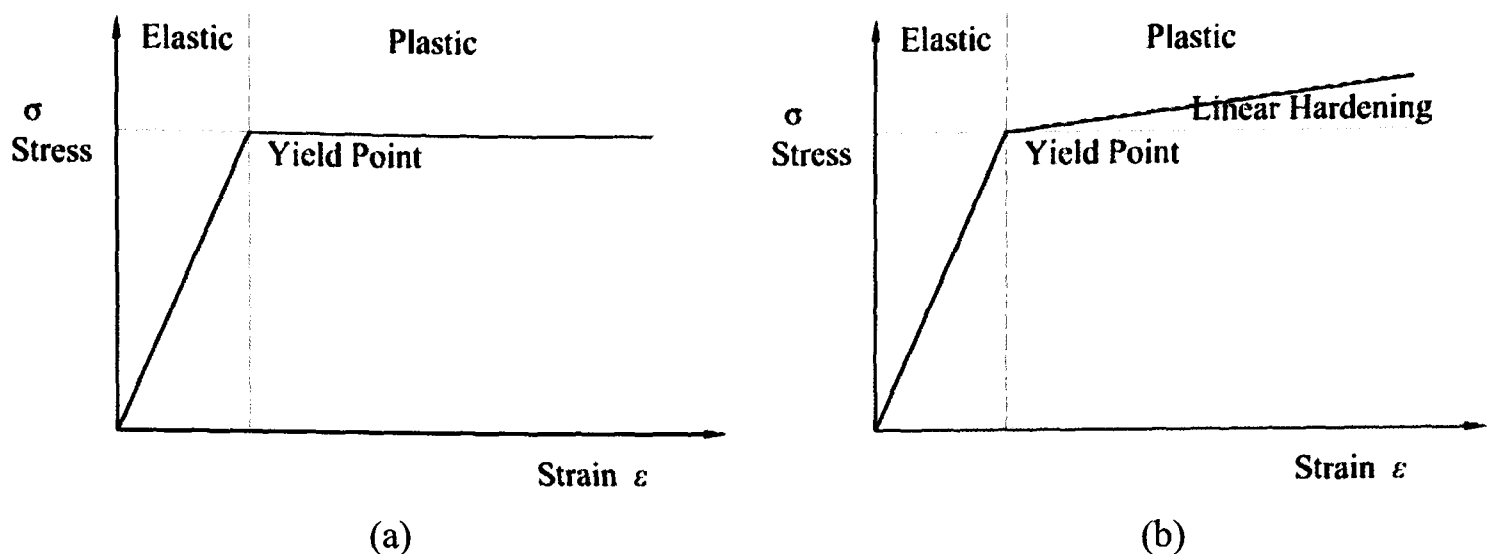
Figure B.1: Plastic material behaviour. (a) Elastic, perfectly plastic and (b) elastic, linear work hardening

B.3 Rate Dependent Material Behaviour

Both of the above descriptions of material behaviour have ignored the effect of time or the rate at which a force is applied to a material. This will affect the stress-strain behaviour of the material both during elastic and plastic deformation. The contribution of time also describes how a material creeps and stress relaxes over time. The importance of time is dependent on the material and loading application be analysed and sometimes it can be ignored.

Visco-Elastic constitutive laws describe the rate dependency behaviour of linear or non-linear elastic materials such as polymers, and rubbers, etc. This behaviour is exploited for smart and shape memory materials, which consists of the full history of the viscous strain development [140].

Visco-Plastic constitutive laws describe the rate dependency behaviour of linear or non-linear plastic materials such as metals. This behaviour always results in permanent deformation of the material and possesses the yield criterion as described for rate independent plasticity. Materials exhibiting visco-plastic behaviour are assumed to be

rate independent below the yield point and rate dependent when the yield point is exceeded.

C. Finite Element Method (FEM)

The finite element method [141][142][143] is a numerical technique for obtaining solutions to a wide variety of engineering problems. In more and more engineering situations today, it is increasingly necessary to use modelling techniques such as the finite element method.

The label 'finite element method' first appeared in the 1960s, when it was used by Clough [145] in a paper on plane elasticity problems. However, the ideas behind the method date back much further. In the 1940s, Hrennikoff [146] and McHenry [147] made the first contribution to the development of finite element method by solving stresses in solids using one-dimensional elements. In 1956, Turner *et al.* [148] proposed the numerical procedures of the direct stiffness method and two-dimensional finite elements.

After more than 50 years of development, the finite element method now has received widespread use in engineering and is applicable to many application areas such as structural analysis, heat transfer, fluid flow and electromagnetic etc.

The solution of a continuum problem using FEM always follows an orderly step-by-step process [144]. The first step is to **discretize the continuum** or solution domain into a mesh called the finite elements. The more elements that are used to model the solution domain, the better the accuracy of the results. However, increasing the number of elements leads to high computational expenses.

The second step is to **select the interpolation functions** to approximate the variation of the variables over each element. Often, although not always, polynomials

are selected as interpolation functions for the variables because they are easy to integrate and differentiate.

The third step is to **calculate the matrices** that represent each element. Once the finite element is established, the matrix equations expressing the properties of the individual elements are determined. For this task, the weighted residual approach also called Galerkin's method is used.

The fourth step is to **assemble all of the matrices into a global matrix.** To find the properties of overall system modelled by the network of elements, the important thing is to combine the matrix expressions expressing the behaviour of the elements and form the matrix equations expressing the behaviour of the entire solution region. The matrix equations for the system have the same form as the equations for an individual element except that they contain many more terms because they include all the nodes that make up the computational mesh.

The last step is to **solve the global system of equations.** The assembly process of the proceeding step gives a set of simultaneous equations that can be solved to obtain unknown nodal values of the field variables. Both direct (*i.e.* Gaussin Elemination) and iterative (*i.e.* Gauss-Seidel or Conjugate Gradient) solvers can be used to solve this global matrix. For non-linear problems where stress is a function of both the stain and stress states numerical techniques such as the Newton-Raphson method can be used in addition to direct and iterative matrix solvers.

Since the finite element solution technique is a numerical procedure, it is necessary to assess the accuracy of the final solution. If the accuracy criteria are not met, the numerical solution has to be repeated with refined solution parameters (such as finer meshes) until a sufficient accuracy is reached.

C.1 Linear Elasticity

A very important application area for finite element analysis is the elastic analysis of solids and structures. This is where the first practical finite element procedures were applied and where the finite element method has obtained its primary impetus of development. In this section, the procedure of using the finite element method to solve the mathematical model of elastic deformation due to both external mechanical forces and thermal, hygroscopic loads is explained.

C.1.1 Equilibrium Equations

The equilibrium equations govern the conservation of force. For a time independent static analysis these equations are:

$$\frac{\partial \sigma_{xx}}{\partial x} + \frac{\partial \sigma_{xy}}{\partial y} + \frac{\partial \sigma_{xz}}{\partial z} = f_x$$

$$\frac{\partial \sigma_{xy}}{\partial x} + \frac{\partial \sigma_{yy}}{\partial y} + \frac{\partial \sigma_{yz}}{\partial z} = f_y \qquad\qquad (C.1)$$

$$\frac{\partial \sigma_{xz}}{\partial x} + \frac{\partial \sigma_{yz}}{\partial y} + \frac{\partial \sigma_{zz}}{\partial z} = f_z$$

where σ_{ij} and f_i are the components of stress and the body forces acting in the direction represented by i. For an isotropic homogeneous material undergoing small strains, the stress is related to the elastic strains via the linear elastic constitutive equation which in matrix form is

$$\sigma = \mathbf{D} \varepsilon^{(e)} \qquad\qquad (C.2)$$

where for an isotropic material the stress σ and elastic strain $\varepsilon^{(e)}$ are represented by vectors of six components:

$$\sigma = \begin{bmatrix} \sigma_{xx} & \sigma_{yy} & \sigma_{zz} & \tau_{xy} & \tau_{yz} & \tau_{zx} \end{bmatrix}^{\mathrm{T}}$$

$$\varepsilon^{(e)} = \begin{bmatrix} \varepsilon_{xx}^{(e)} & \varepsilon_{yy}^{(e)} & \varepsilon_{zz}^{(e)} & \gamma_{xy}^{(e)} & \gamma_{yz}^{(e)} & \gamma_{zx}^{(e)} \end{bmatrix}^{\mathrm{T}}$$

The elastic material matrix **D** contains the elastic material terms which in three dimensions are given by:

$$\mathbf{D} = \frac{E}{(1+\mu)(1-2\mu)} \begin{bmatrix} 1-\mu & \mu & \mu & 0 & 0 & 0 \\ \mu & 1-\mu & \mu & 0 & 0 & 0 \\ \mu & \mu & 1-\mu & 0 & 0 & 0 \\ 0 & 0 & 0 & \dfrac{1-2\mu}{2} & 0 & 0 \\ 0 & 0 & 0 & 0 & \dfrac{1-2\mu}{2} & 0 \\ 0 & 0 & 0 & 0 & 0 & \dfrac{1-2\mu}{2} \end{bmatrix}$$

where E and μ are the Young's modulus and Poisson's ratio, respectively. This is the standard matrix form of the constitutive relationship for a linear elastic material as described in many standard textbooks.

The total strains are related to the displacement via the following equation:

$$\varepsilon^{(tot)} = \mathbf{Ld} \tag{C.3}$$

where $\varepsilon^{(tot)}$ is the total strain and $\mathbf{d} = (u \quad v \quad w)^{\mathrm{T}}$ is the displacement vector representing the displacements in the x, y and z directions, respectively. The matrix L contains the differential operators and is given by:

$$\mathbf{L} = \begin{bmatrix} \dfrac{\partial}{\partial x} & 0 & 0 \\[2mm] 0 & \dfrac{\partial}{\partial y} & 0 \\[2mm] 0 & 0 & \dfrac{\partial}{\partial z} \\[2mm] \dfrac{\partial}{\partial y} & \dfrac{\partial}{\partial x} & 0 \\[2mm] \dfrac{\partial}{\partial z} & 0 & \dfrac{\partial}{\partial x} \\[2mm] 0 & \dfrac{\partial}{\partial z} & \dfrac{\partial}{\partial y} \end{bmatrix}$$

The constitutive equation states that the stresses are dependent on the elastic strains. These elastic strains are dependent on the total stain $\varepsilon^{(tot)}$, thermal strain $\varepsilon^{(th)}$, hygroscopic strain $\varepsilon^{(hy)}$ and plastic strain $\varepsilon^{(p)}$, therefore:

$$\varepsilon^{(e)} = \varepsilon^{(tot)} - \varepsilon^{(th)} - \varepsilon^{(hy)} - \varepsilon^{(p)} \qquad (C.4)$$

Generally, the plastic strain is a function of the stress and the temperature. For simplicity, the plasticity effect is neglected here, i.e. $\varepsilon^{(p)} = 0$. The thermal strains are given by:

$$\varepsilon^{(th)} = \alpha \Delta T$$

where $\alpha = (\alpha_1, \alpha_2, \alpha_3, 0, 0, 0)$ is the vector of coefficients of thermal expansion and ΔT is the thermal load (the temperature change). The α_1, α_2 and α_3 represent the thermal expansion coefficients in x, y and z direction respectively, and the values for them are the same for an isotropic material but can be different for an anisotropic material.

Similarly, the hygroscopic strains are given by:

$$\varepsilon^{(hy)} = \beta C$$

where $\beta = (\beta_1, \beta_2, \beta_3, 0, 0, 0)$ is the vector of coefficients of moisture expansion, and C is the moisture concentration. The β_1, β_2 and β_3 represent the moisture expansion coefficients in x, y and z direction respectively, and the values for them are the same for an isotropic material but can be different for an anisotropic material.

C.1.2 Discretization of Solution Domain

In the finite element method, the geometric domain is divided into a number of simple sub-regions which are called elements or mesh. The fixed points in the element defining their vertices are called nodes. These elements are connected only at the node points in the domain and on the element boundaries.

Figure C.1 shows a 2D domain meshed with two quadrilateral and four triangle elements. Each mesh element can be associated with a different material and temperature load and hence will have material properties such as a modulus and temperature associated with it. For a solid mechanics problem the finite element method firstly solves the displacements of the mesh at the nodal points and then the values for stress and strain at points within each mesh element.
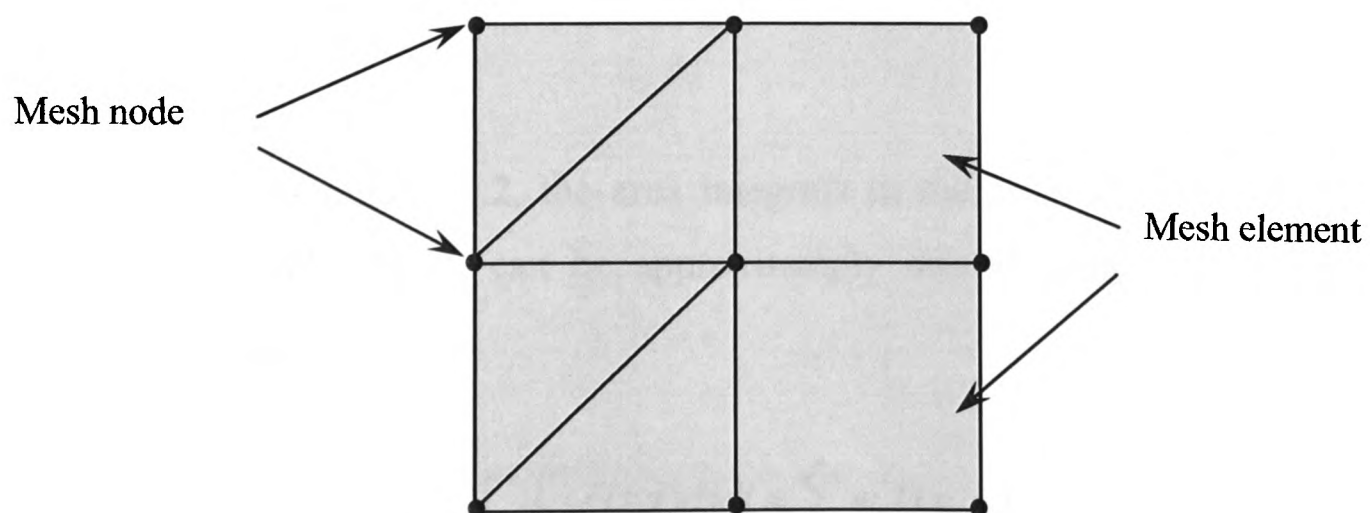
Figure C.1: Mesh elements and mesh nodes

In the FEM, the governing equations of equilibrium are integrated over each mesh element. The volume integrals in the three dimensional, or the area integrals in the two dimensional space can be approximated by using numerical integration techniques such as the Gauss quadrature. The discretized equations are delivered by using the so-called reference elements which represent the mesh elements in a local co-ordinate system (s, t) as shown in Figure C.2 [149].

(a) Global element   (b) Reference element
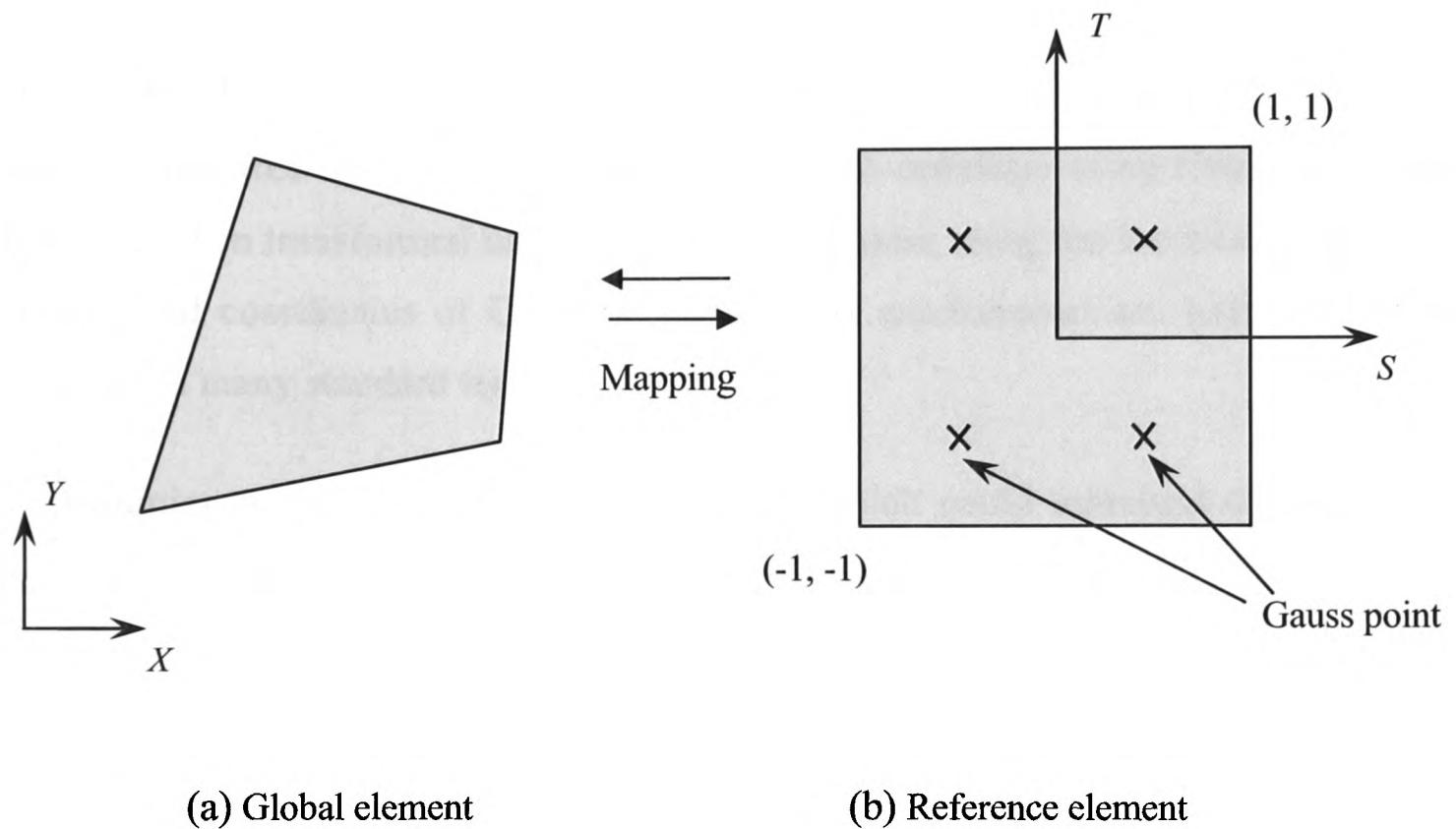
Figure C.2: Mesh element in global and local coordinates

For example, in Figure C.2, the area integrals in the local coordinate system as regards to a variable $f(s,t)$ can be approximately solved using Gauss quadrature technique as follows:

$$\int_{-1}^{+1} \int_{-1}^{+1} f(s,t)\,ds\,dt \approx \sum_{i=1}^{n} w_i f(s_i, t_i)$$

where n is the number of the Gauss points used in the approximation, w_i is the weight of the point in the sum and (s_i, t_i) represents the coordinates of each Gauss point.

The corresponding variable $f(x, y)$ in the global system can be calculated using:

$$I = \int f(x, y)\, dx\, dy = \int_{-1}^{1}\int_{-1}^{1} f(s, t)|J|\, ds\, dt = \sum_{i=1}^{n} w_i f(s_i, t_i)|J|\big|_{(s_i, t_i)} \qquad (C.5)$$

where $|J|$ is the determinant of the Jacobian matrix for the particular mesh element. In this way, the area integral is calculated in local co-ordinates using Gauss quadrature firstly and then transformed back to global coordinates using the Jacobian matrix. The weights and coordinates of Gaussian points on a quadrilateral are well defined and available in many standard textbooks [108].

Assuming a variable ϕ and its derivatives which could represent displacements, etc., can be approximated anywhere within a mesh element via:

$$\phi(s, t, u) = \sum_{i=1}^{m} N_i(s, t, u)\phi_i = N\phi$$

$$\frac{\partial \phi(s, t, u)}{\partial k} = \sum_{i=1}^{m} \frac{\partial N_i(s, t, u)}{\partial k}\phi_i, \quad k = s, t, u \qquad (C.6)$$

where m is the number of nodes making up a mesh element and $N_i(s, t, u)$ is the shape function. For example, for bilinear quadrilaterals, these shape functions are:

$$N_1(s, t) = 0.25(1 + s)(1 + t) \qquad N_2(s, t) = 0.25(1 - s)(1 + t)$$
$$N_3(s, t) = 0.25(1 - s)(1 - t) \qquad N_4(s, t) = 0.25(1 + s)(1 - t)$$

And for eight-node bricks, these shape functions are:

$$N_1(s,t,u) = 0.125(1+s)(1+t)(1+u) \qquad N_2(s,t,u) = 0.125(1-s)(1+t)(1+u)$$
$$N_3(s,t,u) = 0.125(1-s)(1+t)(1-u) \qquad N_4(s,t,u) = 0.125(1+s)(1+t)(1-u)$$
$$N_5(s,t,u) = 0.125(1+s)(1-t)(1+u) \qquad N_6(s,t,u) = 0.125(1-s)(1-t)(1+u)$$
$$N_7(s,t,u) = 0.125(1-s)(1-t)(1-u) \qquad N_8(s,t,u) = 0.125(1+s)(1-t)(1-u)$$

For the eight node brick mesh element, the displacement vector for ϕ is $\mathbf{d} = (u_1, v_1, w_1, \dots\dots u_8, v_8, w_8)^{\mathrm{T}}$. The shape function matrix $\mathbf{N}$ for the eight node brick element is given by:

$$\mathbf{N} = \begin{bmatrix} N_1 & 0 & 0 & N_2 & 0 & 0 & \dots & N_8 & 0 & 0 \\ 0 & N_1 & 0 & 0 & N_2 & 0 & \dots & 0 & N_8 & 0 \\ 0 & 0 & N_1 & 0 & 0 & N_2 & \dots & 0 & 0 & N_8 \end{bmatrix}$$

For other mesh elements including triangles, wedges and tetrahedrals, different shape functions would apply.

The integrated form of the equilibrium equations will contain first-order derivatives of displacements which can be approximated in local coordinates by using Equation (C.6). To map these derivatives back to global coordinates the following transformation is used:

$$\begin{bmatrix} \dfrac{\partial N_i}{\partial x} \\[1.5ex] \dfrac{\partial N_i}{\partial y} \\[1.5ex] \dfrac{\partial N_i}{\partial z} \end{bmatrix} = \begin{bmatrix} \dfrac{\partial x}{\partial s} & \dfrac{\partial y}{\partial s} & \dfrac{\partial z}{\partial s} \\[1.5ex] \dfrac{\partial x}{\partial t} & \dfrac{\partial y}{\partial t} & \dfrac{\partial z}{\partial t} \\[1.5ex] \dfrac{\partial x}{\partial u} & \dfrac{\partial y}{\partial u} & \dfrac{\partial z}{\partial u} \end{bmatrix}^{-1} \begin{bmatrix} \dfrac{\partial N_i}{\partial s} \\[1.5ex] \dfrac{\partial N_i}{\partial t} \\[1.5ex] \dfrac{\partial N_i}{\partial u} \end{bmatrix}$$

where the 3×3 matrix above represents the Jacobian matrix [J] for the mesh element. All entries in the Jacobian can be calculated using Equation (C.6). For example, at a specific point in the local coordinate system (s, t, u), the derivative of x with respect to s is:

$$\frac{\partial x}{\partial s} = \sum_{i=1}^{m} \frac{\partial N_i}{\partial s} X_i$$

where X_i are the x co-ordinates of the nodes of the corresponding mesh element in the global coordinate. Similar expressions can be obtained for the derivative of y with respect to t and the derivative of z to u.

C.1.3 Discretization of Equilibrium Equations

The equilibrium Equations (C.1) can also be expressed in tensor format as:

$$\frac{\partial \sigma_{ij}}{\partial x_j} = f_i$$

The finite element method integrates the above equations over the mesh elements and uses the approximations detailed above for the space and physical properties to transform the above partial differential equations into a set of algebraic equations which can be solved using matrix solvers and computers.

The Galerkin weighted residual procedure requires that the overall residual R_Ω, after substituting the approximations into the integral of the equilibrium equations, for the whole domain to be zero, i.e.

$$R_\Omega = \int_\Omega W \left(\frac{\partial \sigma_{ij}}{\partial x_j} - f_i \right) d\Omega = 0 \qquad \text{(C.7)}$$

where W are the weighting functions and Ω is the volume of the domain. Considering the x-direction equilibrium equation in weighted residual form gives:

$$\int_\Omega W \left(\frac{\partial \sigma_{xx}}{\partial x} + \frac{\partial \sigma_{xy}}{\partial y} + \frac{\partial \sigma_{xz}}{\partial z} - f_x \right) d\Omega = 0 \qquad \text{(C.8)}$$

Using the product rule of differentiation, the above integral for term σ_{xx} becomes

$$\int_\Omega \left(W \frac{\partial \sigma_{xx}}{\partial x} \right) d\Omega = \int_\Omega \frac{\partial (W \sigma_{xx})}{\partial x} d\Omega - \int_\Omega \frac{\partial W}{\partial x} \sigma_{xx} d\Omega \qquad (C.9)$$

In Equation (C.9), the divergence theorem is used to transform the integral equation by replacing the volume integrals with the corresponding integral over the boundary of the volume domain. If Γ devotes the boundary of the control volume Ω and the $\mathbf{n} = (n_x, n_y, n_z)$ is the outward normal vector at the boundary surface, then:

$$\int_\Omega \frac{\partial (W \sigma_{xx})}{\partial x} d\Omega = \oint_\Gamma W \sigma_{xx} n_x d\Gamma$$

Similar expressions are obtained for the σ_{xy}, σ_{xz} terms. The following integral representation for the equilibrium equation in the x-direction can be reached.

$$-\int_\Omega \left(\frac{\partial W}{\partial x} \sigma_{xx} + \frac{\partial W}{\partial y} \sigma_{xy} + \frac{\partial W}{\partial z} \sigma_{xz} + W f_x \right) d\Omega + \oint_\Gamma W \left(\sigma_{xx} n_x + \sigma_{xy} n_y + \sigma_{xz} n_z \right) d\Gamma = 0$$

Therefore, the equilibrium Equation (C.7) can be written as:

$$-\int_\Omega \frac{\partial W}{\partial x} \sigma_{ij} d\Omega + \oint_\Gamma W \sigma_{ij} \cdot n_j d\Gamma = \int_\Omega W f_i d\Omega$$

which in the matrix form is:

$$-\int_\Omega \mathbf{L}^T \mathbf{W} \sigma d\Omega + \oint_\Gamma \mathbf{W} \sigma \cdot \mathbf{n} d\Gamma = \int_\Omega \mathbf{W} \mathbf{f} d\Omega \qquad (C.10)$$

With respect to each mesh, and from Equation (C.2) and Equation (C.4), the stress can be expressed as a function of the total, thermal and hygroscopic strains:

$$\sigma = \mathbf{D} \left(\varepsilon^{(tot)} - \varepsilon^{(th)} - \varepsilon^{(hy)} \right) \qquad (C.11)$$

If Equation (C.3) is used to substitute the total strain into Equation (C.11) and also take into account the relationship $\mathbf{d} = \mathbf{N}\mathbf{u}$ between the displacement vector at a point ($\mathbf{d}$) and the nodal displacement vector ($\mathbf{u}$), the following stress-displacement relationship in matrix form is derived:

$$\sigma = \mathbf{D}\mathbf{L}\mathbf{N}\mathbf{u} - \mathbf{D}\varepsilon^{(th)} - \mathbf{D}\varepsilon^{(hy)}$$

If $\mathbf{B} = \mathbf{L}\mathbf{N}$ and by substituting the stress in Equation (C.10) using the above relationship, it can be expressed in terms of the nodal displacement $\mathbf{u}$ for each mesh element control volume:

$$-\int_{\Omega}\mathbf{L}^{\mathrm{T}}\mathbf{W}\left(\mathbf{D}\mathbf{B}\mathbf{u} - \mathbf{D}\varepsilon^{(th)} - \mathbf{D}\varepsilon^{(hy)}\right)d\Omega + \oint_{\Gamma}\mathbf{W}\left(\mathbf{D}\mathbf{B}\mathbf{u} - \mathbf{D}\varepsilon^{(th)} - \mathbf{D}\varepsilon^{(hy)}\right)\cdot\mathbf{n}d\Gamma = \int_{\Omega}\mathbf{W}\mathbf{f}d\Omega$$

The Galerkin finite element approach takes the weighting functions $\mathbf{W}$ equal to the shape functions for the mesh element ($\mathbf{W} = \mathbf{N}^{\mathrm{T}}$) and zero elsewhere. For the internal adjacent mesh element the surface integral balances and does not contribute explicitly in the discretized equation for displacement. The surface integral contributes to the mesh element at the boundary of the domain. It is approximated by using the specified boundary conditions. The Galerkin finite element method expresses the discretized equation for an internal mesh element with volume V as:

$$-\int_{V}\mathbf{B}^{\mathrm{T}}\mathbf{D}\mathbf{B}\mathbf{u}dV = \int_{V}\mathbf{N}^{\mathrm{T}}\mathbf{f}dV - \int_{V}\mathbf{B}^{\mathrm{T}}\mathbf{D}\varepsilon^{(th)}dV - \int_{V}\mathbf{B}^{\mathrm{T}}\mathbf{D}\varepsilon^{(hy)}dV \qquad (\text{C.}12)$$

This equation represents the discretized form of equilibrium equations for a single element and can be written in the form:

$$\mathbf{A}^{e}\mathbf{u} = \mathbf{b}^{e}$$

The above volume integrals are calculated in local coordinates using Gauss quadrature and transformed back to global coordinates using the Jacobian matrix. Hence for $\mathbf{A}^{e}$ we have:

$$-\int_V \mathbf{B}^{\mathbf{T}}\mathbf{DB}dV = -\int_{-1}^{+1}\int_{-1}^{+1}\int_{-1}^{+1}\mathbf{B}^{\mathbf{T}}\mathbf{DB}|J|dsdtdu$$

where $|J|$ is the determinant of the Jacobian matrix for this mesh element.

Boundary conditions are incorporated into the finite element procedure by reintroducing the surface integral into the formulation for the control volumes whose faces lie on the boundary of the domain. The following integral is added to the right side of Equation (C.12) to include boundary conditions in a general way.

$$-\int_\Gamma \mathbf{N}^{\mathbf{T}}\mathbf{DBu}\cdot\mathbf{n}d\Gamma$$

where Γ represents the boundary of domain. The boundary conditions can be in the form of prescribed displacement, force or pressure.

C.1.4 Solution Procedure

The contributions from each mesh element to each displacement degree of freedom i.e. (u, v, w) at each node are combined to form the following matrix system for the whole domain:

$$\mathbf{Ax} = \mathbf{b} \tag{C.13}$$

where **A** is a banded systems matrix, containing the coefficients relating each degree of freedom. $\mathbf{x} = (u_1, v_1, w_1, \ldots, u_n, v_n, w_n)^{\mathbf{T}}$ is the vector containing all degrees of freedom and **b** represents the source terms.

In FEM, Equation (C.13) is obtained by assembling contributions from all the elements, where:

$$\mathbf{A} = \sum_{ele=1}^{totele}\left[\int_V -\mathbf{B}^{\mathbf{T}}\mathbf{DB}dV\right]_{ele}$$

$$b = \sum_{ele=1}^{totele} \left[\int_v \mathbf{N}^T \mathbf{f} dV - \int_V \mathbf{B}^T \mathbf{D} \varepsilon^{(th)} dV - \int_V \mathbf{B}^T \mathbf{D} \varepsilon^{(hy)} dV \right]_{ele} - \int_\Gamma \mathbf{N}^T \mathbf{DBu} \cdot \mathbf{n} d\Gamma \quad (C.14)$$

where *toele* is the total number of mesh elements and the *sum* indicates the assembling contributions from all elements.

The Equation (C.13) represents the final sets of discretised equations that results from the finite element discretisation of the equilibrium equations. This linear system of equations can be solved by matrix solvers. The variables being solved at this stage are the components of displacement in the x, y, and z directions. These are solved at the nodal locations. After this the equations for strain and stress are solved usually at the gauss points within each element.

C.2 Elasto Visco-Plasticity

The finite element method has been used for a number of years to solve plastic material behaviour. This section describes the numerical procedure used to solve elastic visco-plastic material behaviour. This is a rate dependent material behaviour model, which can also recover the rate-independent elasto-plastic model as solution time approaches infinity [151].

C.2.1 Elasto-Viscoplasticity Material Model

The basic physical features of the elasto-viscoplastic model can be introduced by means of a one dimensional mechanical system as depicted in Figure C.3. The system consists of a spring with elastic properties, serially coupled to a friction slider and a dashpot, which comprise the viscoplastic contribution. The friction slider is inactive if the stress is below the yield point, resulting in no viscoplastic deformation. The dashpot reflects the viscous properties of viscoplasticity when the slider is active. The total deformation then consists of the elastic displacement in the spring plus the displacement of the viscous dashpot.
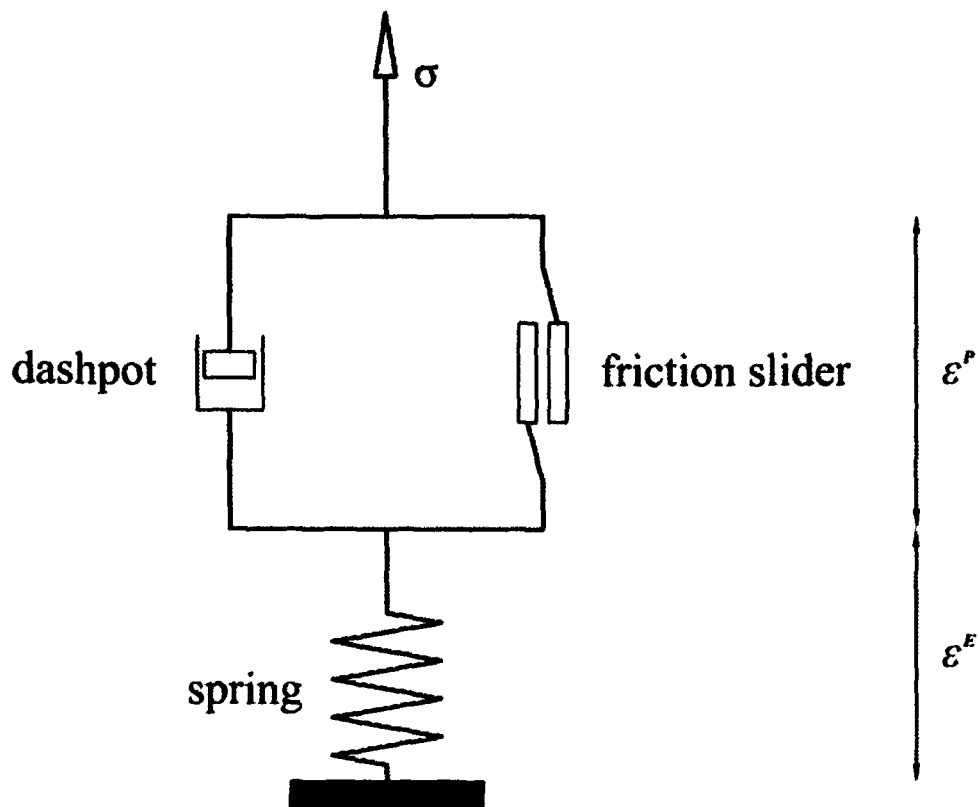
Figure C.3: Sketch of a mechanical model that reflects the basic physics of elasto-viscoplastic deformation

Equilibrium of any part of the structure implies that the sum of the normal stresses is σ every where. The onset of viscoplastic deformation occurs when $\sigma = C_Y$, where C_Y is the yield stress. For $\sigma < C_Y$ the deformation is purely elastic, whereas for $\sigma \geq C_Y$, the material is in a combined elasto-viscoplastic state. The friction slider develops an internal stress:

$$\sigma^P = \begin{cases} C_Y, \sigma \geq C_Y \\ \sigma, \quad \sigma < C_Y \end{cases}$$

When the friction slider is active ($\sigma > C_Y$), the dashpot experiences a stress $\sigma^D = \sigma - \sigma^P$, which is related to the viscoplastic strain rate $\dot{\varepsilon}^P$ by the constitutive relation $\sigma^D = \mu\dot{\varepsilon}^P$, in analogy with viscous fluid flow, μ is a viscosity coefficient.

The constitutive law for the viscoplastic part of structure can be expressed as:

$$\dot{\varepsilon}^P = \left\langle \Phi(F) \right\rangle \frac{1}{\mu} \sigma^D$$

where $F = \sigma - C_Y$, the notation $\left\langle \Phi(F) \right\rangle = \begin{cases} \Phi(F), F > 0 \\ 0, F \le 0 \end{cases}$

Therefore, the relationship between the total stress and strain in the two cases can be developed. In the purely elastic case, $\sigma < C_Y$ and $\varepsilon^P = 0$, we get:

$$\sigma = E\varepsilon$$

Whereas, $\dot{\varepsilon}^P = \frac{1}{E}\dot{\sigma} + \gamma\left(\sigma - C_Y(\varepsilon^P)\right)$

where $\gamma = 1/\mu$ is the material property fluidity. C_Y is treated as a function of the total viscoplastic strain ε^P when considering the stain hardening behaviour of the material.

C.2.2 Three Dimensional Elasto-Viscoplastic Model

The fundamental assumption of elasto-viscoplasticity is that the total deformation can be separated into elastic and viscoplastic parts. More specifically, one can express the total rate of strain $\dot{\varepsilon}$, according to:

$$\dot{\varepsilon} = \dot{\varepsilon}^E + \dot{\varepsilon}^P \tag{C.15}$$

where $\dot{\varepsilon}^P$ is the viscoplastic strain rate, and $\dot{\varepsilon}^E$ is the elastic strain rate. The strain rate is related to the stress through the time-differentiated version of Hook's generalized law,

$$\dot{\sigma} = D\dot{\varepsilon}^E \tag{C.16}$$

The constitutive law for the viscoplastic strains can be written as:

$$\dot{\varepsilon}^{P} = \gamma \left\langle \Phi(F) \right\rangle \frac{\partial Q}{\partial \sigma} \qquad (C.17)$$

where $F = f(\sigma_{ij} - C_{Y})$, Q is the plastic potential, the common case of associated plasticity corresponds to taking $Q = F$. A widespread choice of the $\Phi(F)$ is $\Phi(F) = (F/C_{Y})^{N}$ for some prescribed constant N.

In elastic case, we have:

$$\int_{\Omega} B_{i}^{T} \sigma \, d\Omega + f_{i} = 0, \qquad i = 1, ..., n \qquad (C.18)$$

where f_{i} contains body forces and surface integrals of the tractions. The relation between the total stain and the displacement field is expressed in the following time differentiated and spatially discrete form:

$$\dot{\varepsilon} = \sum_{j=1}^{n} B_{j} \dot{u}_{j} \qquad (C.19)$$

The quantities like B_{j}, u_{j} and D can be recalled from the elastic analysis.

In the elasticity problem, the stress and strain quantities can be easily eliminated to obtain a vector equation for the displacement field. This is more complicated in the present elasto-viscoplastic problem, because of the nonlinearities introduced by the $\dot{\varepsilon}$ term. By proper discretizations, an iterative procedure can be derived where a linear system is solved with respect to the displacement field. In its simplest form, the linear system appearing in this numerical method has a coefficient matrix identical to that of the elasticity problem.

Combining Equation (C.15), Equation (C.16) and Equation (C.19) yields:

$$\dot{\sigma} - D \left(\sum_{j} B_{j} \dot{u}_{j} - \dot{\varepsilon}^{P} \right) = 0 \qquad (C.20)$$

Since $\dot{\varepsilon}^P$ depends nonlinearly on σ, making the above equation a nonlinear ordinary differential equation for σ. Hence, we can not eliminate σ and must work with essentially two types of spatially discrete equations governing σ and u_j, using Equation (C.18) and Equation (C.20).

In Equation (C.20), the time derivatives can be approximated by a θ-rule [151]. Depending on the value taken we obtain an explicit or implicit formulation.

$$\frac{\Delta\sigma}{\Delta t} - D\sum_{j=1}^{n} B_j \frac{\Delta u_j}{\Delta t} + D\theta\dot{\varepsilon}^{P,l} + D\left(1-\theta\right)\dot{\varepsilon}^{P,l-1} = 0$$

where the notation $\Delta\sigma \equiv \sigma^l - \sigma^{l-1}$, $\Delta u_j \equiv u_j^{\,l} - u_j^{\,l-1}$, .

Utilizing these approximations in Equation (C.18) and Equation (C.20) gives the following nonlinear discrete problem:

$$\int_{\Omega} B_i^T \sigma^l d\Omega + f_i^l = 0, \qquad i = 1,...,n$$

$$\Delta\sigma - D\sum_{j}^{n} B_j \Delta u_j + \Delta t D\theta\dot{\varepsilon}^{P,l} + \Delta t D(1-\theta)\dot{\varepsilon}^{P,l-1} = 0$$

C.2.3 A Newon-Raphson-Based Iteration Method

The above nonlinear problem can be solved using a Newon-Raphson procedure, and the nature of the resulting approximations enables us to eliminate $\Delta\sigma$ and derive a linear system for $\Delta u_j (j = 1,...,n)$. For example, if we define:

$$\Psi_i^l \equiv \int_{\Omega} B_i^T \sigma^l d\Omega + f_i^l, \tag{C.21}$$

$$R^l \equiv \Delta\sigma - D\sum_{j} B_j \Delta u_j + \Delta t D\theta\dot{\varepsilon}^{P,l} + \Delta t D(1-\theta)\dot{\varepsilon}^{P,l-1} \tag{C.22}$$

And then consider $\Psi_i^l = 0$ and $R^l = 0$ as a simultaneous nonlinear system of algebraic equations for σ^l, and u^l, $i = 1,..,n$. A Newton-Raphson approach consists in making first-order Taylor-series expansions of Ψ_i^l and R^l around an approximation $\sigma^{l,k}$, $u^{l,k}$ in iteration k. Enforcing the linear Taylor-series expansion to vanish results in linear equations for the increments $\delta\sigma^{l,k+1}$, $\delta u^{l,k+1}$:

$$\Psi_i^{l,k+1} \approx \Psi_i^{l,k} + \int_\Omega B_i^T \delta\sigma^{l,k+1} d\Omega = 0 \qquad (C.23)$$

$$R^{l,k+1} \approx R^{l,k} + (\frac{\partial R}{\partial \sigma^l})^{l,k} \delta\sigma^{l,k+1} + \sum_{j=1}^{n} (\frac{\partial R}{\partial u_j^l})^{l,k} \delta u_j^{l,k+1}$$

$$= R^{l,k} + \delta\sigma^{l,k+1} - D\sum_{j=1}^{n} B_j \delta u_j^{l,k+1} + \Delta t D\theta C \delta\sigma^{l,k+1} = 0 \qquad (C.24)$$

with $C = \left(\dfrac{\partial \dot{\varepsilon}^P}{\partial \sigma}\right)^{l,k}$.

Equation (C.24) can be solved with respect to the stress increment, resulting in:

$$\delta\sigma^{l,k+1} = \hat{D}\sum_j B_j \delta u_j^{l,k+1} - QR^{l,k} \qquad (C.25)$$

where $\hat{D} = (D^{-1} + \theta\Delta t C)^{-1}$, $Q = (I + \theta\Delta t DC)^{-1}$.

Inserting this $\delta\sigma^{l,k+1}$ in Equation (C.23) yields a linear system for $\delta u_j^{l,k+1}$:

$$\sum_j \left(\int_\Omega B_i^T \hat{D} B_j d\Omega \right) \delta u_j^{l,k+1} = \int_\Omega B_i^T QR^{l,k} d\Omega - \Psi_i^{l,k}$$

At time $t = 0$, $\dot{\varepsilon}^{P,0} = 0$, and the stresses correspond to a purely elastic state. That is, u^0 is determined from a standard elasticity problem:

$$\sum_j \left(\int_\Omega B_i^T \hat{D} B_j \, d\Omega \right) u_j^0 = -f_i^0, \qquad i = 1, \ldots, n.$$

With the associated stresses $\sigma^0 = D \sum_j B_j u_j^0$. Suppose u^{l-1}, σ^{l-1} and $\dot{\varepsilon}^{P,l-1}$ are known.

New displacements u^l are generally computed by an iteration procedure. As an initial guess for the iterations, we set $u_j^{l,0} = u_j^{l-1}$, $\sigma_j^{l,0} = \sigma_j^{l-1}$, $\dot{\varepsilon}_j^{P,l,0} = \dot{\varepsilon}_j^{P,l-1}$. For $k = 0, 1\ldots$, until convergence of the Newton-Raphson method, to assemble and solve the linear system for the correction $\delta u_j^{l,k+1}$ of the displacement field. And then calculate the displacements and stresses according to:

$$\sigma^{l,k+1} = \sigma^{l,k} + \delta\sigma^{l,k+1}$$
$$u^{l,k+1} = u^{l,k} + \delta u^{l,k+1}$$

where $\delta\sigma^{l,k+1}$ can be found from Equation (C.25).

The final step is to calculate the new viscoplastic strain rate from the following equation and then proceed with the next iteration.

$$\dot{\varepsilon}^{P,l,k+1} = \gamma \left\langle \Phi\left(F(\sigma_{i,j}^{l,k+1}) \right) \right\rangle \left(\frac{\partial F}{\partial \sigma} \right)^{l,k+1}$$

If the iterative procedure converges in m iterations, we can define u^{l-m} as the converged solution u^l at this time level.

The calculation of the viscoplastic strain increment can be explicit or implicit. If the method is implicit then the latest values of stress will change the viscoplastic strain increment, and possibly the matrix system, requiring an iterative procedure at each increment. If the procedure is explicit, then the viscoplastic strain increment will be based on the values of stress at the previous step. For example, the explicit approximation at time step $l+1$ is given by:

$$\Delta \varepsilon_{l+1}^{p} = \Delta t \left(\frac{\partial \varepsilon^{p}}{\partial t} \right)_{l}$$

where t is the time step and the viscoplastic strain rate is approximated using values of stress etc., obtained from the previous step. The use of an explicit will require very small time steps [150].

D. PHYSICA - A Simulation Tool

PHYSICA [152] is a software environment for the modelling and analysis of multi-physics phenomena where material may behave as a solid or fluid during its processing. This analysis tool is a collection of interacting solution procedures, including CFD finite volume (FV) based techniques for heat transfer, fluid flow and Finite Element (FE) based elasto-visco-plastic solid mechanics. A numerical modelling tool such as PHYSICA is used in three stages, which are:

- Pre-processing

- Solution

- Post-processing

At the pre-processing stage, the geometry to be analysed will be generated in the computer using a suitable computer aided design (CAD) package. Boundary conditions and suitable properties for the materials in the domain will then be applied to the geometry. Finally, the domain will be broken down into a mesh over which the governing equations are solved. PHYSICA is linked to a software package called FEMGV [153] which is used as the pre-processor and post-processor and this environment has been used in this research.

In the solution stage, the design engineer will inform the programme on the relevant physics to solve, and then the software will check to ensure that all the

relevant data including boundary conditions, material properties etc., have bee:
provided and that the quality of the mesh is suitable for the solution to take place
Matrix solvers will then be used to solve the algebraic equations, resulting from th:
discretisation process, for variables such as fluid velocities, temperature and soli:
displacements.

In the post-processing stage, FEMVIEW which is integrated with the softwar:
package FEMGV, will be used for post-processing and visualization of the simulatioi
results. There are some options for presenting the result data including vector plots
plots of displaced shape of the design, contour plots of the solved quantity etc. T:
achieve accurate results from a simulation may require further analysis using a fine
mesh to ensure that the results are mesh independent.

E. Liquid Crystal Display: A Case Study Using PHYSICA

This section describes the modelling process and results obtained from the analysi:
of the behaviour of a Liquid Crystal Display (LCD) that was packaged for use in harsl
environments. The packaging processes used adhesive materials and their effect on the
reliability and performance of the LCD was analysed.

The core of the LCD package is an Active Matrix Liquid Crystal Displa\
(AMLCD) which needs to be protected from severe environments. The ruggedisatioi
or packaging process consists of laminating the LCD with cover glasses. This provide:
a more robust structure. The top view of the final LCD package is showed in Figur:
E.1.

A section view of this laminated LCD package is shown in Figure E.2, where th:
structure and materials involved are described. There is a very thin layer of Liquic
Crystal which is sealed between the two AMLCD glasses. The material in yellov
represents the silicon resin which is soft and easily to be deformed, and thus it can b:
used for protecting the LCD package from external forces and also releasing the buil

stress inside. Outside of the silicon resin, there are two sets of Borosilicate glass which are used for protection purpose. The silicon perimeter seals provide the adhesive strength to join the materials to the Borosilicate Glass.
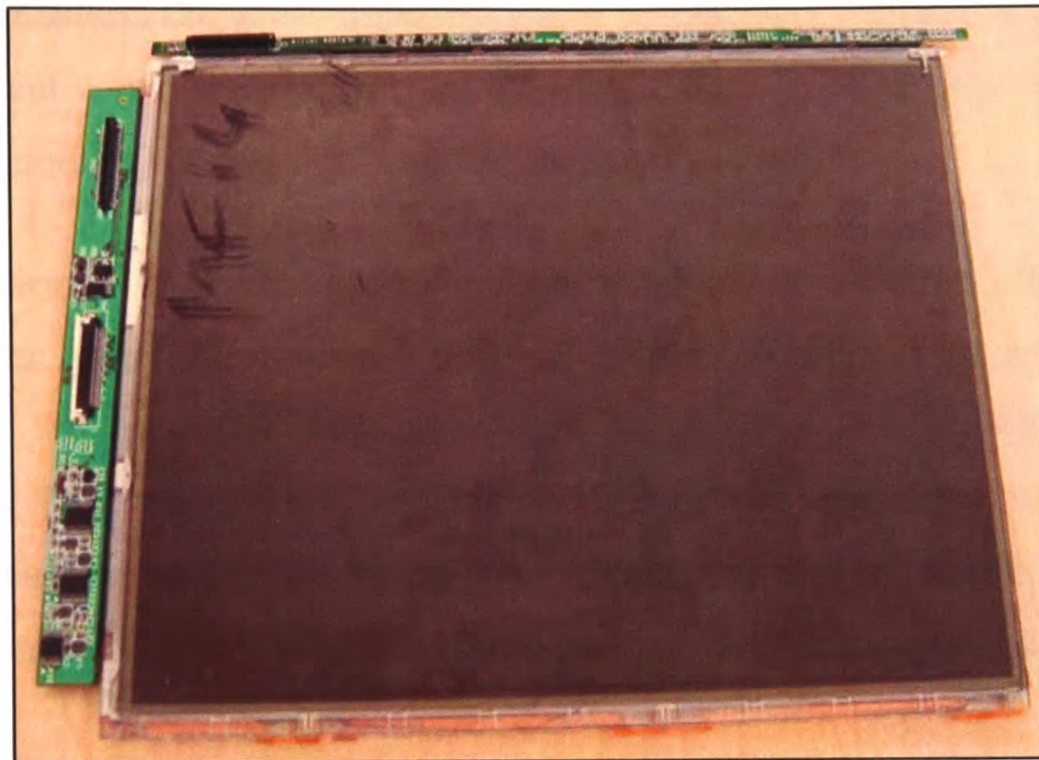
Figure E.1: The LCD sample to be modelled
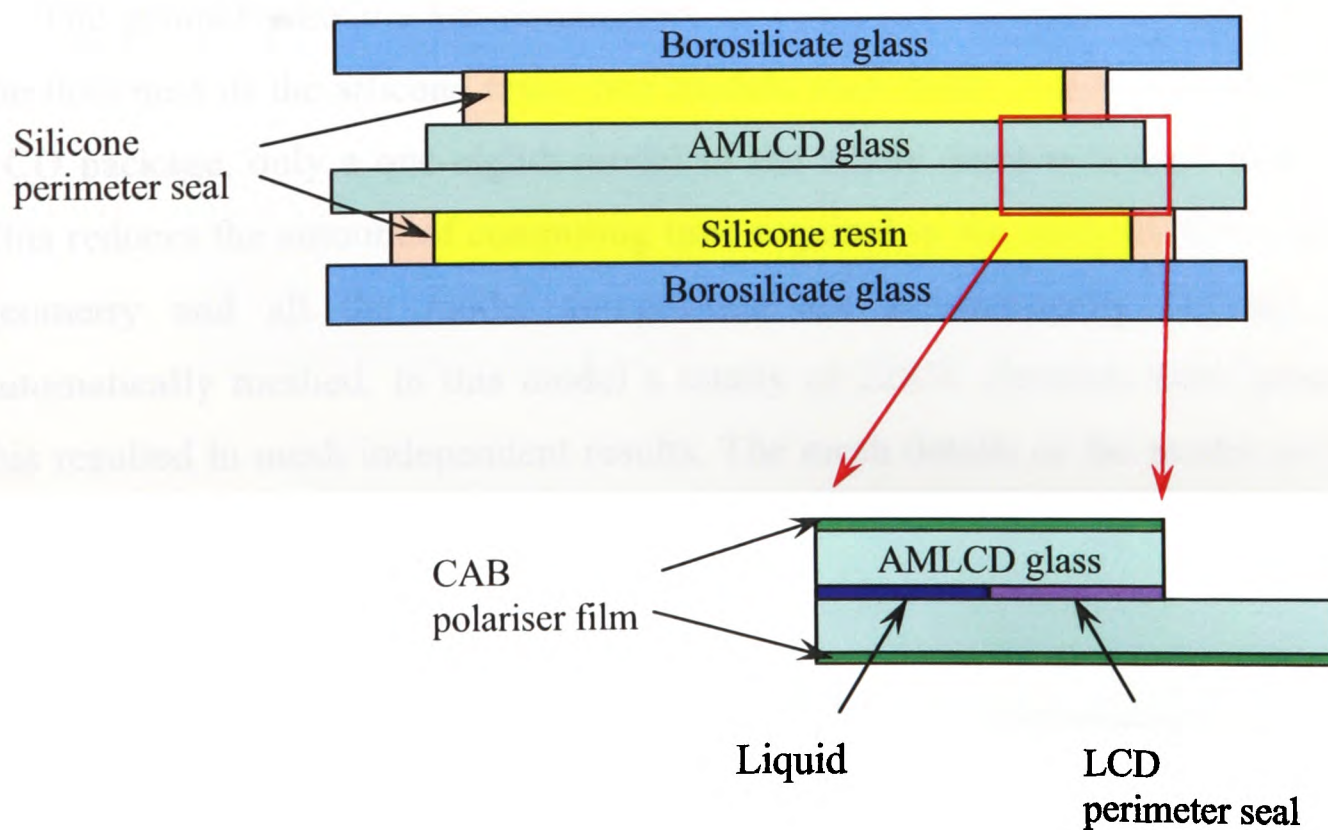
Figure E.2: A section view of the LCD and material information

E.1 Problem Description

When used in service this ruggedised display will experience extremes of temperature both hot and cold. When passed through qualification the display design will have to withstand the stress imposed due to temperature cycling. As the materials all have different coefficients of thermal expansion, each material will tend to expand by a different amount and this will result in stress.

A certain degree of stress within the LCD structure is of course allowed but too much stress can affect the structural integrity of the display and its performance. A concern from the industrial partner on this project was the stresses around the interfaces and joint materials. Computer modelling was suggested as a means to predict these stresses and to investigate how changes to design variables such as the material properties of the filled silicon resin and its thickness could affect these stresses.

E.2 Geometry and Computational Mesh

The geometry details are summarized in Table E.1. In order to study the effect of the thickness of the silicone resin, two models were built. Due to the symmetry in the LCD package, only a one-eighth model of the whole domain is used in the analysis. This reduces the amount of computing time required in the analysis. Once the package geometry and all the model components are parametrically defined, they are automatically meshed. In this model a totally of 22858 elements were generated and this resulted in mesh independent results. The mesh details of the model are shown in Figure E.3.

Table E.1: The geometry details of the LCD package

Material	Thickness (mm)	Width (mm)	Length (mm)
Borosilicate glass	1.1	170	170
AMLCD glass	0.7	170/158	170/168
Silicone resin	1.0 or 0.1	165/153	165/153
Silicone perimeter seal	1.0 or 0.1	1.5	perimeter
CAB polarizer film	0.2	170/158	170/158
Liquid Crystal	0.006	152	152
LCD perimeter seal	0.006	3.0	perimeter

(a) Top view of the whole LCD   (b) FE model: 1/8 of the whole LCD
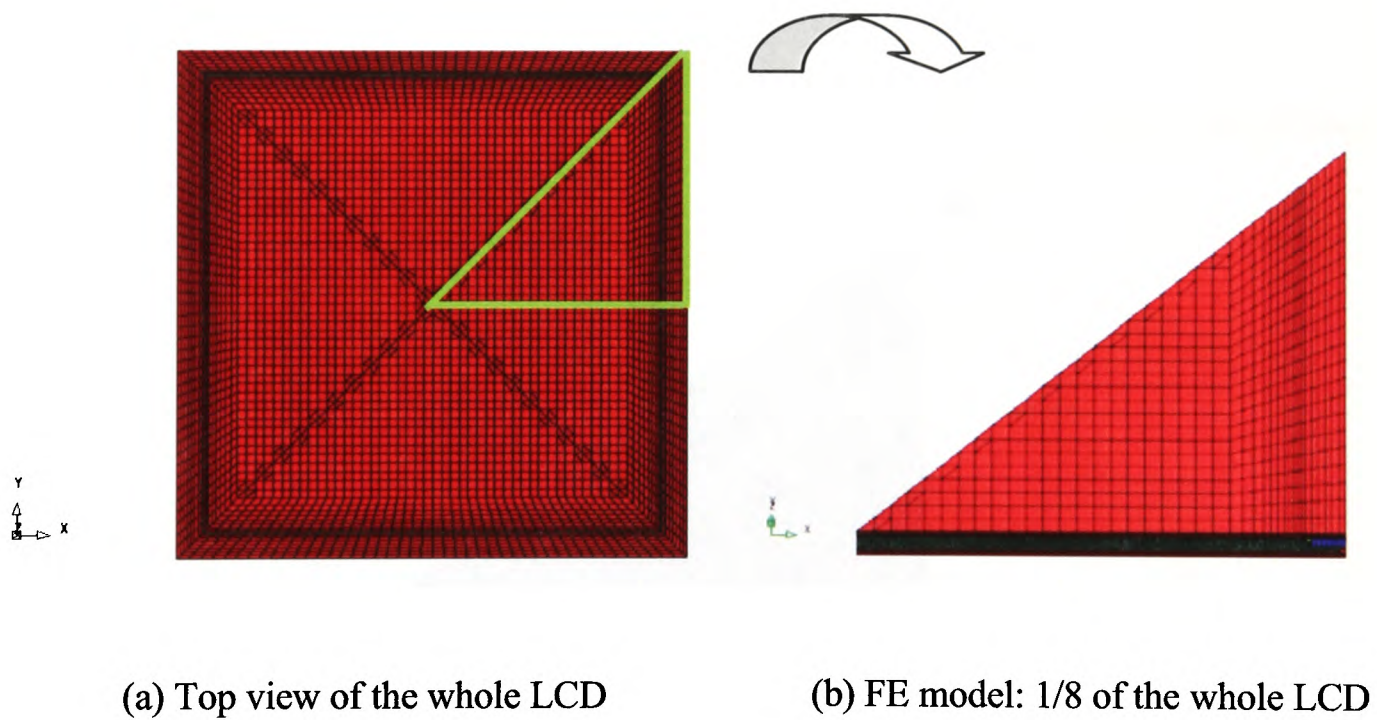
Figure E.3: The finite element model

Once the meshing process is complete, all the information is saved into a geometry file (*. geo), this file is called by an inform file, which describes the physics to be

solved, and then both of them are submitted to the PHYSICA tool to start the simulation.

E.3 Boundary Conditions and Material Properties

Within the inform file the values of the boundary conditions are stated. These boundary conditions are important for achieving the correct modelling results. For the LCD described above, the boundary conditions were added into the four following patches which are illustrated in Figure E.4.

1. Displacements of point A were fixed to be zero in all directions;
2. Displacements of the points on Plane A were fixed to be zero in Y direction;
3. Displacements of the points on Plane B were fixed in the plane of X = Y;
4. Displacements of points on the symmetry line were fixed to be zero in X direction.
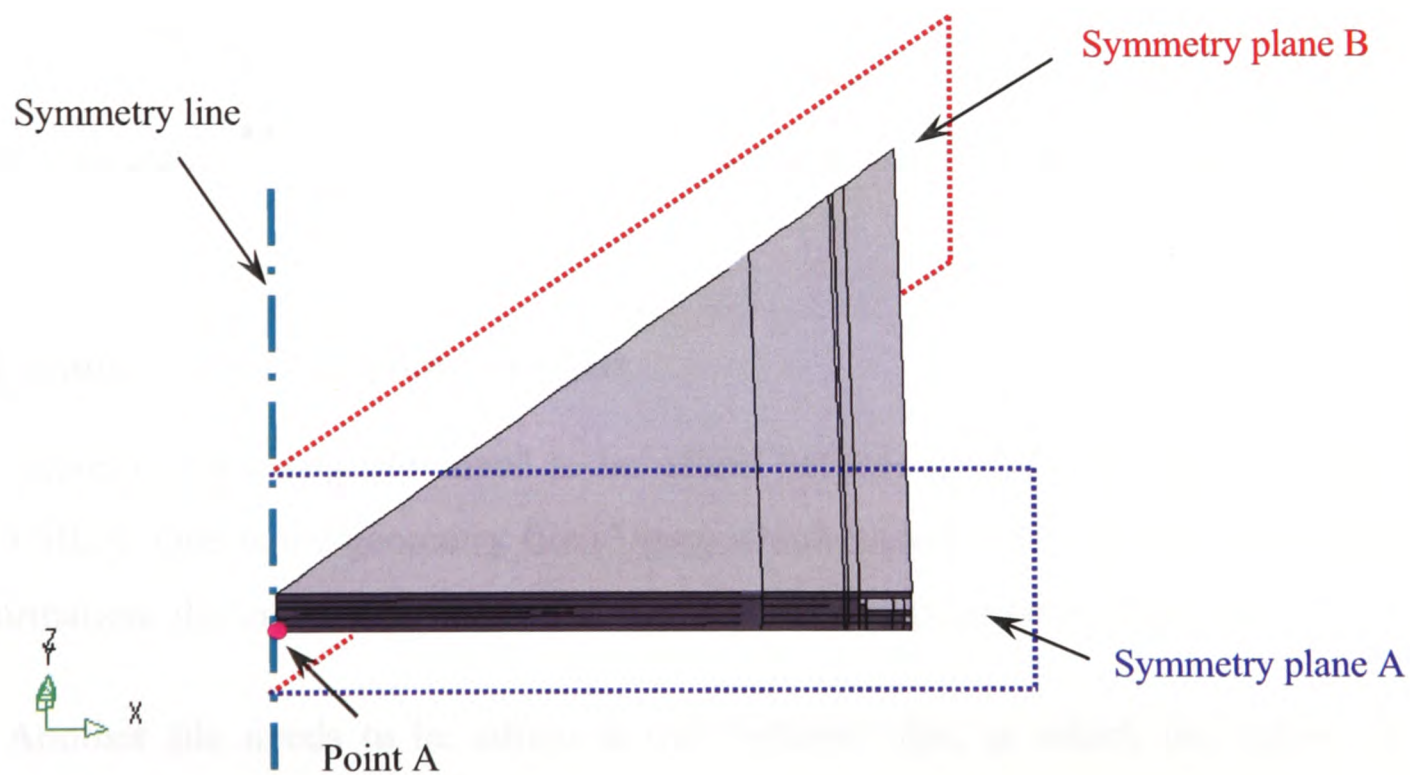
Figure E.4: The boundary condition used in modelling

A temperature load from 25°C to 100°C was applied to the whole domain. The properties of all the materials are listed in Table E.2. All the material was considered as elastic material, isotropic and homogeneous. The temperature dependent material properties were not considered in this analysis due to lack of data.

Table E.2: The basic material information

	Young's Modulus E (GPa)	CTE (ppm/°C)	Poisson's Ratio
Borosilicate Glass	67.6	4.6	0.28
AMLCD Glass	67.6	4.6	0.28
Silicone Resin (soft gel)	0.001	350	0.3
Silicone Resin (firm gel)	0.1	300	0.3
Silicone Perimeter Seal	0.1	300	0.3
Liquid Crystal	0.001	200	0.3
LCD Perimeter Seal	20	70	0.3
CAB Polarizer Film	1.0	140	0.3

E.4 Solution of the Modelling Analysis

There are two data files need to be edited before doing the modelling analysis in PHYSICA. One is the geometry file (*.geo) which includes all the geometry and mesh information, the index and location of the material and boundary conditions.

Another file needs to be edited is the "Inform" file, in which the values of the material properties and boundary conditions, having the same index number as the geometry file, are defined. There are several modules that are used for different applications such as the Heat Module, EVP module etc. Different numerical solvers based on iterative methods are available in PHYSICA, such as the over relaxed forms

of the Jacobi method (JOR), Gauss Seidel (SOR), and the Jacobi preconditioned conjugate gradient method (JCG) *etc.*

Finally, the geometry and inform files are submitted to the PHYSICA tool and to start running the simulation.

E.5 Results Analysis

The deformation of the package at 100°C is shown in Figure E.5, which is magnified by fifty times. It is found that when the soft silicone fill was used, the package had the tendency to expand more in the vertical direction and due to the CTE mismatch between the silicone fill and the perimeter seal, there was a clear curvature effect at the edge of the glasses which could result in delamination.

(a) Soft fill

(b) Firm fill
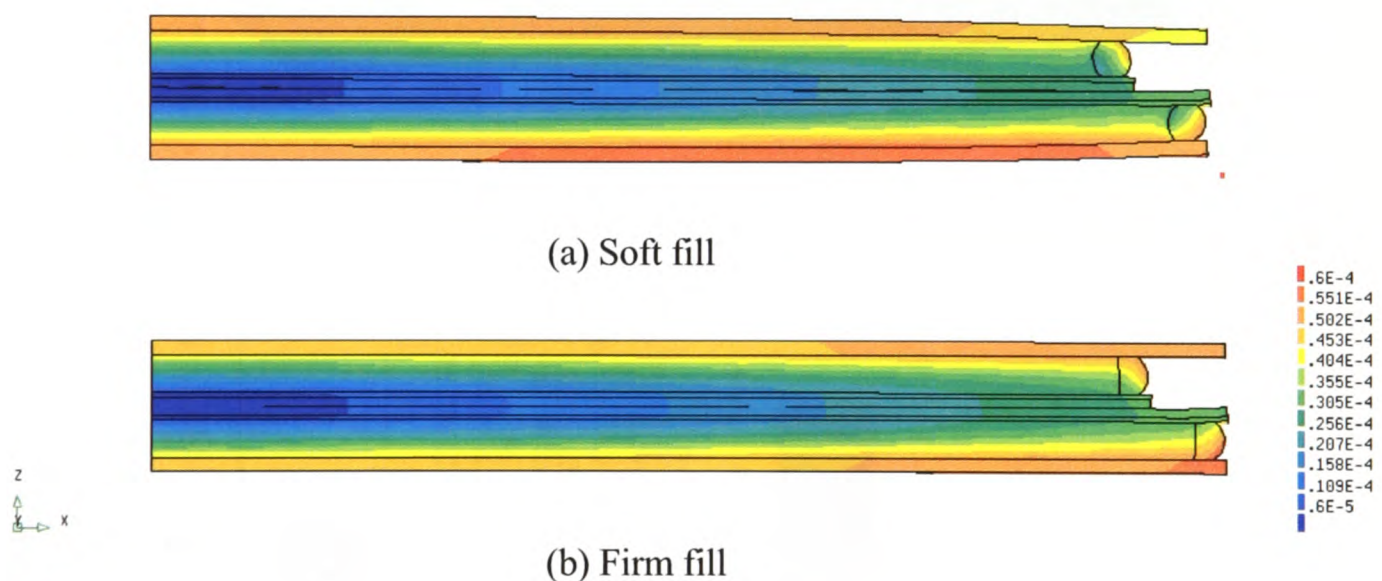
Figure E.5: The deformation of the package at 100°C

The shear stress distribution near the end of the package where the 1.0mm thickness firm gel is used is shown in Figure E.6. Higher stress was detected at the corner of the package and the interface between the glass and seal joint. In order to investigate the effect of the thickness/softness of the gel on the interfacial stresses, a parametric analysis was conducted and the shear stress values at four locations (Point

1, 2, 3 and 4) as illustrated in Figure E.7. It was found that the thickness of the gel had a substantial effect on the shear stress at the selected locations. When using a thicker gel, higher stress was identified. However, the effect of the material properties on the shear stress was not as significant as the geometry factor.
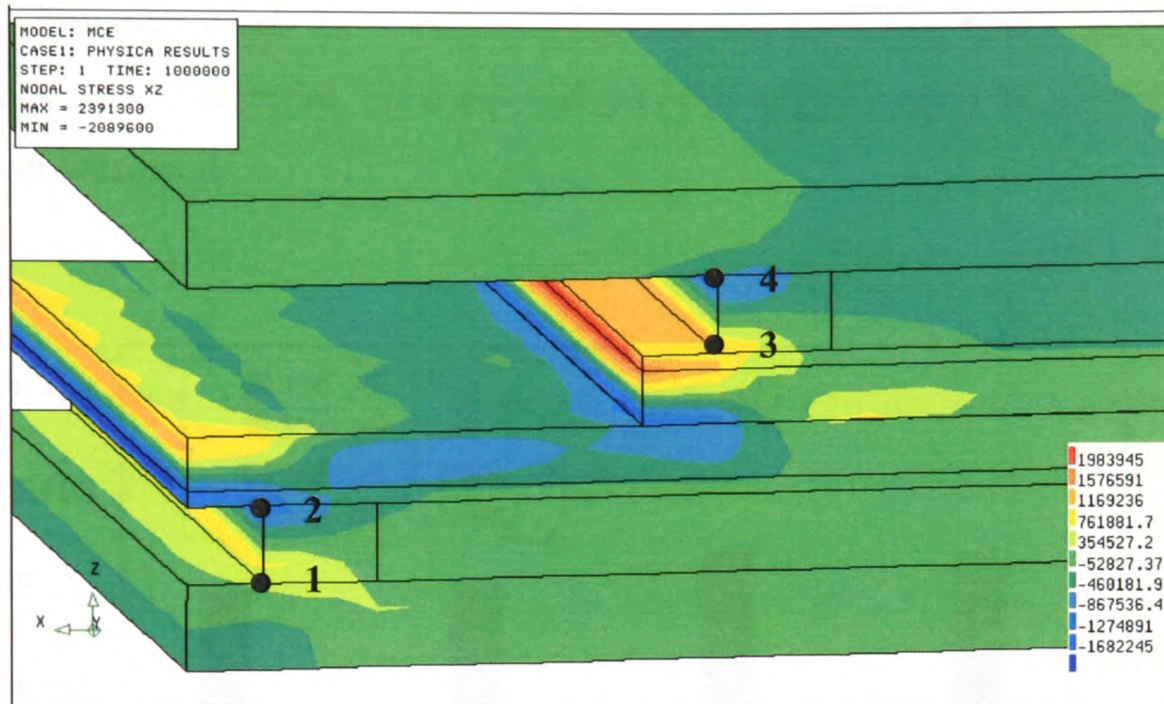
Figure E.6: Shear stress distribution in the package at 100°C
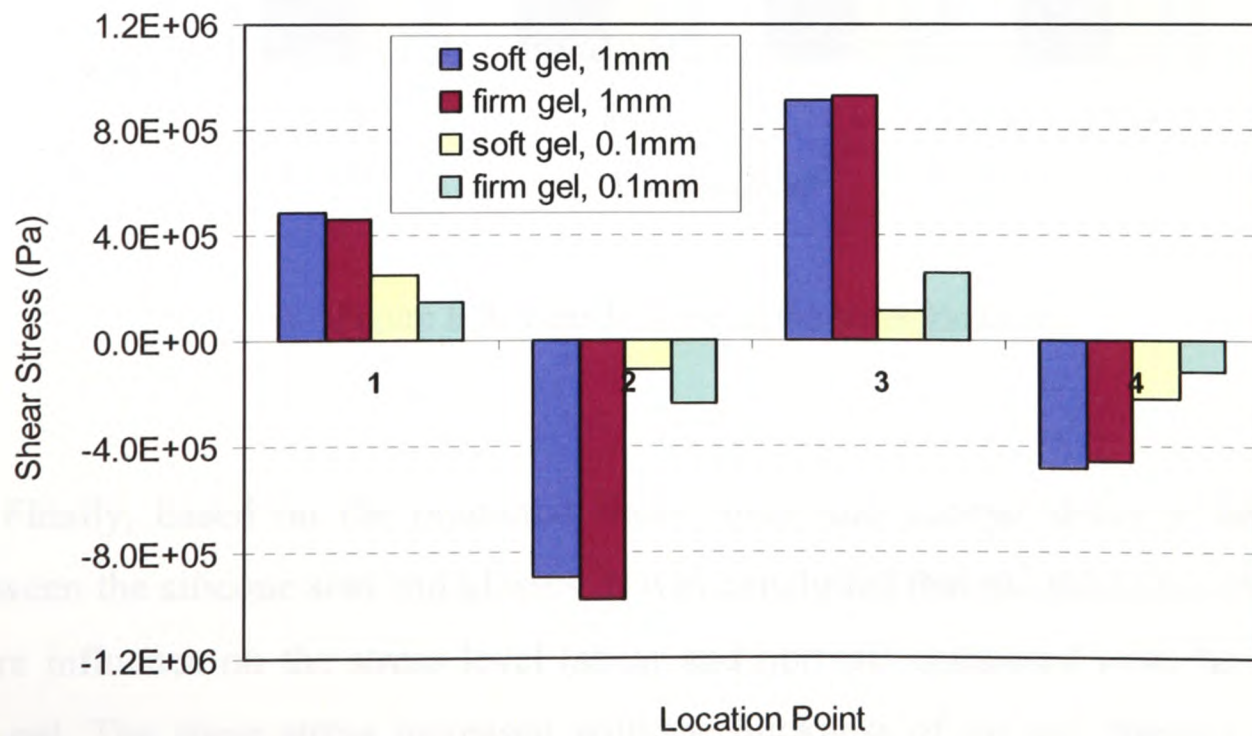
Figure E.7: Values of shear stress at weak locations

The tensile stress values at these selected locations are plotted in Figure E.8. Once again, the tensile stress increased with the thickness of the silicone fill, the effect of material properties was dependent on the thickness of the silicone fill.

When a thinner layer of gel was used, the effect of the material properties was not significant, however when the thicker silicone fill was used, the tensile stress increased with hardness of the material. This material property effect cannot be ignored when the thicker layer was used.
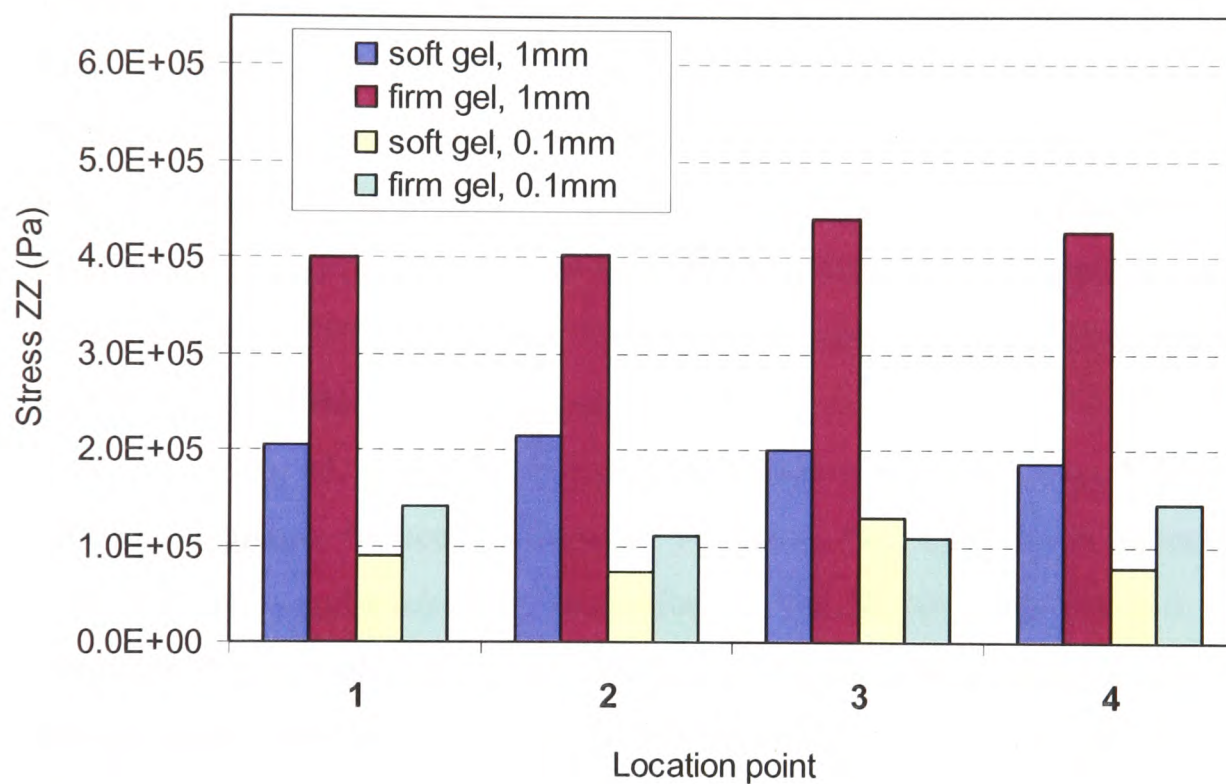
Figure E.8: Tensile stress at the weak locations

Finally, based on the predicted shear stress and normal stress at the interfaces between the silicone seal and glasses, it was concluded that the thickness of the gel had more influence on the stress level (shear and normal) compared with the hardness of the gel. The shear stress increased with the thickness of the gel. Similar trends were observed when the temperature decreased from 25 to -65°C.

References

[1] Lau, J.H. (2000), *Low Cost Flip Chip Technologies for DCA, WLCSP, and PBGA Assemblies*, Published by McGraw Hill, ISBN: 0-07-135141-8, pp1-17.

[2] Tummala, R.R. (2006), Moore's Law Meets Its Match Continued, http://www.spectrum.ieee. org/jun06/3649.

[3] Ulrich, R.K. and Brown, W.D. (2006), *Advanced Electronic Packaging*, published by John Wiley & Sons, Inc. ISBN: 13978-0-471-46609-X, pp.1-28.

[4] Liu, J. (1999), *Conductive Adhesives for Electronics Packaging*, Electrochemical Publications Ltd, Port Erin, Isle of Man, ISBN 0901-150-37-1, pp.1-14.

[5] Liu, J. (1999), *Conductive Adhesives for Electronics Packaging*, Electrochemical Publications Ltd, Port Erin, Isle of Man, ISBN 0901-150-37- 1, pp.234-248.

[6] Charles, A.H. (1997), *Electronic Packaging & Interconnection Handbook*, Published by McGraw-Hill, ISBN: 0-07-26694-8.

[7] Teh, L.K., Teo, M., Anto, E., Wong, C.C., Mhaisalkar, S.G., Teo, P.S. and Wong, E.H. (2005), "Moisture-Induced Failures of Adhesive Flip Chip Interconnects", IEEE Trans on Components and Packaging Technologies, Vol.28, No.3, pp.506-516.

[8] Ferguson, T.P. and Qu, J.M. (2004), "Moisture and Temperature Effects on the Reliability of Interfacial Adhesion of a Polymer/Metal Interface", Proceedings of the 54th IEEE Electronic Components and Technology Conference (ECTC), Las Vegas, pp.1752-1758.

[9] Tan, C.W., Chan, Y.C. and Yeung, N.H. (2003), "Effect of Autoclave Test on Anisotropic Conductive Joints", Journal of Microelectronics Reliability, Vol.43, Issue: 2, pp.279-285.

[10] Caers, J.F.J.M., Zhao, X.J., Lekens, G., Dreesen, R., Croes, K. and Wong, E.H. (2003), "Moisture Induced Failures in Flip Chip on Flex Interconnections using Anisotropic Conductive Adhesives", Proceedings of International IEEE Conference on the Business of Electronic Product Reliability and Liability, Hong Kong & ShenZhen, pp.171-176.

[11] Wei, Z, Waf, L.S., Loo, N.Y., Koon, E.M. and Huang, M. (2002), "Studies on Moisture-induced Failures in ACF Interconnection", Proceedings of the 7th Electronics Packaging Technology Conference (EPTC), pp.133-138.

[12] Mercodo, L.L., White, J., Sarihan, V. and Lee, T.Y.T. (2003), "Failure Mechanism Study of Anisotropic Conductive Film (ACF) Packages", IEEE Transactions on Components and Packaging Technologies, Vol.26, No.3, pp.509-516.

[13] Kim, W.K., Ikeda, T. and Miyazaki, N. (2004), "Mechanical Reliability of Anisotropic Conductive Adhesive Films under Moisture/Reflow Sensitivity Test", WCCM VI in conjunction with APCOM'04, Beijing, China, pp.501-510.

[14] Kristiansen, H. and Liu, J. (1998), "Overview of Conductive Adhesive Interconnection Technologies for LCD's", IEEE Transactions on Components, Packaging, and Manufacturing Technology, Part A, Vol.21, No.2, pp.208-214.

[15] Lee, K.K., Ng, K.T., Tan, C.W.; Chan Y.C. and Cheng L.M. (2004), "Fabrication of Smart Card Using UV Curable Anisotropic Conductive Adhesive (ACA.) Part I: Optimization of the Curing Conditions", Proceedings of International Conference on Business of Electronic Product Reliability and Liability, Portland, Oregon, USA, pp.134-139.

[16] Lee, K.K., Tan, C.W. and Chan, Y.C. (2005), "Investigation of Conductive Bonding Using UV Curable Anisotropic Conductive Adhesives at Different Curing Conditions", Journal of Electronic Packaging, Transaction of ASME, pp.52-58.

[17] Tan, C.W., Siu, Y.M., Lee, K.K., Chan, Y.C. and Cheng, L.M. (2004), "Fabrication of Smart Card Using UV Curable Anisotropic Conductive Adhesive (ACA) Part II: Reliability Performance of the ACA joints", 2004 International Conference on Business of Electronic Product Reliability and Liability, Portland, Oregon, USA, pp.140-144.

[18] Zhang, J.H., Chan, Y.C., Zeng, Z.M. and Chiu, Y.W. (2002), "Research on the Interfacial Reaction between Anisotropically Conductive Film and Bumpless Die", Proceedings of the 52nd Conference on Electronic Components and Technology (ECTC), San Diego, USA, pp.1569-1574.

[19] Ogunjimi, A.O., Boyle, O.A., Whalley, D.C. and Williams, D.J. (1992), "A Review of the Impact of Conductive Adhesive Technology on Interconnection", Journal of Electronic Manufacturing, Vol.2, No.3, pp.109-118.

[20] Chang, W.K. and Chan, Y.C. (2005), "Reliability of Anisotropic Conductive Film Joints Using Bumpless Chip—Influence of Reflow Soldering and Environmental Testing", ASME Journal of Electronic Packaging, Vol.127, pp.113-119.

[21] Frisk, L. and Ristolainen, E. (2005), "Flip Chip Attachment on Flexible LCP Substrate Using an ACF", Journal of Microelectronics and Reliability, Vol.45, Issues 3-4, pp.583-588.

[22] Paik, K.W., Yim M.J. and Jay, Y.D. (2000), "Flip Chip Assembly on Organic Boards Using Anisotropic Conductive Adhesives (ACAs) and Ni/Au Bumps", Proceedings of the 50th IEEE Electronic Components and Technology Conference (ECTC), pp.378-384.

[23] Yim, M.J., Jeon, Y.D. and Paik, K.W. (2000), "Reduced Thermal Strain in Flip Chip Assembly on Organic Substrate using Low CTE Anisotropic Conductive Film", IEEE Transactions on Electronics Packaging Manufacturing, Vol.23, No.3, pp.171-176.

[24] Yim, M.J., Hwang, J.S. and Kim, JG. (2004), "Anisotropic Conductive Adhesives with Enhanced Thermal Conductivity for Flip-Chip Applications", Proceedings of the 54th IEEE Electronic Components and Technology Conference (ECTC), pp.159-164.

[25] Pataki, W.S. (1997), "Optimization of Free Radical Initiation Reactions in the Electrical Industry", Proceedings of the Electrical Insulation Conference and Electrical Manufacturing and Coil Winding Conference, pp.745-751.

[26] Jacob, J., Chia, L.H.L. and Boey, F.Y.C. (1995), "Comparative Study of Methyl Methacrylate Cure by Microwave Radiation Versus Thermal Energy", Polymer Testing, Vol.14, No.4, pp.343-354.

[27] Davis, C., Tanikella, R., Sung, T., Kohl, P. and May, G. (2003), "Optimization of Variable Frequency Microwave Curing Using Neural Networks and Genetic Algorithms", Proceedings of the 53rd IEEE Electronic Components and Technology Conference, pp.1718-1723.

[28] Fu, Y., Wang, T. and Liu, J. (2003), "Microwave-transmission, Heat and Temperature Properties of Electrically Conductive Adhesive", IEEE Transactions on Components and Packaging Technologies, Part A, Vol.26, Issue: 1, pp.193-198.

[29] Islam, R.A. and Chan, Y.C. (2004), "Effect of Microwave Preheating on the Bonding Performance of flip chip on flex joint", Journal of Microelectronics Reliability, Vol.44, Issue 5, pp.815-821.

[30] Wang, T.B., Fu, Y., Becher, M. and Liu, J. (2001), "Microwave Cure of Metal-Filled Electrically Conductive Adhesive", Proceedings of the 51st IEEE Electronic Component Technology Conferenc (ECTC), Orlando, USA, pp.593-597.

[31] Shiming, L. and Liu, J. (2002), "Development and Characterization of Single Mode Microwave Cured Adhesives for Electronics Packaging Application", Proceedings of 52nd IEEE Electronic Components and Technology Conference (ECTC), pp.1147-1150.

[32] Chang, S.M., Jou, J.H., Hsieh, A., Chen, T.H., Chang, C.Y., Wang, Y.H. and Huang, C.M. (2001), "Characteristic Study of Anisotropic Conductive Film for Chip-on-film Packaging", Journal of Microelectronics Reliability, Vol.41, Issue 12, pp.2001-2009.

[33] Chan, Y.C. and Luk, D.Y. (2002), "Effects of Bonding Parameters on the Reliability Performance of Anisotropic Conductive Adhesive Interconnects for Flip-chip-on-flex Packages Assembly I. Different Bonding Temperature", Journal of Microelectronics Reliability, Vol.42, Issue: 8, pp.1185-1194.

[34] Chan, Y.C. and Luk, D.Y. (2002), "Effects of Bonding Parameters on the Reliability Performance of Anisotropic Conductive Adhesive Interconnects for Flip-chip-on-flex Packages Assembly II Different Bonding Pressure", Journal of Microelectronics Reliability, Vol.42, Issue 8, pp.1195-1204.

[35] Chen, X., Zhang, J., Jiao C.L., Liu, Y.M. (2006), "Effects of Different Bonding Parameters on the Electrical Performance and Peeling Strengths of ACF Interconnection", Journal of Microelectronics Reliability, Vol.46, pp.774–785.

[36] Uddin, M.A., Alam, M.O., Chan, Y.C. and Chan, H.P. (2004), "Adhesion Strength and Contact Resistance of Flip Chip on Flex Packages—Effect of Curing Degree of Anisotropic Conductive Film", Journal of Microelectronics Reliability, Vol.44, Issue: 3, pp.505-514.

[37] Tan, S.C., Chan, Y.C., Chiu, Y.W. and Tan, C.W. (2004), "Thermal Stability Performance of Anisotropic Conductive Film at Different Bonding Temperatures", Journal of Microelectronics Reliability, Vol. 44, Issue: 3, pp.495-503.

[38] Cao, L.Q., Lai, Z.H. and Liu, J (2005), "Interfacial Adhesion of Anisotropic Conductive Adhesives on Polyimide Substrate", ASME Journal of Electronic Packaging, Vol.127, pp.43-46.

[39] Vries, J.D., Delft, J.V., Slob, C. (2005), "100μm Pitch Flip Chip on Foil Assemblies with Adhesive Interconnections", Journal of Microelectronics Reliability, Vol.45, pp.527–534.

[40] Lam, D.C.C., Yang, F. and Tong, P. (1999), "Chemical Kinetic Model of Interfacial Degradation of Adhesive Joints", IEEE Transactions on Components and Packaging Technology, Vol.22, No.2, pp.215-220.

[41] Kwon, W.S., Yim, M.J., Paik, K.W., Ham, S.J. and Lee, S.B. (2005), "Thermal Cycling Reliability and Delamination of Anisotropic Conductive Adhesives Flip Chip on Organic Substrates with Emphasis on the Thermal Deformation", ASME Journal of Electronic Packaging, Vol.127, pp.86-90.

[42] Ali, L., Chan, Y.C. and Alam M.O. (2005), "The Effect of Thermal Cycling on the Contact Resistance of Anisotropic Conductive Joints", Journal of Soldering and Surface Mount Technology, Vol.17, No.3, pp.20-31.

[43] Palm, P., Määttänen, J., Tuominen, A., Ristolainen, E. (2001), "Reliability of 80μm Pitch Flip Chip Attachment on Flex", Journal of Microelectronic Reliability, Vol.41, pp.633-638.

[44] Vries, J.D. (2004), "Failure Mechanism of Anisotropic Conductive Adhesive Interconnections in Flip Chip ICs on Flexible Substrates", IEEE Transactions on Components and Packaging Technologies, Vol. 27, No.1, pp.161-166.

[45] Veris, J.D., Delft, J.V. and Slob, K., (2005), "SMT- Compatibility of Adhesive Flip Chip on Foil Interconnections with 40-μm Pitch" IEEE Transactions on Components and Packaging Technologies, Vol.28, No.3, 2005, pp.499-505.

[46] Wu, Y.P., Alam, M.O., Chan, Y.C. and Wu, B.Y. (2004), "Dynamic Strength of Anisotropic Conductive Joints in Flip Chip on Glass and Flip Chip on Flex Packages", Journal of Microelectronics Reliability, Vol.44, Issue: 2, pp.295-302.

[47] Tan, C.W., Chan, Y.C. and Yeung, N.H. (2003), "Behaviour of Anisotropic Conductive Joints under Mechanical Loading", Journal of Microelectronics Reliability, Vol.43, Issue: 3, pp.481-486.

[48] Rizvi, M.J., Chan, Y.C., Bailey, C. and Lu, H. (2005), "Study of Anisotropic Conductive Adhesive Joint Behaviour Under 3-point Bending", Journal of Microelectronics Reliability, Vol.45, Issues: 3-4, pp.589-596.

[49] Kim, J.W., Jung, S.B. (2006), "Effects of Bonding Pressure on the Thermo-Mechanical Reliability of ACF Interconnection", Journal of Microelectronic Engineering, dio:10.1016/j.mee.2006.10.029.

[50] Reports from International Technology Roadmap for Semiconductors (ITRS) (2005 edition), www.itrs.org

[51] Whalley, D.C., Chen, L. and Liu, J. (2001), "Modelling of the Anisotropic Adhesive Assembly Process", Proceedings of the Fourth International Symposium on Electronic Packaging Technology, Beijing, pp.319-324.

[52] Ogunjimi, A.O., Mannan, S.H., Whalley, D.C. and Williams D.J. (1995), "The Assembly Process for Anisotropic Conductive Joints Some New Experimental and Theoretical Results", Journal of Electronic Manufacturing, Vol.5, pp.263-272.

[53] Mannan, S.H., Whalley, D.C., Ogunjimi, A.O. and Williams, D.J. (1995), "Modelling of the Initial Stages of the Anisotropic Adhesive Joint Assembly Process", Proceeding of the 17th Japan IEEE IEMTS, Omiya, pp.142-145.

[54] Dudek, R., Meinel, S., Schubert, S., Michel, B., Dorfmüller, L., Knoll, P.M. and Baumbach, J. (1999), "Flow Characterization and Thermo-mechanical Response of Anisotropic Conductive Films", IEEE Transactions on Components and Packaging Technology, Vol.22, pp.177-185.

[55] Mannan, S.H., Whalley, D.C., Ogunjimi, A.O. and Williams, D.J. (1996), "Assembly of the Planar Array Components using Anisotropic Conducting Adhesives- a Benchmark Study: Part II Theory", IEEE Transactions on Components, Packaging and Manufacturing Technology -Part C, Vol.19, pp.264-269.

[56] Whalley, D.C., Glinsky, G., Bailey, C. and Liu, J. (2001), "Computational Modelling of the Anisotropic Conductive Adhesive Assembly Process", Proceeding of the 3rd International Symposium on Electronics Materials and Packaging, Jeju, Korea.

[57] Liu, J. (2000), "ACA Bonding Technology for Low Cost Electronics Packaging Applications- Current Status and Remaining Challenges", Proceedings of the 4th IEEE International Conference on Adhesive Joining and Coating Technology in Electronics Manufacturing. Espoo, Finland, pp.1-15.

[58] Buratynski, E.K. (1993), "Thermo-mechanical Modelling of Direct Chip Interconnection Assembly", Journal of Electronic Packaging, Vol.115, pp.382-391.

[59] Wu, S.X., Hu, K.X. and Yeh, C.P. (1999), "Contact Reliability Modelling and Material Behaviour of Conductive Adhesive under Thermo-mechanical Loads", Chapter 6 in Conductive Adhesive for Electronics Packaging, edited by Johan Liu, Electrochemical Publications Ltd, (Port Erin, Isle of Ma n, UK).

[60] Pinardi, K., Lai, Z.H., Vogel, D., Kang, Y.L., Liu, J., Liu, S., Haug R. and Willander, M. (2000), "Effect of Bump Height on the Strain Variation during the Thermal Cycling Test

of ACA Flip- Chip Joints", IEEE Transactions on Components and Packaging Technologies, Vol.23, No.3, pp.447- 451.

[61] Wu, C.M.L., Liu, J. and Yeung, N.H. (2001), "The Effects of Bump Height on the Reliability of ACF in Flip-Chip", Journal of Soldering and Surface Mount Technology, Vol.13, pp.25-30.

[62] Yeung, N.H., Chan, Y.C., and Tan, C.W. (2003), "Effect of Bonding Force on the Conducting Particle with Different Sizes", Journal of Electronic Packaging, Vol.125, No.4, pp.624-629.

[63] Williams, D.J. and Whalley, D.C. (1993), "The Effects of Conducting Particles Distribution on the Behaviour of Anisotropic Conducting Adhesives- Non Uniform Conductivity and Shorting between Connections", Journal of Electronic Manufacturing , Vol.3, pp.85-94.

[64] Williams, D.J. and Whalley, D.C., Boyle, O.A. and Ogunjumi, A.O. (1993), "Anisotropic Conducting Adhesives for Electronic Interconnection", Journal of Soldering and Surface Mount Technology, Vol.14, pp.4-8.

[65] Yim, M.J., and Paik, K.W. (1998), "Design and Understanding of Anisotropic Conductive Films (ACFs) for LCD Packaging", IEEE Transactions on Components, Packaging and Manufacturing Technology- Part A, Vol.21, pp.226-234.

[66] Shi, F.G., Abdullah, M., Chungpaiboonpatana, S., Okuyama, K., Davidson, C. and Adams J.M. (1999), "Electrical Conduction of Anisotropic Conductive Adhesive: Effect of Size Distribution of Conducting Filler Particles", Material Science in Semi-conducting Processing, Vol.2, pp.263-269.

[67] Chiang, K.N., Chang, C.W. and Lin, J.D. (2000), "Analysis of ACA/ACF package Using Equivalent Spring Method", Proceeding of the 50th IEEE Electronics Packaging Technology Conference, Las Vegas, pp.110-116.

[68] Määttänen, J. (2003), "Contact Resistance of Metal-coated Polymer Particles Used in Anisotropically Conductive Adhesives", Journal of Soldering and Surface Mount technology, Vol.15, No.1, pp.12-15.

[69] Dou, G., Chan, Y. C. and Liu, J. (2003), "Electrical Conductive Characteristics of Anisotropic Conductive Adhesive Particles", Journal of Electronic Packaging, ASME, Vol.125, pp.609-616.

[70] Shiozawa, N., Isaka, K. and Ohta, T. (1995), "Electric Properties of Connections by Anisotropic Conductive Film", Journal of Electronic Manufacturing, Vol.5, No.1, pp.33-37.

[71] Liu, J. (1999), Conductive Adhesives for Electronics Packaging, Electrochemical Publications Ltd, Port Erin, Isle of Man. Chapter 8, pp.189.

[72] Dou, G., Whalley, D. C. and Liu, C. (2004), "Electrical Conduction Characteristics of Solid Metal Anisotropic Conductive Adhesive Particles", the 4th International IEEE Conference on Polymers and Adhesives in Microelectronics and Photonics, Portland, Oregon, pp.132-136.

[73] Tummala, R.R. (1998), *Fundamentals of Microsystems Packaging*, Published by McGraw-Hill, ISBN: 0-07-137169-9, pp.342-397.

[74] Larson, M.C., Verges, M.A. and Liu, X. (2006), "Residual Compression in Area Array Packages Induced by Underfill Shrinkage", Journal of Microelectronics and Reliability, Vol.46, Issue: 2-4, pp. 496-502.

[75] Wolf, M.J., Engelmann, G., Dietrich, L. and Reichl, H. (2006), "Flip Chip Bumping Technology-Status and Update", Journal of Microelectronics Reliability, Vol.565, Issue: 1, pp: 290-295.

[76] Ho, P.S., Wang, G.T., Ding, M., Zhao, J.H., Dai, X. (2004), "Reliability Issues for Flip-Chip Packages", Introductory Invited Paper for Journal of Microelectronics Reliability Vol.44, pp.719–737.

[77] Lau, J.H., Chang, C. (1999), "TMA, DMA, DSC and TGA of Lead Free Solders", Journal of Soldering & Surface Mount Technology, Vol.11, No. 2, pp.17-24.

[78] Environment Agency, "The Restriction of Hazardous Substances in Electrical and Electronic Equipment" (ROHS) Directive 2002/95/EC, www.environmental-agency.gov.uk

[79] EC Directive on Waste Electrical & Electronic Equipment (WEEE). DTI. Sustainable Development. www.dti.gov.uk

[80] Directive 2000/53/EC of the European Parliament & Council of 18th Sept 2000. End of Life Vehicles.

[81] Kim, K.S., Yu, C.H., Yang, J.M. (2006), "Tin Whisker Formation of Lead-free Plated Lead Frames", Journal of Microelectronics Reliability, Vol.46, pp.1080–1086.

[82] Fang, T., Osterman, M., Pecht, M. (2006), "Statistical Analysis of Tin Whisker Growth", Journal of Microelectronics Reliability, Vol.46, pp.846–8491.

[83] Surface Mounting Technology Assembly Guidelines for Fairchild's Microcouplers™ (Ball Grid Array) www.fairchildsemi.com ₁

[84] Vanfleteren, J., Vandecasteele, B., Podprocky, T. (2002), "Low Temperature Flip-Chip Process using ICA and NCA for Flexible Displays Application", Proceedings of the 50th IEEE Electronic Components and Technology Conference, pp.1385-1389.

[85] Liu, J. (1999), *Conductive Adhesives for Electronics Packaging*, Electrochemical Publications Ltd, Port Erin, Isle of Man. ISBN 0901-150-37-1, pp.183-208.

[86] Zenner, R., Connell, G. and Gerber, J.A. (1997), "Adhesive and Conductive Adhesive Flip Chip Bonding" Proceedings of the 3rd international Symposium on Advanced Packaging Materials, pp.117-119.

[87] Liu, J. (1999), *Conductive Adhesives for Electronics Packaging*, Electrochemical Publications Ltd, Port Erin, Isle of Man. ISBN 0901-150-37-1, pp.376-396.

[88] Hsieh, Y.T. (2002), "Reliability and Failure mode of Chip-on-Film with Non-conductive adhesive" Proceeding of the 4th International Symposium on Electronic Materials and Packaging, TaiWan, pp.157-160.

[89] Yim, M.J. and Hwang, J.S. (2002), "High Reliable Non-Conductive Adhesives for Flip Chip CSP Applications", Proceeding of the 52nd IEEE Electronic Components and Technology Conference (ECTC), pp.1385-1389.

[90] Caers, J.F.J.M., Zhao, X.J., Sy, H.G. and Wong, E.H. (2004), "Towards a Predictive Behaviour of Non-Conductive Adhesive Interconnects in Moisture Environment", Proceedings of the 54th IEEE Electronic Components and Technology Conference (ECTC), pp.106-112.

[91] Liu, J. (1999), *Conductive Adhesives for Electronics Packaging*, Electrochemical Publications Ltd, Port Erin, Isle of Man, ISBN: 0901 150 37 1, pp. 256-270.

[92] Pecht, J. and Pecht, M. (1995), "Long-Term Non-operating Reliability of Electronic Products". CRC press, Boca Raton, FL.

[93] http://www.eia.org/

[94] http://www.jedec.org/

[95] Chiu, Y.W., Chan, Y.C. and Lui, S.M. (2002), "Study of Short-circuiting between Adjacent Joints under Electric Field Effects in Fine Pitch Anisotropic Conductive Adhesive Interconnects" Journal of Microelectronics Reliability, Vol.42, Issue:12, pp.1945-1951.

[96] Sony Chemicals Corporation, Japan, http://www.sccj.co.jp/

[97] Luk, C.F., Chan, Y.C. and Hung, K.C. (2002), "Application of Adhesive Bonding Techniques in Hard Disk Drive Head Assembly", Journal of Microelectronics Reliability, Vol.42, Issue: 4-5, pp.767-777.

[98] Opdahl, P.J. "Anisotropic Conductive Film for Flip-chip Applications: An Introduction", The Tutorial 05 on website: http://www.flipchips.com/tutorial05.html

[99] Gonon, P., Sylvestre, A., Teysseyre, J. and Prior, C.(2001), "Combined Effects of Humidity and Thermal Stress on the Dielectric Properties of Epoxy-silica Composites", Materials Science and Engineering B83, pp.158-164.

[100] Ko, M. and Kim, M. (1998), "Effect of Postmold Curing on Plastic IC Package Reliability", Journal of Applied Polymer Science, Vol.69, No.11, pp.2187-2193.

[101] Whalley, D.C., Chen, L. and Liu, J. (2001), " Modelling of the Anisotropic Adhesive Assembly Process" Proceedings of the International Symposium on Electronic Packaging Technology, Beijing, pp.319-324, ISBN 0-7803-9811-4b.

[102] Theoretical Manual of VisualDOC, Design Optimization Software. Version 5.1.

[103] Ransom, J. B., Knight, J. N. (1990), "Global/local Stress Analysis of Composite Panels" Computers & Structures, Vol.37, pp.375-95.

[104] Woo, K., Whitcomb, J. (1994), "Global/local Finite Element Analysis for Textile Composites". Journal of Composite Materials; Vol.28, pp.1305-1321.

[105] Fenner, R.T. (1986), *Engineering Elasticity—Application of Numerical and Analytical Techniques*, Published by Ellis Harwood Ltd. ISBN: 0-85312-837-5, pp.74-104.

[106] ANSYS, Inc., Canonsburg, PA, http://www.ansys.com.

[107] Voleti, S.R., Chandra, N. and Miller, J.R. (1996), "Global-Local Analysis of Large-Scale Composite Structures Using Finite Element Methods", Computer & Structures, Vol.58, No.3, pp.453-464.

[108] Akin, J.E. (1986), *Finite Element Analysis for Undergraduates*, Published by Academic Press Limited, London, ISBN: 0-12-047655-X, pp.197-242.

[109] Database for Solder Properties with Emphasis on New Lead-free Solders, http://www.boulder.nist.gov

[110] Chan, Y.C., Hung, K.C., Tang. C.W. and Wu, C.M.L. (2000), "Degradation Mechanism of Anisotropic Conductive Adhesive Joints for Flip Chip on Flex Applications" Proceedings of the 4th International Conference on Adhesive Joining and Coating Technology in Electronics Manufacturing, pp.141-146.

[111]Crank, J. (1956), *The Mathematics of Diffusion*, Oxford University Press, Ely House, London, pp.1-50.

[112]Jain, A., Gupta, V., Basu, S.N.(2002), "A Quantitative Study of Moisture Absorption in Polyimide and Its Effect on The Strength of the Polyimide/Silicon Nitride Interface", Journal of Acta Materialia, Vol.53, pp.3147-3153.

[113]Dubek, R., Walter, H. and Michel, B. (2002), "Studies on Moisture Diffusion and Popcorn Cracking", Proceedings of the 3rd IEEE Conference on Benefiting from Thermal and Mechanical Simulation in Micro-Electronics, Paris, pp.225-232.

[114]Wong, E. H., Teo, Y. C., Lim, T. B., (1998), "Moisture Diffusion and Vapour Pressure Modelling of IC Packaging", Proceedings of the 48th IEEE Electronic Components and Technology Conference (ECTC), pp.1372-1378.

[115]Wong, E.H., Koh, S.W., Lee, K.H. and Rajoo, R. (2002), "Advanced Moisture Diffusion Modelling and Characterisation for Electronic Packaging", Proceedings of the 52nd of IEEE Electronic Component and Technology Conference (ECTC), pp.1297-1303.

[116]Wong, E.H., Chan, K.C., Rajoo, R. and Lim, T.B. (2000), "The Mechanics and Impact of Hygroscopic Swelling of Polymeric Materials in Electronic Packaging", Proceedings of the 50th of IEEE Electronic Component and Technology Conference (ECTC), pp.576-580.

[117]Tee, T.Y. and Ng, H.S. (2002), "Whole Field Vapour Pressure Modelling of QFN during Reflow with Coupled Hygro-mechanical Thermo-mechanical Stresses", Proceedings of the 52nd Electronic Components and Technology Conference (ECTC), pp.1552-1559.

[118]Tee, T.Y., Kho, C.L., Yap, D., Toh, C., Baraton, X. and Zhang, Z. (2003), "Reliability Assessment and Hygro-swelling Modelling of FCBGA and No-flow Underfill", Journal of Microelectronics Reliability, Vol.43, pp.741-749.

[119]Kirsten, W.Z., Walter, H., Hélène, F. (2005), "Moisture Diffusion in Printed Circuit Boards: Measurements and Finite-Element-Simulations", Journal of Microelectronics Reliability, Vol.45, pp.1662-1667.

[120]Ardebili, H., Hillman, C., Natishan, M.A.E., McCluskey, P., Pecht, M.G. and Peterson, D. (2002), "A Comparison of the Theory of Moisture Diffusion in Plastic Encapsulated Microelectronics With Moisture Sensor Chip and Weight-Gain Measurements", IEEE Transactions on Components and Packaging Technologies, Vol.25, No.1, pp.132-139.

[121]Liu, J., Wang, Y., Morris, J. and Kristiansen, H. (2005), "Ontology for the Anisotropic Conductive Adhesive Interconnect Technology for Electronics Packaging Applications",

Proceedings of the Seventh IEEE CPMT Conference on High Density Microsystem Design, Packaging and Failure Analysis (HDP'05), pp.156-172.

[122] Yim, M.J., Ryu, W., Jeon, Y.D., Lee, J., Kim, J., Paik, K.W. (1999), "Microwave Model of Anisotropic Conductive Adhesive Flip-Chip Interconnections for High Frequency Applications", Proceeding of the 49th Electronic Components & Technology Conference (ECTC), pp.488-492.

[123] Fan, S.H. and Chan, Y.C. (2002), "Effect of Misalignment on Electrical Characteristics of ACF Joints for Flip Chip on Flex Applications", Journey of Microelectronics Reliability, Vol.42 No.7, pp.1081-1090.

[124] Dou, G.B., Whalley, D.C., Liu, C.Q. (2006), "Effect of Co-planarity Variation on Anisotropic Conductive Adhesive Assemblies", Proceedings of the 56th Electronic Components & Technology Conference (ECTC), San Diego, USA, pp.932-938.

[125] Liu, J (2001), "Life Time Prediction of Anisotropic Conductive Adhesive Joints during Temperature Cycling for Electronics Interconnect", Proceedings of the 1st International IEEE Conference on Polymers and Adhesives in Microelectronics and Photonics, pp.209-212.

[126] Yin, C.Y., Alam, M.O., Chan, Y.C., Bailey, C. and Lu, H. (2003), "The Effect of Reflow Process on the Contact Resistance and Reliability of Anisotropic Conductive Film Interconnection for Flip Chip on Flex Applications", Journal of Microelectronics Reliability, Vol.43, pp.625-633.

[127] Yin, C.Y., Lu, H., Bailey, C. and Chan, Y.C. (2004), "Effects of Solder Reflow Process on the Reliability of Flip-Chip on Flex Interconnections Using Anisotropic Conductive Adhesives", IEEE Transactions on Electronics Packaging Manufacturing, Vol.27, No.4, 2004, pp.254-259.

[128] Yin, C.Y., Lu, H., Bailey, C. and Chan, Y.C (2006), "Macro-Micro Modelling Analysis for an ACF Flip Chip", Journal of Soldering and Surface Mounting Technology, Vol.18, No.2, pp.27-32.

[129] Yin, C.Y., Lu, H., Bailey, C. and Chan, Y.C (2003), "Using the Anisotropic Conductive Adhesive (ACA) for Flip-Chip Interconnects" Proceeding of Postgraduate Research Conference in Electronics, Photonics, Communications and Software (PREP), pp.89-90.

[130] Yin, C.Y., Lu, H., Bailey, C. and Chan, Y.C (2003), "Experimental and Modeling Analysis of the Reliability of the Anisotropic Conductive Films", Proceeding of the 53rd Electronic Component and Technology Conference (ECTC), pp.698-702.

[131]Yin, C.Y., Lu, H., Bailey, C. and Chan, Y.C (2004), "Effects of Reflow Process on the Reliability of Flip Chip on Flex Interconnections Using Anisotropic Conductive Adhesives", Proceeding of the International IEEE Conference on Asian Green Electronics (AGEC), pp.240-245.

[132]Lu, H., Bailey, C., Yin, C., Stoyanvo, S. (2004), "Modeling the Reliability of Green Electronic Interconnects", Proceedings of the International IEEE Conference on Asian Green Electronics (AGEC), pp.63-67.

[133]Yin, C.Y., Lu, H., Bailey, C. and Chan, Y.C (2005), "Moisture Effects on the Reliability of Anisotropic Conductive Films", the 6th International Conference on Thermal, Mechanical and Multiphysics Simulation and Experiments in Micro-Electronics and Micro-Systems (EuroSimE 2005), Berlin, pp.162-167.

[134]Yin, C.Y., Lu, H., Bailey, C. and Chan, Y.C (2005), "Experimental and Modeling Analysis on the Moisture Induced Failures in Flip Chip Interconnections with Anisotropic Conductive Adhesives", International IEEE Conference on Asian Green Electronics (AGEC), ShangHai, pp.172-177.

[135]Yin, C.Y., Lu, H., Bailey, C. and Chan, Y.C (2005), "Macro-Micro Modeling Analysis for High Density Packaged Flip Chips", the 7th International IEEE CMPT Conference on High Density Packaging and Component Failure Analysis (HDP'05), Shanghai, pp.105-108.

[136]Yin, C.Y., Lu, H., Bailey, C. and Chan, Y.C, (2005) " Moisture Effects on the Reliability of Anisotropic Conductive Film Interconnection for Flip Chip on Flex Applications", Proceedings of InterPACK: The Pacific Rim/ASME International Electronic Packaging Technical Conference and Exhibition, San Francisco.

[137]Yin, C.Y., Lu, H., Bailey, C. and Chan, Y.C (2005), "Modeling of the Performance of Flexible Substrates for Lead-Free Applications", Proceedings of the 7th Electronic Packaging Technology Conference (ECTC), Singapore, pp.342-346.

[138]Yin, C.Y., Lu, H., Bailey, C. and Chan, Y.C (2005), "Moisture Effects on the Reliability of ACF Interconnections", Electronics World, pp.20-25, ISBN: 9-770959-833103.

[139]Dieter, G.E. (1988), *Mechanical Metallurgy*, McGraw-Hill Book Company Ltd. ISBN: 0-07-084187-X, pp.17-68.

[140]Taylor, G.A. (1996), "A Vertex Based Discretisation Scheme Applied to Material Non-Linearity within a Multi-Physics Finite Volume Framework", A thesis for the Doctor of Philosophy of the University of Greenwich.

[141] Buchanan, G.R. (1994), *Finite Element Analysis*, ISBN: 0-07-008714-8.

[142] Schwarz, H.R. (1988), *Finite Element Methods*, Academic Press limited, London, ISBN: 0-12-633010-5.

[143] Lewis, P.E., and Ward, J.P. (1991), *The Finite Element Method—Principles and Applications*, published by Addison-Wesley Publishers Ltd, ISBN: 0-201-54415-6.

[144] Akin, J.E. (1986), *Finite Element Analysis for Undergraduates*, Published by Academic Press Limited, London, ISBN: 0-12-047655-X, pp.1-8.

[145] Clough, R.W. (1960), "The Finite Element Method in Plane Stress Analysis", Proceedings of 2nd ASCE Conference on Electronic Computation, Pittsburgh.

[146] Hrennikoff, A. (1941), "Solution of Problems in Elasticity by the Frame Work Method", Journal of Applied Mathematics, Vol.8, No.4, pp.169-175.

[147] McHenry, D. (1943), "A Lattice Analogy for the Solution of Plane Stress Problems", Journal of Institution of Civil Engineers, Vol.21, pp.59-82.

[148] Turner, M., Clough, R., Martin, H., and Topp, L. (1956), "Stiffness and Deflection Analysis of Complex Structures", Journal of Aeronautical Sciences, Vol.23, No.9, pp. 805-824

[149] Bailey, C. and Cross, M. (1995), "A Finite Volume Procedure to Solve Elastic Solid Mechanics Problems in Three Dimensions on An Unstructured Mesh", International Journal for Numerical Methods in Engineering, Vol.38, pp.1757-1776.

[150] Cross, M., Evans, J. W. and Bailey, C. (2001), *Computational Modelling of Materials, Minerals and Metals Processing*, Publication of the Minerals, Metals and Materials Society, ISBN: 0-87339-513-1.

[151] Griebel, M., Keyes, D.E., Nieminen, R.M., Roose, D. and Schlick, T. (1999), *Computational Partial Differential Equations—Numerical Methods and Diffpack Programming*, Spring – Verlag Berlin Heidelberg New York, ISBN: 3-540-65274-4, pp.367-402.

[152] PHYSICA Multi-Physics Ltd, http://www.gre.ac.uk/~physica

[153] Femsys Ltd, http://www.femsys.co.uk/